Hydrodynamic and Morphologic Modelling of Alternative Design Scenarios Using CMS: Shippagan Gully, New Brunswick

Mitchel Provan

Submitted under the supervision of
Dr. Ioan Nistor
Dr. Andrew Cornett

Partially funded by the National Research Council Ocean, Coastal and River Engineering

In partial fulfillment of the requirements
for the degree of
Masters of Applied Science in Civil Engineering

Department of Civil Engineering
University of Ottawa
August, 2013

Abstract

There is a highly dynamic tidal inlet known as Shippagan Gully located on the Gulf of St-Lawrence near Le Goulet, New Brunswick. This tidal inlet is highly unusual due to the fact that the inlet is part of a waterway that transects the Acadian Penninsula, connecting the Bay de Chaleurs and the Gulf of St-Lawrence. Thus, the inlet has two open boundaries with phase lagged tidal cycles that drives flow through the inlet. The phase lag in the tidal cycles causes an imbalance in the flood and ebb flows, which leads to an ebb flow twice as strong as the flood flow. Over the past few decades the shipping activities through the inlet have been threatened due to the narrowing of the navigation channel caused by deposited sediment on the east side of the channel. Many engineering projects have been undertaken at Shippagan Gully in order to try and mitigate the deposition problem. However, these attempts have either been unsuccessful or the engineered structures have deteriorated over the years.

This study uses a numerical model that is based on coupling the most recent CSM-Flow and CMS-Wave models developed by the US Army Corps of Engineers. The numerical model was used to provide guidance concerning the response of the inlet to various potential interventions aimed at improving navigation safety. The development of the model and the methodology followed to calibrate and validate it against field measurements from the site is described. The coupled numerical model is capable of simulating the depth-averaged currents generated within Shippagan Gully and along the neighbouring coastline due to the effects of tides, winds and waves; the transport of non-cohesive sediments; and the resulting changes in seabed morphology. Once the model was calibrated and validated to a reasonable precision, the model was applied to investigate coastal processes for the existing conditions of the inlet and for twenty-one alternative future scenarios (inlet configurations).

A second numerical model, GenCade, was employed to model the potential shoreline change downdrift (south-west) of the inlet due to the addition of a sediment trapping structure. The model was calibrated to net longshore sediment transport rates obtained through the Kamphuis (1991) and CERC (1984) longshore transport equations. The calibrated GenCade model was used to make educated conclusions on any potential changes downdrift of the inlet.

The research described herein contributes towards an improved understanding of the hydrodynamics and sedimentary processes at Shippagan Gully. Moreover, the results presented herein can be used to help select an optimal approach for stabilizing and widening the channel through the inlet mouth in order to improve navigability and increase navigation safety. This thesis was completed in partnership with NRC Ocean, Coastal and River Engineering (NRC-OCRE) and with funding provided in part by Public Works and Government Services Canada (PWGSC).

Acknowledgements

Firstly I would like to thank my two thesis supervisors Dr. Ioan Nistor (University of Ottawa) and Dr. Andrew Cornett (National Research Council). Dr. Nistor is responsible for introducing me to the field of coastal engineering and has spent countless hours providing me with guidance on everything from research, to scholarship applications and my future career. Without Dr. Nistor, my success as a graduate student and as an aspiring engineer would not have been possible. Dr. Cornett has spent many hours going over my research methodology and results, allowing me to produce the best work I could possibly do. Without his coastal engineering knowledge or research guidance, the quality of my work and understanding of my research topic would be nowhere near its current level. To both Dr. Nistor and Dr. Cornett, I owe a bigger thank you than I could ever write.

I would also like to thank everyone else who has helped me during my graduate studies, including Mr. Thierry Faure (NRC), Dr. Mahdi Razmaz (Hiroshima University), Dr. Wayne Jenkinson (NRC), Mr. Martin Serrer (NRC) and the remainder of the staff at the Canadian Hydraulic Centre and the University of Ottawa.

Lastly, I would like to thank all of my family and friends. Even though they may not quite understand all the aspects of my research, they were supportive and encouraging throughout my entire graduate studies.

Table of Contents

List of Tables

List of Figures

Page

List of Symbols

A	empircal coefficient typically ranging from 0.1 to 2 (ND)
A_{cr}	empirical coefficient (ND)
a	empircal coefficient (ND)
a_i	amplitude of tidal constituent (m)
b	empirical coefficient (ND)
b_{rey}	sediment transport coefficient dependent on Reynolds number (ND)
C	wave celerity (m/s)
C_{con}	depth-averaged sediment concentration (volume of sediment/total volume)
C_{ch}	Chezy friction coefficient (ND)
C_b	empirical bottom-stress coefficient
C_d	wind drag coefficient (ND)
C_ε	coefficient determined from an empirical curve (ND)
C_x	characteristic velocity in wave-action density equation (m/s)
C_y	characteristic velocity in wave-action density equation (m/s)
C_Θ	characteristic velocity in wave-action density equation (m/s)
c_f	Darcy-Weisbach fricition coefficient (ND)
c_R	reference concentration in Lund-CIRP formula for suspended load (kg/m^3)
D	characteristic particle diameter (m)
D_{dep}	sediment deposition rate (kg/s)
D_x	diffusion coefficient for the x direction (ND)
D_y	diffusion coefficient for the y direction (ND)
d	water depth (m)
d_b	water depth at wave breaking (m)
D35	grain diamater representing the 35^{th} percentile of finer material (mm)
D50	grain diamater representing the 50^{th} percentile of finer material (mm)
D90	grain diamater representing the 90^{th} percentile of finer material (mm)
d_*	non-dimensionalized grain size (ND)
E_{total}	total energy density (J/m^2)
f	Coriolis coefficient (rad/s)
g	gravitational acceleration (m/s^2)
H	nearshore wave height (m)
H_b	breaking wave height (m)
H_{sb}	significant breaking wave height (m)
h	total water depth (m)
K_r	refraction coefficient (ND)
K_s	shoaling coefficient (ND)
K_x	sediment diffusion coefficient for the x-direction (ND)
K_y	sediment diffusion coefficient for the y-direction (ND)
k	wave number (m^{-1})
L	wavelength (m)
m_b	beach slope (m/m)
N	wave-action density ($J\cdot s/m^2$)
n	Manning's roughness coefficient (ND)
n_{por}	sediment porosity (ND)

P	sediment pick-up rate (kg/s)
Q_k	potential longshore sediment transport (Kamphuis formula) (m^3/year)
Q_s	longshore sediment transport rate (CERC formula) (m^3/year)
Q_{sink}	sink term in a sediment budget (m^3)
Q_{source}	source term in a sediment budget (m^3)
q_{bw}	bed load parallel to wave direction (m^3/m·s)
q_{bn}	bed load normal to wave direction (m^3/m·s)
q_{sb}	bed load rate (m^3/m·s)
$\bar{q}_{sb}$	gravimetric specific bed-load rate (N/m·s)
q_x	flow per unit width parallel to the x-axis (m^2/s)
q_y	flow per unit width parallel to the y-axis (m^2/s)
q_{tot}	total load (suspended and bed load) (m^3/m·s)
R	hydraulic radius (m)
S_{xx}	wave-driven radiation stress (N/m^2)
S_{xy}	wave-driven radiation stress (N/m^2)
S_{yy}	wave-driven radiation stress (N/m^2)
T	wave period (s)
T_{op}	peak wave period (s)
t	time (s)
U	total current velocity (m/s)
U_c	depth average current velocity (m/s)
u	depth-averaged current velocity parallel to the x-axis (m/s)
u_b	mean horizontal wave orbital velocity at the sea bed (m/s)
V	fluid velocity (m/s)
V_*	shear velocity (m/s)
υ	depth-average current velocity parallel to the y-axis (m/s)
W	wind speed (m/s)
w	density of bed material divided by density of water (ND)
z	water elevatoin relative to the bed (m)
α	wave crest angle relative to the shoreline (°)
α_b	breaking wave angle relative to the shoreline (°)
α_i	phase angle of tidal constituent (° or rad)
γ_s	specific gravity (N/m^3)
κ	wave diffraction term (ND)
η	water surface elevation relative to the still water level (m)
ρ	fluid density (kg/m^3)
ρ_a	density of air (kg/m^3)
ρ_s	sediment density (kg/m^3)
ρ_w	density of seawater (kg/m^3)
Θ	wind direction (°)
$\Theta_{cw,m}$	mean Shields parameter for combined waves and currents (ND)
Θ_{cw}	maximum Shields parameter for combined waves and currents (ND)
τ	shear stress (N/m^2)
τ_b^*	dimensionless shear stress (ND)
τ_{bmax}^*	maximum shear stress at the bed (ND)
τ_{cr}	shear stress at incipient motion (N/m^2)

Comment [i2]: Symbols not visible…

Comment [i3]: I could not see these symbols

τ_c^*	dimensionless critical shear stress shear stress (ND)
τ_{bx}	bottom stress parallel to the x-axis (N/m^2)
τ_{by}	bottom stress parallel to the y-axis (N/m^2)
τ_{wx}	surface stress parallel to the x-axis (N/m^2)
τ_{wy}	surface stress parallel to the y-axis (N/m^2)
τ_{Sx}	wave stress parallel to the x-axis (N/m^2)
τ_{Sy}	wave stress parallel to the y-axis (N/m^2)
υ	kinematic viscosity (m^2/s)
ω_i	angular frequencies of tidal constituent (s^{-1})

ND refers to non-dimensional units

1 Introduction

Shippagan Gully is a narrow channel at the mouth of a dynamic tidal inlet located on the Gulf of Saint Lawrence near Le Goulet, New Brunswick, Canada (see Figure 1.1). It is a particularly interesting and complex tidal inlet due to the fact that its tidal lagoon bisects the Acadian peninsula and is open to the sea at two locations where there is an appreciable phase lag in the tidal cycle. Due to the nature of this phase lag in tidal forcing, the ebb flows through Shippagan Gully, which routinely exceed 2 m/s, are roughly twice as strong as the flood flows. As a consequence of this imbalance, the hydrodynamic and sedimentary processes at the inlet, and the morphological features produced by these processes are strongly dominated by the ebb flows. The tides at Shippagan Gully are semi-diurnal, and the tidal range is generally on the order of 2 m or less.

For many years Shippagan Gully has served as an important navigation channel, providing boaters from communities in the Acadian Peninsula and the Bay des Chaleurs with direct access to the open waters of the Gulf of St-Lawrence. The fishing industry, a very important element of the local economy, relies on safe navigation through the inlet. However, over the last few decades, significant volumes of sediment have accumulated within the inlet mouth due to natural processes. These accumulations have constricted the navigation channel, making it more difficult and riskier for fishing vessels to pass safely through the inlet on their way to and from the Gulf of St-Lawrence. Many of the larger vessels which once relied on the inlet for safe and sheltered passage to and from the Gulf of St. Lawrence can no longer safely navigate the constricted channel. These vessels must now circumnavigate the Acadian Peninsula, thus considerably lengthening their journey and forcing passage through the rough waters off Miscou Point.

Figure 1.1 - Shippagan Gully inlet is located on the Acadian Peninsula near Le Goulet, New Brunswick (navigation route through the Acadian Peninsula shown in red).

The local shoreline along the Gulf of St. Lawrence is approximately linear and is oriented along the bearing from SW to NE. The shoreline on both sides of the inlet features sandy beaches backed by low vegetated dunes. The nearshore wave climate at the site features significant wave heights ranging from 0.5 up to ~4 m, and peak periods from 3 to 11s. The historical evolution of the inlet provides clear evidence of a wave-driven net longshore sediment transport flowing from NE to SW. This is consistent with the fact that the local wave climate is dominated by waves approaching from easterly directions. Waves also approach the site from the south and southeast, but waves from these directions tend to occur less frequently and/or tend to be less energetic.

In 2010, Public Works and Government Services Canada (PWGSC), acting for Fisheries and Oceans Canada (DFO), commissioned the National Research Council (NRC) to develop a numerical model of the coastal processes at Shippagan Gully and apply the model to assess the potential impact of several alternative strategies for stabilizing the navigation channel. NRC developed a numerical model based on the Coastal Modelling System (CMS) that was able to simulate the tidal and wave-driven hydrodynamics at the inlet and predict the resulting sediment transport and morphology change over short (days) and long (years) time scales. The hypothetical scenarios that were investigated included new jetties, training walls, bottom armouring and combinations of these various alternatives. The methods and results of this initial study are described in Logan et al., 2012.

In May 2012, NRC was again retained by PWGSC to conduct further numerical simulations of coastal processes at Shippagan Gully inlet and help assess methods to mitigate the sedimentation problem and promote the formation of a safer navigation channel. The main objectives of this Phase II study were to improve the resolution and precision of the numerical model employed in Phase I (through the use of new features in the CMS numerical model), to re-calibrate the improved/refined model to observed hydrodynamics and past morphology change, and then use the improved model to estimate the future hydrodynamics and morphology changes at Shippagan Gully for a number of additional scenarios. The Phase II study was conducted principally by the present author and in partnership with the University of Ottawa, thereby forming the bases of this thesis.

1.1 Thesis Objectives

The main objective of this study is to utilize the Coastal Modeling System (CMS) numerical model to produce simulations of various design options to provide guidance for future coastal works and maintenance at the Shippagan Gully tidal inlet. The steps taken in order to successfully meet the objective of this study are as follows:

1. Site visit and collection of sediment and hydrodynamic data
2. Refinement of the CMS numerical model developed in Phase 1;
3. Calibration of hydrodynamic processes;
4. Validation of hydrodynamic processes;
5. Calibration of morphodynamic processes;
6. Simulation of coastal processes for existing conditions;
7. Simulation of coastal processes for selected scenarios previously modelled in Phase 1;
8. Simulation of coastal processes for new scenarios not previously modelled; and
9. Assessment of potential impacts downdrift of the inlet.

The numerical model that was selected to be used in this study is the Coastal Modeling System (CMS) (developed by the Coastal Inlet Research Program of the US Army Corps of Engineers). The CMS numerical model is composed of two coupled numerical models; CMS-Flow (Buttolph *et al.*, 2006) and CMS-Wave (Lin *et al.*, 2008). The CMS models are the state of the art numerical models for simulating the hydrodynamics, sediment transport and morphology change of coastal and tidal inlets. The CMS models were calibrated and validated to field measurements (hydrodynamic and hydrographic surveys) and were then applied to simulate the current situation at Shippagan Gully as well as numerous design scenarios (developed in collaboration with PWGSC) in an attempt to find an inlet configuration that will provide a stable, navigable channel.

1.2 Importance and Novelty of the Thesis

Since the 1800's there have been multiple attempts at maintaining a stable navigation channel through the Shippagan Gully tidal inlet. In an effort to stabilize the channel, multiple jetties have been constructed and dredging work has been completed, however the navigation channel continues to fill with sediment thereby constricting the current navigation channel. The work presented in this thesis is an attempt to find a practical solution to the sedimentation problem and to provide the local fishers (which are crucial to the local economy) a safe, navigable channel to use. This thesis will provide an important contribution to the future coastal works at the Shippagan Gully inlet, and therefore significantly affect those who utilize the inlet on a daily basis.

The CMS numerical model that was constructed for this study utilizes some of the newest features available for the CMS model; telescoping mesh and multiple grain sized sediment transport (these features are explained in detail within this thesis). There is little documentation of these features being incorporated outside of studies conducted by the USACE (the developers of the numerical model). This thesis provides an example of how these new features can be applied in an attempt to improve the numerical results of a tidal inlet study as well as a comparison with an earlier constructed CMS model that does not utilize these features.

Another novelty of this study lies in the complexity of the morphology patterns and hydrodynamics of the Shippagan Gully tidal inlet. The studied inlet does not exhibit the expected morphology characteristics normally found in a tidal inlet. The extensive history of engineering activities at Shippagan Gully has produced a complicated and unique morphologic situation. Unlike other tidal inlets, the processes that contribute to the formation of the morphologic structures and movement of sediment around the inlet are not easily identified. In addition, the hydrodynamics of the inlet are rather atypical. Shippagan Gully transects the Acadian Peninsula and is therefore subjected to tidal forcing from two sources; the Gulf of St. Lawrence and the Bay de Chalieurs. This can lead to a phase lag in the tides, which may result in uneven ebb and flood flows. Therefore, standard methods that are used to classify and analyze the hydrodynamics of tidal inlets, such as escoffier curves and tidal prisms, are not easily applied to this inlet. Due to the complex nature of the morphology characteristics and hydrodynamics of Shippagan Gully, this inlet cannot be studied or properly understood based on past knowledge and experience obtained from previous tidal inlet studies. Therefore, the complex nature of this inlet makes the research completed in this thesis, both novel and unique.

1.3 Organization of the Thesis

This thesis is divided into 13 main sections:

Section1 - Introduction: This section provides a brief introduction on the Shippagan Gully tidal inlet, as well as the objectives and importance of the study.

Section 2 - Literature Review: Provided in Section 2 is a literature review of the main scientific concepts that are crucial in order to understand the complexity of the hydrodynamics and sediment transport found in and around a tidal inlet. A summary of past tidal inlet case studies are also included in this section to demonstrate some of the scientific concepts in a practical situation.

Section 3 - Historical Background: A brief history is presented on the man-made coastal structures that have been constructed at the Shippagan Gully inlet beginning in the 1800's and extending to the present day.

Section 4 - Summary of Phase I Findings: The main conclusions from the Phase I study are summarized in Section 4. In addition, the two best performing scenarios (according to the Phase I numerical model results) are reviewed.

Section 5 - Field Investigations: Multiple field investigations have been conducted to gather information on the hydrodynamics, sediment characteristics and bathymetry of Shippagan Gully and its surrounding areas. The methodology and resulting data from these field investigations is summarized in this section.

Section 6 - CMS Model Development: All of the tasks needed to construct the numerical model used in this study are presented in this section. Some of the tasks include: numerical model grid development, CMS-Flow and CMS-Wave boundary conditions, hydrodynamics calibration and validation and morphology change calibration. The governing numerical equations and numerical methods are also discussed.

Section 7 - Modelling of Coastal Processes for Existing Conditions and Alternative Inlet Configurations: This section describes the twenty-one alternative inlet configurations that were modelled as well as how these configurations were implemented into the numerical model.

Section 8 - Baseline Results for Existing Conditions - Using the calibrated numerical model, the existing conditions for the Shippagan Gully inlet were simulated for a long-term period (6 years) and a short-term period (25 hour storms) using 2010 bathymetry. The hydrodynamics, sediment transport patterns and morphology change for the existing conditions are presented and discussed in detail.

Section 9 - Results for Phase I Scenarios: Three scenarios from the Phase I study were selected and remodelled with the refined and recalibrated numerical model constructed for this study. The hydrodynamics, sediment transport and morphology change are analyzed and the difference between the results from the Phase I model and the current model are discussed.

Section 10 - Results for New Inlet Configurations: The results for twenty-one new inlet configurations (developed in collaboration with PWGSC) were simulated and the results are presented in Section 9.

Section 11 - Assessment of Potential Impacts Southwest of the Inlet: Since any sort of sediment trapping coastal structure (such as the jetties modeled in this study) can impact the shoreline downdrift of the inlet (in the case of Shippagan Gully, SW of the inlet). Using the simulation results from Section 9 and the numerical model GenCade, the potential impacts SW of the inlet are assessed for 4 of the scenarios.

Section 12 - Conclusions and Recommendations: This section of the report provides an overall conclusion of the modelled scenarios and based on the model results, recommendations for the future coastal works at Shippagan Gully.

Section 13 - Future Work: The final section of this thesis outlines future work that the author views important for the ongoing study of the Shippagan Gully tidal inlet and for the numerical modeling of tidal inlets in general.

It is important to note that there is not a specific "Results and Discussion" section. Instead, the results and corresponding discussion of the results are presented over four sections (Sections 8-11). This approach was taken to organize the results of this study in a more concise and easy to follow manner.

2 Literature Review

Before the research for this thesis is presented and discussed, it is important to understand the complex hydrodynamics and morphologic processes that occur within and around a tidal inlet. A review has been conducted on the available literature in order to provide the necessary theoretical background of tidal inlets. This includes a description of tidal inlets and their importance to society, the various hydrodynamic processes that drive flow through the inlet, the numerous complex morphology characteristics observed at tidal inlets, the formation of these morphology characteristics and various field investigation techniques that are required to gather data to help understand and model these inlets. In addition, a brief summary of two case studies is provided in order to show how these theoretical processes are applied at two tidal inlets around North America.

2.1 Tidal Inlets

A tidal inlet is a short, narrow waterway which connects a lagoon to a larger body of water, such as the ocean or sea. Tidal inlets are distinguished from other coastal inlets in that the primary driving hydrodynamic force is the astronomical tides. The tides drive water through the inlet, filling and emptying the lagoon based on the tidal cycle. Typically, tidal inlets are formed by waves penetrating a barrier island, allowing water to be transferred between the ocean and the lagoon that was sheltered by the barrier island. Barrier islands are morphologic features composed of narrow strips of sand running parallel to the mainland coast. Once the barrier island has been penetrated, the tides are able to force a flow through the newly formed inlet. However, if the tidal flow is too weak, the inlet will close over time due to the littoral drift (sediment transport along the coastline) causing deposition within the inlet, reconnecting the barrier islands. However, with a large enough hydrodynamic forcing, the tidal flow can create a self-scouring channel through the inlet. Therefore, the cross-sectional area of the inlet depends on either the volume of the tidal lagoon, or the tidal range. Generally, inlets with large cross-sectional areas are found in locations where the tidal lagoon is large or the tidal range is high, or both. Either scenario produces enough water entering and exiting the lagoon, known as the tidal prism, to scour a large natural channel. The opposite can occur where the tidal prism is small, or the tidal range is limited, which would result in an inlet with a smaller cross-section. An example of a barrier island with a tidal inlet is shown in Figure 2.1.

Tidal inlets have both an important ecological and socio-economic impact on the area where they are located. The inlets serve an essential ecological function in the exchange of lagoon water with the ocean during the tidal cycles. The tide flushes the lagoon of sediment and pollutants while also maintaining water quality and salinity levels required for aquatic life (Dean and Dalrymple, 2002). On the socio-economic level, a tidal inlet provides a natural channel which is widely used as a transportation system for commercial, military and recreational vessel traffic. The vessels are able to traverse from the ports and harbours located within the lagoons, closer to the mainland, out to the ocean in a relatively quick and easy fashion. This is extremely important aspect in the research completed for this thesis, as the Shippagan Gully inlet is mainly utilized by local fishers to travel from the harbours to the fishing grounds in the Gulf of St. Lawrence. Since the local economy thrives on the fishing industry, the tidal inlet at Shippagan is crucial to the surrounding community.

Figure 2.1 - Example of a barrier island transected by a natural tidal inlet in North Carolina (Google Earth, 2013).

2.2 Hydrodynamics of Tidal Inlets

There are two main mechanisms that are responsible for forcing the hydrodynamics at tidal inlets: astronomical tides and water waves. Combined, these two processes create a complex flow field at and around tidal inlets and is the primary driving force behind the morphology structures. Therefore, it is crucial to have a basic understanding of the separate hydrodynamic processes in order to try and understand the intricate situation present at a tidal inlet.

2.2.1 Tides

Astronomical tides are the result of a combination of four forces acting on individual water particles: gravitational attraction of the Earth, centrifugal force generated by the rotation of the Earth-Moon combination, gravitational attraction of the Moon and gravitational attraction of the sun (Kamphuis, 2000). The most significant of these four forces are the gravitational pull of the Moon and sun. Based on these two forces, two equilibrium tides can be theorized; one case where the force of the sun is neglected (only the force of the Moon is applied) and another case where both the force of the Moon and the sun are taken into account. An equilibrium tide is the assumption that the tidal forces act on the water for a long enough time such that equilibrium is achieved between the tide generating force and gravity (Kamphuis, 2000). If it is assumed that the entire Earth is covered with water and the first equilibrium tide case is applied (only the force from the Moon is applied), then the resulting force on the water particles is a small horizontal one. On the side of the Earth facing the Moon, the water particles are moved towards the Moon and on the side of the Earth facing away from the Moon, the water particles are moved away from the Moon (see Figure 2.2). The end result is two bulges of high water on each side of the Earth, with the bulges being in line with the Moon. As the Earth rotates it would pass through two high water levels and two low water levels each day, which would produce a resulting tidal period of 12 hours. However, since the Moon also orbits the Earth as the Earth rotates, the bulges of water follow the position of the Moon and the actual tidal period would be slightly longer, at 12.42 hours.

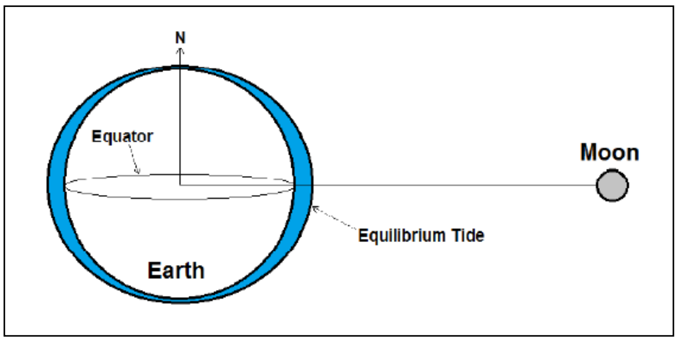

Figure 2.2 - Equilibrium tide created by the Moon's gravitational force with a period of 12.42 hours (Logan, 2012).

Once the force of the sun is added to the idealized water covered Earth, a second, smaller set of bulges would be created; one toward the sun and one away from the sun. The resulting period of the tide generated by the sun would be 12 hours. Combining the forces of the Moon and the sun will create tides higher than average and lower than average depending on the location of the sun and the Moon relative to the Earth. The higher tides, called spring tides, occur when the Moon and the sun are aligned, creating a summation of the forces acting on the water particles. The smaller tides, called neap tides, occur at quarter Moon, when the forces of the sun and the Moon are 90° out of phase.

So far, it has been assumed that the Moon and the sun lie in the plane of the equator, which is rarely the case. When the Moon or sun has a North or South declination with respect to the equator, as shown in Figure 2.3, one of the water bulges will lay above the equator, and one of the water bulges will lay below the equator. In this case, as the Earth rotates, an area on the Earth will be subjected to two unequal tides per day, otherwise known as daily inequality. The daily inequality generated by the force of the Moon repeats itself every lunar month (29.3 days), while the daily inequality generated by the force of the sun repeats itself every year.

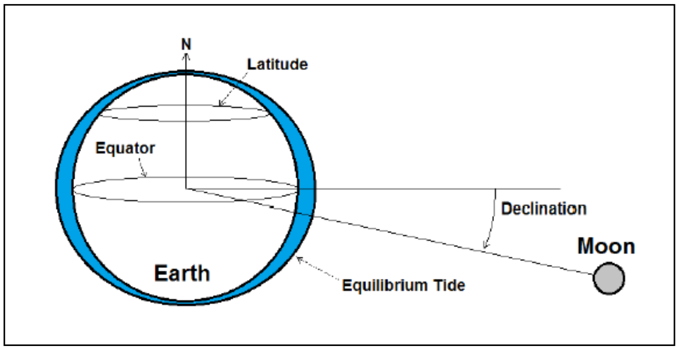

Figure 2.3 - Effect of Moon’s declination on the equilibrium tide, producing a daily inequality which repeats every 29.3 days (Logan, 2012).

The tides created by the gravitational forces of the Moon and sun, as well as the declination of the Moon and the sun, are only the main four influences on the tidal characteristics. In reality, there are many secondary effects, which all influence the tides. These secondary effects can be viewed as separate tide generators, each having its own strength, frequency and phase angle with respect to the others. Each of these tidal components is called a tidal constituent, and the resulting tide is a combination of the effects of the Moon, the sun and these secondary components (Dronkers, 1964).

In the discussion above, two overlaying assumptions have been made; that the Earth is uniformly covered with water and the same forces act everywhere. These assumptions would allow for an equilibrium tide to develop. However, when the Earth's land masses are introduced, it further complicates the simple tidal picture discussed so far. The land would not turn through the tide, but instead move the water as the Earth rotates. Therefore, the only place where an equilibrium tide can develop is in the Southern Hemisphere, where the Earth is circled by one uninterrupted band of water. An equilibrium tide can form in this band of water and propagate into the various oceans around the world. Since it takes time for the tide to propagate around the world, an actual tidal constituent lags behind the theoretical tidal constituent. For example, the spring tide should theoretically occur when there is a full Moon, however in reality, the spring tide actual occurs some time after the full Moon.

In addition, the land masses on the Earth also cause some tidal constituents to resonate within various seas, bays and estuaries. This results in some tidal constituents being amplified and others completely disappear, making the tide unique at every location. One constituent that is often magnified is the daily inequality, which increases the difference between the larger and smaller daily tides. In some cases the difference is so large that the smaller daily tides become almost non-existent, turning the semi-diurnal (twice per day) tides to a diurnal (once per day) tide (Kamphuis, 2000).

2.2.1.1 Tidal Analysis and Prediction

In order to determine which tidal constituents affect the tide in a certain location, a tidal analysis can be conducted. A tidal analysis consists of separating the recorded tide into as many of its constituents as possible (Dronkers, 1964). Assuming that the tide is represented by the harmonic summation:

$$\eta_T(t) = a_0 + \sum_{i=1}^{I} a_i \cos(\omega_i t + \alpha_i) \qquad (2.1)$$

where η_T(t) is the tidal water level at time t, a_0 is the mean water level, a_i and α_i are the amplitudes and phase angles of the tidal constituents and ω_i are the angular frequencies. Given the harmonic summation, the main goal is to determine the values of a_i and α_i. Since the tides are made up of many constituents, determining the amplitude and phase angle of the constituents from a measured data set can be challenging. Various tidal analysis software are available from different research groups (Universities, government research programs) which are all able to analyze the tidal constituents. Most of the tidal analysis software can also provide tidal predictions once the constituents are known. In order to predict future tides, the relevant tidal constituents at a location are used to calculate the water levels in the future. Future tides are predicted for all major ports around the world and provides navigators with crucial high and low water level information.

2.2.1.2 Tidal Propagation and Currents

The propagation of a tide can be viewed as a long water wave with a wave length that is hundreds of kilometers long. Due to the size of these large tidal systems, the tides are significantly influenced by the rotation of the Earth. Thus, the tides do not propagate in a straight line, but rotate around a centre point, called amphidromic points. There are many amphidromic points in the Earth's oceans and at these points, there is no vertical tidal fluctuation. Figure 2.4 shows an example of the rotating tides in the Gulf of St. Lawrence, where the Shippagan Gully tidal inlet is located. The dashed lines, which are called co-range lines, indicate areas where the tidal range is the same and the solid lines, called co-tidal lines, indicate where the tide has the same phase. Also, the arrows in Figure 2.4 indicate the direction in which the tide rotates around the amphidromic point.

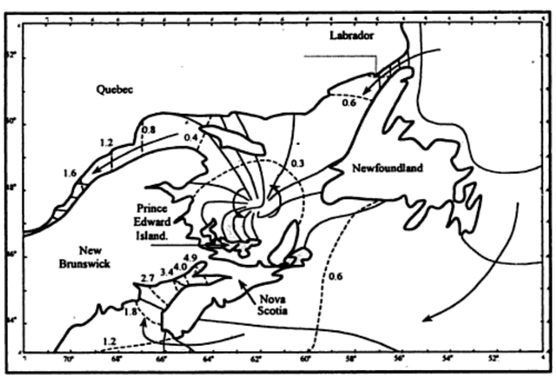

Figure 2.4 - Semi-diurnal tide in the Gulf of St. Lawrence (Forrester, 1983).

The raising and lowering of water levels due to the tides develops substantial currents in the oceans. In the deep, open ocean, the tidal current is in phase with the tidal water fluctuations. Therefore, at high water, there is a maximum current velocity in the same direction the tide propagates. However, as the tide approaches land, the phase relationship between the tide velocity and water level fluctuations changes, especially at tidal inlets. Rising water levels in the ocean drives a current through a tidal inlet, causing the water level within the tidal lagoon to rise as well. This inflow of water is called the flood flow. Similarly, when the water levels in the ocean are lowering, a current is forced out of the inlet, lowering the water levels within the tidal lagoon. This exiting of water through the inlet is called the ebb flow. A depiction of an ebb and flood flow through a tidal inlet is shown in Figure 2.5. In some cases where the inlet is wide or the lagoon is small, there is no phase lag between the vertical tide in the ocean and the lagoon. At the time of high water level in the ocean, the maximum water level is reached in the lagoon and both will begin to lower simultaneously. Therefore, at the time where the maximum water level is reached in the ocean and in the lagoon, there is no flow through the inlet, which is referred to as high water slack tide. A similar situation occurs during low tide and is referred to as low water slack tide. In the case where the inlet is narrow, or the lagoon is large, the maximum water level in the lagoon will occur later than in the ocean. This means that flow will continue through the inlet for a period of time after the high water level in the ocean is reached.

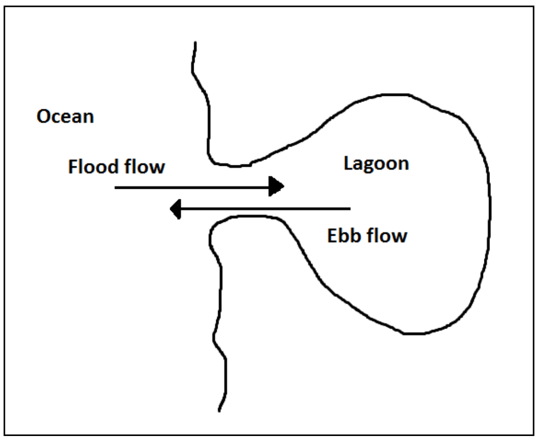

Figure 2.5 - Tidal inlet and lagoon indicating directions of flood and ebb flows.

2.2.2 Waves

Along with tides, waves also play a key role in the hydrodynamics located in the areas surrounding a tidal inlet. An understanding of how water waves are formed and how they transform as they approach the coastline is essential in understanding the hydrodynamics of a tidal inlet. There are many types of water waves produced in the oceans, ranging from waves with periods as short as 0.1s (capillary waves) to waves with periods on the scale of hours (tsunamis). In the middle of this very large range lies waves that tend to have wave heights which are rarely greater than 10m and periods that typically range from 1-30s (Kamphuis, 2000). These waves are called gravity waves, as gravity is the force that tries to restore the still water level. Gravity waves are created by the wind blowing on the ocean, which applies a shear stress to the water surface. The shear stress creates ripples in the water, which eventually grow into fully developed waves. There are three important variables that dictate the height of the created waves: wind speed, wind duration and fetch (distance over which the wind blows) (Kamphuis 2000).

Wind waves can be classified into two categories: sea and swell. Sea waves are locally generated wind waves and consist of many different wave heights and periods. They generally propagate in the direction of the wind. During times with very strong winds, a rough and confused sea state can be created. Once waves have been created and have travelled away from where they were generated, they are called swell waves. As these waves travel away from their origin, individual waves separate and waves with similar periods group together, which creates a much more uniform group of waves than what is experienced in the case of sea waves. The difference between both types of waves is illustrated in Figure 2.6, where the sea waves (on the left) produce a choppy and rough ocean and the swell waves (right) are much more uniform. While these two types of waves are classified differently, they can occur simultaneously at a certain location. For example, as swell waves travel from another location, they can be subjected to the local wind conditions. In these situations, the sea and swell components can be indentified and separated based on the period of the waves. Typically, swell waves have a larger period than sea waves, which allows for the two types of waves to be identified and separated (Goda, 2000).

Figure 2.6 - Example of sea waves (left) and swell waves (right) (OAR Northwest 2012 and NOAA 2010).

2.2.2.1 Nearshore Wave Transformation

As waves travel from the deep waters offshore to the more shallow waters along the coast, they begin to be affected by the ocean floor; a phenomenon called wave transformation. Four main kinds of wave transformations exist: shoaling, breaking, refraction and diffraction. Wave transformation plays a key role in the hydrodynamics around a tidal inlet because it produces changes in the wave height, wavelength, celerity and wave angle as the waves approach the shore.

As the waves approach shallow waters, the wave celerity and wave lengths decrease. In order to maintain a constant energy flux, the wave heights begin to increase (Longyet-Higgins and Stewart, 1964). Due to this process, the height of the waves experienced nearshore is typically higher than the height of the same waves in deeper waters. A shoaling coefficient, K_s, is used to relate the wave height at any depth to the deep water wave height using the following equation:

$$K_s = \frac{H}{H_0} = \sqrt{\frac{1}{2}\frac{1}{n}\frac{1}{\tanh kd}} \qquad (2.2)$$

Where H is the wave height at any depth, H_0 is the wave height in deep water, k is the wave number, d is the local water depth and n can be calculated from the following equation:

$$n = \frac{1}{2}\left(1 + \frac{2kd}{sinh\ 2kd}\right) \qquad (2.3)$$

The shoaling coefficient is 1 in deep water and decreases with the water depth to 0.91 until it rises to infinity as the water depth approaches zero (Kamphuis, 2000). Even though the shoaling coefficient rises to infinity (implying the shallow water wave height grows to infinity) this obviously does not occur in reality. Instead, there is a physical limit to the steepness of the waves, H/L (wave height over wave length), and once this limit is exceeded, the waves will break.

Wave breaking occurs once the waves grow too steep and become unstable, leading to the crest of the wave to overturn. During this process, a large amount of wave energy is turned into turbulent kinetic energy, which plays a significant role in sediment transport in the near shore region. The form of the wave at the breaking point can be divided into four main groups: spilling, plunging, collapsing, and surging (Galvin, 1968), which are all illustrated in Figure 2.7. In spilling breakers, the wave crest becomes unstable and cascades down the shoreward face of the wave, producing a foamy water surface. In plunging breakers, the crest curls over the shoreward face of the wave and falls into the base of the wave, resulting in a high splash. In collapsing breakers, the crest remains unbroken while the lower part of the shoreward face steepens and then falls, producing an irregular turbulent water surface. In the surging breakers, the crest remains unbroken and the front face of the wave advances up the beach with minor breaking (CEM, 1984). The type of wave breaking mainly depends on the steepness of the wave and the slope of the beach. In order to estimate what type of breaking will occur, the breaking type can be correlated to the surf similarity parameter, otherwise known as the Iribarren number:

$$\xi_0 = \tan\beta \left(\frac{H_0}{L_0}\right)^{-\frac{1}{2}} \qquad (2.4)$$

Where ξ_0 is the surf similarity parameter, β is the beach slope, H_0 is the deep water wave height and L_0 is the deep water wave length. Once the surf similarity parameter is calculated for a given wave, it can be related to the type of breaking in the following way:

if $\xi_0 > 3.3$, wave breaking type will be surging or collapsing;
if $0.5 < \xi_0 < 3.3$, wave breaking type will be plunging;
and if $\xi_0 < 0.5$, wave breaking type will be spilling.

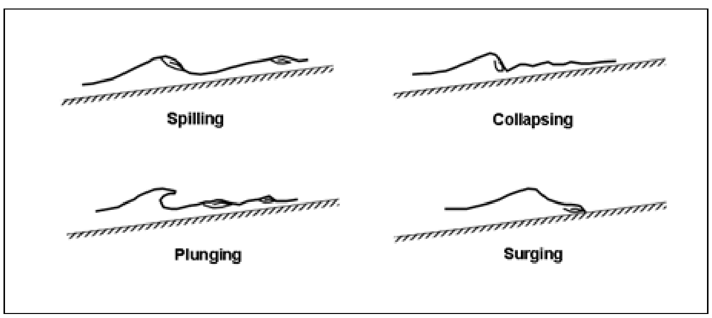

Figure 2.7 - Four types of wave breaking: spilling, collapsing, plunging and surging (CEM 1984).

Another important aspect of wave breaking for engineering applications is the breaking wave height, H_b, and the breaking wave depth, d_b. There are many accepted formulas to calculate these two parameters given the deep water characteristics of a wave. The simplest and oldest equation developed by McCowan in 1894 and is still used to provide a reasonable approximation for wave breaking to use in engineering practices. This equation is as follows:

$$H_b = 0.78 d_b \qquad (2.5)$$

where H_b is the wave height at breaking and d_b is the wave depth at breaking. Since McCowan developed that equation in 1894, a number of researchers have shown that breaking wave heights and depths are influenced by other variables such as wave length and beach slope (Goda (1970), Weggle (1972), Komar and Gaughan (1972), Battjes (1974) and Smith and Krause (1990) among others).

The discussion so far has assumed that waves are approaching the coast at an angle that is perpendicular to the bathymetry contours. However, in reality it is rare that waves approach the coast at a 90° angle. Instead, the waves will typically approach the coast at an oblique angle. As the waves approach the coast at an angle, one end of the wave crest will reach shallower water before the other end. The portion of the wave crest in the shallower water will slow down as the waves begin to shoal, which allows the other end, which is still located in the deeper water, to catch up. Therefore, as the waves approach the coast, the wave crests will bend to align themselves with the bottom contours and the wave direction becomes more perpendicular to the shoreline. This phenomenon is known as wave refraction (shown in Figure 2.8) and it basically consists of wave crests bending to align themselves with the bathymetric contours.

Similar to wave shoaling, wave refraction can be represented by a refraction coefficient, K_r. Assuming straight and parallel shoreline contours, the refraction coefficient can be calculated as such:

$$K_r = \sqrt{\frac{\alpha_0}{\alpha}} \qquad (2.6)$$

where α_0 is the deep water wave angle and α is the wave angle at the location of interest. Before this equation can be implemented, an estimation for α is required. Again, assuming that the shoreline and depth contours are relatively straight and parallel, Snell's law of wave refraction can be used (Kamphuis, 2000):

$$\frac{\sin\alpha}{\sin\alpha_0} = \tan\frac{2\pi d}{L} \qquad (2.7)$$

where d is the local water depth, and L is the wave length. Once the refraction and shoaling coefficient (as shown above) is known, the wave height at any given area of interest can be calculated using:

$$H = H_0 K_s K_r \qquad (2.8)$$

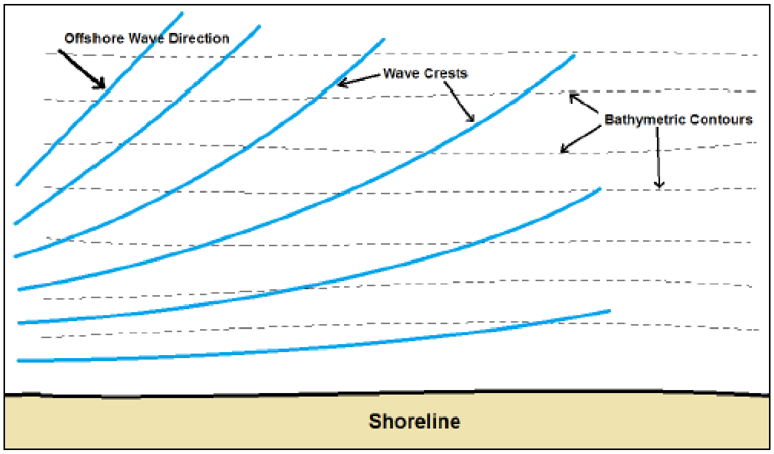

Figure 2.8 - Illustration of waves refracting as they approach the shoreline (Logan, 2012).

Refraction and shoaling occur when the water depth gradually changes, thereby allowing the wave crests to bend and reshape based on the bathymetric contours. However, when there are sudden changes in the wave field, another near shore transformation called diffraction occurs. One example of wave diffraction is the presence of an offshore breakwater. The breakwater separates a wave zone and a shadow zone (a zone in the breakwater's lee where there is no wave action). As the waves approach the breakwater, the waves will diffract around the ends of the breakwater, bending the wave crests and causing them to propagate inwards directly in the breakwater's lee (the shadow zone), as shown in Figure 2.9.

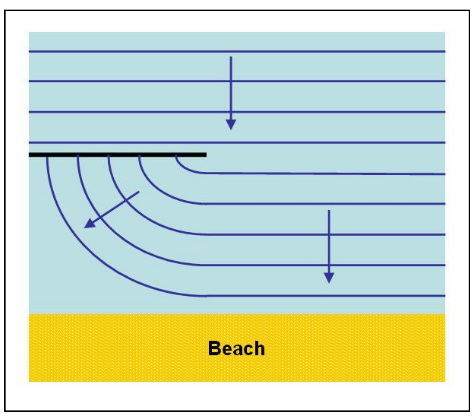

Figure 2.9 - Illustration of waves diffracting around the head of a breakwater (Cronodon, 2012).

2.2.2.2 Wave Induced Currents

As waves approach the shoreline, they undergo the near shore transformations that are described above. However, at the same time the waves also cause a mean transport of water toward the shoreline, which is called mass transport. Unlike the predictions by the linear wave theory (Airy, 1845), water particles under the influence of waves do not travel in closed elliptical orbits. Instead, the elliptical orbits actually move in the direction of wave propagation, as shown in Figure 2.10. It can be shown that there is a nonlinear transport of water in the wave direction because of the larger forward transport of water under the wave crest. This is due to the total depth being greater when compared to the backward transport under the wave trough. This mass transport that is created has a momentum associated with it. Therefore, forces will be generated anytime the momentum changes magnitude or direction (Dean and Dalrymple, 2002). In recognition of this, Longuet-Higgins and Steward (1963) introduced the concept of wave momentum flux, designating the sum of the momentum flux and the mean pressure as the radiation stress. The radiation stress drives water currents in the direction of wave propagation.

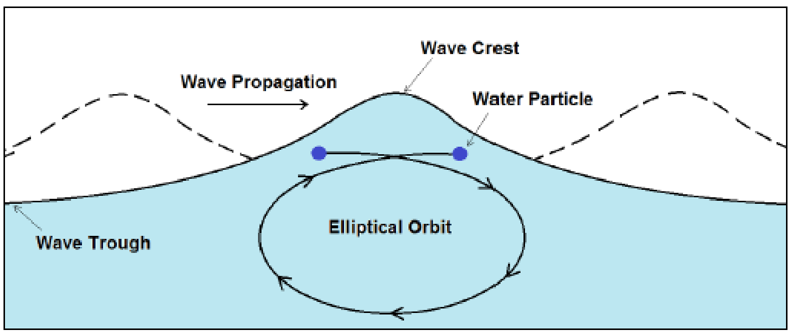

Figure 2.10 - Elliptical orbit of a water particle caused by waves (Logan, 2012).

As a wave shoals and increases in height prior to wave breaking, the radiation stress also increases. In order to balance out this increase in radiation stress, the mean water level decreases, otherwise known as wave set-down. The opposite occurs once the wave breaks and starts to reduce in height. After the wave breaks, the radiation stress decreases and there is an increase in the mean water level, called wave setup, to balance the decreasing radiation stress.

The wave induced currents can be separated into two categories based on their direction; cross-shore currents and longshore currents. Cross-shore currents generally act perpendicular to the coastline while longshore currents act along the coastline. Cross-shore currents are generated because the wave-induced mass transport must be returned to the ocean since there cannot be a net onshore flow of water due to the presence of the beach. Depending on the orientation of the beach, two types of wave induced cross-shore currents can occur; undertow and rip currents. Undertow is a type of cross-shore current that typically forms in the case of a long, uniform beach. As the waves break and approach the beach, an undertow current develops and flows toward the ocean and along the seabed, underneath the breaking waves. A rip-current (shown in Figure 2.11) is the second type of cross-shore current and typically forms in areas where a non-uniform shoreline exists. Unlike undertow, rip currents are a return flow that act along the entire water column and typically form in trenches between sandbars, under piers or along jetties. In most scenarios, undertow and rip currents are found in combination, both returning the shoreward flow of water back into the ocean.

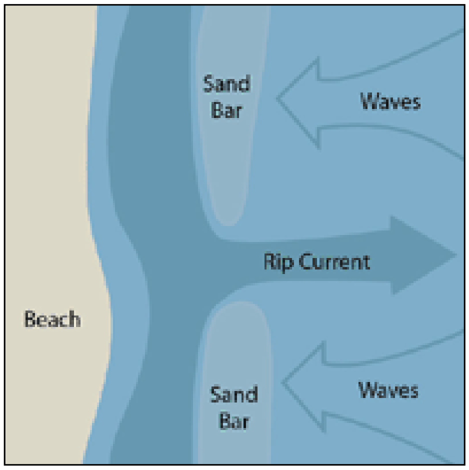

Figure 2.11 - Illustration of a rip current between two sand bars (Sea Grant, 2012).

Currently, it has been assumed that the elliptical orbit of a water particle, shown in Figure 2.10, only occurs in two-dimensions. This is true for the case where waves approach the shore perfectly perpendicular; however when the waves approach the shore at an oblique angle, the two-dimensional elliptical orbit changes to a three-dimensional helix orbit. This third-dimension in which the water particle travels creates radiation stresses that have a longshore component (Dean and Dalrymple, 2002). From this, a longshore current that flows along the coastline is created. The direction of the longshore current is dependent on the direction of the waves which create it. Waves approaching from >90° will create a current in one direction and waves approaching from <90° will create a longshore current in the opposite direction. Most coastlines around the world have a predominate longshore current direction, which is dictated by the local wave climate. This current, as expected, creates sediment transport in the direction of the longshore current and is the main reason why coastal structures such as jetties and groins are built. Further detail on this topic is discussed in the following sections.

2.2.2.3 Numerical Models for Wave Propagation

Due to the complex transformations waves undergo as they approach the coast, it is impossible to hand calculate the various wave characteristics that may be needed for a project. Therefore, many wave numerical models have been developed to model the propagation and transformation of water waves. There are two main categories of wave numerical models; phase-averaged models and phase-resolving models. Phase-averaged models ignore the changes in wave phase and instead calculate the wave action density for a given wave spectra (Aquaveo, 2011). From this, the wave characteristics can be calculated and can be used to find the significant wave height, the peak period, the breaking wave height etc. Phase-averaged models typically have a smaller computational cost compared to the phase-resolving models, and are therefore more practical for simulating wave propagation over large domains and long time frames. Some examples of popular phase-averaged models include: SWAN (Riss, 1997), CMS-Wave (Lin *et al*., 2008), STWave (Smith *et al*., 2001) and MIKE 21 (DHI, 2011) among others.

Phase-resolved models calculate the entire wave profile as the waves propagate through the computational domain. This provides a realistic simulation of individual waves and wave trains in motion. Due to the intensive computational time, phase-resolved models are much more applicable to smaller applications or applications where near shore wave transformations are important. Some examples of popular phase-revolved models include CG-Wave (Demirbilek and Panchang, 1998) and BOUSS-2D (Nwogu and Demirbilek, 2001).

2.3 Morphology of Tidal Inlets

The currents produced by the hydrodynamic forces described above all have the ability to move sand. The tides and waves both produce currents which exert a shear stress on the seabed, causing sand to be transported in the direction of the current. As mentioned, these currents are complex and unique at each tidal inlet, leading to complex and unique morphologic features at each tidal inlet. The morphologic features and sediment transport patterns of a tidal inlet rarely fit into predisposed categories, and are instead a combination of the many categories. Nonetheless, it is important to have a basic understanding of how sediment is moved around an inlet and the types of morphologic features that can form.

2.3.1 Sediment Transport

The first step in sediment transport is incipient motion, which is getting the sand (or any particle) to move. The motion of a sand particle is caused by the current induced shear stress acting on the particle. If the shear stresses acting on a particle are larger than the critical shear stress (the shear stress required for that particle to move), then the particle will move. In 1936, A. Shield developed a numerical representation of the requirement for particle motion, which is known as the Shields parameter, τ_* . The Shields parameter is a dimensionless parameter and is the ratio of shear forces on the sediment particle acting to mobilize it to the submerge weight of the particle which acts to keep it stable (Dean and Dalrymple, 2002). This parameter is represented by the following equation:

$$\tau_* = \frac{\tau}{(\rho_s - \rho) g D} \qquad (2.9)$$

where τ is the shear stress, ρ_s is the density of the sediment, ρ is the density of water, g is the gravitational acceleration and D is the sediment diameter. In order for incipient motion to take place, the following relationship must be met:

$$\tau_b^* = \tau_c^* \qquad (2.10)$$

where τ_b^* is the dimensionless shear stress and τ_c^* is the dimensionless critical shear stress. Shields plotted the empirical relationship between the Shields parameter and the Reynolds number based on the shear velocity, u_*. The shear velocity is a measure of bed shear stress (Dean and Dalrymple, 2002). The Reynolds number on the Shields curve is defined as:

$$Re = \frac{u_* d}{\upsilon} \qquad (2.11)$$

where υ is the kinematic viscosity and the shear velocity is defined as:

$$u_* = \sqrt{\frac{\tau_b}{\rho}} \qquad (2.12)$$

An example of the Shields curve is shown in Figure 2.12.

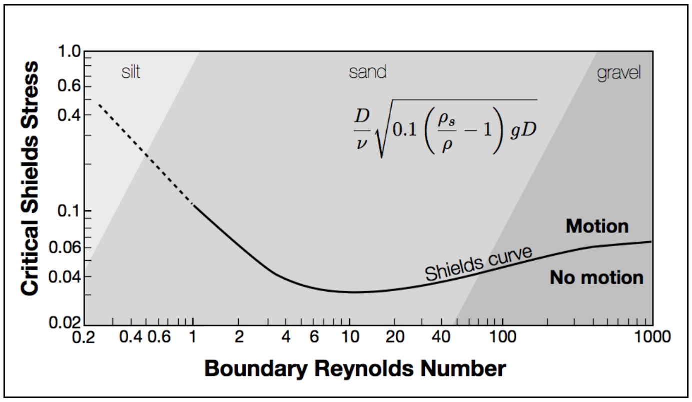

Figure 2.12 – Example of the Shields curve, empirically relating the critical shear stress to the Reynolds number (CSIRO, 2011).

2.3.1.1 Types of Sediment Transport

Once the shear stresses are large enough to produce sediment motion, two main types of sediment transport may occur; bed load transport and suspended load transport. Bed load transport generally occurs within about 5-10cm from the bed and the sediment moves primarily by rolling, sliding and hopping along the seabed at only a fraction of the current velocity. Many researchers have developed empirical formulas to calculate the bed load transport rate, which include: DuBuoys 1879, modified Ackers White 1982, Einstein 1950, Parker 1990, Bridge and Bennett 1992, and Schmeekle and Nelson 2003 among others.

Suspended sediment transport is sediment that is entrapped within the water column through the turbulence created by the currents. Similar to bed load transport rates, many suspended load transport rates have been developed. One of the more popular equations to calculate the suspended load rate is the Rousse-Einstein equation, developed in 1937 and 1954:

$$\phi_{SS}\int_{\eta_a}^{\eta_b} = C_\varepsilon \frac{2.5ln\frac{h}{K_S}+B_s}{(\frac{1}{\eta_\varepsilon}-1)^m}\int_{\eta_a}^{\eta_b}\eta^{\frac{1}{7}}(\frac{1}{\eta}-1)^m d\eta \qquad (2.13)$$
$$\bar{q}_{ss}\int_{\eta_a}^{\eta_b} = V_* h\gamma_s\phi_{ss}$$

where η is the relative water depth, C_ε is determined from an empirical curve, m is equal to $2.5\omega/V_*$ and ω is determined from an empirical curve. There is another popular suspended load equation, especially in numerical modeling applications, the Advection-Diffusion equation (Buttolph *et al.*, 2006) and is as follows:

$$\frac{\partial(Cd)}{\partial t}+\frac{\partial(Cq_x)}{\partial x}+\frac{\partial(Cq_y)}{\partial y}=\frac{\partial}{\partial x}(K_x d\frac{\partial C}{\partial x})+\frac{\partial}{\partial y}(K_y d\frac{\partial C}{\partial y})+P-D \qquad (2.14)$$

where:
C=depth-averaged sediment concentration
d=total depth
h = still water depth
η = deviation of water surface from still water level
t = time
q_x = flow per unit width parallel to the x-axis
q_y = flow per unit width parallel to the y-axis
u = depth-averaged current velocity parallel to the x-axis
v = depth-averaged current velocity parallel to the y-axis
K_x = sediment diffusion coefficient for the x-direction
K_y = sediment diffusion coefficient for the y-dirn
P = sediment pick-up rate
D = sediment deposition rate

Once the bed load and suspended load are calculated, the two values can be combined to give the combined sediment load. An alternative solution is to use empirical equations that calculate the total load, composed of both bed and suspended load, in one single equation. This approach is popular in the numerical modeling of sediment transport due to the computational simplicity compared to calculating the bed and suspended load separately. One of the popular total load transport formulas is the Soulsby-van Rijn formula (1997), which is as follows:

$$q_{t*} = \rho_s A_s U \left[\left(U^2 + 0.018\frac{u_{rms}^2}{C_d}\right)^{0.5} - U_{cr}\right]^{2.4} \qquad (2.15)$$

where:
- q_{t*}=equilibrium total-load transport
- ρ_s = sediment density
- A_s = empirical coefficient
- U = depth-average current velocity
- u_{rms} = peak bottom wave orbital velocity based on the root mean squared wave height
- C_d = drag coefficient due to currents alone
- U_{cr} = critical depth-averaged velocity for initiation of motion

Other popular total load formulas include Watanabe (1987) and Van Rijn (1998) among others. As shown, there are many formulas that can be used to calculate the quantities of sediment transport. However, the sediment transport direction and the corresponding morphologic features are as equally important to understand.

2.3.1.2 Cross-shore and Longshore Sediment Transport

As discussed previously, the currents forced by the hydrodynamic processes at a tidal inlet are composed of two directional components; cross-shore and longshore. Since it is these currents that drive sediment transport, the direction of sediment transport at a tidal inlet is composed of two directions, cross-shore sediment transport and longshore sediment transport. While both transport directions occur simultaneously, it is useful to break them down into the individual directions in order to understand how the sediment transport direction influences the morphologic features of a tidal inlet.

Cross-shore sediment transport consists of sediments moving almost perpendicular to the shoreline (as opposed to longshore sediment transport where sediment moves along the shoreline). Cross-shore sediment transport at a tidal inlet can be driven by either tides or waves approaching the inlet. As discussed in Section 2.2.1.2, a current is forced through the inlet as the tides in the ocean rise and fall. The flow rate through the inlet is governed by the cross-sectional area of the inlet and the tidal prism. This flow through the inlet exerts a shear stress on the seabed, and if the shear stress is larger than the critical shear stress, the flow will transport sediment. During the flood tide, when water is flowing into the inlet, the flow will carry sediment into the inlet. As the flood flow exits the inlet and into the tidal lagoon, there is a sudden expansion in the cross-sectional area. This expansion reduces the current velocity and if the governing criteria required for sediment motion is no longer met, the transported sediment will be deposited. A similar situation occurs during the ebb flow, where transported sediment will be deposited offshore of the inlet as the tidal current travels into the ocean. This deposition in the lagoon and ocean produce the tidal inlet morphologic features known as flood and ebb shoals, which are discussed further in Section 2.3.2.

As discussed in Section 2.2.2.1, as waves approach a certain water depth, they will being to shoal. Once the waves shoal to a certain height, the crest of the wave becomes unstable and the wave will break. As waves break a large amount of wave energy is converted into turbulent kinetic energy. This turbulent energy produces a large shear force on the seabed and has the potential to create large amounts of sediment transport. Cross-shore sediment transport created by breaking waves can be deposited in two areas; the swash zone and next to the breaking point. If sediment is deposited in the swash zone, a berm will be created on the beach. If the sediment is deposited near the breaking point the deposited sediment will create a sand bar. These two morphologic features are illustrated in Figure 2.13. The location and size of the sand bar depends on the breaking wave height. Larger waves will break further offshore and create larger shear stresses, producing a large sand bar further offshore. The opposite case occurs with smaller waves, where a smaller sand bar is created closer to the shoreline. Therefore, it is not unusual to see two sand bars in the same location, a winter sand bar and a summer sand bar. Typically, larger storms occur in the winter months, producing larger waves, which subsequently will create a larger sand bar located further offshore compared to the smaller sand bar created by the smaller summer storms.

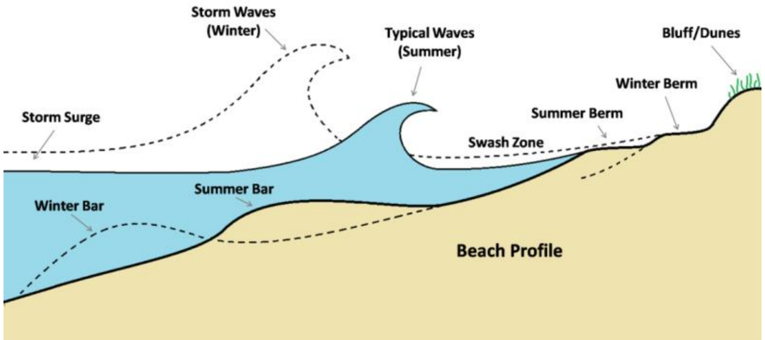

Figure 2.13 – Illustration of winter and summer sand bars and berms (Logan, 2012).

Longshore sediment transport is caused by waves approaching the coastline at an oblique angle. The shear stresses created by the breaking waves can be divided into two directional components; one perpendicular to the coast (causing cross-shore transport) and one parallel to the coast. If the breaking waves produce shear stresses that are larger than the critical shear stress, sediment will be transported along the coastline.

It is useful to calculate the longshore sediment transport rate in order to calculate a sediment budget for a given location. Sediment budgets are a coastal management tool used to analyze the different sediment inputs and outputs along the coast (Komar, 1998) and are useful to predict morphological change along the coastline during a given time period. Like the sediment transport formulas discussed so far, many empirical equations have been developed in order to predict the longshore sediment transport rate. Two of the more popular equations were published by Kamphuis (1991) and CERC (1984). The CERC equation estimates the longshore transport rate as follows:

$$Q_s = \frac{I_s}{(\rho_s - \rho)(1-n)g} \qquad (2.16)$$

where:

$$I_s = 0.39 P_{asb}$$

and

$$P_{asb} = \frac{1}{16} \frac{\rho g^{3/2}}{16 \gamma_{sb}^{1/2}} H_{sb}^{5/2} \sin 2\alpha_b$$

Where Q_s is the bulk sediment transport rate, ρ_s is the sediment density, ρ is the water density, η is the sediment porosity, H_{sb} is the significant wave breaking height, d_b is the breaking water depth and α_b is the breaking wave angle relative to the shoreline. The second longshore sediment rate equation is the Kamphuis equation, which is as follows:

$$Q_k = 6.4 \times 10^4 H_{sb}^2 T_{op}^{1.5} m_b^{0.75} D^{-0.25} (\sin 2\alpha_b)^{0.6} \qquad (2.17)$$

where T_{op} is the peak wave period, m_b is the beach slope and D is the mean sediment grain diameter. As shown, the Kamphuis equation takes into account some additional factors such as the wave period, beach slope and grain size which are not considered in the CERC equation.

Once the longshore transport rates have been estimated, the sediment budget can be calculated. The sediment budget is essentially a mass balance of sediment, including sediment sources and sinks. There are two main sediment sources that are accounted for in a sediment budget, rivers and sea cliff erosion. Rivers can carry large amounts of sediments, especially during river floods. When the flow from the river exits into the ocean, the sediment will be introduced to the coastal system and act as a sediment source. The other sediment source accounted for in a sediment budget is cliff erosion. Cliff erosion can introduce sediment into the system when waves attack cliffs lining the coasts. Along with sediment sources, there are also sediment sinks that need to be taken in account when calculating a sediment budget. The main sediment sink in most systems are estuaries or tidal inlets. As the tides transfer water into a tidal inlet, any sediment suspended in the current will also travel into the inlet. Depending on the hydraulic conditions, the sediment may be deposited inside of the lagoon, resulting in a loss of sediment, or sediment sink, within the sediment budget.

Similar to the longshore currents discussed in Section 2.2.2.2, the direction of the longshore sediment transport depends on the direction on the approaching waves. Therefore, depending on the angle of the approaching waves, longshore sediment transport can move in either direction along the coast. In most locations, there will be a predominant longshore transport direction. The predominant direction can typically be indentified based on the morphologic features present on the coast. This is particularly evident in the areas surrounding a sediment trapping structure, such as a groin. When a groin is placed perpendicular to the coast, it traps the sediment travelling along the coastline. Over time, sediment will accumulate on the side of the groin which corresponds to the direction the sediment is travelling from, known as the updrift side of the structure. Since the sediment is trapped by the groin, there is a reduction in available longshore sediment. This leads to erosion occurring on the other side of the groin, which is called the downdrift side of the structure. This pattern of erosion and deposition can be seen in Figure 2.14.

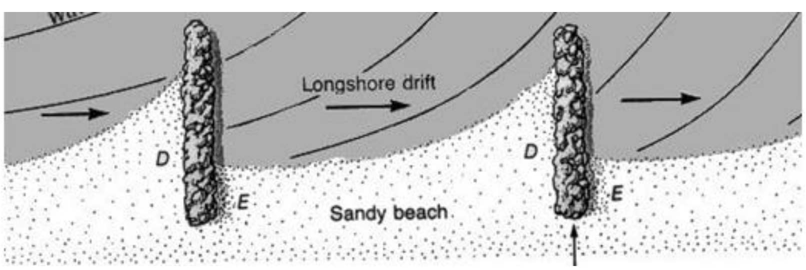

Figure 2.14 - Example of how a sediment trapping structure can cause deposition up the updrift side and erosion its downdrift side (Studyblue, 2013).

A similar phenomenon occurs at tidal inlets. The flow of longshore sediment transport can be interrupted by the deeper waters and currents located at the inlet. This will lead to an accumulation of sediment on the updrift side of the inlet and erosion on the downdrift side. The interaction of longshore sediment transport with an inlet can cause a variety of different morphological features, all of which are discussed below. At an engineered inlet, such as inlets with a jetty, downdrift erosion may be increased due to the structure trapping sediment. This may potentially cause problems due to the extensive erosion. In these cases, sediment bypassing can be implemented in order to ensure that erosion is controlled. There are many techniques that are available to ensure sufficient sediment bypassing, especially by artificial means (Seabergh and Kraus, 2003). These techniques generally include some sort of sediment trapping, where accretion rates are predictable and can be transferred downdrift of the shoreline through dredging. An example of a sediment trapping technique is a weir-jetty system, which is shown in Figure 2.15. In a weir jetty system, the structure traps some of the longshore sediment on the upside of the jetty, ensuring an adequate beach is maintained. Any spill over sediment is mechanically bypassed, typically by dredging, to the downdrift shoreline (Seabergh and Kraus, 2003). Another method that facilitates sediment bypassing is proper alignment of inlet jetties. If done correctly, the jetties can stabilize the inlet, while streamlining flow along a pathway by which sediment can bypass the inlet (Bruun, 1986). When designing new additions to an inlet, the interaction between new coastal structures and longshore sediment transport should always be kept in mind and if needed, bypassing should be considered in order to mitigate the erosion of beaches downdrift of the inlet.

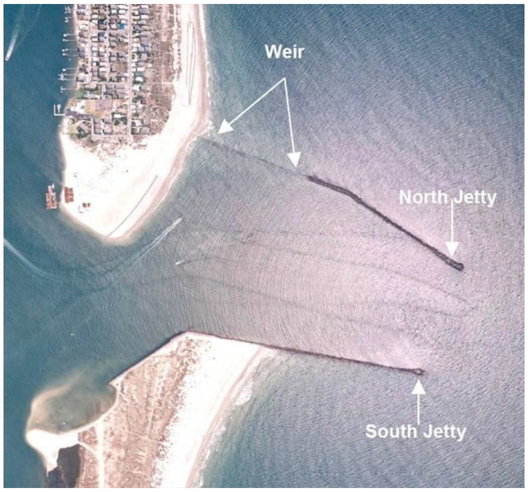

Figure 2.15 - Example of a weir jetty system, a technique used to trap longshore sediment transport (Geocaching, 2012).

2.3.2 Morphology Characteristics of a Tidal Inlet

The combination cross-shore and longshore sediment transport processes that have been discussed thus far combine to produce the morphologic features found at tidal inlets. While the morphologic features at tidal inlets are complex and unique for every individual inlet, it is useful to look at the typical morphologic characteristics exhibited by a tidal inlet. Figure 2.16 illustrates the typical morphology structures found at a natural tidal inlet.

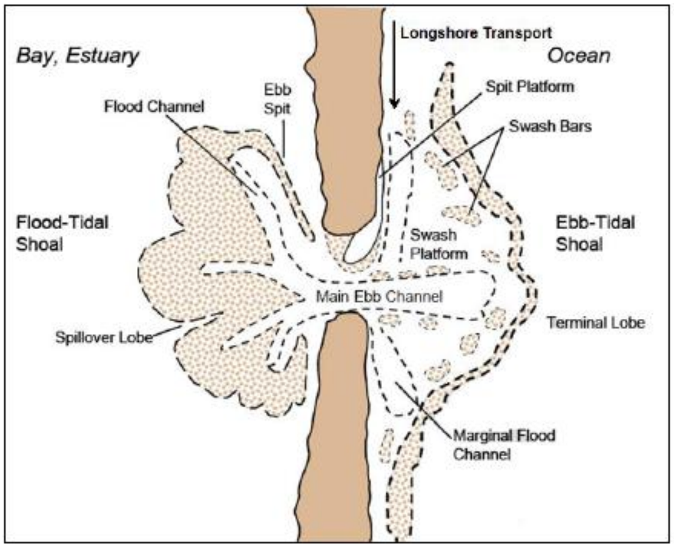

Figure 2.16 - Typical morphologic features found at an idealized, natural tidal inlet (Davis and Fitzgerald, 2004).

The main morphologic features are the ebb and flood shoals created by the ebb and flood tides. As discussed in Section 2.3.1.2, sediment can become entrapped in the tidal flows that travel through the inlet. As these flows enter either the ocean or lagoon, the entrapped sediment is deposited and ebb and flood shoals are created. The ebb shoal plays an important role in natural sediment bypassing. It provides a pathway where longshore sediment transport can travel past the inlet and eventually reattach to the coastline at a certain distance downdrift of the inlet. In addition, wave-induced features called the spit platform and the swash platform, both created by longshore sediment transport, are present at some tidal inlets.

The inlet in Figure 2.16 is an idealized inlet where the features are essentially symmetrical and well balanced. However, most inlets do not exhibit well defined morphologic features and instead, vary depending on the various hydrodynamic and sediment transport processes that have been discussed thus far. For example, the relative strength of the longshore sediment transport has a large effect on the geometry of a tidal inlet. The inlet geometry will be quite different in the case where there is a large net sediment transport compared to a situation that has an equal longshore sediment transport in both directions. The effects of the net longshore sediment transport on the inlet geometry can be seen in Figure 2.17 by Galvin (1971).

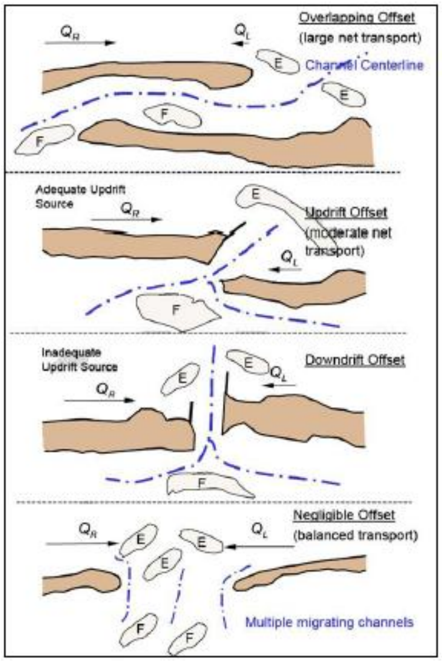

Figure 2.17 - Effects of longshore sediment transport on inlet geometry (Galvin, 1971).

The geometry of an inlet can also be classified based on the relative strength of the wave or tidal forcing. The graph in Figure 2.18 by Davis and Hayes (1984) shows that inlets can be classified as tide dominated or wave dominated. A tide dominated inlet has a mean tidal range which is larger than the mean wave height. The opposite scenario is a wave dominated inlet that has a mean wave height which is larger than the mean tidal range. Other scenarios have been identified by Davis and Hayes (1984) that lay in the middle of these two extreme cases, where the wave and tidal energy are more equal. A more recent analysis between these processes was completed by D'Alpais *et al.* (2010), where it is recommended that tidal inlet morphology should be based on the tidal prism, rather than the mean tidal range. This is because the magnitude of the tide induced forces not only depends on the tidal range, but on the size of the tidal lagoon as well. As discussed in Section 2.2.1.2, the tidal prism is a product of tidal range and volume of the tidal lagoon.

Figure 2.18 also shows the difference in inlet configuration for a tide or wave dominated inlet. Wave dominated inlets tend to have a semi-circular ebb shoal. This ebb shoal allows longshore sediment transport to bypass the inlet due to waves breaking along the ebb shoal. In a tide dominated inlet, the ebb shoal consists of channel margin bars, which are shaped similar to dual jetties on each side of the inlet (Davis and Hayes, 1984). Sediment bypassing at tide dominated inlets is driven by the flood and ebb flows. Sediment enters one side of the inlet during the flood flow and a portion of that sediment eventually returns to the opposite side during the ebb flow (as shown in Figure 2.18). Mixed energy inlets, where waves and tides produce equal forcing on the inlet, show a combination of the morphological characteristics found in the tide or wave dominated cases.

The semi-circular ebb shoal found in the wave dominated and mixed dominated inlets has been subdivided into the five sections by Kraus (2000), as shown in Figure 2.19, which is at the East Pass inlet in Florida. The five sections include: updrift attachment bar, updrift bypassing bar, ebb shoal proper, downdrift bypassing bar and downdrift attachment bar. The ebb shoal is subdivided because the location and size of the ebb shoal proper is dependent on the tidal jet, while the bypassing bars and attachment bars are controlled by sediment transport produced primarily by breaking waves (Kraus, 2000).

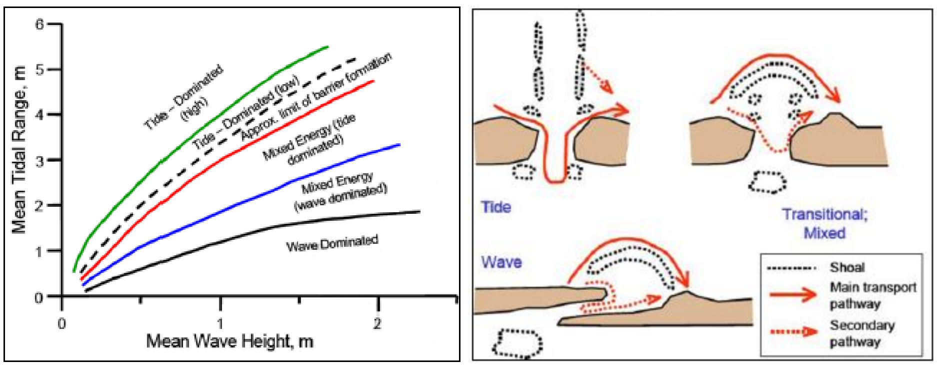

Figure 2.18 - Types of process dominated inlets (left) and their effects on inlet geometry (right) (Davis and Hayes, 1984).

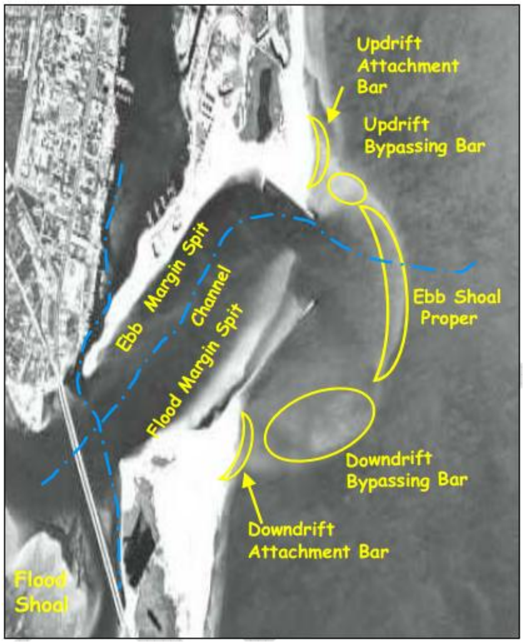

Figure 2.19 - Five classified sections of an ebb shoal (Kraus, 2000).

2.3.3 Numerical Modelling of Tidal Inlet Morphology

Due to the overall complexity of the various processes driving the morphologic features of a tidal inlet, it is impractical, if not impossible, to analytically calculate the required parameters needed to understand or predict these morphologic features. Instead, numerical models are used to create a model of these processes. Typically, a morphological numerical model consists of a hydrodynamic model which has been equipped with sediment transport schemes. The hydrodynamic model will calculate the various hydrodynamic parameters, which are then used to calculate the sediment transport direction and rates. Morphological models take the modelling one step further and use the calculated sediment transport rates in order to update the model bathymetry. This gives an estimate of any bed changes that may occur, such as channel infilling or changing of the ebb and flood shoals.

There are a few numerical models which are able to estimate morphology change, these models include: Mike21 (DHI, 2011), CMS-Flow (Buttolph *et al*., 2006) and Delft-3D (Deltares, 2011). These models are all two-dimensional, depth-averaged numerical models (except for Delft-3D which can be run in two or three dimensions) and can be very computational intense depending on the simulation time period. These models are useful for calculating the complex interaction of the coastal processes at small time steps and with a relatively fine grid. Therefore, if the modelling of processes on a large time scale is needed, such as shoreline change, then using these models would be impractical. In this case, a model which utilizes a more simplistic approach, which typically reduces computation time, is needed. One example of this kind of model is GenCade (Frey *et al*., 2012). GenCade is a one-dimensional shoreline change model that is able to model shoreline change over a long time period (such as years or decades).

While these models are able to model morphology change in a coastal setting, it is important to note that the numerical models are only providing a representation of the system, not a replication of the system. As discussed in this literature review, the development and interaction of the many coastal processes can be extremely complex and many factors, such as sediment transport, rely on empirical formulas derived from laboratory experiments. Therefore, a morphologic model, as with any numerical model, needs to be calibrated and validated to measured data (usually recorded field data) in order to produce results that can be used to support engineering analysis and judgment. The accuracy of a numerical model is highly dependent on the quality and extent of recorded field data which can be acquired through an extensive field data collection campaign.

2.4 Field Investigation

One of the first steps in successfully analyzing a tidal inlet is to collect field data which can be used to provide a better understanding of the coastal processes at the site and to provide data to calibrate and validate any numerical models used in the study. There are several useful parameters that can be obtained from a tidal inlet. A summary of the types of data as well as collection techniques has been completed by Pratt *et al.* (2000). The parameters are as follows:

- Water levels;
- Salinity;
- Suspended sediments;
- Wave characteristics;
- Meteorological data;
- Currents;
- Bathymetry; and
- Sediment properties

The water levels at a site are typically recorded with a solid-state electronic instrument. These instruments contain a strain gauge or quartz type pressure transducer that records the absolute pressure of the water column above the instrument. These instruments should be vented; otherwise changes in barometric pressure will appear as changes in water level. If the instrument is not vented, a second instrument should be placed in the study area in order to record atmospheric pressure changes, which can then be used to account for changes in barometric pressure. Typically, the water levels should be recorded for a complete lunar cycle (approximately one month) so the tidal constituents can be extracted using the methods discussed in Section 2.2.1.1.

The salinity of the water can be measured through water quality data loggers which measure conductivity and temperature. The salinity concentrations can be computed from these measurements and corrected by a known calibration. Typically, these recorders use a specific conductance electrode cell and a thermistor-type temperature sensor.

Several methods are available to record the concentrations of suspended sediments entrapped in the flow. These methods include mechanical instruments, optical backscatter and acoustic backscatter.

Mechanical instruments collect a volume of water, which can then be analyzed in the lab to find the suspended sediment concentration and grain size. A number of mechanical instruments exist, including bottle samplers (shown in Figure 2.20) or pump samplers. Bottle samplers are lowered into the water and collect a small sample of water as it flows past the instrument. Pump samplers are placed into the water and pump a large water sample directly to the surface. The optical backscatter method uses infrared light that is shone into a small sample of water. The suspended particles in the water sample scatter the light and the backscatter light intensity is measured and compared to a calibrated sediment concentration (Wren *et al.*, 2000). Acoustic backscatter is able to measure the suspended sediment concentration and velocity through the backscatter of the sound pulse caused by the sediment (to get concentration) and Doppler frequency shift of the sound pulse (to get velocity).

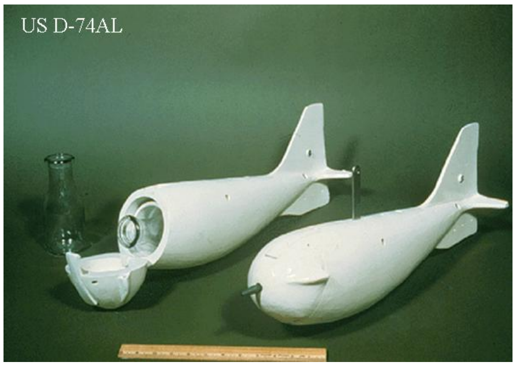

Figure 2.20 - Example of bottle samplers used to collect suspended sediment samples (USGS, 2005).

The wave parameters of a site, such as wave height and period, can be recorded using two types of devices: a wave gauge and a buoy gauge. A wave gauge operates in a similar fashion to the water level gauge which has been discussed above. This gauge is typically placed on the seabed and measures the absolute pressure of the water column above the instrument. The second instrument that can measure wave parameters is a buoy gauge. A buoy gauge is tethered to the seabed by an elastic shock cord and floats on top of the water. Since the buoy is sitting on the water surface, it moves and follows the motion of the waves as they travel past the buoy. Accelerometers inside of the wave buoy records the motion of the buoy and a flux-gate compass inside of the buoy is able to determine the direction of the waves.

Meteorological data such as wind speed, wind direction, precipitation, evaporation, temperature, relative humidity etc. are recorded by weather stations. These stations are typically powered by a battery which is charged using solar panels on top of the instrument. Various programming options are typically available to set the sampling interval and averaging period. Ideally, the weather station should be mounted in the center of the study area and approximately 10 m above land, as specified by the American Meteorology Society standards. However, if the weather station is to be mounted in the sea, it should be placed 2-3 m above the maximum wave height during a storm.

In order to calibrate and validate the hydrodynamics of a numerical model, current meters are needed to measure the current velocity and direction. The most popular method to measure the current is to use an

Acoustic Doppler Current Profiler (ADCP). These instruments emit sound bursts into the water column, which are scattered back to the instrument by interacting with particles entrapped in the flow. The ADCP instrument listens for the returning sound and assigns a depth and velocity based on the return time and the change of frequency of the sound pulse, caused by the Doppler effect.

Measuring the bathymetry of a study site is extremely important as it controls local water depth and near shore wave transformations. In addition, bathymetry is also important in numerical modelling. If the bathymetry in the model is incorrect or inaccurate, then the numerical model will be inaccurate no matter how advanced the model. There are a number of ways to measure bathymetry of a study site. The most common method is using an acoustic depth sounder which measures the travel time of a sound wave reflected off the seabed. More advanced surveying techniques, such as LiDAR (light detection and ranging) and multi-beam swath systems, are increasing in popularity due to the decreased time to survey an area or the improved accuracy that these methods provide.

The last dataset that is commonly required for a coastal engineering project is the properties of the local sediment. Sediment samples are typically taken from the beach or seabed and are analyzed in order to find the various sediment properties such as grain size distribution, porosity and specific gravity.

2.5 Case Studies

In order to support the theory discussed thus far in this literature review, a number of case studies were analyzed. While all case studies are useful to some degree, the two that were selected and analyzed below closely reflect the information provided in this literature review and therefore are the most useful in support of the current study. The two selected case studies are as follows:

- Ocean City Inlet, Maryland
- John's Pass and Blind Pass, Florida

2.5.1 Ocean City Inlet, Maryland

A study completed on the Ocean City Inlet in Maryland was published as a conference paper in the 30th Coastal Engineering Conference Proceedings and is entitled "Natural Sand Bypassing and Response of Ebb Shoal to Jetty Rehabilitation, Ocean City Inlet, Maryland, USA". The authors of this paper are A.M. Buttolph, W. G. Grosskopf, G.P. Bass and N.C. Kraus.

The Ocean City Inlet, shown in Figure 2.21, was formed in August 1933 as a breach in the barrier island. In an effort to stabilize the inlet, a jetty on the north side of the inlet was constructed between September 1993 and October 1934 and a jetty on the south side was constructed by May 1935. Following the construction of the two jetties, the inlet was dredged in August 1935 to a depth of 2.6 m and a width of 61 m. Within three years, the accretion updrift of the north jetty caused the beach to reach the tip of the jetty. This allowed for large amounts of sand to enter the inlet. Consequently, there was significant erosion of the northern Assateaugue Island (located downdrift of the inlet) due to the longshore sediment transport being trapped by the north jetty. Over time, the natural inlet processes formed ebb and flood shoals at the expense of adjacent beaches. A crescentic ebb shoal offset to the south of the jetties was created and a two part flood shoal was formed in the coastal bay. By the mid 1970s, a bypassing bar and attachment bar were formed between the ebb shoal and Assateague Island, which allowed for partial natural bypassing to take place. Over the past several decades, various coastal projects around the Ocean City Inlet have continued to contribute to the evolution of this inlet. Some of these projects include: storm protection beach nourishment along 11 km of beach near the inlet, placement of scour protection beneath the bridge connecting Ocean City to the mainland (which altered the tidal flow) and various shorefront structures constructed in the back bays, such as marinas and entrance channels.

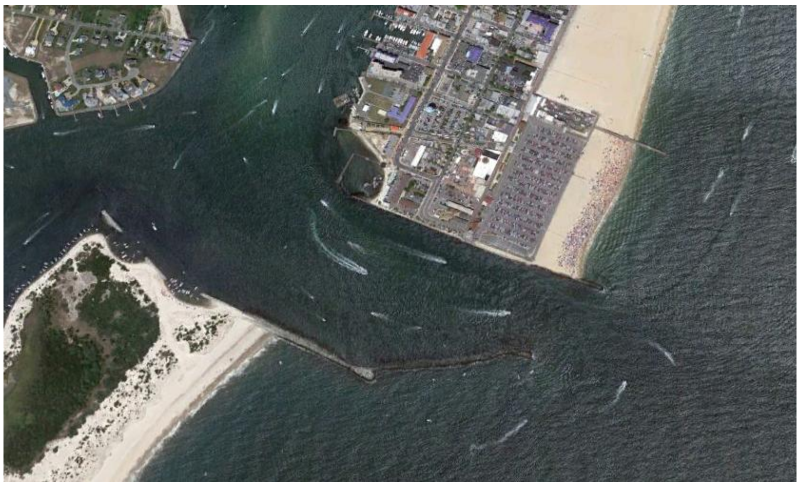

Figure 2.21 - Aerial photo of Ocean City Inlet, Maryland (Google Earth, 2011).

Numerous bathymetric surveys have been completed at the Ocean City Inlet in an effort to document the morphologic changes that have occurred since the inlet was stabilized in 1933. Pre and post-1933 beach surveys were conducted, which illustrate the changes in the shoreline caused by the 1933 storm. Periodic surveys of the beach both to the north and south of the inlet have continued since the initial beach surveys in 1933. More recently, 9 high resolution multi beam bathymetric surveys have been completed at the Ocean City inlet since 2004. The result of the August 2005 bathymetric survey is shown in Figure 2.22, which outlines the main morphologic features of the inlet. One of the morphologic features is a semi-circular ebb shoal that is skewed to the south. From the skewed ebb shoal, it can be concluded that the longshore sediment transport is in the north to south direction. The northern part of the ebb shoal exhibits a “tongue” that impinges on the Ocean City beach as well as the navigation channel that runs in a north-south direction between the beach and the tongue. The authors attribute this feature to sand that is driven toward the north by the ebb jet and transport by waves from the southeast. Another main morphologic feature of the inlet is the attachment bar. This attachment bar allows for some natural bypassing of the longshore sediment transport to Assateague Island.

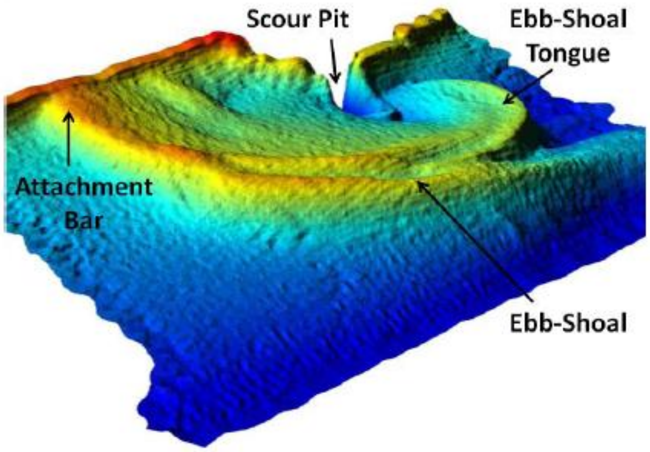

Figure 2.22 - August 2005 bathymetric survey showing major morphologic features (Buttolph *et al*., 2006).

The first step in the study was to develop a numerical model capable of modelling the circulation, waves and sediment transport at the Ocean City Inlet. The model that was chosen for this study was the CMS model developed by the U.S Army Corps of Engineers. Circulation and sediment transport were calculated with CMS-M2D, while wave propagation and transformation were calculated with WABED. CMS-M2D calculates the depth-averaged current, water level, sediment transport and morphology change in the two horizontal dimensions. The CMS-M2D model has three options for calculating sediment transport and morphology change: Watanabe total load formulation, Lund-CIRP total load formulation and the advection-diffusion transport equation.

The WABED model is a two-dimensional, phase-averaged, half-plane spectral wave model that is able to compute wave propagation and transformation. The wave spectra are specified at the offshore boundaries and are propagated into the WABED domain. In addition, local wind-generated waves can be calculated by WABED if the wind speed and direction are specified by the user.

The interaction between the two numerical models is automatically controlled through a steering module. The user specifies the time intervals, known as the steering interval, at which CMS-M2D and WABED interact. The two models interact by mapping the numerical solutions from one model to the grid of the other and providing the mapped solution as input for the following steering interval.

For the Ocean City Inlet study, the CMS-M2D and WABED models were constructed with bathymetry for the Atlantic Ocean and back-bay area obtained from an existing regional model of the Ocean City Inlet area. The bathymetry for the inlet and ebb shoal area was built with survey data measured in 2000. The cell size of the computational mesh for the CMS-M2D model ranges from 37.8 m (at the inlet) to 182.5 m at the offshore boundary. For the grid used for the WABED model, the cell size was constant at 44.9 m throughout the entire computational domain. The tidal and wave boundary conditions were applied for 1-year starting on January 1, 1997. The authors used this time period because of the availability of directional wave data from the nearby wave buoy, NDBC 44009. The sediment transport rates were modelled using the Lund-CIRP total load formulation and a median grain size of 0.2 mm was specified. The morphology change was set to be calculated at 0.25 hour intervals. The steering interval was specified at 3 hours, meaning that radiation stress gradients and wave properties were supplied to CMS-M2D from WABED every three hours, while total water depth was provided to WABED from CMS-M2D every 3 hours.

The constructed numerical model was used to study three main objectives:

- the various bypassing mechanics at the inlet,
- the physical processes that control the morphologic features at Ocean City Inlet, and
- the response of the inlet and ebb shoal to the rehabilitation of the south jetty.

Bypassing of sediment around the Ocean City inlet primarily takes place when waves are arriving from the northeast. The longshore sediment transport is directed southward and across the ebb shoal, as shown in Figure 2.23. The authors found that this bypassing can occur at a large range of wave heights, but it is strongest during storms.

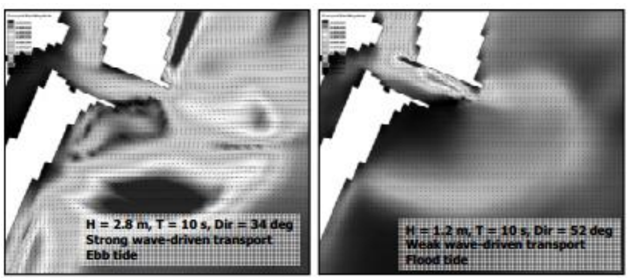

Figure 2.23 – Longshore sediment transport interacting with the ebb tide (left) and flood tide (right).

Through the numerical simulations, the authors indentified the ebb jet as the key process controlling the maintenance of the sand tongue located at the northern end of the ebb shoal. During the ebb portion of the tidal cycle, the ebb jet sweeps from south to north, which is shown in Figure 2.24. The sand tongue is located where the outer ebb jet loses speed because the spatial deceleration at the tip of the ebb jet promotes deposition of entrapped sediment. Since the ebb jet is a tidal process, the maintenance of the sand tongue does not rely on large storms or seasonal processes. Therefore, sand can be removed from the tongue to be placed elsewhere and the ebb jet will refill the dredged area with sand, providing a renewable source of dredging material. In addition, the dredging on the tongue will not have any effect on the sand bypassing from the north to south.

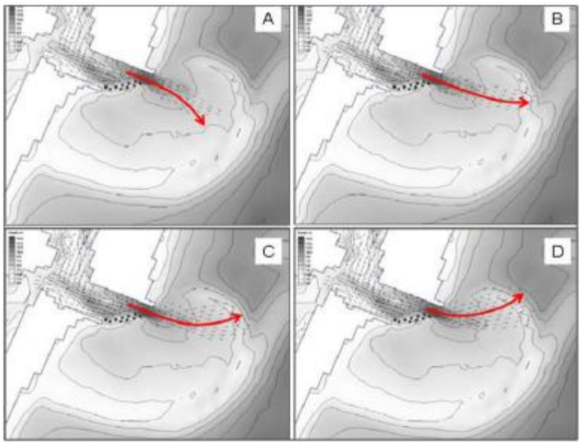

Figure 2.24 – Numerical model output showing the sweeping motion of the ebb jet from south to north.

The model results showed that the rehabilitation of the south jetty in 2002 constricted flow at the inlet mouth, which results in a stronger ebb jet that transports materials further offshore from the inlet. The ebb shoal morphology responds by migrating seaward, which can be seen in the morphology change results presented in Figure 2.25.

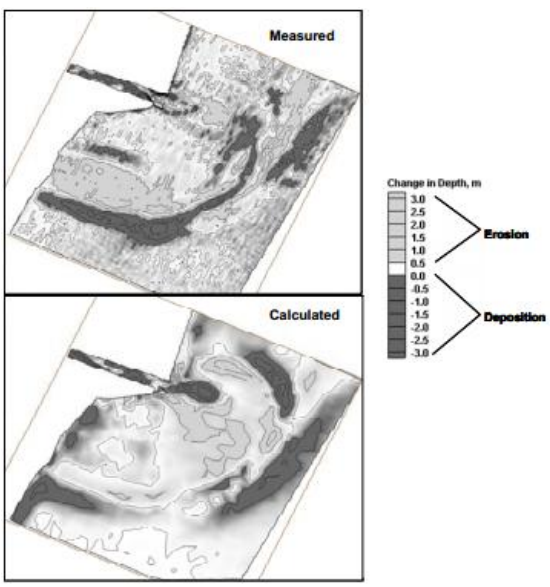

Figure 2.25 – Measured and calculated morphology change at Ocean City Inlet and ebb shoal area.

The reviewed study of the Ocean City Inlet is a good example of a case where a numerical model has been applied at a complex tidal inlet in order to try and improve understanding of the natural processes occurring at the inlet. It is important to note that the authors did not try and use the model results to make quantitative observations of the morphology change. Instead, the focus was on the qualitative changes. This shows that even with large amounts of calibration and validation data, such as the datasets that were available for the Ocean City Inlet study, numerical modelling cannot replicate the complex processes occurring at a tidal inlet. Instead, the model can only be used as an analytical tool.

2.5.2 John's Pass and Blind Pass, Florida

The paper entitled "Morphodynamics of an anthropogenically altered dual-inlet system: John's Pass and Blind Pass, west-central Florida, USA" was published in the Marine Geology journal. The author's of this paper are P. Wang and T. M. Beck.

The John's Pass and Blind Pass tidal inlets are located along the west-central Florida coast, as part of the west-central Florida barrier-island chain that extends north from Tampa Bay. The average wave climate experienced along this coastline is a significant wave height of 0.26 m with a wave period of 5.8 s and the spring tide has a range of 0.8 to 1.2 m, compared to the range of the neap tide of 0.4 to 0.5 m. The mean sediment grain size in the study area ranges from 0.2 mm to 1.0 mm.

The John's Pass inlet, shown in Figure 2.26, was opened in 1848 by a breach the in barrier islands by a hurricane and has since been stabilized by two inlets, constructed in the 1950s. This inlet can be classified as a mixed-energy inlet, with a large ebb shoal skewed to the south, which is the direction of the southward net longshore sediment transport. The detailed 2008 bathymetry in Figure 2.27 illustrates the various morphologic features of this inlet, including the channel-margin bar along the north side, the relatively shallow terminal lobe and the swashbar complex located over the downdrift portion of the ebb shoal. The beach immediately downdrift (south) of the inlet experiences chronic erosion and has been nourished numerous times by the sand dredged from the John's Pass ebb shoal.

Figure 2.26 - Aerial photograph of the John's Pass and Blind Pass inlet system.

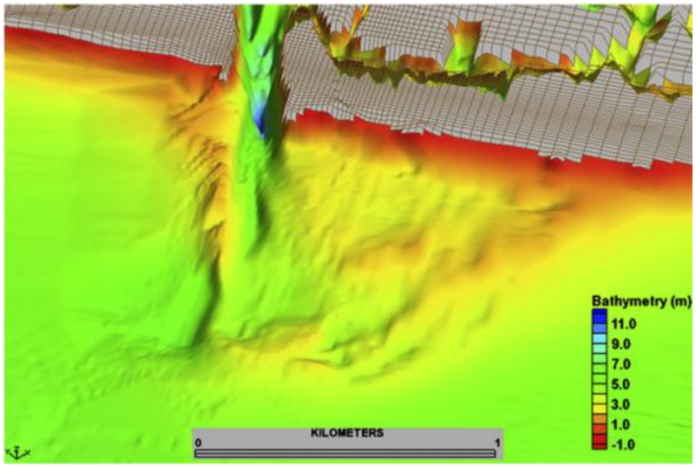

Figure 2.27 - Detailed 2008 bathymetry of the John's Pass inlet. Positive values indicate depth relative to mean sea level.

Unlike John's Pass, the origin of the Blind Pass inlet, shown in Figure 2.26, is not historically recorded. Prior to the opening of John's Pass in 1848, Blind Pass appeared to be the dominate inlet serving the Boca Ciega Bay, having large ebb and flood shoals. However, when John's Pass was opened, the newly opened inlet began to gradually capture a large portion of the tidal prism that was originally received by Blind Pass. Blind pass was eventually stabilized in 1937 with the construction of two jetties. Between the 1940s and 1960s, the construction of engineered islands and causeways in the back-bay area of Blind Pass further reduced the Blind Pass tidal prism and caused the ebb shoal to disappear in 1985. Without an ebb shoal to allow for natural sediment bypassing, large amounts of longshore sediment transport would get trapped in the inlet, causing severe erosion of the adjacent beaches.

A number of field investigations have been conducted at the John's Pass and Blind Pass inlet since 2001. Quarterly bathymetry surveys have been completed from August 2002 to June 2004 using a precision echo-sounder for depth measurements and a GPS for position. In addition, 9 cross-sections of the northern Blind Pass shoal were surveyed using a total station on a monthly basis from February 2003 to February 2004. Along with the bathymetric surveys, several flow measurements were conducted at the John's Pass and Blind Pass inlet system, with the first of these measurements completed in the winter of 2001. Two upward looking Acoustic Doppler current Profilers (ADCP) were deployed in the main channel of both John's Pass and Blind Pass, near the inlet mouth. The goal of the ADCP measurements was to compare the flow at each inlet and calculate the tidal prism. A second set of flow measurements were taken between 2002 and 2003 using an upward looking ADCP combined with a side-looking ADCP. The goal of these measurements was to capture the sediment transport patterns occurring within the Blind Pass channel. The third and final set of flow measurements were conducted during the summer of 2008. A total of four instruments were deployed: an offshore wave-tide gauge and three tide gauges located in the inlets and back-bay. The goal of these measurements was to provide input conditions into the numerical model and to have a dataset which could be used to validate the numerical model.

The numerical model that was used in this study was the Coastal Modeling System (CMS), which is a process-based suite of models that integrate hydrodynamics, sediment transport and morphologic change through the coupling of two models; CMS-Flow and CMS-Wave. CMS-Flow solves depth-integrated continuity and momentum equations using a finite-volume method and was developed for the specific purpose of modeling inlet processes and morphology changes. The CMS-Wave model is a steady-state, spectral transformation wave model and is an improved version of the WABED model (which was used in the previous case study of the Ocean City inlet). CMS-Wave computes wave refraction, shoaling, reflection, diffraction and breaking. The two models are coupled together and pass certain parameters between themselves in order to properly model the complex coastal processes found at a tidal inlet. The authors developed a CMS grid with varying resolution ranging from 10 x 10 m at the inlets to 80 x 100 m near the ocean boundary.

The CMS-Flow model was driven by a four week measured tidal cycle at the offshore boundary that was replicated to cover a two year period. For the CMS-Wave model, the Wave Information Study (WIS) hindcast data, developed by the U.S. Army Corps of Engineers, was used to provide the model with a continuous wave record. After analyzing the hindcast dataset, the authors chose wave sets from 1997 and 1999 as representative wave conditions for the study site. For sediment transport, the authors chose to use the unified sediment transport formula, Lund-CIRP, and a non-equilibrium transport formula. A spatially constant grain size of 0.26 mm was used in all sediment transport calculations.
The numerical model results show a differing hydrodynamic situation for the two tidal inlets. The John's Pass inlet (shown in Figure 2.28) experiences strong flows of up to 1.2 m/s throughout the entire channel during both the ebb and flood flow. The ebb jet, which is important for the formation of the ebb shoal, extends approximately 1km offshore. The tidal flow at Blind Pass (shown in Figure 2.29) on the other hand, is much different. The flood flow is relatively weak and uniform across the entire width of the channel. The ebb flow however, appears to be focused along the south side of the inlet with much larger velocities than the flood flow. The ebb flow along the north side of the inlet on the other hand, is quite weak. The ebb jet in the Blind Pass inlet extends along the south side and extends approximately 400 m in the offshore direction. A strong longshore current travelling north to south was modelled in the nearshore zone, which corresponds to the longshore sediment transport direction hypothesized from aerial photos.

During the flood tide at the John's Pass inlet, the interaction of the longshore current and the flood tides leads to the formation of a large eddy downdrift (south) of the inlet. This eddy creates a current reversal at the eroding Sunshine Beach downdrift of the John's Pass inlet. During the ebb tide, the strong ebb jet blocks the longshore current, leading to the formation of an eddy updrift of the inlet. The authors believe that this eddy provides the mechanism needed for the development of the channel margin bar.

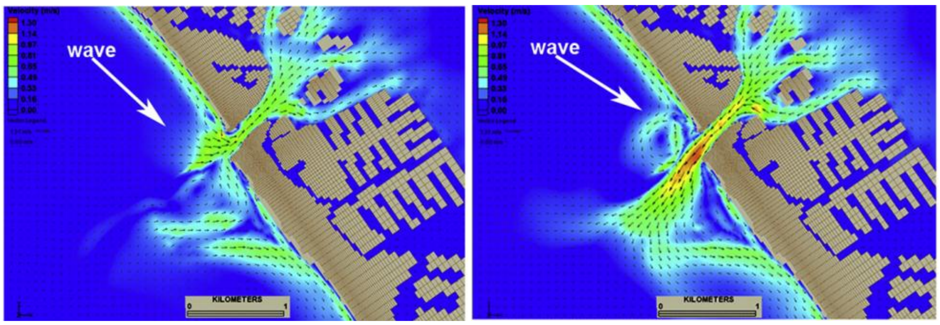

Figure 2.28 - Wave-current interaction at John's Pass under large northerly approaching waves during peak flood tide (left) and peak ebb tide (right).

The hydrodynamics of the wave-current interaction at Blind Pass is quite different than the situation seen at John's Pass. The strong longshore current created by waves approaching from the north overwhelms the weak ebb and flood tidal flows. Therefore, the two large eddies seen at the John's Pass inlet were not observed at Blind Pass. In addition, a strong longshore current was calculated around the north jetty during the flood tide, which is likely responsible for transport sediment into the inlet. The weak ebb jet is not able to mobilize any of the sediment within the inlet and is deflected southward (downdrift) by the longshore current. This is likely what is causing erosion of the beaches downdrift of the inlet, as the majority of the sediment would be carried into the inlet while the ebb jet is not able to entrap any sediment downdrift of the inlet.

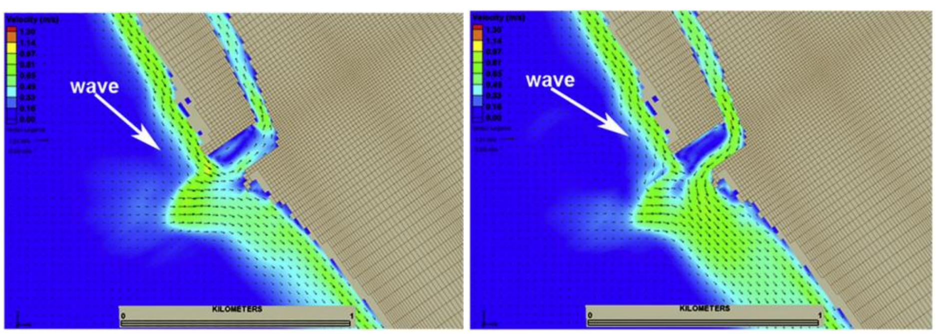

Figure 2.29 - Wave-current interaction and Blind Pass under large northerly approaching waves during peak flood tide (left) and peak ebb tide (right).

When comparing the calculated flow field (Figure 2.28) and sediment transport pattern (Figure 2.30) for John's Pass inlet during a peak flood, the significance of breaking waves on sediment transport is evident. The largest sediment transport rates occur at locations where breaking waves occur in combination with strong currents. The result is three main areas of large sediment transport: the nearshore area north of John's Pass inlet, over the channel-margin linear bar and along the terminal lobe of the downdrift portion of the ebb shoal. While a strong flow was calculated through the inlet itself, the rates of sediment transport were relatively low due to the absence of breaking waves in that area. During a peak ebb tide, the sediment transport patterns are quite different than during the flood tide. Four areas of large sediment transport rates were indentified based on the model results: 1) the nearshore area north of the inlet, 2) the channel margin linear bar and the nearby ebb channel, 3) along the terminal and downdrift lobe of the ebb-tidal delta and 4) over a broad area of the ebb delta. The authors concluded that the sediment transport in area 1 is responsible for the longshore sediment supply to the ebb shoal. The transport in area 2 represents an area where sediment is scoured by the ebb jet and helps develop the channel-margin linear bar. Area 3 provides the required mechanism for sand bypassing the inlet and area 4 illustrates the formation of the ebb shoal.

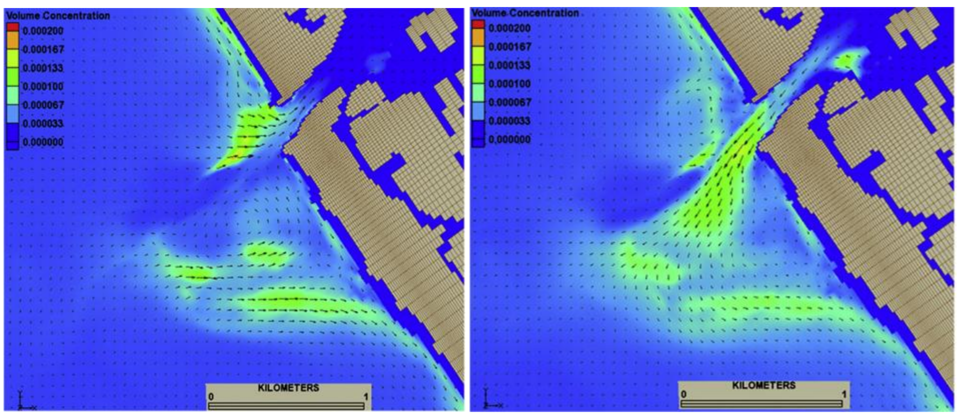

Figure 2.30 - Calculated depth-averaged sediment volume concentration and transport vectors at John's Pass under strong northerly approaching waves during peak flood tide (left) and peak ebb tide (right).

During flood flow at Blind Pass (Figure 2.31), three areas of high sediment transport rates were indentified: 1) along the Sunset Beach north of the inlet, 2) over the newly developed ebb shoal and 3) along the downdrift Upham Beach. The erosion along the adjacent beaches, Sunset Beach and Upham Beach, is a result of the active sediment transport observed in areas 1 and 3. The deposition of sediment within the inlet channel is primarily caused by the sediment transport found in areas 1 and 2. During the peak ebb tide, high sediment transport rates were calculated in two areas: 1) updrift Sunset Beach and 2) along Upham Beach. The weak ebb jet along the northern side of the inlet is not capable of scouring the sediment deposited there during the flood tide. The large amount of sediment transport in area 2 is due to the southward deflected ebb jet combining with the already strong longshore current.

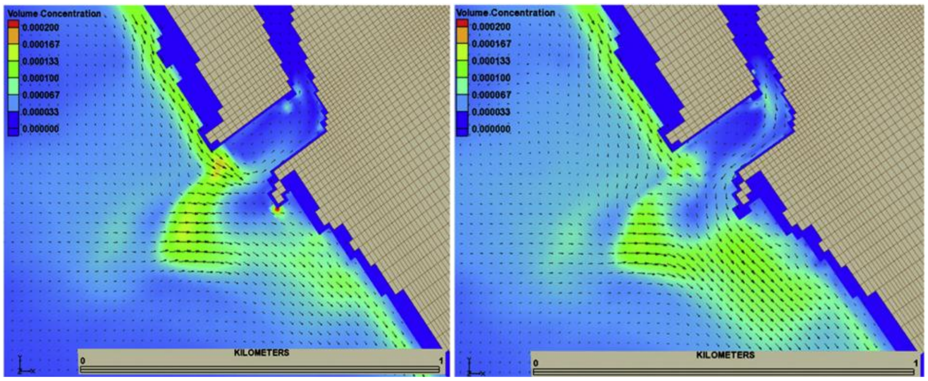

Figure 2.31 - Calculated depth-averaged sediment volume concentration and transport vectors at Blind Pass under strong northerly approaching waves during peak flood tide (left) and peak ebb tide (right).

2.6 Discussion

A number of key topics have been reviewed and discussed in this literature review, ranging from the basic theoretical concepts of coastal engineering to the complex interaction of waves and tides at tidal inlets. All of these concepts are crucial to understanding the inlet morphology of Shippagan Gully, which is the basis of this thesis.

It is obvious from the literature review that the driving processes behind tidal inlet morphology are quite complex. This complexity is what makes tidal inlets so difficult to study. Previous research has provided a good understanding of the individual processes, however the interaction of these processes is still not well understood. This interaction is what makes tidal inlet morphology both complex and unique to each location. As discussed in the literature review, the strength of longshore sediment transport and relative strength of waves and tides all significantly affect the orientation of the inlet morphology. This results in each tidal inlet being unique and cannot be easily classified into any preconceived categories. Therefore, much more research still needs to be done until we will be able to predict the morphology of a tidal inlet with any confidence.

The two presented case studies provide a good application of the theoretical topics discussed in this literature review. Much can be learned from these previous works including study methodology, however the studies also show that inlet morphology is not a process that is easily predicted. The sediment transport mechanisms at an inlet are too complex and sensitive to the local conditions to be entirely understood. Even with large amounts of quality field data, such as the situation in the reviewed case studies, neither analytical nor numerical models can be expected to provide accurate results when assessing tidal inlet morphology. The case studies use the numerical modeling results to assess the sediment transport patterns, not the actual sediment transport quantities. However, numerical model results can be useful when paired with a good understanding of coastal engineering processes and experience to make educated engineering decisions.

3 Historical Background

Shippagan Gully has been maintained by man-made coastal structures since the late 1800's in an effort to stabilize its position and promote its navigability. A detailed history for Shippagan Gully was developed by Logan et al. (2012) from a synthesis of local knowledge and analysis of available data, including documentation of past coastal works and a complete dredging record (1882 to present time). Attempts to control and stabilize the inlet date back to 1882, when two 300 m long jetties were initially constructed on either side of the inlet mouth. Engineering drawings dating from the late 19th century show periodic extensions to the east jetty, as sediment was accumulating on its east face and ultimately passing around its seaward limit and into Shippagan Gully. This accumulation of sediment on the east side of the inlet, along with severe erosion which was observed to the west of the inlet, supports the hypothesis that a net longshore transport exists from NE to SW. It further indicates that natural sediment bypassing was interrupted at Shippagan Gully by the introduction of these original coastal structures in the late 19th century.

Throughout the mid 20th century, several engineering works were completed at Shippagan Gully, most notably during the 1960's and 1970's. A new jetty was constructed on the east side of the inlet near the inlet mouth (see Figure3.1). This new structure was built on the inlet side (west) of the older east jetty, its angle differing such that it was nearly parallel to the shoreline. The new jetty stretched 90 meters to the south west, across the inlet mouth, effectively reducing the inlet width. The second major coastal works undertaken in the 1960's and 1970's was the two phase construction of a 600 m long curved, vertical sheet pile training wall within the inlet. This structure was constructed off the inner tip of the west jetty, progressing inland (north) and into the tidal lagoon. The structure was built with the purpose of maintaining a self-scouring navigation channel between the two jetties. As a result of this new construction, a sheltered small craft harbour, known locally as Le Goulet, was formed between the west jetty and curved training wall.

Figure 3.1: Aerial photograph from 1980 showing coastal works completed in late 1960's and early 1970's.

No significant coastal works have been undertaken at Shippagan Gully since the 1970's. Furthermore, no dredging has been completed in Shippagan Gully since 1983 (although the small craft harbour was dredged in 1989 and 1993). It is worth noting that the inlet was dredged many times prior to 1983. As such, natural morphologic processes have taken hold of the inlet over the past 30 years, resulting in its present state. Severe degradation of the existing coastal structures has become apparent, most notably characterized by a complete collapse of the outer 40 m of the newer east jetty sometime between 1998 and 2004. The northern part of the curved training wall is also severely corroded. The current configuration of structures (see Figure 3.2) includes a short 25 m long damaged jetty on the east side of the inlet mouth, a 325 m long jetty on the west side, and a 600 m long curved vertical training wall extending northwards from the tip of the west jetty.

Historical aerial photographs provided by PWGSC were geo-referenced in order to provide a means for quantitative comparison of historical shoreline positions and sediment deposition patterns. From this information, morphologic trends at Shippagan Gully were deduced, providing a basis of understanding for the unique features present at the site. From this analysis it was determined that in a typical year, approximately 2100 m^3 of sediment is deposited within the confines of Shippagan Gully (not including the ebb shoal complex). Moreover, the navigation channel passing through the inlet has become narrower and has migrated westward, closer to the curved training wall. Today the navigation channel is less than 75 m wide at its narrowest point, where it is constricted by a large sand spit that has formed along the eastern side of the inlet mouth (see Figure 3.2).

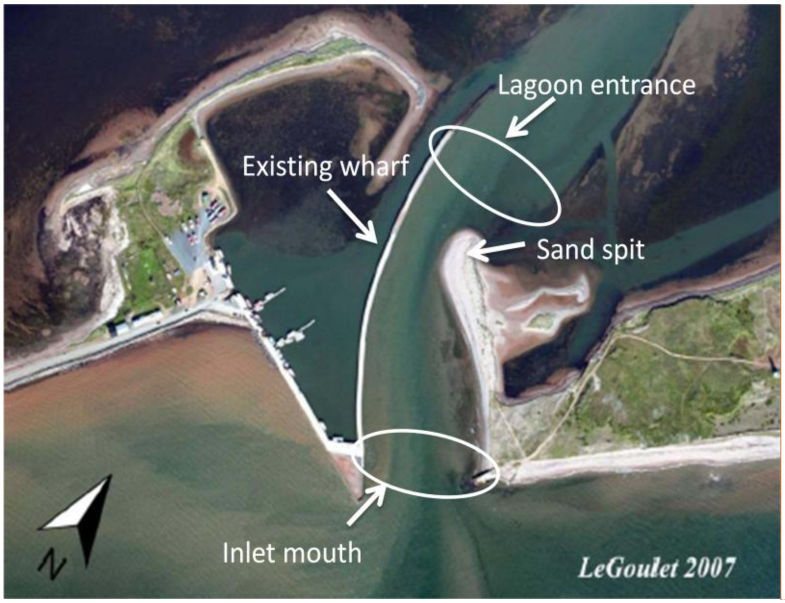

Figure 3.2 - Aerial photograph of Shippagan Gully inlet and Le Goulet harbour in 2007 indicating inlet terminology used throughout this thesis.

Comment [m4]: Rearrange picture, you cannot see the caption

Measured bathymetric cross-sections at the inlet mouth from 1992-2009 are plotted in Figure 3.3. This figure illustrates how sediment continues to accumulate on the eastern side of the inlet mouth, narrowing the navigation channel and pushing it further towards the west against the curved training wall. Furthermore, navigable depths in the offshore region are highly variable and often dangerously low due to the presence of a highly dynamic crescentric ebb shoal, which is skewed to the SW. Figure 3.4 shows a map of the bathymetry in and around the inlet, based on a synthesis of data from a bathymetric survey conducted in 2010 and a recent navigation chart.

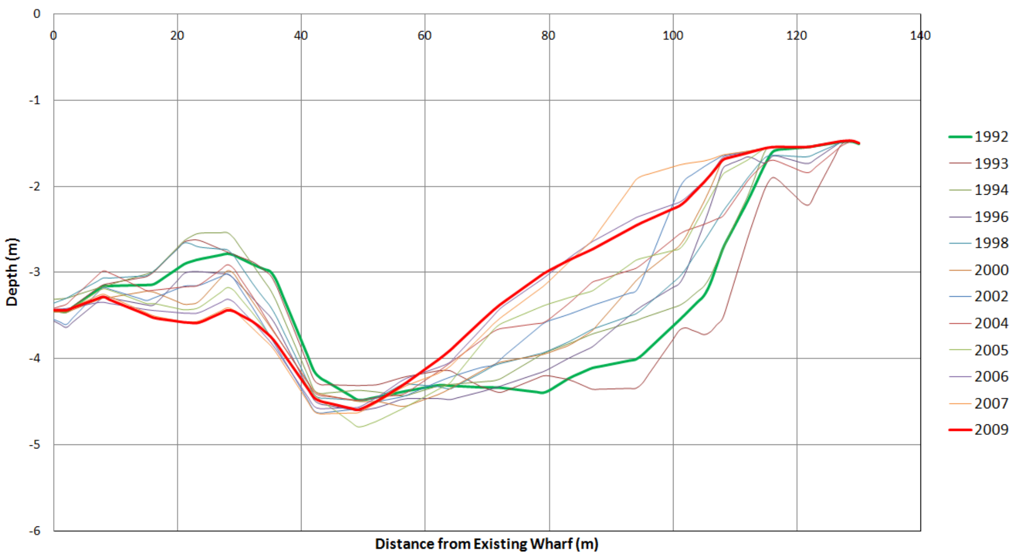

Figure 3.3 - Surveyed bathymetry cross-sections at Shippagan Gully inlet mouth from 1992-2009.

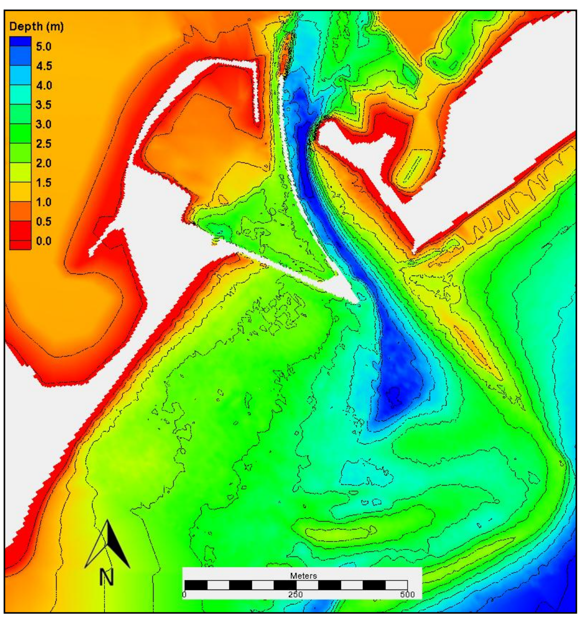

Figure 3.4 - 2010 bathymetry contours at Shippagan Gully, interpolated from bathymetric survey data and navigation charts.

4 Summary of Phase I Findings

An initial study of coastal processes at Shippagan Gully inlet was conducted by NRC in 2010-11. This Phase I study included many components, such as:

- Analysis and assessment of historical morphology changes;
- Site visit, field investigation and analysis of field data;
- Analysis of the local wave climate;
- Analysis of tidal hydrodynamics;
- Assessment of longshore transport rates;
- Development of a numerical model of wave- and tide-driven hydrodynamics and coastal processes, based on the Coastal Modelling System (CMS);
- Development of simplified boundary conditions representative of typical annual conditions;
- Calibration and validation of the numerical model;
- Simulation of hydrodynamics and coastal processes for existing conditions;
- Investigation of governing morphological processes for existing conditions; and
- Simulation and assessment of seventeen alternative scenarios.

This study developed an understanding of the complex natural processes causing deposition within and around Shippagan Gully. Furthermore, a numerical model based on the Coastal Modelling System (CMS) was developed to simulate the wave-and tidal-driven hydrodynamic and sedimentary processes at the inlet. The model was applied to simulate coastal processes for existing conditions and for seventeen alternative scenarios, to help assess their relative performance. The detailed methodology and results of the Phase I study are described in Logan (2012). A very brief summary of the main findings are presented below.

4.1 Coastal Processes

Numerous numerical simulations were conducted to try and understand the cause for the deposition within the inlet. Natural processes such as tides, storm waves and storm surge were modelled independently of each other to try and identify the impact of each process on the sedimentation at Shippagan Gully. Three main zones of sediment deposition were identified, each being driven by a different natural process. As seen in Figure 4.1, the deposition at the mouth of the inlet is thought to be governed by waves, the deposition on the sand spit on the east side of the inlet may be due to storm surge and waves, and the deposition further into the inlet may be due to ebb-flow deposition. The water along the eastern side of the inlet mouth flows north during both ebb tide and flood tide, and this current transports sediments into the inlet, contributing to the growth of the sand spit that has formed along the eastern side of the inlet mouth.

Figure 4.1 - Summary of deposition zones and their corresponding natural processes (from Logan, 2012).

4.2 Modelling and Assessment of Alternative Scenarios

Table 4.1 provides a summary of the various scenarios that were modelled in the Phase I study. In addition to existing conditions, a total of seventeen alternative future scenarios comprised of various structure additions such as jetties and training walls were modelled. Overall, the model results showed that sedimentation within the navigation channel could be reduced by constructing new structures in various arrangements. Among the most promising scenarios were scenario B5, a long shore-perpendicular jetty, and scenario H2b, a curved training wall ending in the B5 jetty. The configuration of new structures for scenarios H2b and B5 are shown in Figure 4.2, while Figure 4.3 shows the morphology changes that were predicted for each scenario. However, the inlet width for both of these scenarios was just 80 m, and subsequent feedback from local stakeholders (mainly local fishers) indicates that a wider channel is required for safe navigation. In addition, as per directions from PWGSC, dredging was not included in any of the Phase I scenarios.

Table 4.1 - Summary of scenarios modelled in the Phase I study.

Simulation ID	Scenario Description	Simulation Duration
A	Status Quo	6 years
B1	70 m east jetty, perpandicular to shoreline, 140 m wide inlet	6 years
B2	140 m east jetty, perpandicular to shoreline, 140 m wide inlet	6 years
B3	140 m east jetty, elbow at 70 m, start perpandicular to shoreline, 140 m wide inlet	6 years
B4	70 m east jetty, perpandicular to shoreline, 80 m wide inlet	6 years
B5	140 m east jetty, perpandicular to shoreline, 80 m wide inlet	6 years
B6	140 m east jetty, elbow at 70 m, start perpandicular to shoreline, 80 m wide inlet	6 years
D	Amour west bank with scour blanket, 10 m width from toe of curved breakwater	6 years
E	Armour west bank with scour blanket, reduce curvature with 30 m width at center of curved breakwater, reducing to 10 m at both ends	6 years
H1-a	Training wall parallel to curved breakwater, 140 m wide through inlet, ending in B1 jetty	6 years
H1-b	Training wall parallel to curved breakwater, 140 m wide through inlet, ending in B2 jetty	6 years
H1-c	Training wall parallel to curved breakwater, 140 m wide through inlet, ending in B3 jetty	6 years
H2-a	Training wall parallel to curved breakwater, 80 m wide through inlet, ending in B4 jetty	6 years
H2-b	Training wall parallel to curved breakwater, 80 m wide through inlet, ending in B5 jetty	6 years
H2-c	Training wall parallel to curved breakwater, 80 m wide through inlet, ending in B6 jetty	6 years
I1	Status Quo with rubble removed at north limit of curved breakwater	5 days
I2	H1-a simulation with 100m shorter parallel wall at north limit	5 days
I3	H2-a simulation with 100m shorter parallel wall at north limit	5 days

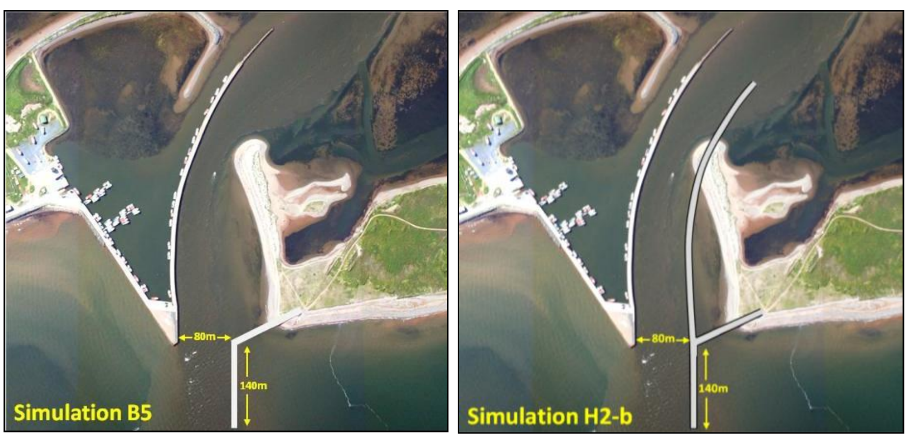

Figure 4.2 – Schematic of scenarios B5 and H2b; 2 of 17 scenarios modelled in the phase I study (from Logan, 2012).

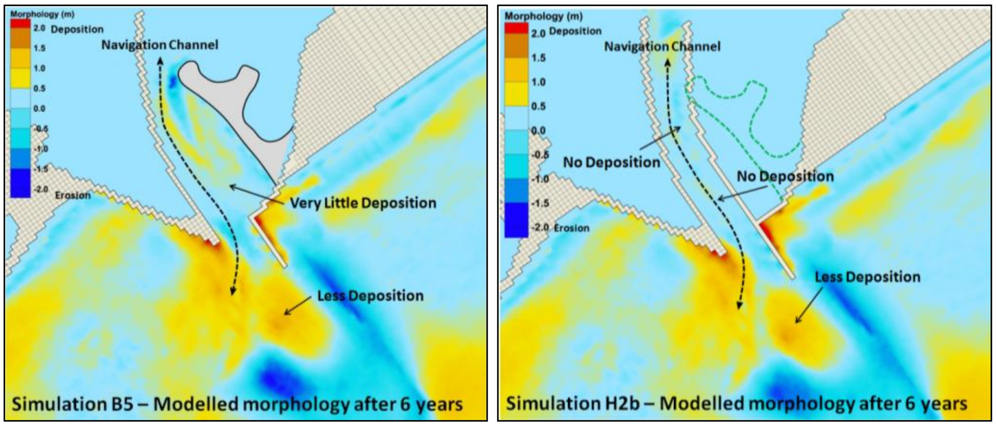

Figure 4.3 – Simulated 6-year morphology change for scenarios B5 and H2b (from Logan, 2012).

5 Field Investigations

Several field investigations have been conducted at the site to collect data to support the modelling effort. PWGSC has conducted hydrographic surveys of the navigation channel on an annual basis over the past decades. This data has been used to define the bathymetry along the channel and quantify the changes over various time periods. A team from the University of Ottawa and the National Research Council (NRC) visited the site in August 2010 and collected sediment samples and velocity data using an electromagnetic current meter. Researchers with the University of Ottawa returned to the site in May 2012 and June 2012, collecting additional sediment samples and acquiring velocity data within the inlet using an Acoustic Doppler Current Profiler (ADCP). The firm GEMTEC was retained by PWGSC to collect additional sediment samples from the seabed in 10 different locations, including the navigation channel and the ebb shoal. All of this field data was utilized in the setup, calibration and validation of the refined CMS numerical model developed for this study.

5.1 Velocity data collection and analysis

Velocity measurements were obtained from the site in August 2010 and again in June 2012, and were used to help calibrate the hydrodynamic model (CMS-Flow) and validate that it was able to replicate the tidal hydrodynamics at the site, with reasonable precision. In August 2010, velocity data was recorded throughout the inlet using an electromagnetic current meter suspended from a boat and measurement positions were recorded using a global positioning system (see Figure 5.1). The measured velocities were used to calibrate the hydrodynamic models that were developed in both the Phase I and Phase II studies. The detailed methodology and results of the calibration can be found Section 6.4.

a) 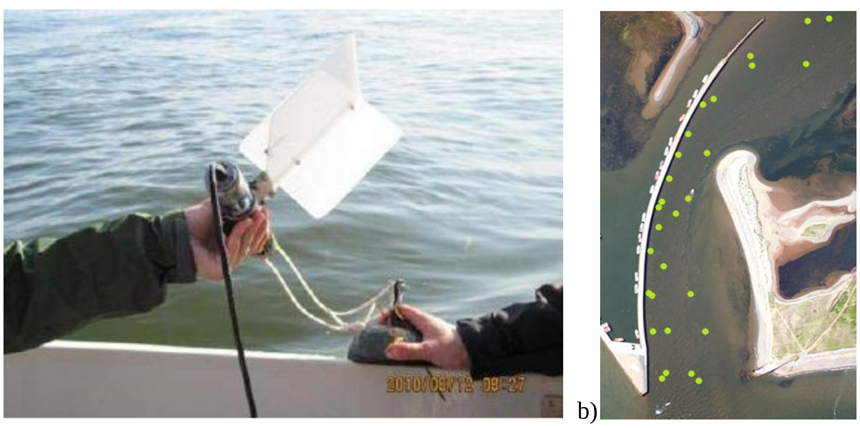 b)

Figure 5.1 - Electromagnetic current meter (left) and measurement locations (right).

Additional velocity data was collected using an Acoustic Doppler Current Profiler (ADCP) on June 14th, 2012. The ADCP instrument was suspended from a boat that moved slowly across the water surface. The boat position was recorded using a GPS within the ADCP instrument, while the time and the orientation of the instrument were also recorded simultaneously. Figure 5.2 shows the approximate transects along which ADCP data was collected. The red line denotes data collected approximately 5 m away from the curved training wall, the blue line represents data collected near the centre of the navigation channel, the green line represents data collected in the eastern part of the inlet mouth and the black line represents data collected along a series of transects running diagonally across the inlet. Velocities were recorded during both flood and ebb flows. Figure 5.3 shows the boat near the training wall while following the red transect.

Figure 5.2 - Location of ADCP transects.

Figure 5.3 - Collecting ADCP data near the curved training wall (red transect).

Figure 5.4 shows an example of the raw velocity data that was collected by the ADCP device. The colours denote the variation of velocity with depth and distance along the transect. This raw velocity data was subsequently processed to convert it into a form that could be used to validate the CMS-Flow model. The data processing included computing a series of depth-averaged and spatially averaged velocity vectors along each transect. An example of the velocity vectors derived from the ADCP data collected near the curved training wall (red transect in Figure 5.2) is shown in Figure 5.5. Further information on the use of this data to validate and assess the skill of the numerical model can be found in Section 6.4.2.

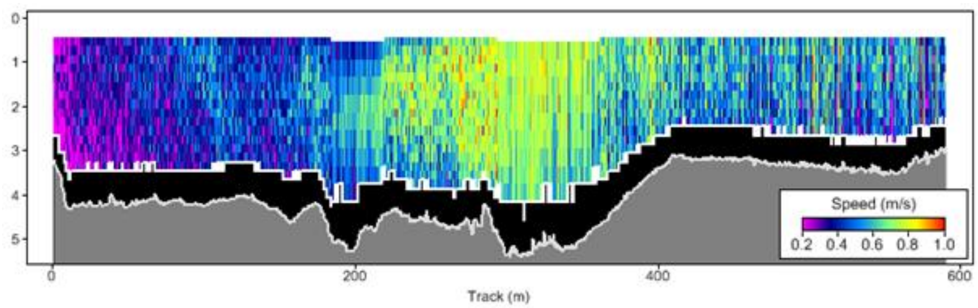

Figure 5.4 - Example of raw ADCP data.

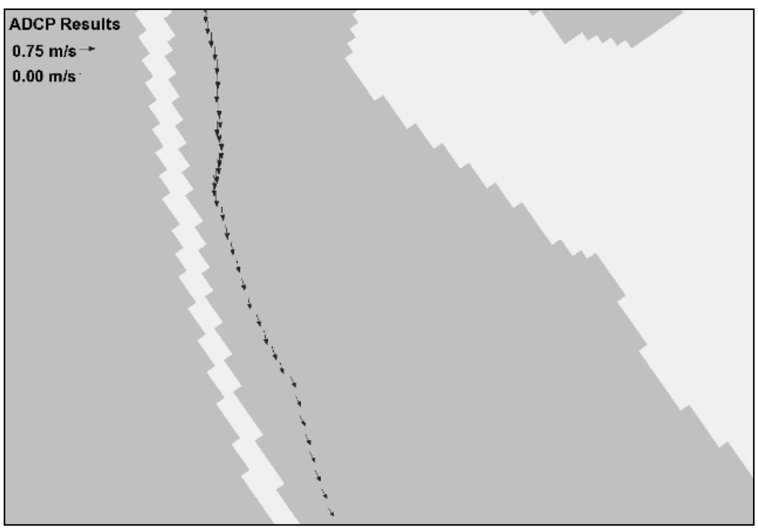

Figure 5.5 - Example of processed ADCP velocity vectors (along red transect).

5.2 Sediment sample collection analysis

During three separate field investigations, a total of twenty-one sediment samples have been collected and analyzed. The first set of sediment samples was collected during the site visit in August 2010, where various samples were taken from the beaches located NE and SW of the inlet and on the beach located along the east side of the inlet. A second set of sediment samples was collected during a site visit on May 29-31, 2012. During this site visit, additional sediment samples were taken NE of the inlet, within the inlet (along the eastern beach) and at the reattachment point SW of the inlet. The third and final set of sediment samples was collected by the consulting firm GEMTEC, who was retained by PWGSC to collect sediment samples from the seabed in 10 different locations within the inlet and on the ebb shoal area. The location of all 21 sediment samples is shown in Figure 5.6. The various samples were analyzed by the team which had collected them, and grain size distribution curves were developed. The developed grain size distribution curves can be found in Appendix B - Grain Size Distribution Curves. Table 5.1 provides a summary of the D_{35}, D_{50} and D_{90} values that characterize the grain size distributions. The beaches NE and SW of the inlet are comprised of non-cohesive sediments with D_{50} ranging from 0.17 up to ~18 mm. The field data suggest that the ebb shoal contains a wide range of sands and fine gravels, with grain sizes ranging from 0.15 to ~10 mm. Within the inlet mouth, where peak velocities regularly exceed 2 m/s, the navigation channel is evidently armoured with a blend of coarse sand and gravel with particle sizes ranging from 1 mm up to 85 mm.

Figure 5.6 - Location of sediment samples.

Table 5.1- Sediment sample grain sizes.

Sample	D_{50} (mm)	D_{35} (mm)	D_{90} (mm)
A	7.00	0.65	18.00
B	0.34	0.26	0.45
C	12.00	6.00	18.00
D	0.34	0.30	0.60
E	0.55	0.40	2.50
F	1.90	0.90	9.00
G	0.20	0.17	0.26
H	0.25	0.20	0.30
I	0.20	0.17	0.50
J	0.43	0.37	15.00
K	0.35	0.27	0.42
L	0.45	0.37	0.42
M	24.80	15.00	52.00
N	0.38	0.34	0.47
O	4.00	0.60	60.00
P	0.37	0.34	0.48
Q	6.00	2.00	50.00
R	52.80	40.00	90.00
S	0.28	0.25	0.40
T	1.20	0.20	40.00
U	0.33	0.28	0.45

5.3 Bathymetric surveys

Over the past several decades, PWGSC has conducted annual hydrographic surveys of the navigation channel. Figure 5.7 shows an example of the typical extent of each survey. The survey data typically features a horizontal resolution of ~1m and covers the navigation channel from the bridge located at the NW corner of the lagoon and extending offshore, including a portion of the ebb shoal. The hydrographic survey data was converted from chart datum (CD) to geodetic datum (GD) using a linear interpolation of the corrections shown in Table 5.2 (provided by DFO). The converted data was used to define the bathymetry along the navigation channel and quantify the changes over various periods of time. In addition, the hydrographic surveys were interpolated and combined with information from navigational charts to create the starting bathymetry for the CMS numerical model.

Figure 5.7 - Example of hydrographic survey data extent (2004).

Table 5.2 - Corrections to convert from Chart Datum (CD) to Geodetic Datum (GD).

Location	Correction CD to GD
Shippagan Harbour	0.75 m
Le Goulet - 250 m north of north end of existing breakwater	0.65 m
Le Goulet – 60 m south of south end of existing breakwater	0.53 m
Tracadie tidal station	0.60 m

6 CMS Model Development

6.1 Description of CMS-Flow, CMS-Wave and SMS

The Coastal Modelling System (CMS) is an integrated suite of numerical models developed by the Coastal Inlets Research Program (CIRP) of the United States Army Corps of Engineers (USACE) for simulating flow, waves, sediment transport, and morphology change in coastal areas (Sanchez *et al.*, 2012). The system is specifically designed for practical applications relating to navigation channel performance and sediment management for coastal inlets and adjacent beaches. CMS is composed of two different models; a model which calculates hydrodynamics and sediment transport (CMS-Flow) and a wave model (CMS-Wave). Both models operate on a rectangular finite difference grid with variable grid spacing, such that areas of interest can be modelled at a higher resolution without greatly sacrificing computation time. In this study the numerical models CMS-Flow and CMS-Wave were applied in a coupled manner to simulate the wave and tidal hydrodynamics, sediment transport and morphology change within and around Shippagan Gully inlet.

CMS-Flow is a coupled hydrodynamic and sediment transport model capable of simulating depth-averaged circulation, salinity and sediment transport due to tides, wind and waves. The hydrodynamic model solves the conservative form of the shallow water equations and includes terms for the Coriolis force, wind stress, wave stress, bottom stress, vegetation flow drag, bottom friction, and turbulent diffusion. Three different sediment transport models are available in CMS: a sediment mass balance model, an equilibrium advection-diffusion model, and non-equilibrium advection-diffusion model. The salinity transport is simulated with the standard advection diffusion model and includes evaporation and precipitation. All equations are solved using the Finite Volume Method on a non-uniform (telescoping) Cartesian grid. CMS-Flow is suitable for simulating hydrodynamics and sediment transport over a wide range of time scales extending from hours to years (Buttolph *et al.*, 2006).

CMS-Wave is a spectral wave transformation model that solves the steady-state wave-action balance equation on a non-uniform Cartesian grid. It considers wind wave generation and growth, diffraction, reflection, dissipation due to bottom friction, whitecapping and breaking, wave-wave and wave-current interactions, wave runup, wave setup, and wave transmission through structures (Lin *et al.*, 2008).

In this study, the Surface Modelling System (SMS), developed by Acquaveo Inc., was used to facilitate the preparation of input files and the viewing and analysis of model outputs. SMS is a user-friendly interface which is used alongside the CMS models for grid creation, model setup and visualization of results. Most model results presented herein were developed and plotted using the SMS software.

6.1.1 Governing Equations

CMS-Flow and CMS-Wave use a number of hydrodynamic and sediment transport equations that govern the modelled processes. However, only the key equations will be described and presented in this thesis and any further information can be found in Buttolph *et al*. (2006). Beginning with the continuity and momentum equations, the assumption is made that the depth-uniform currents are in the presence of oscillatory waves, which results in the set of equations being written as:

$$\frac{\partial h}{\partial t} + \frac{\partial (hV_j)}{\partial x_j} = S_M \qquad (6.1)$$

$$\frac{\partial(hV_i)}{\partial t}+\frac{\partial(hV_jV_i)}{\partial x_j}-\varepsilon_{ij}f_c hV_j=-gh\frac{\partial\bar{\eta}}{\partial x_j}-\frac{h}{\rho}\frac{\partial p_{atm}}{\partial x_i}$$
$$+\frac{\partial}{\partial x_j}\left(v_i h\frac{\partial V_i}{\partial x_j}\right)-\frac{1}{\rho}\frac{\partial}{\partial x_j}\left(S_{ij}+R_{ij}-\rho hU_{wi}U_{wj}\right)+\frac{\tau_{si}}{\rho}-\frac{\tau_{bi}}{\rho} \qquad (6.2)$$

where: t = time (s)
f_c = Coriolus parameter (rad/s)
h = wave-averaged total water depth
$\bar{\eta}$ = wave-averaged water surface elevation with respect to reference datum (m)
S_M = water source/sink term due to precipitation, evaporation and structures (m/s)
V_i = total flux velocity
U_i = wave and depth averaged current velocity vector (m/s)
U_{wi} = wave flux velocity vector (m/s)
g = gravitational constant (9.806 m/s^2)
p_{atm} = atmospheric pressure (Pa)
ρ = water density (kg/m^3)
v_i = turbulent eddy viscosity (m^2/s)
τ_{si} = wind surface stress vector (Pa)
S_{ij} = wave radiation stress tensor (Pa)
R_{ij} = surface roller stress tensor (Pa)
τ_{bi} = combined wave-current mean bed shear stress vector (Pa)

The above continuity and momentum equations are similar to those derived by Svendsen in 2006 except for the inclusion of the water source/sink term in the continuity equations and the atmospheric pressure and surface roller terms in the momentum equation (Sanchez *et al.*, 2012). Figure 6.1 shows the vertical conventions used for mean water surface elevations and bed elevations.

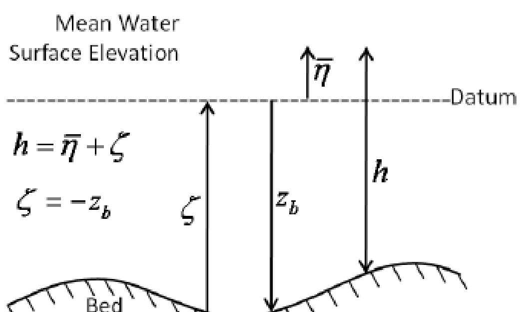

Figure 6.1 – Vertical conventions used for mean water surface elevation and bed elevations (Sanchez *et al.*, 2012).

When waves are presence, the oscillatory motion of the waves produces a net mass transport referred to as Stokes Drift. The wave mass flux velocity is defined as the wave mass flu divided by the local wave-averaged water depth and can be approximated by (Phillips 1977; Svendsen 2006):

$$U_{wi} = \frac{(E_w + 2E_{sr})w_i}{\rho hc} \qquad (6.3)$$

where: c = wave speed (m/s)

E_w = wave energy (N/m)

E_{sr} = surface roller energy density

H_s = significant wave height (m)

w_i = wave unit vector

The wave radiation stresses are calculated based on the linear wave theory with the following equation:

$$S_{ij} = \iint E_w(f,\theta)\left[n_g w_i w_j + \delta_{ij}(n_g - \tfrac{1}{2})\right] df d\theta \qquad (6.4)$$

where: f = wave frequency (1/s)

θ = wave direction (°)

δ_{ij} = delta function where δ_{ij}=1 for $i = j$ and δ_{ij}=0 for $i \neq j$

and

$$n_g = \frac{c_g}{c} = \frac{1}{2}\left(1 + \frac{2kh}{\sinh 2kh}\right) \qquad (6.5)$$

where c_g is the wave group velocity, c is the wave celerity and k is the wave number.

The eddy viscosity is a parameter that is intended to simulate the dissipation of energy at smaller scales than the model can simulate. Eddy viscosity is needed because the model cannot simulate small-scale vortices or eddies which are of the same order of the grid cell size (Sanchez *et al.*, 2012). In CMS-Flow, total eddy viscosity, v_t, is calculated as the sum of a base value v_0, the currently related eddy viscosity v_c and the wave related eddy viscosity v_w. This is done with the following equation:

$$v_t = v_0 + v_c + v_w \qquad (6.6)$$

The base value, v_0, for the eddy viscosity is approximately equal to the kinematic eddy viscosity. There are four options for the current related eddy viscosity: Falconer, Parabolic, Subgrid and Mixing-Length. The subgrid option was employed for this study, which is calculated by:

$$V_c = c_1 u_* h + c_2 \Delta |\bar{S}| \qquad (6.7)$$

where c_1 and c_2 are empirical coefficients related to the turbulence produced by the bed shear and horizontal velocity gradients and Δ is the average grid area. $|\bar{S}|$ can be calculated from:

$$|\bar{S}| = \sqrt{2e_{ij}e_{ij}} \text{ with } e_{ij} = \frac{1}{2}\left(\frac{\partial V_i}{\partial x_j} + \frac{\partial V_j}{\partial x_i}\right) \qquad (6.8)$$

The wave related eddy viscosity is calculated using the following equation:

$$v_w = c_3 u_w H_s + c_4 h (\frac{D_{br}}{\rho})^{1/3} \qquad (6.9)$$

where $c_3$and c_4 are empirical coefficients, H_s is the significant wave height and u_w is the peak bottom orbital velocity based on the significant wave height. The R.H.S of the equation can be divded into two terms. The first term represent the component due to wave bottom friction and the second term represents the component due to wave breaking.

CMS-Flow has two main options for calculating sediment transport within the model; nonequilibrium total-load transport and equilibrium transport. The nonequilibrium total-load transport model has only one sediment transport equation to choose from, the total-load transport equation. If the equilibrium transport option is chosen, there are four available sediment transport equations:

- Lund-CIRP Sediment Transport Formula,
- Van Rijn Sediment Transport Formula,
- Soulsby-van Rijn Total-load Transport Formula and
- Watanabe Total-Load Transport Formula
-

The sediment transport equation that was chosen for this study was the Lund-CIRP Sediment Transport Formula because it was specifically created for use in coastal inlet sediment transport modelling by the USACE (the CMS model developers). Since this is the only sediment transport equation used in this study, it will be the only equation that will be discussed.

The Lund-CIRP Sediment Transport Formula is a combination of a bed load formula and a suspended load formula. Starting with the bed load, which can be calculated as follows:

$$\frac{q_{b*}}{\sqrt{(s-1)gd_{50}^3}} = f_b \rho_s 12 \sqrt{\Theta_c} \Theta_{cw,m} \exp\left(-4.5 \frac{\Theta_{cr}}{\Theta_{cw}}\right) \qquad (6.10)$$

where: q_{b*} = equilibrium bed load transport (kg/m/s)

d_{50} = median grain size (m)

s = sediment specific gravity or relative density

g = gravitational constant (9.81 m/s^2)

ρ_s = sediment density (kg/m^3)

Θ_c = Shields parameters due to currents

$\Theta_{cw,m}$ = mean Shields parameters due to waves and currents

Θ_{cw} = maximum Shields parameters due to waves and currents

Θ_{cr} = critical Shields parameter

f_b = bed-load scaling factor

The suspended load transport is calculated from the following formula:

$$\frac{q_{s*}}{\sqrt{(s-1)gd_{50}^3}} = f_s \rho_s c_R U \frac{\varepsilon}{\omega_s}\left[1 - \exp\left(-\frac{\omega_s h}{\varepsilon}\right)\right] \tag{6.11}$$

where: q_{s*} = suspended load transport (kg/m/s)

U = Depth-averaged current velocity (m/s)

h = time-averaged total water depth (m)

ω_s = sediment fall velocity (m/s)

ε = vertical sediment diffusivity (m^2/s)

c_R = reference bed concentration (kg/m^3)

f_s = suspended-load scaling factor

The sediment fall velocity used in the suspended load transport formula is calculated using the formula developed by Soulsby (1997):

$$\omega_s = \frac{v}{d}\left[(10.36^2 + 1.049 d_*^3)^{1/2} - 10.36\right] \tag{6.12}$$

where d is the grain size. The vertical sediment diffusivity used in the suspended load transport formula is calculated as:

$$\varepsilon = h\left(\frac{D_e}{\rho}\right)^{1/3} \tag{6.13}$$

where D_e is the total effective dissipation given by:

$$D_e = k_b^3 D_b + k_c^3 D_c + k_w^3 D_w \tag{6.14}$$

where k_b, k_c, k_w are coefficients, D_b is the wave breaking dissipation and D_c and D_w are the bottom friction dissipation due to currents and waves respectively.

The main equation used in the CMS-Wave model is the wave-action balance equation. This equation represents the two-dimensional variation of wave energy in space and accounts for the effect of an ambient horizontal current on the wave behavior. This equation is as follows (Sanchez *et al*., 2012):

$$\frac{\partial(C_xN)}{\partial x}+\frac{\partial(C_yN)}{\partial y}+\frac{\partial(C_\theta N)}{\partial \theta}=\frac{\kappa}{2\sigma}\left[\left(CC_g\cos^2\theta N\varepsilon_y\right)_y-\frac{CC_g}{2}\cos^2\theta N_{yy}\right]-\varepsilon_bN-S \qquad (6.15)$$

where: C = wave celerity

C_g = group velocity

κ = empirical parameter representing the intensity of the diffraction effect

ε_b = parameterization of wave breaking energy dissipation

S = additional source and sinks (wind forcing, bottom friction loss, etc.)

and

$$N=\frac{E(\sigma,\theta)}{\sigma} \qquad (6.16)$$

which is the wave-action density to be solved and is a function of frequency, σ, and direction, θ. E(σ,θ) is the two-dimensional spectral wave density representing the wave energy per unit water-surface area per frequency and direction interval (Sanchez *et al*., 2012).

6.1.2 Numerical Methods

The CMS-Flow model has both an explicit and implicit solution scheme available to the user. The explicit solver is designed for situations with extensive wetting and drying, which require small computational time steps. The implicit solver is intended for the simulation of tidal and wave-induced circulation at tidal inlet and navigation channels (Sanchez *et al*., 2012). Therefore, for this study, the implicit solution scheme was used for every simulation presented in this thesis.

One of the important aspects of an incompressible flow model is the location of the velocity and pressure variables. On a staggered grid, the pressure is located at the center of the cells and the velocities are located on the faces of the cells. On a non-staggered grid, these variables are located at the center of the cells, which is shown in Figure 6.2. In CMS-Flow, the non-staggered grid approach is used because it is better at handling the interface between coarse and fine cells where five or six control volumes are used.

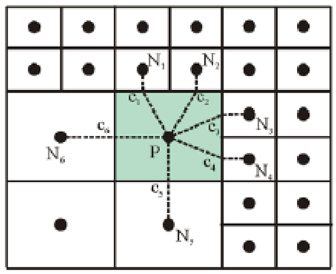

Figure 6.2 – Location of the variables when using a telescoping grid.

Since all of the governing equations described in Section 6.1.1 are some form of transport equation, the same discretization is applied to all of the equations. The general transport equation is given by:

$$\frac{\partial(h\phi)}{\partial t} + \frac{\partial(hU_j\phi)}{\partial x_j} = \frac{\partial}{\partial x_j}\left(\Gamma h \frac{\partial \phi}{\partial x_j}\right) + S_\phi \qquad (6.17)$$

where: ϕ = general scalar

t = time

h = total water depth

U_j = depth averaged current velocity

Γ = diffusion coefficient for ϕ

S_ϕ = represents all remaining terms

For spatial discretization, the CMS model uses a control-volume technique in which the governing equations are integrated over each control volume in order to obtain an algebraic equation that can be solved numerically. Integrating the previous equation over a control volume and the application of the Green theorem gives:

$$\int_A \frac{\partial(h\phi)}{\partial t} dA + \oint_L h[(\hat{n}_i U_i)\phi - \Gamma(\hat{n}_i \nabla_i \phi)]\, dL = \int_A S_\phi dA \qquad (6.18)$$

$$\frac{\partial(h_p\phi_p)}{\partial t}\Delta A_p + \sum_f \Delta l_f h_f \left[U_f\phi_f - \Gamma_f(\nabla_\perp \phi)_f\right] = S_\phi \Delta A_p$$

For temporal discretization, the transport equation can be rewritten as:

$$\int \frac{\partial(h\phi)}{\partial t} dt = \int F dt \qquad (6.19)$$

where "F" includes all of the remaining terms. CMS employs a fully implicit time stepping scheme, which is as follows:

$$\frac{(1+0.5\theta)h^{n+1}\phi^{n+1}-(1+\theta)h^{n}\phi^{n}+0.5h^{n-1}\phi^{n-1}}{\Delta t} = F^{n+1} \qquad (6.20)$$

The θ term is a weighting factor between 0 and 1. When θ = 0, the scheme is equal to the first-order back Euler scheme and when θ = 1, the scheme is equal to the second-order backward scheme.

There are three advection schemes used in the CMS model; the hybrid scheme, the exponential scheme and the hybrid linear/parabolic scheme. The hybrid scheme is composed of the first-order upwind scheme and the second-order central difference scheme. The Peclet number is used in order to determine which scheme is applied. When the Peclet number is larger than 2, the first-order upwind scheme is used; otherwise, the central difference scheme is used (Sanchez *et al.*, 2012):

$$\phi_f = \begin{cases} \frac{\phi_D+\phi_C}{2} \, for \, |P_f| < 2 \\ \phi_C \qquad for \, |P_f| > 2 \end{cases} \qquad (6.21)$$

Where the subscripts D and C indicate the downstream and first upstream nodes respectively and P_f is the Peclet number. The Peclet number is the ratio of the advective transport rate to the diffusive transport rate. The exponential scheme interpolates the face value using an exact solution to the one-dimensional steady advection-diffusion equation, which is as follows:

$$\frac{\phi_f-\phi_0}{\phi_L-\phi_0} = \frac{\exp\left(\frac{P_f x_f}{|\delta_\perp|}\right)-1}{\exp(P_f)-1} \qquad (6.22)$$

This exponential scheme has automatic upwinding and is stable. However, the scheme is usually less than second order. The last advection scheme, the Hybrid Linear/Parabolic Approximation scheme, is written as:

$$\phi_f = \begin{cases} \phi_C + (\phi_D - \phi_C)\hat{\phi}_C \; for \;\; 0 \le \hat{\phi}_C \le 1 \\ \phi_C \qquad\qquad\qquad\qquad otherwise \end{cases} \qquad (6.23)$$

where the subscripts D and C indicate the downstream and first and second upstream cells respectively.

CMS offers a number of iterative solvers to solve the algebraic equations that can be chosen by the user, including: GMRES, BiCGStab and Gauss-Seidel. The solver that was used in all of the simulations in this study is the default iterative solver, GMRES (Generalized Minimum Residual) method (by Saad in 1993). The original GMRES method uses the Arnoldi process to reduce the coefficient matrix to the Hessenburg form and minimizes at every step the norm of the residual vector over a Krylov subspace (Saad and Schultz, 1986). A variation of the GMRES method was recommended by Saad (1993), which allows changes in the precondition at every iteration step. The GMRES solver employed in the CMS model is applicable to both symmetric and non-symmetric matrices and leads to the smallest residual for a fixed number of iterations. The only downside is the large memory requirements and computational costs when applying it to large systems.

The governing equations are descritized using the described methods above and are solved in a segregated manner in which each equation is solved separately with the latest values from the other equations until a converged solution is reached. The SIMPLEC algorithm is used to couple the momentum and continuity equations. The main issue when solving the momentum equations is that the water level is not known and must be calculated as part of the solution.

Starting with an initial or estimated water level, the corresponding velocity is given by:

$$\frac{\partial(hV_i^*)}{\partial t} + \frac{\partial(hV_j^*V_i^*)}{\partial x_j} = \frac{\partial}{\partial x_j}\left(v_i h \frac{\partial V_i'}{\partial x_j}\right) - \frac{h}{\rho}\frac{\partial p^*}{\partial x_i} + S_i^* \qquad (6.24)$$

where $p^* = \rho g \bar{\eta}^*$ and S_i^* includes all of the remaining terms.

The SIMPLEC algorithm can then be implemented and is summarized in the following steps:

1. Guess the water level and pressure field p^*
2. Solve the momentum equations to obtain U_i^*
3. Use the Rhie and Chow's momentum to determine the velocities and fluxes at cell faces
4. Solver the pressure equation to obtain p'
5. Correct velocities and water levels
6. Treat the corrected water pressure, as a new guess, and repeat the procedure from step 2 until convergence.

The sediment transport calculations are done in a semi-coupled method where the sediment calculations are decoupled from the hydrodynamics but the sediment transport, bed change and bed material sorting equations are coupled at the time step level and solved simultaneously. The procedure of the sediment transport is as follows (Sanchez *et al*., 2012):

1. Calculate boundary layer variables and bed form roughness
2. Estimate the potential sediment concentration capacity C_{tk}^{*n+1}
3. Guess the new bed composition as $p_{bk}^{n+1} = p_{bk}^{n}$
4. Calculate the fractional concentration capacity $C_{t*k}^{n+1} = p_{bk}^{n+1} C_{t*k}^{n+1}$
5. Solve transport equations for each sediment size class
6. Estimate the mixing layer thickness
7. Calculate the total and fractional bed changes
8. Determine the bed sorting in the mixing layer
9. Update the bed elevation
10. Go back to step 4 and iterate until convergence
11. Calculate the bed gradation in the bed layer below the mixing layer
12. Calculate avalanching
13. Correct the sediment concentration due to flow depth change $C_{tk}^{n+1} = (h - \Delta z_b) C_{tk}^{n+1}/h$

6.1.3 Improvements and new features

Several improvements and new features have been included in the CMS-Flow model since the Phase I study was completed in June 2011. Two of the main new features which are relevant to the current study are support for a telescoping rectangular grid and the ability to simulate the transport of sediments with multiple grain sizes. Only a single sediment grain size could be modelled in previous versions of CMS-Flow.

6.1.3.1 Telescoping Grid

Currently four different types of numerical grids (shown in Figure 6.3) are available when creating a grid for the CMS-Flow model: a regular grid; a non-uniform grid; a telescoping grid; and a stretched telescoping grid. However, when the Phase I study was conducted, only the regular grid and non-uniform grid were supported. Of these two options, the non-uniform grid was selected and employed in the Phase I study. While the non-uniform grid performed well, it was inefficient because it forced the creation of grids with high resolution in areas where such high resolution was unnecessary and unhelpful (see Figure 6.4).

The new telescoping grid option makes it possible to discretize the domain using a high resolution in areas of high interest (such as the inlet mouth), while less important areas are modelled with courser resolution. This approach improves computational efficiency and makes it possible to model large domains while also modelling important areas with very high spatial resolution. The present study takes advantage of the telescoping grid; further information is presented in Section 6.2.

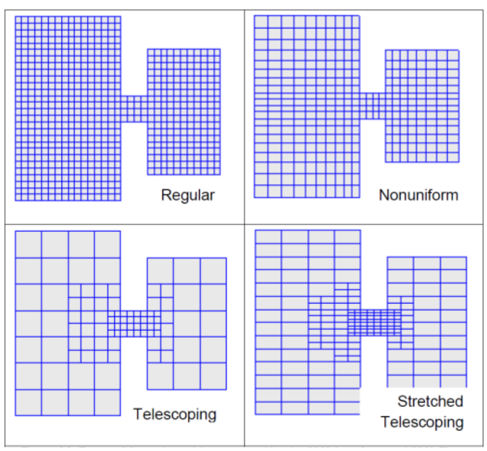

Figure 6.3 - Illustration of the four different grid types available in CMS-Flow (Sanchez et. al., 2012).

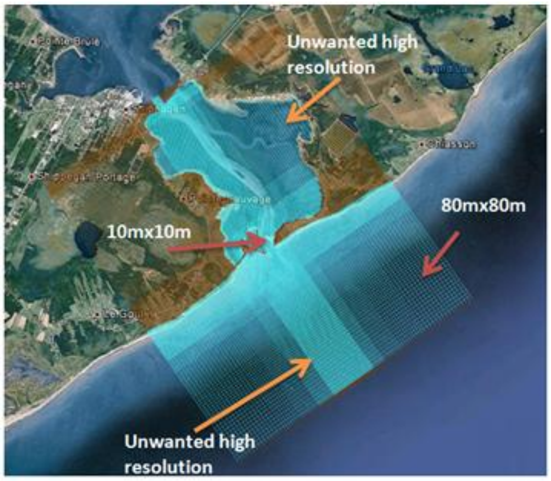

Figure 6.4 - CMS-Flow computational grid used in Phase I, note areas of unnecessary high resolution (offshore of the inlet and within the lagoon).

6.1.3.2 Multiple Grain Size Sediment Transport

The second important new feature available in CMS-Flow is the ability to simulate the mobilization, transport and deposition of sediments with multiple grain sizes. In the Phase I study, an initial D_{50} map (describing the spatial variation in the nominal diameter of seabed sediments) and a single transport grain size D_t were specified, and the sediment transport was calculated in the following steps:

- If the hydrodynamic forces are large enough to initiate sediment transport for the specified D_{50} in a cell, then sediment from that cell is mobilized and transported.
- This transported sediment takes on the user-specified transport grain size D_t.
- When transported sediment is deposited in a new location, the sediment assumes the D_{50} value of the seabed in the new location.
-

This approach is clearly unrealistic since a sediment particle may change size twice each time it is transported, once when it is mobilized, and again when it is deposited. This approach can cause issues when trying to model morphology change. For example, if sediment is transported from an area of fine sand to an area with gravel, the transported sediment will change grain size from fine sand to gravel once it is deposited. The result is a potentially unrealistic build up of deposition in areas where large seabed sediments are specified.

The modelling conducted in the current study utilizes multiple grain size sediment transport - a new addition to CMS-Flow. Instead of specifying a single initial D_{50} value in each cell (as was done in the Phase I study), an initial grain size distribution curve describing the range of sediments on the seabed is specified in each cell. There are numerous ways in which the grain size distribution can be specified within the model. In the present study, a log-normal grain size distribution was assumed in each cell and the initial distribution was specified in terms of D_{35}, D_{50} and D_{90} values. Next, the specified grain size distribution is divided into a number of discrete bins (or size classes). This allows the model to calculate the sediment transport for multiple grain sizes by applying the sediment transport equations independently for each size class, in each computational cell. The end result is that the bottom sediments in each cell are represented by a dynamic grain size distribution that evolves over time in response to the inflow and outflow of each sediment size class. The values of D_{35}, D_{50} and D_{90} in each cell can all change at every time step.

Figure 6.5 shows an example of how the spatial variation of sediment D_{50} can vary over the course of a simulation. This figure shows how the D_{50} value for each cell can change during a simulation depending on the sediment transport that occurred in each cell. In some areas the bottom sediments become coarser over time, while in other areas they become finer. This method of multiple grain size sediment transport provides a more realistic representation of natural processes and should therefore enhance the realism with which sedimentary processes are modelled.

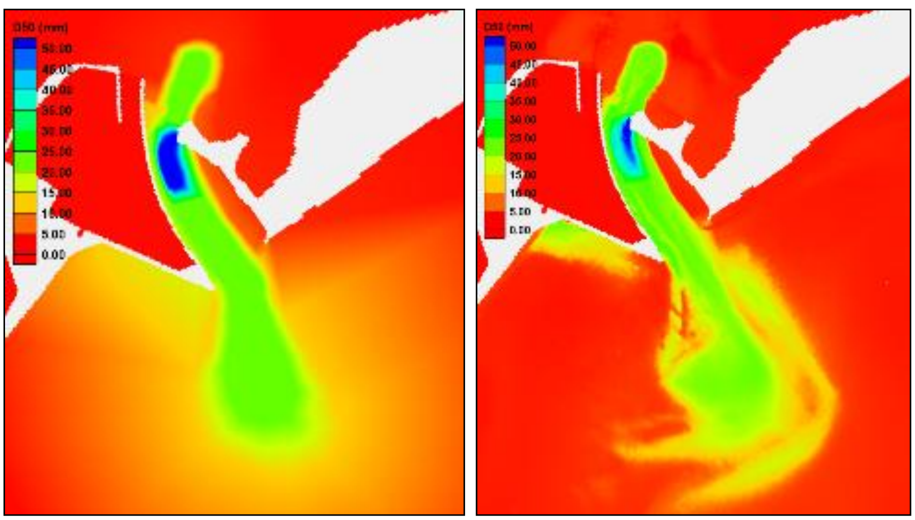

Figure 6.5 - D_{50} map before simulation (left) and after simulation (right).

6.1.4 Coupling of CMS-Wave and CMS-Flow

The CMS-Flow and CMS-Wave models were coupled through a steering module, which exchanges information back and forth between the two models at specified time intervals. As shown in Figure 6.6, CMS-Wave passes a number of variables to CMS-Flow, including: significant wave height, peak wave period, wave direction, wave breaking dissipation and radiation stress gradients (which force wave-induced currents). CMS-Flow provides CMS-Wave with updated information on bathymetry, water levels and current velocities (Militello et. al., 2003). Such coupling is essential for modelling a highly dynamic coastal inlet such as Shippagan Gully, where coastal processes result from complex interactions between tide-driven flows and nearshore waves.

The rate at which this information is transferred is called the steering interval. For this study, the steering interval was set to one hour, meaning that the information is transferred between the two models at hourly intervals (simulation time).

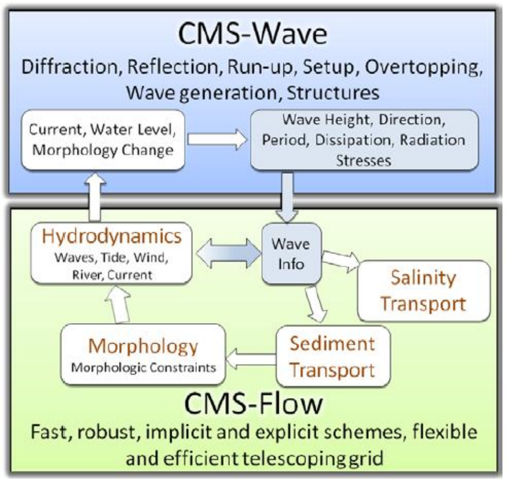

Figure 6.6 – Schematic of coupling between CMS-Wave and CMS-Flow models (Sanchez et al., 2012).

6.2 Model domains and computational grids

The CMS-Flow model domain for the phase II study was similar to domain considered in the Phase I study. The domain covers the entire lagoon, up to the bridge at Shippagan, and extends approximately 3 km in the offshore direction, out to a depth of ~12 m. Extending the domain 3 km offshore was deemed far enough in order for the longshore currents created by the tidal flow and breaking waves to be negligible at the offshore boundary. In the longshore direction the CMS-Flow grid covered a stretch of coastline 6 km in length with Shippagan Gully at its centre, thus providing ample shoreline to either side of the inlet for the development of longshore sediment transport. The CMS-Flow domain has three model boundaries where water level fluctuations are specified: the northwest limit of the tidal lagoon, the northeast longshore limit and the southwest longshore limit of the numerical domain. The offshore (southeast) boundary of the numerical model was set to be a closed boundary. This closed boundary forced the currents to travel in the longshore direction, which re-creates the existing longshore current in the Gulf of St-Lawrence.

Figure 6.6 shows the computational grid for the CMS-Flow model that was developed for the phase II study. The model grid consists of approximately 120,000 computational cells and utilizes the telescoping grid option to produce a high resolution (4m x 4m) grid around the inlet, while maintaining a lower resolution (128m x 128m) offshore of the inlet and within the lagoon. (By way of comparison, in the phase I study, the inlet mouth was modelled using a coarser resolution of 10m x 10m.) In addition, in order to properly model longshore sediment transport, the shoreline is discretized with a resolution of 8m x 8m. The navigation channel through the lagoon is covered by a 16m x 16m grid.

Unfortunately, the CMS-Wave model used in this study does not support telescoping grids. Therefore, the same grid that was developed in the Phase I study was used again in the current study without modification. The CMS-Wave grid contains approximately 72,000 computational cells and is shown below in Figure 6.7. The grid describes a numerical domain that extends approximately 5km in the offshore direction and 2km inside of the lagoon. The offshore boundary of the CMS-Wave domain included the location where information on the local wave climate was known; specifically a node from the MSC50 wave hindcast, developed by Environment Canada (Swail et al., 2006). (Further information is provided in the phase I work, Logan, 2012). This allowed for the wave climate that was determined from the MSC50 hindcast to be directly input along the offshore boundary of the CMS-Wave model. The CMS-Wave domain includes ~14 km of coastline, stretching from a point ~6 km southwest of the inlet to a point ~8 km northeast of the inlet. The cell sizes vary from 80 m x 80 m at the offshore boundary to 10 m x 10 m over the ebb-shoal and within the inlet.

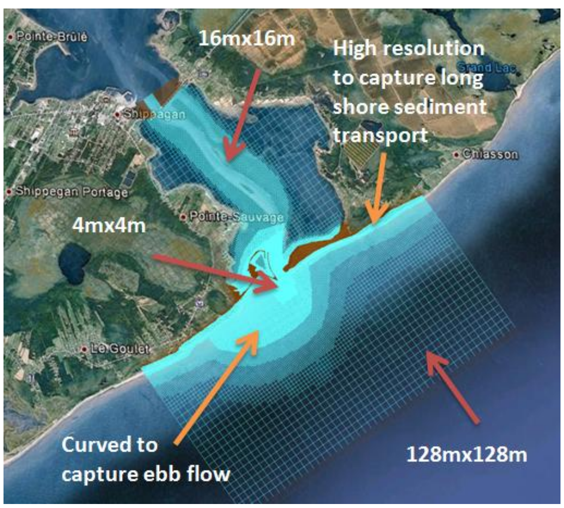

Figure 6.6 - CMS-Flow computational grid; stretching 3 km offshore and covering 6 km of coastline.

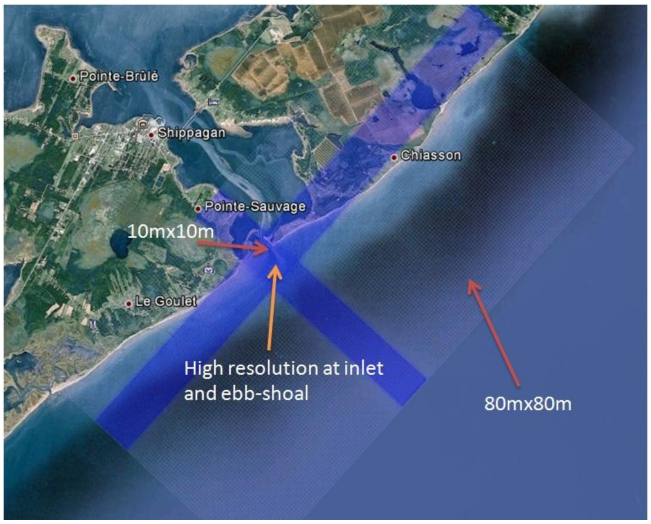

Figure 6.7 - CMS-Wave computational grid; stretching 5 km offshore and covering 14 km of coastline.

6.3 Boundary Conditions

Each model, CMS-Flow and CMS-Wave, is driven by a set of boundary conditions. CMS-Flow is driven by three different water level time histories, applied at the SW extent of the model, the NE extent of the model and the NW limit of the tidal lagoon. Alternatively, CMS-Wave is driven by a time series of two-dimensional wave spectra applied along the offshore limit of the computational domain. The wave spectra are specified in terms of significant wave height, peak wave period and mean wave direction.

Two types or sets of boundary conditions were developed for each model: one set for simulating long-term processes (over 6 years) and a second set for simulating coastal processes during a series of idealized 25-hour storms. Several different storms with waves approaching from different directions were modelled. The effects of storm surge were included in some of the 25-hour simulations.

6.3.1 Water levels

The CMS-Flow model was forced using time-varying water levels applied along the NW, SW and NE boundaries. Two offshore boundaries were implemented in order to capture the strong counter-clockwise hydrodynamic circulation present in the Gulf of St. Lawrence, which drives longshore currents flowing from north to south along the New Brunswick coastline. This phenomenon is reproduced in the CMS-Flow model by implementing two offshore boundaries, one at each longshore limit of the model domain. These two offshore boundaries have slightly phase-lagged tidal cycles (extracted from the regional TELEMAC-2D model), thus driving flow in the longshore direction from northeast to southwest. An inland water level boundary was placed at the north-western limit of the CMS-Flow model domain, as water levels at this location (within the tidal lagoon) differ greatly from those along the Gulf coast. This is due to the prominent phase lag that exists between tides in the Baie des Chaleurs and the Gulf of St. Lawrence. It is this phase lag that is responsible for the strong imbalance in the strength of the ebb and flood flows through Shippagan Gully inlet, where ebb flows routinely exceed 2m/s while flood flows are typically ~50% slower.

The long-term water level boundary conditions used in the current study were identical to those used previously in the phase 1 study. These water level boundary conditions were obtained from a regional model of tidal hydrodynamics that was developed for the phase 1 study, based on the TELEMAC (finite-element) modelling system (see Figure 6.8). The regional tidal model was forced using boundary conditions developed from tidal constituent data (30 constituents) provided by the Canadian Hydrographic Service (CHS). Using the 30 tidal constituents, a full year of water level fluctuations was generated along each of the three Telemac model boundaries. The Telemac model was then used to obtain corresponding water level fluctuations at the locations of the three CMS-Flow model boundaries. From these year-long time histories, 14 day periods encompassing the maximum spring tide and minimum neap tides were identified and combined to produce a 28 day water level time series at each of the CMS-Flow boundaries. These 28-day time series, shown in Figure 6.9, were considered representative of the tides throughout a typical year. These 28-day water level signals can be repeated as many times as necessary to approximate water level fluctuations over longer time periods.

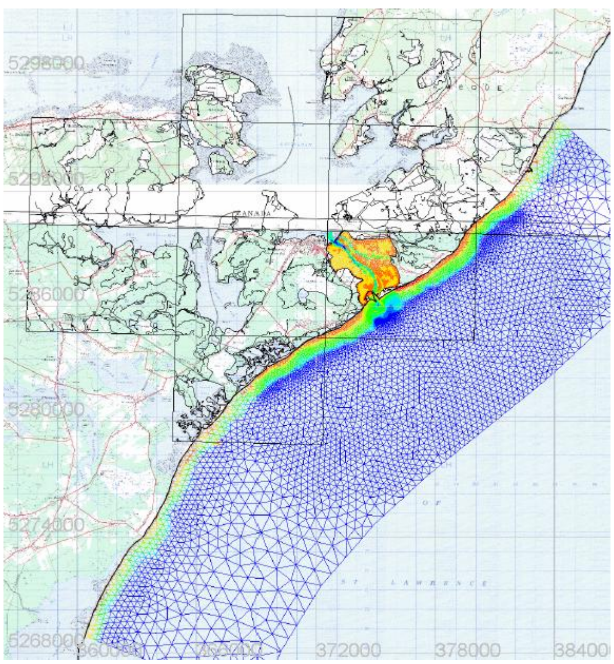

Figure 6.8 – Domain and mesh for the regional finite-element (Telemac-2D) model used to establish boundary conditions for CMS-Flow.

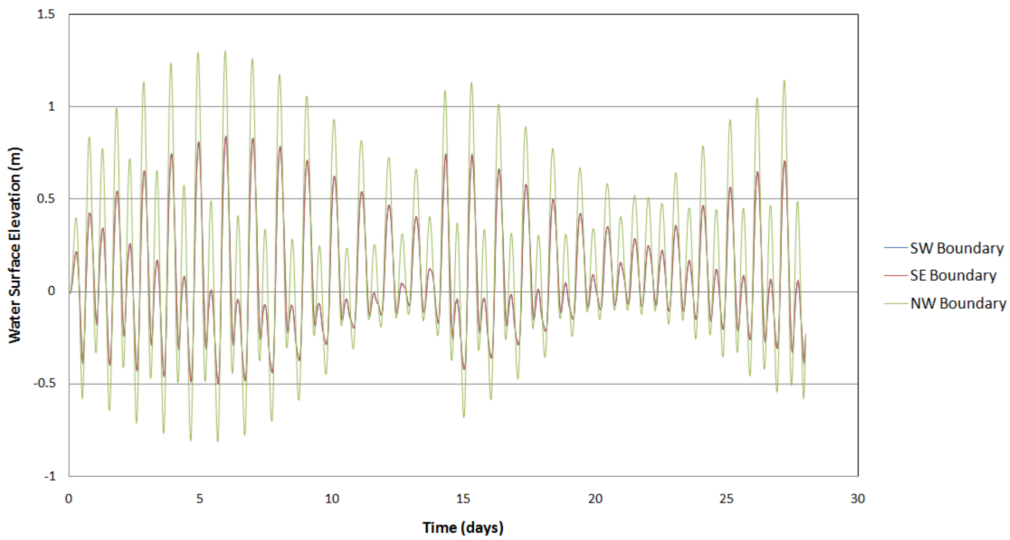

Figure 6.9 - Generic 28 day tidal cycle at all 3 model boundaries.

Short term water level boundary conditions were also developed in order to simulate several different idealized 25-hour storms, with and without storm surge. The storm boundary conditions were developed by extracting data for a 25-hour period with average tides from the 28-day tidal cycles shown in Figure 6.9. In some cases, a 1m high storm surge was superimposed on the tidal signals. The surge was assumed to increase linearly from 0 m to 1 m over a 6hr period, remain steady at +1 m for 13hr, then decrease linearly back to 0 m over the final 6 hours. Two examples of the water level boundary conditions prepared to simulate a 25-hour storm, with and without storm surge, are compared in Figure 6.10. It is important to note that the 1 m storm surge is not based on field measurements, but rather on discussions with local fishers who utilize the inlet on a daily basis.

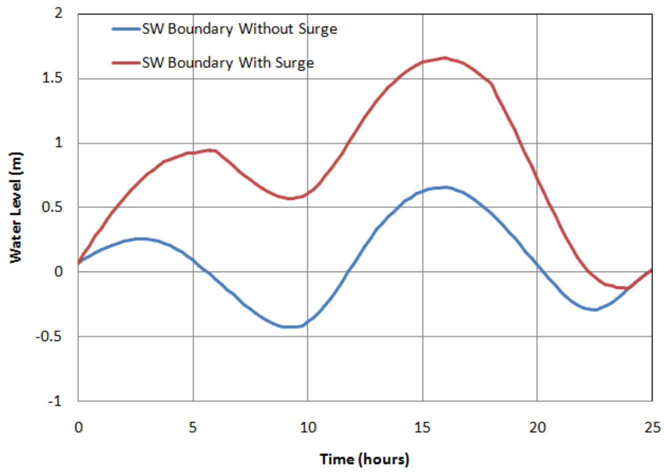

Figure 6.10 - SW boundary condition for 25 hour storm with and without inclusion of storm surge.

6.3.2 Wave conditions

Similarly, two sets of wave conditions were developed to drive the CMS-Wave model: one set for long-term simulations (6 years) and a second set for short term simulations (25 hours). In the phase I study, information on the wave climate at the site was developed from analysis of the MSC50 Atlantic Wave Hindcast produced by Environment Canada (Swail *et al*., 2006). The MSC50 hindcast provides hourly estimates of wave height, period and direction across the entire Gulf of St. Lawrence with 0.1° resolution over the 54 year period from 1954 to 2008. The hindcast has previously been successfully calibrated and validated against available buoy data. Data for a MSC50 hindcast grid point located 5 km offshore Shippagan Gully in a water depth of 16 m was analyzed to define the local wave climate. The wave conditions were separated into 30° directional bins and the peak over threshold method was employed to establish extreme wave conditions for each bin, associated with various return periods from 1 year to 25 years. Significant wave heights near Shippagan Gully rarely exceed 3 m, and peak wave periods rarely exceed 12s. As shown in Figure 6.11, the wave climate is dominated by waves approaching from the east (ESE to ENE); however, waves approaching from the south are also common. Storms with Hs ≥ 3 m can approach from the E, SE and S directions.

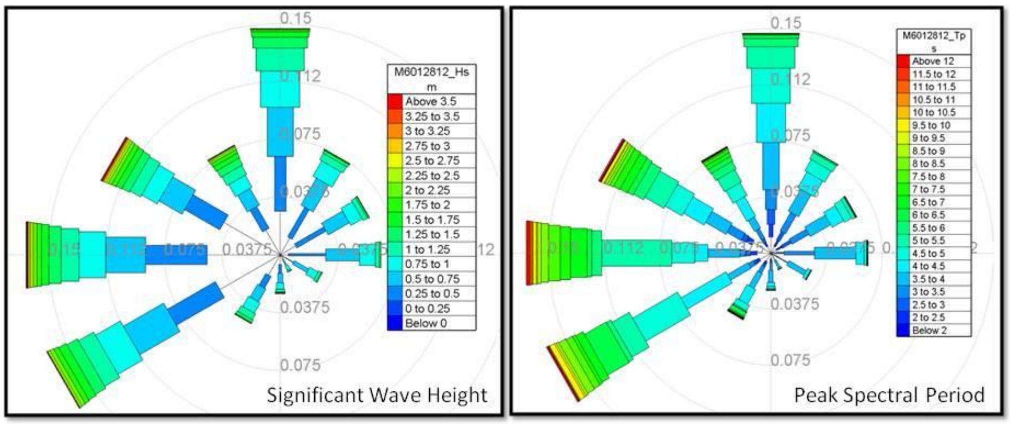

Figure 6.11 - Wave height and wave period roses at a location 5 km offshore from Shippagan Gully.

For the long term simulations, the same boundary conditions developed for the phase I study were re-used without modification. As shown in Figure 6.12 and Figure 6.13, the wave conditions varied with time over a 3,280 hour (137 day) duration in a manner which replicated, in a statistical sense, the average wave climate offshore Shippagan Gully. The synthetic wave dataset included both normal and extreme wave conditions approaching from 5 directions (60°, 90°, 120°, 150° and 180°) and also included calm periods without any waves. The developed wave conditions statistically represent the frequency of daily and storm waves from each direction, for each month of the year. This statistically representative boundary condition can be repeated as many times as necessary to force longer simulations. Further details on the statistical analysis and construction of the synthetic wave dataset can be found in the Logan (2012).

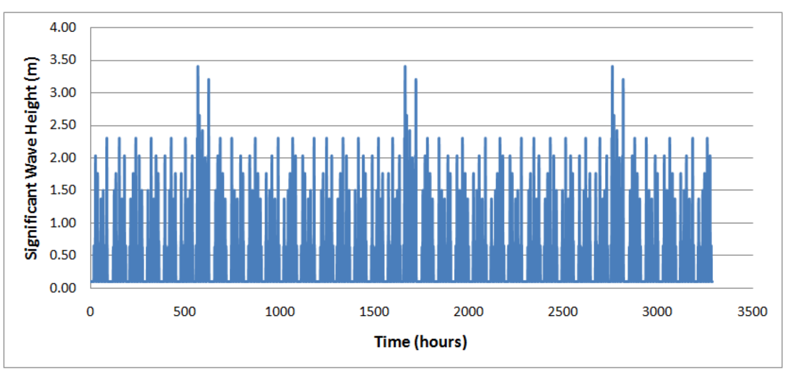

Figure 6.12 - Long-term CMS-Wave boundary conditions; temporal variation of significant wave height.

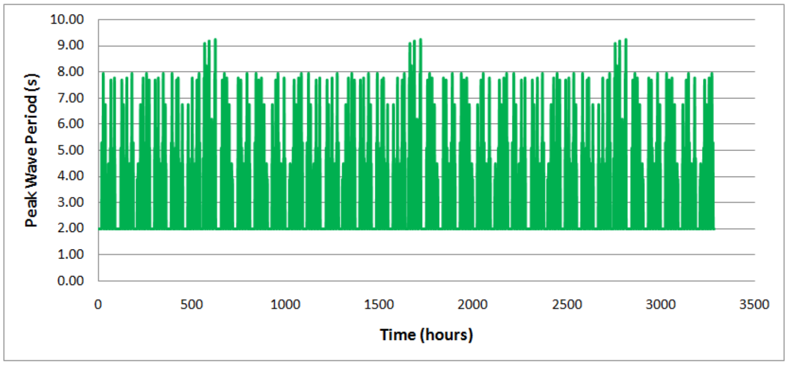

Figure 6.13 - Long-term CMS-Wave boundary conditions; temporal variation of peak wave period.

In addition to the long-term wave boundary conditions discussed above, three different 25-hour long storm wave boundary conditions were created to force independent simulations focused on investigating and understanding the hydrodynamics and coastal processes at the inlet during storms. CMS-Wave boundary conditions were constructed to simulate three different idealized storms approaching the inlet from three different directions; the east (90°), the south-east (135°) and the south (180°). Each of the three storm directions has a unique significant wave height (H_s) and peak wave period (T_p), which corresponds roughly to a 5 year return period obtained from the storm event analysis completed during the Phase I study. The resulting wave conditions are:

- Storm approaching from the east (90°): H_s= 4 m; T_p= 10s;
- Storm approaching from the south-east (135°): H_s= 4 m; T_p= 10s; and
- Storm approaching from the south (180°): H_s= 3 m; T_p= 9s.

The assumed variation with time of wave height and wave period for the easterly storm is shown in Figure 6.14 and Figure 6.15. The other storms followed a similar pattern. For each storm case, both the wave height and wave period were assumed to linearly increase over a 6 hour time period from zero until the maximum value is reached. The maximum value then remains constant for the next 13 hours. Following this, the period remains constant while the significant wave height is assumed to decrease linearly down to zero over the final 6 hours.

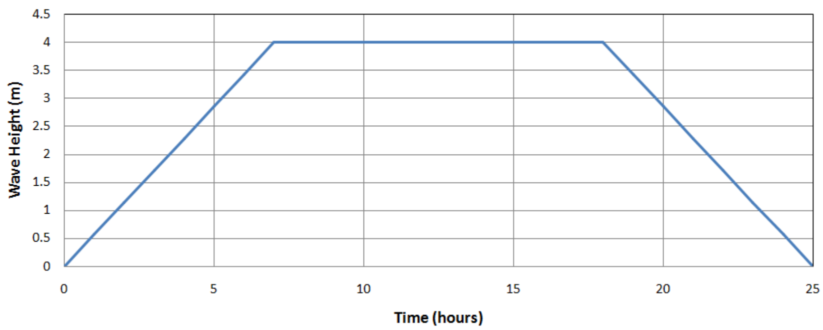

Figure 6.14 -Wave height variation with time for idealized 25-hour storm.

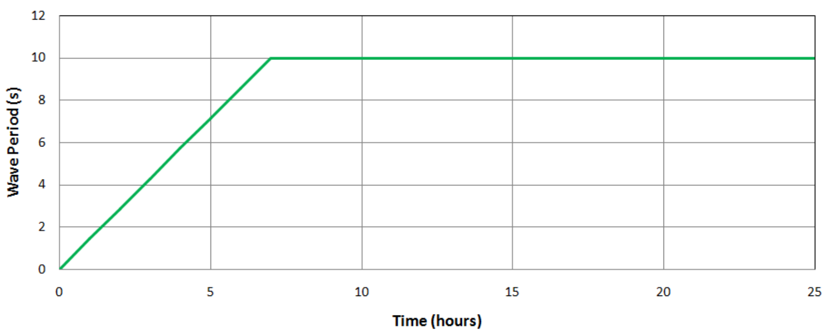

Figure 6.15 - Wave period variation with time for idealized 25-hour storm.

6.4 Hydrodynamic Calibration and Validation

The new CMS-Flow model required calibration to ensure that it provided a fairly realistic simulation of the true flows at Shippagan Gully. Following successful calibration, the flow model was also validated by confirming that it provided a reasonably accurate simulation of the true hydrodynamics for a second time period.

6.4.1 Hydrodynamic Calibration

The hydrodynamic model (CMS-Flow) was calibrated so that it was able to replicate with good precision the flow conditions (levels and current speeds) observed during a field investigation conducted in August 2010. The calibration involved making adjustments to the bottom friction factor used in different parts of the model domain to minimize the overall error between the model's predictions and the velocities observed during the site visit. For this purpose the model was driven using boundary conditions that approximated conditions during the field investigation as closely as possible.

The velocity measurements were obtained at discrete points within the inlet using an electromagnetic current meter suspended at various depths from a small boat. A GPS receiver was used to record the location of each measurement while the time of measurement was also noted. Velocities were measured in the inlet during both ebb and flood tides. The measurement locations are plotted in Figure . Velocities recorded near mid-depth were assumed to be representative of depth-averaged velocities, while velocities measured near the surface were reduced by a factor of 0.85 to obtain values more representative of depth-averaged conditions. It should be noted that almost all of the velocity measurements were made along the navigation channel in the inlet mouth, thus the calibration was restricted to flows in this region.

The numerical model CMS-Flow was configured to replicate 2010 bathymetry and forced using estimated boundary conditions (water level fluctuations) from August 11, 2010 to August 13, 2010. These tidal boundary conditions were obtained from a regional model of the tidal flows (see Section 6.3.1). The sea was calm on August 12, 2010, and the effect of waves was not included in the modelling.

The depth-averaged velocities predicted by the numerical model were compared to the measured velocities on a point-by-point basis, taking care to ensure that the locations and times were always in close agreement. Three different statistics were computed to quantify the overall error between the modelled and measured velocities, namely, the relative error, the absolute error and the root-mean-square (RMS) error. The hydrodynamic calibration involved adjusting the bottom roughness coefficient (Manning's n value) in different parts of the model domain until the overall RMS error between the measured and modelled velocities was minimized.

The computational domain was divided into the following five sub-regions (see Figure 6.16):

1. Northern boundary underneath the bridge,
2. Navigation channel through the tidal lagoon,
3. Remainder of the tidal lagoon,
4. Inlet, and
5. Offshore;

and a different Manning's coefficient value was used in each sub-region. These five sub-regions were chosen based on the differences in roughness present in each area. For example, the inlet and the tidal lagoon have different levels of vegetation, which significantly affect the effective roughness. In addition, an artificially high Manning's n value was required near the north boundary in order to properly model the timing of the change from ebb flow to flood flow.

Figure 6.16 - Model sub-regions 1 - 5.

Figure 6.17 shows the map of Manning's coefficient values used in the Phase I study, while the revised map developed for the Phase II study is shown in Figure 6.18. As mentioned previously, the map shown in Figure 6.18 was the one that minimized the RMS error between the modelled velocities and the velocities measured (mainly) along the navigation channel on August 12, 2010. The error statistics for the Phase I and Phase II studies are compared in Table 6.1. These results show that the new model developed for this Phase II study, with the spatial distribution of Manning's coefficient values shown in Figure 6.18, does a slightly better job of simulating the velocities observed in the inlet than the original model developed for Phase I. This improvement can be attributed to both the finer spatial resolution (due to the telescoping mesh) and a map of Manning's coefficient that is better optimised.

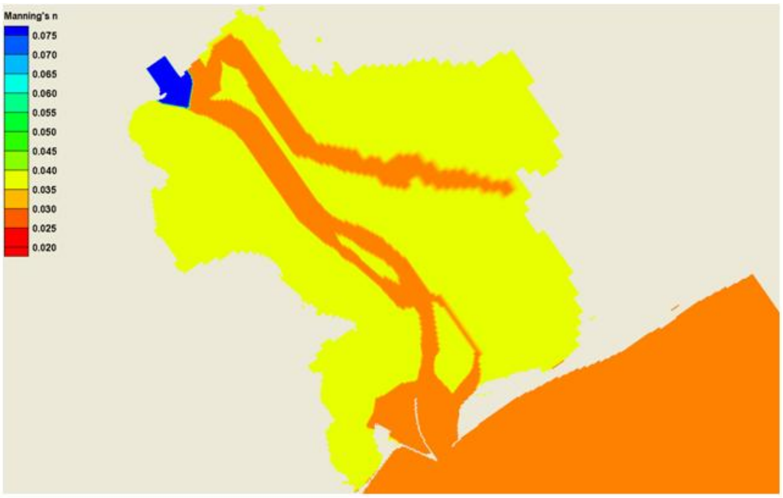

Figure 6.17 - Map of Manning's coefficient values used in the phase 1 study.

Figure 6.18 - Optimized map of Manning's coefficient values used in the current study.

Table 6.1 - Error statistics from hydrodynamic calibration in Phase 1 and Phase 2 studies.

Manning's Map	Optimized	Phase I
Rel Error	0.059	0.050
Abs Error	0.164	0.200
RMSE	0.209	0.239

A sensitivity analysis was conducted to investigate, for each sub-region, the influence of changes in Manning's value on the velocities in the inlet. This provided an understanding of how the modelled hydrodynamics were affected by the roughness in the different sub-regions, which in turn allowed for an improved calibration of the hydrodynamics. A summary of the sensitivity analysis results is presented in Table 6.2. The sensitivity analysis showed that velocities at the inlet could be increased by decreasing the Manning's n value for the inlet (Section 4) and the navigation channel (Section 2). However, to increase velocities on the ebb flow only, then the Manning's n value for the lagoon (Section 3) should be decreased. Similarly, the flood velocities in the inlet can be increased by decreasing the Manning's value for the offshore sub-region.

Table 6.2 - Sensitivity of inlet velocity to Manning’s coefficient.

Section	Change to Manning's Value	Observation
1 - Bridge	Decrease	Change in current direction occurs earlier
2 - Navigation Channel	Decrease	Small increase in velocities
3 - Lagoon	Decrease	Increase in ebb current, decrease in flood current
4 - Inlet	Decrease	Significant increase in velocities
5 - Offshore	Decrease	Small increase in flood current, small decrease in ebb current

6.4.2 Hydrodynamic Validation

Following successful calibration of the CMS-Flow model to observations from August 2010, a validation analysis was undertaken to verify that the model was able to correctly predict hydrodynamic flows for other time periods with reasonable precision. The calibrated numerical model was used to predict hydrodynamics at Shippagan Gully inlet for June 14, 2012, when an ADCP velocity survey was undertaken (see Section 5.1). The calibrated CMS-Flow model was configured to replicate 2012 bathymetry and forced using estimated boundary conditions (water level fluctuations) from June 13, 2012 to June 15, 2012. These tidal boundary conditions were obtained from a Telemac-2D model of the tidal flows around the Acadian Peninsula. The effect of waves was not included in the modelling.

Figure 6.19 through Figure 6.21 show the depth-averaged and spatially-averaged velocity vectors derived from the ADCP data (red) compared to the velocity vectors predicted by the CMS-Flow model (black). Note that the scale for the vectors is different in each figure, in order to properly visualize the data. It can be seen that the measured and modelled velocity vectors are in reasonably good agreement along the training wall and along the navigation channel centerline. The agreement is less satisfactory along the north-eastern side of the inlet; the main reason being that the ADCP data was collected over a ~25 minute period near slack tide, when the flows were weak and changing direction, whereas the modelled vectors represent conditions at a single instant.

As before, an RMS error statistic was calculated to quantify the quality of the agreement between the measured and modelled velocities for each transect. An RMS error of 0.101 m/s was obtained for the transect along the training wall, while an RMS error of 0.136 m/s was obtained for the transect along the center of the navigation channel. For the transect on the north-eastern side of the inlet, the RMS error was 0.234 m/s. These results are considered to be acceptable, given that the errors are similar to those obtained during model calibration (RMS error 0.209 m/s).

These results demonstrate that the CMS-Flow model can be relied on to predict the main features of the tidal flows through the inlet with reasonable precision. However, it is important to recognize that some flow details, such as eddies formed during slack tide, are not well represented in the model. Moreover, while it is felt that the model also provides a reasonable simulation of tidal flows in other areas (i.e. on the ebb shoal), since no field data was available for other areas, the model skill in other areas could not be assessed or verified.

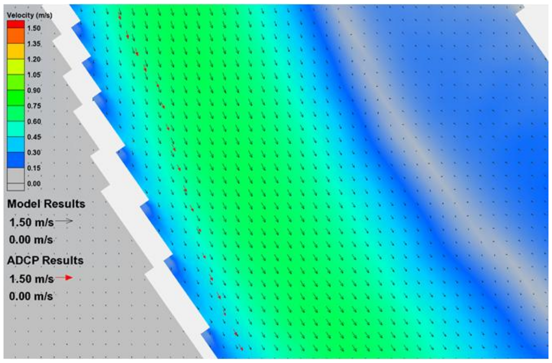

Figure 6.19 - Measured and modelled velocity vectors near the training wall.

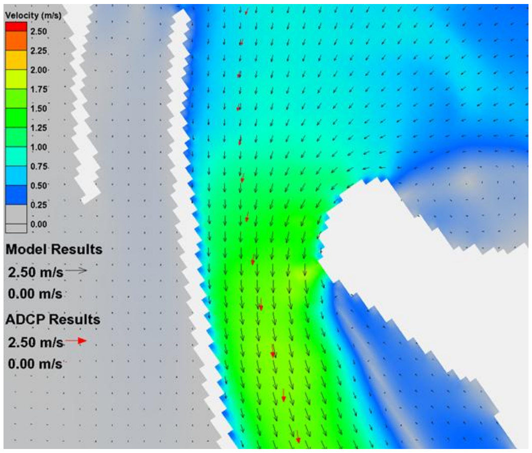

Figure 6.20 - Measured and modelled velocity vectors along the navigation channel.

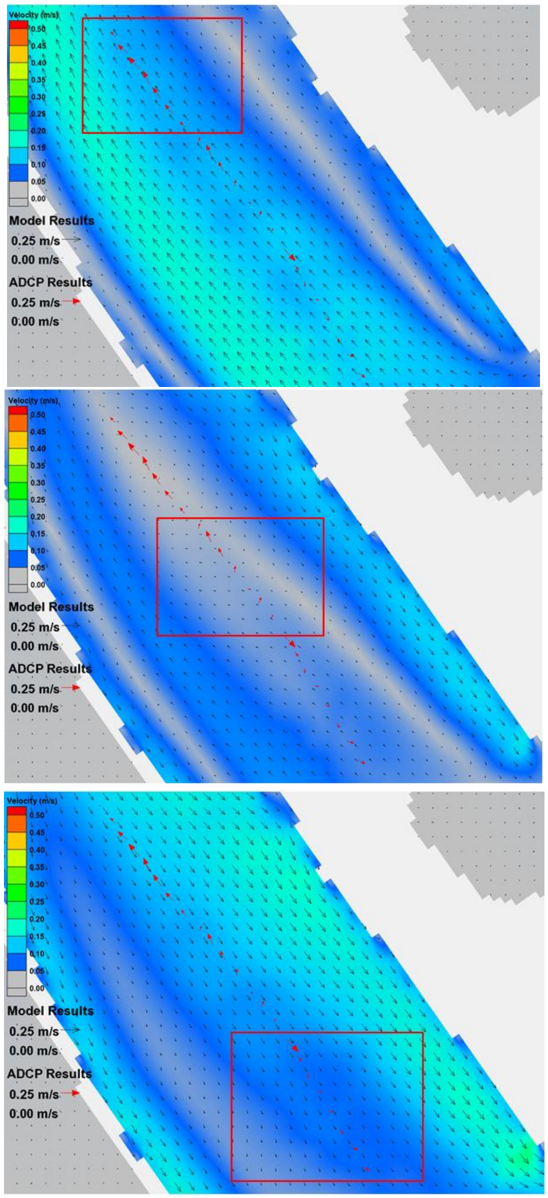

a)

b)

c)

Figure 6.21 - Measured and modelled velocity vectors on the northeast side of the navigation channel: a) end of flood; b) flow reversal; c) start of ebb.

6.5 Morphologic Calibration

The sedimentary processes in the model were also calibrated to measurements from the site. The sedimentary processes were initially tuned to provide a reasonable simulation of the morphology change observed at the inlet over the two year period from 2004 – 2006. Later on, a six year period from 2004 to 2010 was also considered.

The model's simulation of sedimentary processes was tuned by manipulating two different aspects of the model: the initial map defining the size of sediments on the seabed over the model domain; and the following three calibration parameters governing the rate of sediment transport: the bed load scaling factor, the suspended load scaling factor and the bed slope coefficient. Changing these parameters affects the rate of erosion, transport and deposition predicted by the model.

6.5.1 Calibration of Morphology Change

Following the successful calibration and validation of the numerical model hydrodynamics, a morphologic calibration was performed in order to ensure that the coupled model was capable of reproducing the historical bed elevation changes observed at Shippagan Gully with reasonable precision. Not surprisingly, optimizing the model's ability to simulate morphology change at this complex and dynamic site proved to be far more challenging and time-consuming than calibrating the tidal hydrodynamics alone.

The sedimentary processes in the model were initially tuned to provide a reasonable simulation of the morphology change observed in the inlet over the two year period from 2004 – 2006. An estimate of the actual change in the bed elevation was derived by differencing two bathymetric surveys conducted in 2004 and 2006. This produced the measured bed elevation change map showed in Figure 6.22. Towards the end of the morphology calibration process, a six year period from 2004 to 2010 was also considered. Again, an estimate of the change in bed elevation at the inlet over this period was obtained by differencing bathymetric survey data gathered in 2004 and 2010. The measured change in bed elevation over this six year period is shown in Figure6.23. These figures show that the depth of the navigation channel remained fairly constant over this period, but the channel slowly grew narrower and migrated slightly towards the curved training wall. Erosion occurred near the training wall, particularly near the north end of the training wall, while deposition took place along the northeast side of the channel, particularly at the end of the sand spit that has grown within the inlet. The elevation of the ebb shoal located outside the inlet is also quite variable over these time periods. This is to be expected, as the sediment on the ebb shoal is routinely re-shaped by larger storm events.

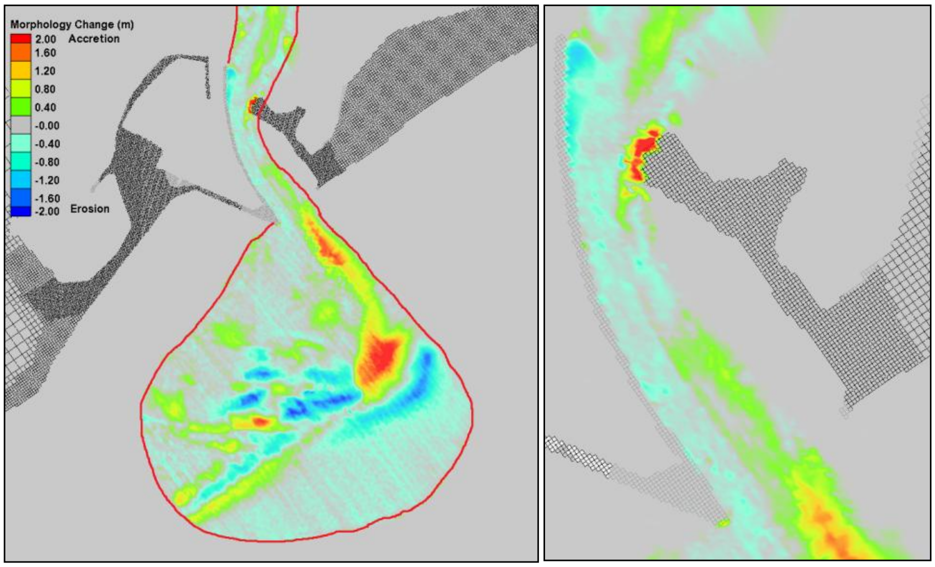

Figure 6.22 - Measured morphology change 2004-2006 (blue = erosion, yellow = accretion, red line = sounding data limit).

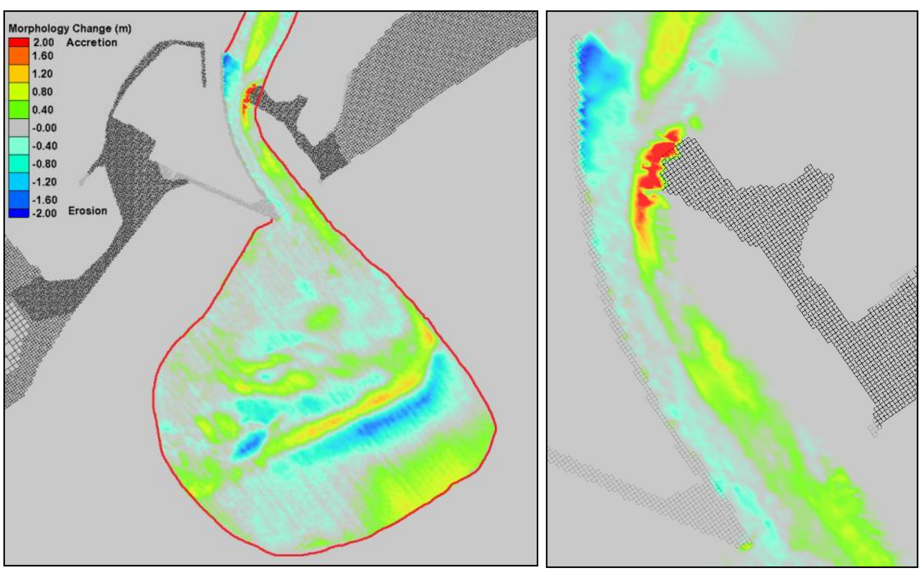

Figure 6.23. Measured morphology change 2004-2010 (yellow = erosion, blue = deposition, red line = sounding data limit).

The model's simulation of sedimentary processes was tuned by manipulating two different aspects of the model: the initial map defining the size of sediments on the seabed over the model domain; and three calibration parameters governing the rate of sediment transport. The three calibration parameters are: the bed load scaling factor, the suspended load scaling factor and the bed slope coefficient. Changing these parameters affects the rate of erosion, transport and deposition predicted by the model.

The CMS-Flow model used in this study was able to simultaneously reproduce the mobilization, transport and deposition of multiple sediment sizes. The initial sediment properties at any location were specified in terms of the D_{35}, D_{50} and D_{90} values, representing the 35^{th}, 50^{th} and 90^{th} percentiles of the cumulative grain size distribution. These sediment properties had a strong influence on the tendency for sediments to be mobilized and transported, and hence on the temporal changes in seabed elevation. Creating a map of initial sediment properties that was consistent with field investigations and led to reasonable estimates of morphology change was the main challenge in calibrating the numerical model. The sedimentary processes and morphology change within the inlet were found to be strongly influenced by the bottom sediment properties specified at each location. In general, erosion could be reduced by increasing the initial bed grain size in that location, and conversely, erosion could be increased by reducing the initial bed grain size.

The morphologic calibration process involved configuring the coupled model to simulate hydrodynamic and sedimentary processes over the desired calibration period (2004 - 2006 or 2004 – 2010), specifying initial maps of bottom sediment properties, specifying the three sediment calibration parameters, and then launching the simulation. Initial maps of bed sediment size (D_{50}, D_{35}, D_{90}) were created based on maximum velocity contours and information on bed sediment grain sizes obtained from field investigations. Larger grain sizes were generally specified in locations with stronger peak velocities, while also taking into account the available information on bed sediment properties from the site. When the simulation was finished, the results were analyzed and the predicted change in seabed elevation was assessed and compared with the measured changes shown in Figure 6.22 and Figure6.23. Next, the three sediment distribution maps (D_{50}, D_{35}, D_{90}) and/or the sediment calibration parameters were adjusted to attempt to improve the agreement between the measured and modelled estimates of morphology change, and the simulation was repeated. The initial maps of D_{35}, D_{50} and D_{90} were modified numerous times in order to improve the agreement between the observed and modelled morphology change. Numerous simulations with various initial sediment distribution maps and different sets of sediment calibration parameters were conducted; however, only the best results are reported herein.

The D_{35}, D_{50} and D_{90} maps that were eventually adopted are shown in Figure 6.24 - Figure 6.26. Medium sands with D_{50} = 0.45 mm were assumed over most of the computational domain away from the inlet, which is generally consistent with sediment samples collected at the site. The seabed over a large portion of the inlet mouth was assumed to be armoured with coarse sediments (D_{50}>20 mm). The largest sediments (D_{50}~50 mm) were co-located with the strongest currents in the central part of the navigation channel. Sediments with D_{50}~25 mm were assumed over a portion of the ebb shoal where the flood jet emerges from the inlet mouth. A gradual transition was assumed between the gravels in the inlet and the sands elsewhere. Cobbles with D_{50}~80 mm were assumed at the northern tip of the training wall in order to represent the large pile of rubble located in that area.

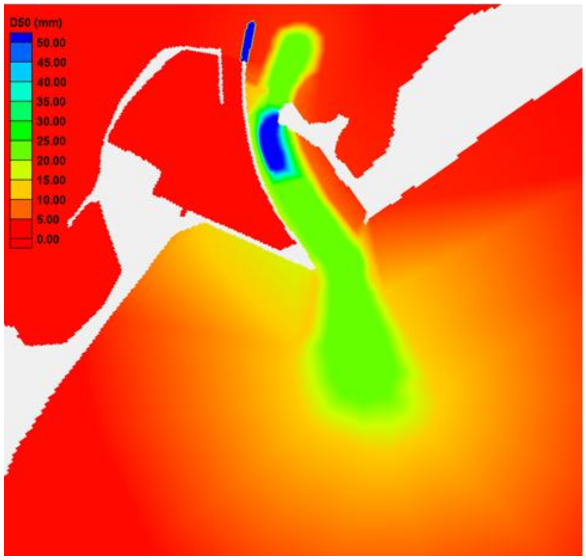

Figure 6.24 - Optimized map of initial median grain size; D_{50}.

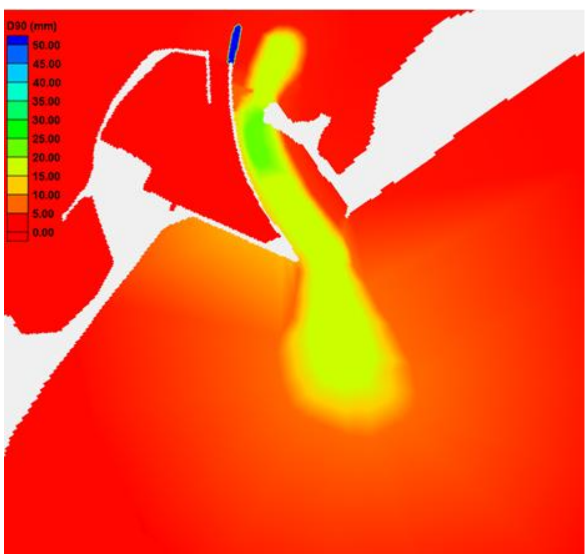

Figure 6.25 - Optimized map of D_{35}.

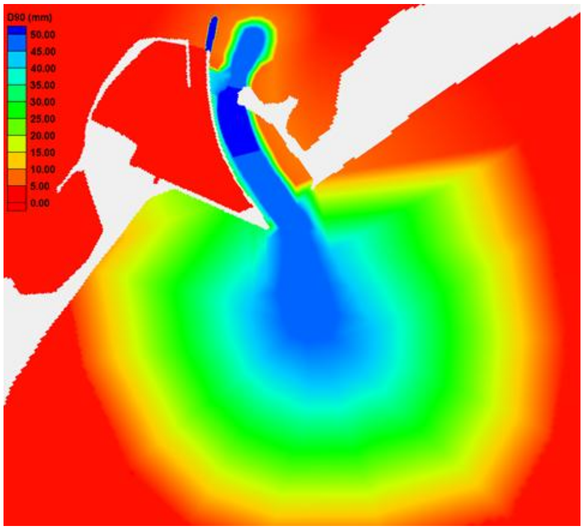

Figure 6.26 - Optimized map of D_{90}.

6.5.1.1 Calibration Period: 2004-2006

The bed elevation changes predicted by the tuned model over the two year period from 2004 – 2006 are shown in Figure 6.27. These modelled results can be compared with the measured bed elevation changes shown in Figure 6.22. These results were obtained using the initial D_{35}, D_{50} and D_{90} maps shown in Figure 6.24 - Figure 6.26 together with the following sediment calibration parameters:

- bed load scaling factor = 1.3;
- suspended load scaling factor =1.0; and
- bed slope coefficient = 1.3.

As in the Phase 1 study, the model was forced using simplified tidal boundary conditions and a statistical representation of the annual wave climate. The tidal fluctuations and wave conditions that actually occurred at the site from 2004 to 2006 were not modelled. Instead, a representative 28-day tidal signal was developed for each boundary, and the tidal signals were repeated 26 times over the 2-year simulation. Similarly, a time history of wave conditions (wave spectra approaching from different directions) that approximated the annual wave climate was synthesized and applied along the offshore boundary.

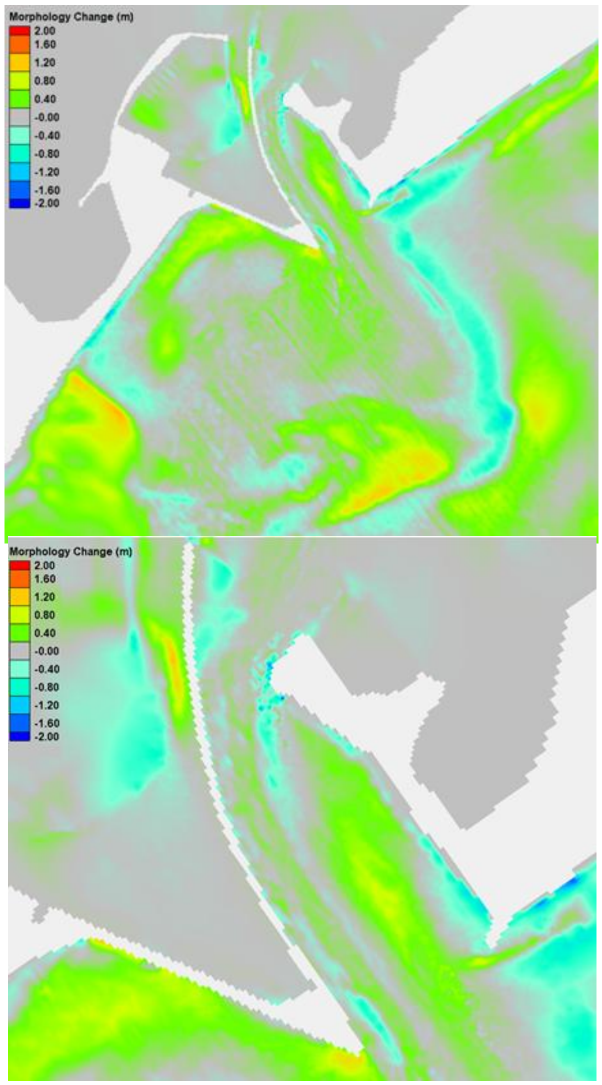

a)

b)

Figure 6.27 - Modelled morphology change 2004-2006 (blue=erosion; yellow=deposition): a) overview; b) detail at inlet.

The six channel cross-sections shown in Figure 6.28 were defined to help assess the numerical model performance. The measured and modelled changes in bed elevation along each of these six cross-sections are compared below in Figure 6.29. In these figures, the blue line denotes the bed elevation measured in 2004, the green line denotes the bed elevation measured in 2006, while the magenta line denotes the 2006 bed elevation predicted by the numerical model. On the whole, the model is predicting the correct erosional and depositional trends in the correct places within the inlet. The magnitudes of the measured and modelled changes are also similar in most places within the inlet. It should be noted that the model is unable to predict the re-shaping of the ebb shoal that occurred between the bathymetric surveys conducted in 2004 and 2006, nor is it able to predict the deposition near the tip of the sand spit located along the eastern side of the inlet mouth.

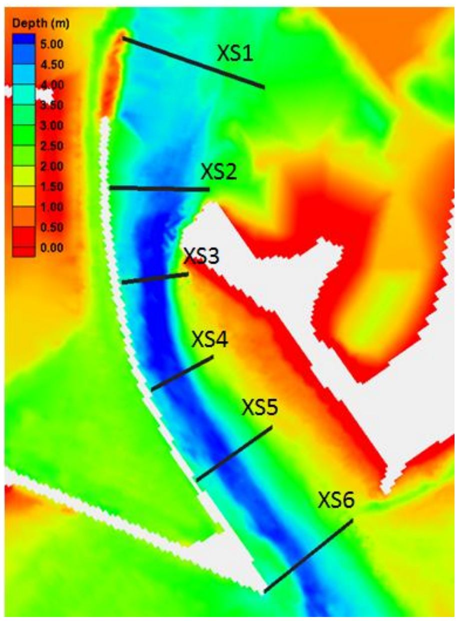

Figure 6.28 - Location of channel cross-sections 1-6.

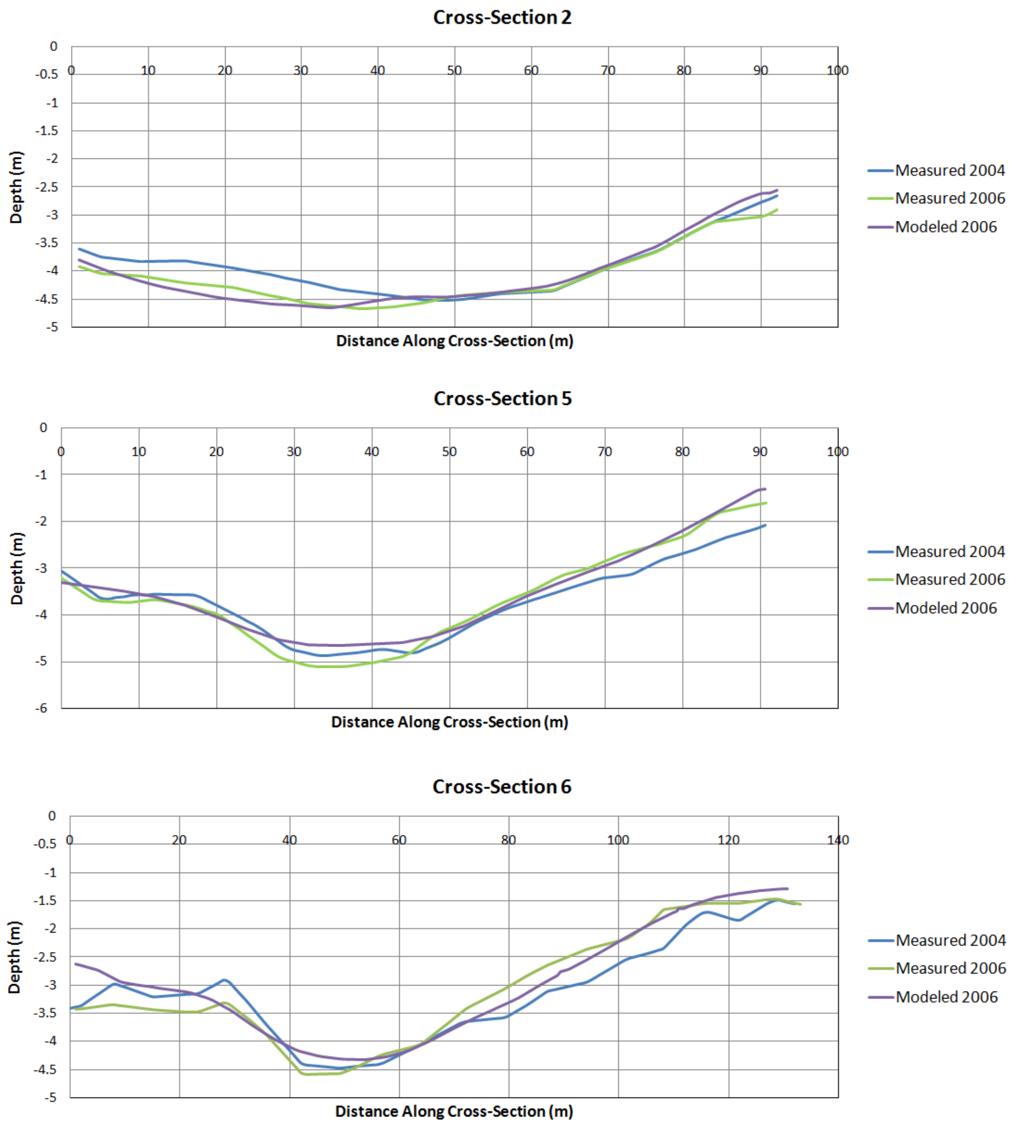

Figure 6.29 - Measured and modelled bed elevations for cross-sections 2, 5 and 6; 2004-2006.

6.5.1.2 Calibration Period: 2004-2010

The bed elevation changes predicted by the tuned model over the six year period from 2004 – 2010 are shown in Figure 6.30. These modelled results can be compared to the measured bed elevation changes shown in Figure6.23. As in the phase 1 study, the model was forced using simplified tidal boundary conditions and a statistical representation of the annual wave climate. The tidal fluctuations and wave conditions that actually occurred at the site from 2004 to 2010 were not modelled.

The measured and modelled changes in bed elevation along three of the six cross-sections identified in Figure 6.28 are compared below in Figure 6.31; the remainder of the cross-section can be found in Appendix A. Although there are significant differences between the measured and modelled results at specific locations, notably along cross-section 3, on the whole, the calibrated model provides a reasonable estimate of the erosional and depositional trends within the inlet. As noted previously, the numerical model has difficulty predicting the bathymetric changes that have occurred on the ebb shoal. This can be attributed to the fact that the shape of ebb shoal likely varies significantly each year in response to forcing by winter storms. It also has difficulty simulating the deposition that has occurred near the northern tip of the sand spit located on the eastern side of the inlet mouth.

In conclusion, the model is able to simulate general patterns and trends within the inlet reasonably well, but cannot be relied on to reliably predict fine details of the flow or the sediment transport, nor provide accurate detailed predictions of the morphology change. Such high precision remains elusive due to the fact that even a state-of-the-art numerical model, such as the one employed in this study, only provides a highly simplified and discretized representation of the many complex physical processes governing the hydrodynamics and sediment transport at a dynamic tidal inlet such as Shippagan Gully. Moreover, some potentially important processes, such as storm surge and ice runup are not included in the simulations. It is also important to recognize that the spatial variation of initial bed sediment properties assumed in the numerical modelling is very likely an approximation of actual conditions. Any differences between these assumptions and reality will degrade the realism of any numerical estimates of morphology change.

It is also worth noting that the morphologic calibration was by necessity limited to areas where bathymetric survey data was available, namely along the navigation channel running through the inlet. While it is felt that the model also provides a reasonable simulation of sedimentary processes in other areas, since no field data was available for other areas, the model's ability to accurately simulate morphology change in other areas could not be assessed or verified.

a)
b)

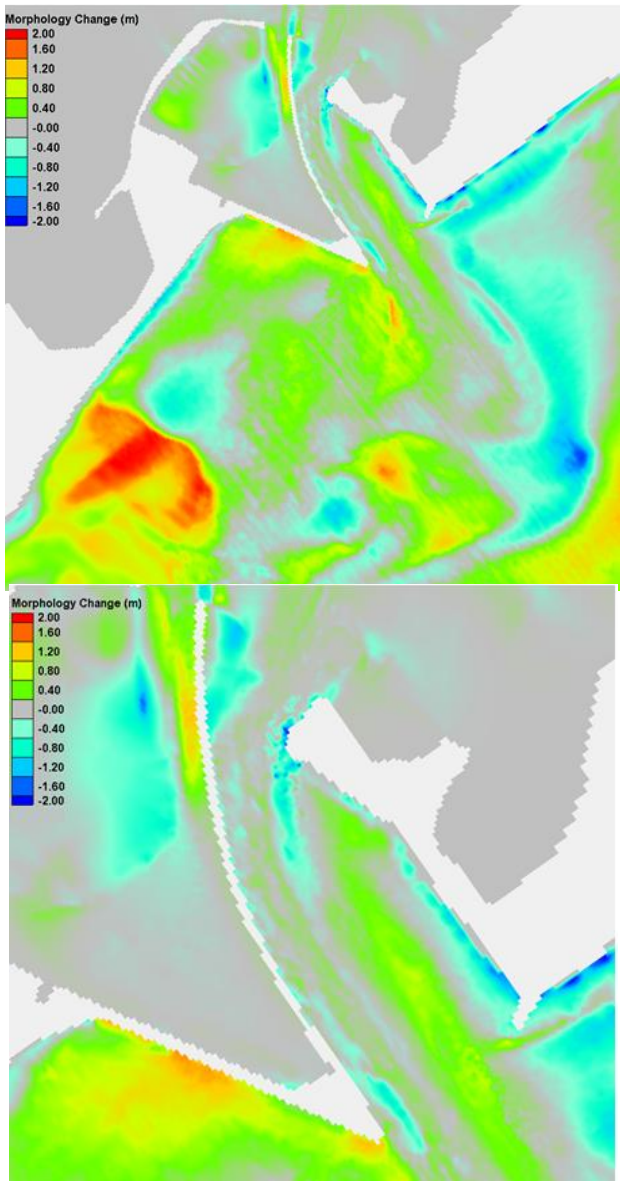

Figure 6.30 - Modelled morphology change 2004-2010 (blue=erosion; yellow=deposition): a) overview; b) detail at inlet.

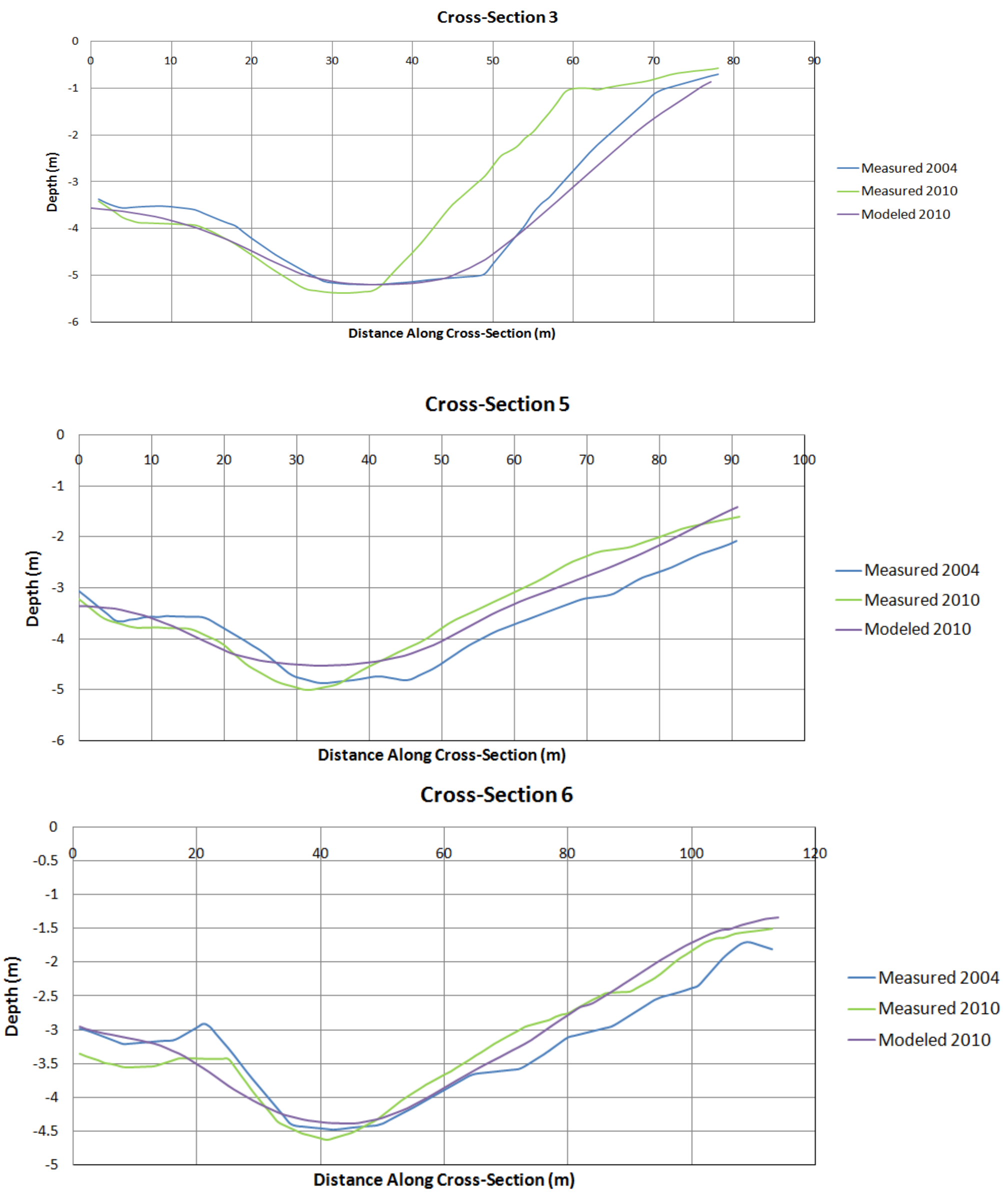

Figure 6.31 – Measured and modelled bed elevations for cross-sections 3, 5 and 6: 2004-2010.

6.6 Model Limitations and Uncertainty

The CMS suite of models, like any numerical model, represents an attempt to reproduce highly complex physical processes and systems using a combination of mathematics and numerical methods. In the present case, which concerns wave- and tide-driven coastal processes at a dynamic tidal inlet, these processes are highly complex and particularly difficult to simulate numerically. Due to the complex nature of this physical system, there will always be some amount of simplification and assumption within any numerical model; leading to inaccuracies in the model outputs. Even the most advanced numerical model, such as the one employed in this study, can only provide a simplified and discretized representation of the many complex physical processes governing the hydrodynamics and sediment transport at a dynamic tidal inlet such as Shippagan Gully.

Based on the results from attempts to calibrate and validate the CMS model using hydrodynamics and morphology changes observed at the site, it was concluded that the model is able to simulate general patterns and trends within the inlet reasonably well, but it should not be relied on to reliably predict fine details of the flow (hydrodynamics) or the sediment transport, nor provide accurate detailed predictions of morphology change, especially over longer durations. The model's predictions of sediment transport and morphology change, especially the long-term predictions, are uncertain. The model's prediction of sediment processes and morphology change in shallow water near shorelines is also unreliable. This uncertainty and lack of precision can be traced back to a number of sources, including:

- The mathematical descriptions used in the model to represent many physical processes (such as the generation and behaviour of wave-induced currents and the mobilization and transport of sediments) are simplified and approximate descriptions of the true physical processes.
- The boundary conditions used to force the model were simplified representations of the actual conditions.
- The model operates on a rectangular grid which provides a discretized (simplified) representation of nature.
- The model operates at a discrete numerical time step that provides a simplified representation of continuous natural processes.
- In nature, the coupling between waves, currents and sediments occurs continuously, whereas a steering interval of 1 hour was assumed in the present modelling.
- Significant assumptions were made concerning the spatial variation of bottom sediment sizes; and these assumptions exert a strong influence on the model's predictions of morphology change.
- Some potentially important processes, such as storm surge and ice runup were not included in the numerical simulations.
- The CMS model has difficulty simulating sediment transport and morphology change in areas that are intermittently submerged, and therefore cannot be relied on to simulate processes near shorelines or predict shoreline movement.

As noted previously, the hydrodynamic calibration and validation was limited to areas where velocity data was available, namely within the inlet mouth. Similarly, the morphologic calibration was by necessity limited to areas where bathymetric survey data was available, namely along the navigation channel running through the inlet and onto the ebb shoal. While it is felt that the model also provides a reasonable simulation of hydrodynamic and sedimentary processes in other areas, this assumption could not be assessed or verified. For these reasons, the simulation results presented herein must be interpreted with caution and should only to be used as a guide to help assess the relative performance of alternative scenarios.

7 Modelling of Coastal Processes for Existing Conditions and Alternative Inlet Configurations

Following the calibration and validation of the numerical model, the model was applied to simulate coastal processes for existing conditions and for seventeen alternative future inlet configurations or scenarios. The alternative scenarios were specified by PWGSC with input from the project team, and each scenario represented a different combination of new coastal structures and/or dredging. The overall aim was to stabilize and widen the navigation channel passing through the inlet mouth in order to improve navigability and increase navigation safety. Since minimizing future maintenance costs was also a priority, it was also important to find a solution for which sediment deposition within the navigation channel would be minimal.

7.1 Description of Alternative Inlet Configurations

A total of twenty-one alternative inlet configurations or scenarios were modelled using the refined numerical model described in Section 6. The various scenarios, which comprised different combinations of dredging work, new jetties, new training walls and/or new revetments, are summarized in Table 7.1 and illustrated in Figure 7.4 and Figure 7.7. In these figures, black is used to denote new structures, red is used to denote dredging, while blue is used to denote a new revetment or armouring. Figure 7.1 to Figure 7.3 show schematic cross-sections across the inlet mouth for each scenario. The various scenarios can be grouped into four classes based on the type of channel cross-section that is formed, as follows:

- Group 0, No change to existing bathymetry (status quo, scenario B, C1)
- Group 1, cross-section type 1: dredging to new training wall with vertical faces on the east side of the inlet (scenario D1, D2, D3, D4, D5, D6, D7, G3, G4)
- Group 2, cross-section type 2: dredging ending in 1:5 slope to existing grade (scenario F, C2, E1)
- Group 3, cross-section type 3: dredging ending in 1:1.5 sloped revetment to +3m elevation (scenario C3, E2a, E2b, E3, E4, G1, G2)

Table 7.1 - Summary of simulated scenarios.

Scenario ID	Description	Cross-Section Type	Total Jetty Length (m)
A	Status quo; no changes to structures or bathymetry	Existing	N/A
B	Removal of 100m of structure at north end of curved training wall	Existing	N/A
C1	50m long jetty with vertical walls on east side of inlet; reducing inlet mouth to 110m	Existing	50
C2	110m wide channel dredged to -4m; 1:5 slope of east side from -4m to existing grade; same jetty as C1	Type 2	150
C3	110m wide channel dredged to -4m; 1:1.5 rock revetment on east side from -4m to +3m elevation; same jetty as C1	Type 3	150
D1	Curved training wall on east side of inlet; 110m channel width at inlet mouth gradually reducing to 80m width at tip of sand spit; dredging to -4m	Type 1	N/A
D2	Same as scenario D1 but with dredging to -3m	Type 1	N/A
D3	Same training wall configuration as scenario D2 but ending in 100m curved jetty	Type 1	150
D4	Same as scenario D3, but with 100m inlet mouth width	Type 1	150
D5	110m wide channel dredged to -4m; vertical training wall on east side ending in 100m curved jetty	Type 1	150
D6	Same as scenario D3, but with dredging to -4m	Type 1	150
D7	Same as scenario D4, but with dredging to -4m	Type 1	150
E1	110m wide channel dredged to -4m; 1:5 slope on east side from -4m to existing grade; 100m curved jetty with vertical walls	Type 2	150
E2a	Same as scenario E1 but with 1:1.5 rock revetment from -4m to +3m elevation on east side of dredged channel	Type 3	150
E2b	Same as scenario E2a, but curved jetty is made out of rock instead of vertical sheet pile wall	Type 3	150
E3	Same as scenario E2a, but with 150m curved jetty with vertical walls	Type 3	200
E4	Same as scenario E2a, but with a 50m curved jetty with vertical walls	Type 3	100
F	110m wide channel with dredging to -4m; 1:5 slope on east side from -4m to existing grade; no new structures	Type 2	N/A
G1	130m wide channel dredged to -4; 1:1.5 rock revetment on east side from -4m to +3m	Type 3	50

	elevation, same 50m jetty as C1		
G2	130m wide channel dredged to -4m; 1:1.5 rock revetment on east side from -4m to +3m elevation, same 200m jetty as E3	Type 3	200
G3	130m wide channel dredged to -4m; vertical training wall on east side ending in same 50m jetty as C1	Type 1	50
G4	130m wide channel dredged to -4m; vertical training wall on east side ending in same 200m jetty as E3	Type 1	200

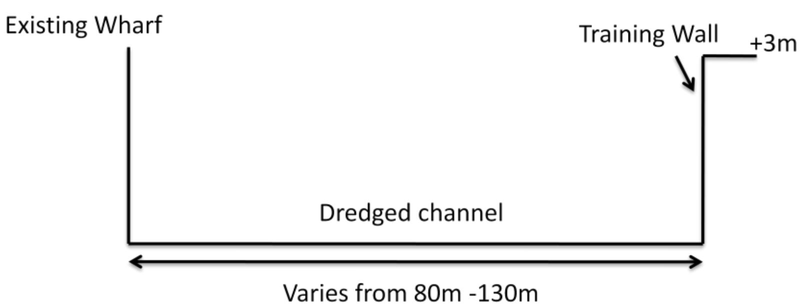

Figure 7.1 - Cross-section type 1 (scenarios D1, D2, D3, D4, D5, D6, D7, G3, G4).

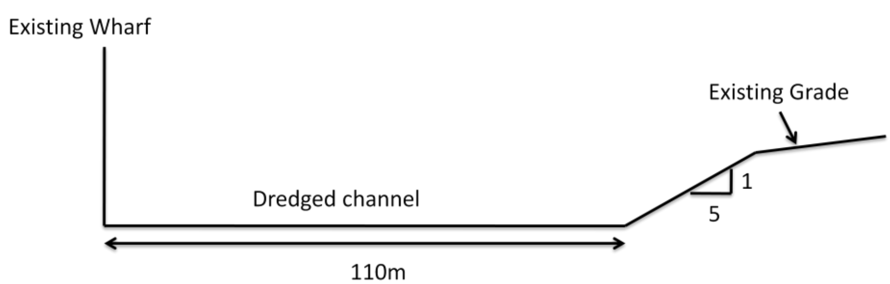

Figure 7.2 - Cross-section type 2 (scenarios C2, E1, F).

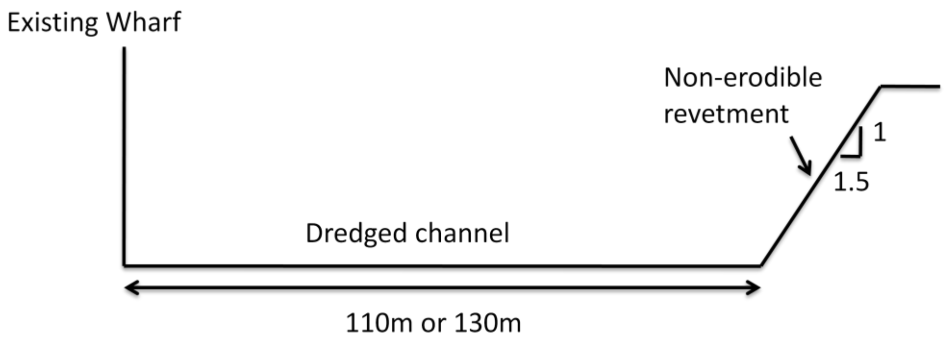

Figure 7.3 - Cross-section type 3 (scenarios C3, E2a, E2b, E3, E4, G1, G2).

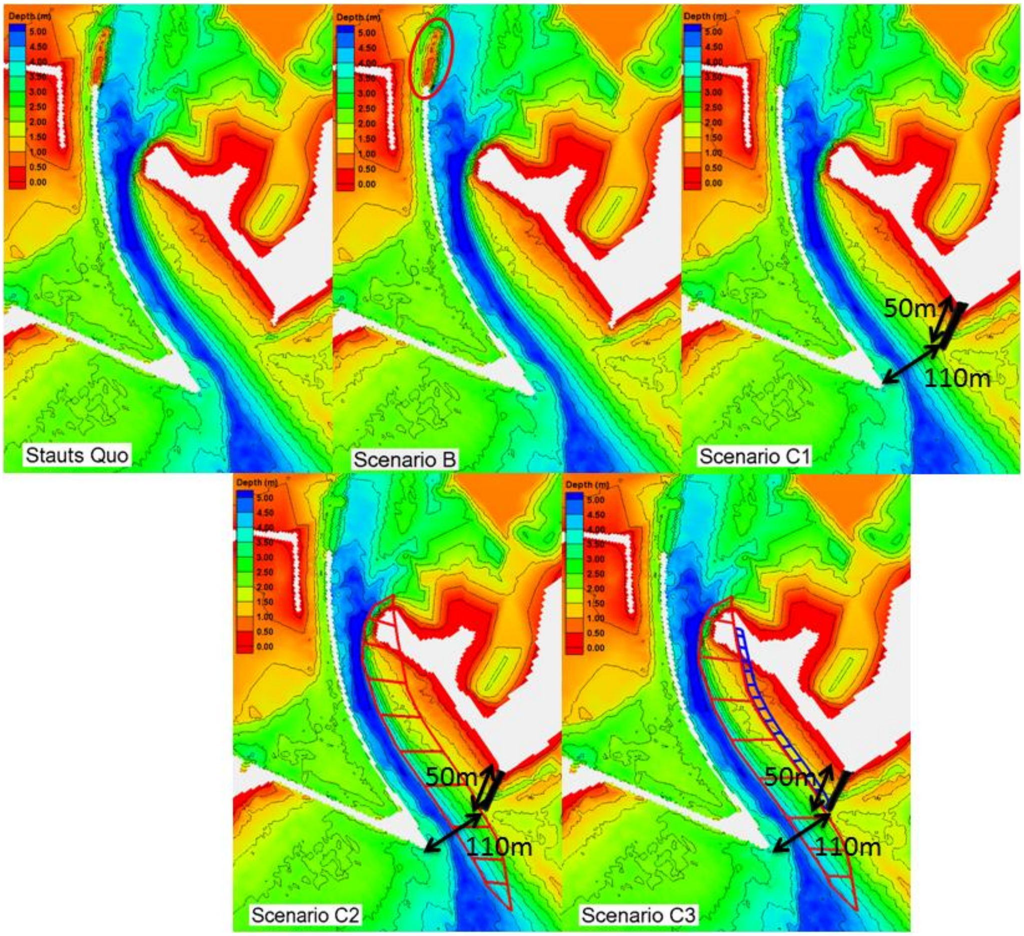

Figure 7.4 – Inlet configurations for the status quo and scenarios B, C1, C2 and C3.

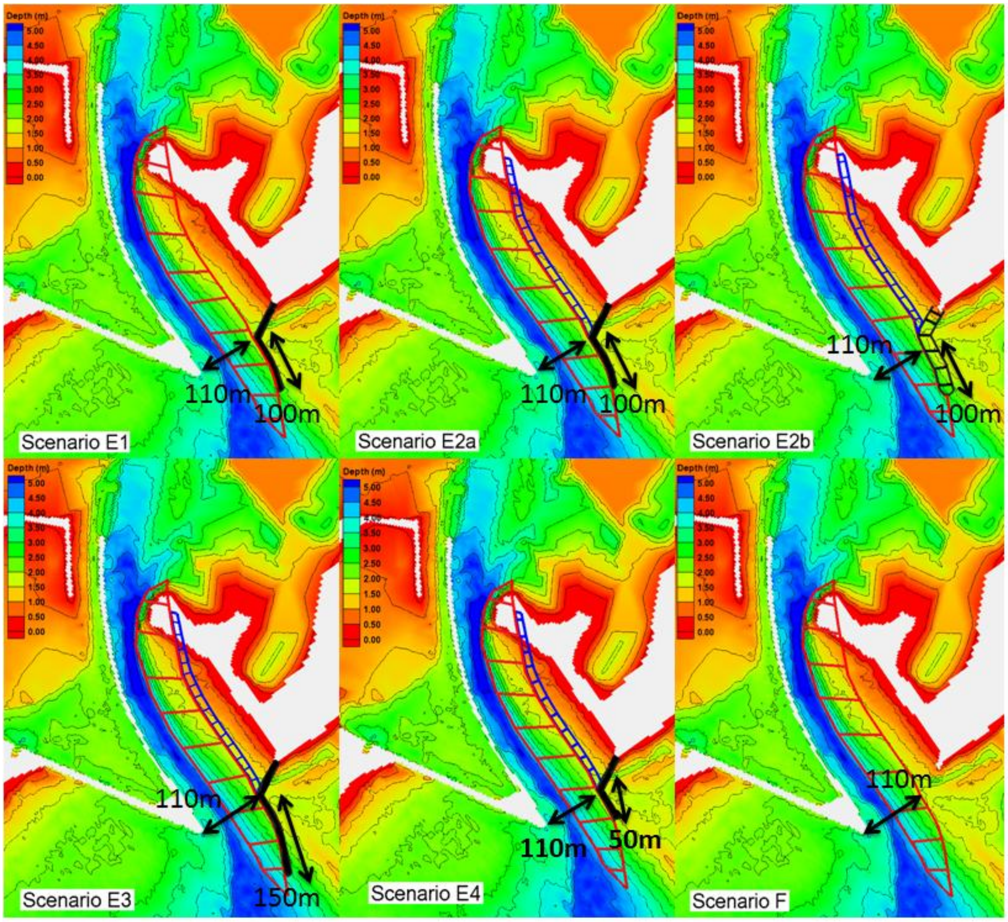

Figure 7.5 - Inlet configurations for scenarios E1, E2a, E2b, E3, E4 and F.

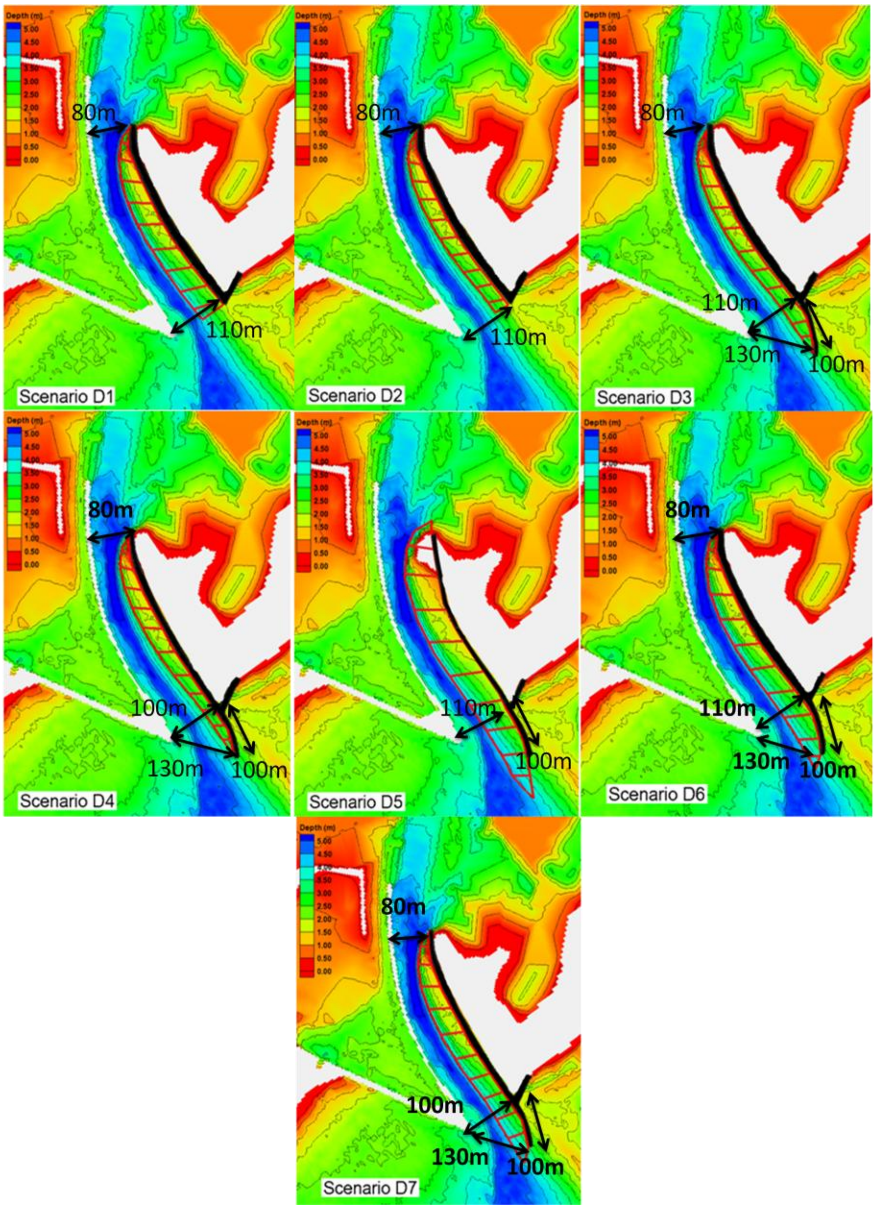

Figure 7.6 - Inlet configurations for scenarios D1, D2, D3, D4, D5, D6 and D7.

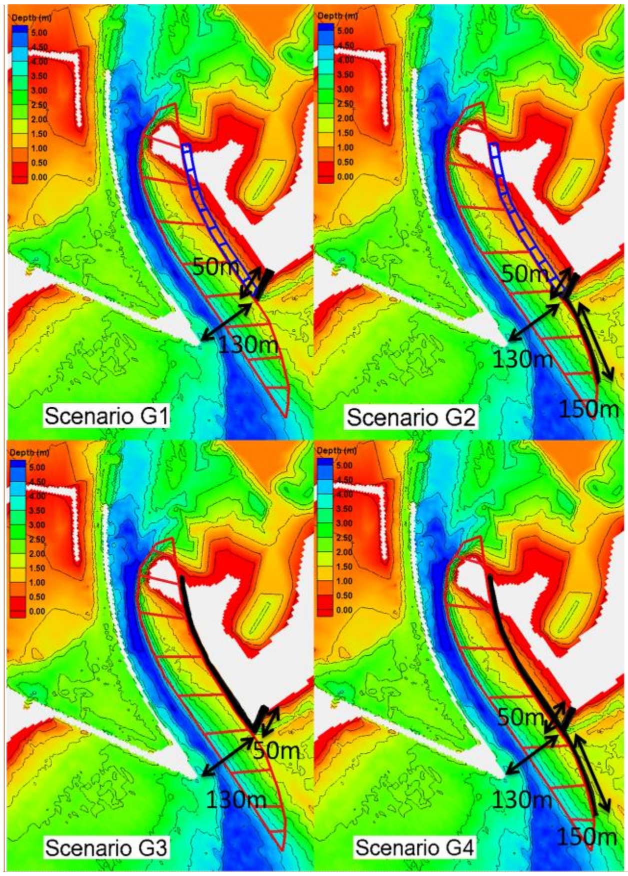

Figure 7.7 - Inlet configurations for scenarios G1, G2, G3 and G4.

Comment [m5]: These figures are not fitting the page format…

Formatted: Caption

7.2 Implementation in the Numerical Model

The various future scenarios were modelled by carefully incorporating all of the proposed dredging and new structures into both the CMS-Flow and CMS-Wave models, specifying appropriate boundary conditions, initial conditions and model-control parameters, and then launching the run. The first step in setting up a scenario was to alter the bathymetry to include dredging (if required). This was done by manually adjusting the depths of the cells located within the dredged area. Gradual changes in elevation were linearly interpolated between the dredged elevation and the desired elevation. Next, if the scenario included a new revetment, it was modelled by creating a 1:1.5 slope (from -4m to +3m elevation) in the bathymetry and specifying the corresponding computational cells to be non-erodible. This ensured that an non-erodible rock revetment was properly represented within the model. The final step in setting up a scenario was to model new jetties and training walls, as required. Most structures, except for the jetty in scenario E2b, were modelled by specifying the cells within the structure footprint to be non-

Comment [m6]: Please use model with one “l” throughout!

computational, or as dry land. Neither water currents nor waves were able to pass through these non-computational cells. In essence, the structures were modelled as solid vertical walls extending from the seabed up to the +3m elevation. The jetty in scenario E2b was specified as a rubble-mound structure and consequently had to be modelled differently than the vertical wall structures. The rubble-mound jetty was modelled by modifying the bathymetry to include the sloping jetty structure - a 1:1.5 slope was assumed from seabed (-4m) to an elevation of +3m. The computational cells within the rubble-mound jetty were set as non-erodible to ensure the jetty remained stable and non-changing throughout the entire duration of the simulation.

The seventeen alternative scenarios discussed thus far were modelled using the calibrated numerical model, starting with an interpolated 2010 bathymetry and forced using the wave and tidal boundary conditions described in Section 6.3. The long term simulations were performed using the implicit solution scheme for a duration of 136.875 days with a 15 minute time step, with model output every 6 hours. As in the phase I study, a morphologic acceleration factor of 16 was used to extend the simulation duration from 137 days to 6 years. In essence the morphology changes predicted by the model after 137 days were multiplied by a factor of 16. Since each 137 day simulation took approximately 132 hours to complete, running on a machine with six 3.5 GHz CPUs, using a morphologic acceleration factor was the only practical way in which long-term simulations could be performed.

The short term storm simulations were also performed using the implicit solution scheme; however, in this case the time step was 5 minutes, the duration was only 25 hours, and model outputs were stored every 5 minutes. For the short term simulations, the morphologic acceleration factor was not used, and was therefore set to 1.

The model output included a large number of spatial and temporal datasets that were subsequently analyzed to assess the relative performance of the various potential future inlet configurations. The datasets that proved most useful in the scenario assessment were: the magnitude and direction of the depth-averaged currents; the magnitude and direction of the sediment flux; the change in seabed elevation and the updated (final) bathymetry. The SMS was used to compute a number of derived quantities to support the assessment, including: the maximum velocity at each cell; the residual (time-averaged) circulation; the time-averaged sediment flux, the sediment flux across certain user-defined cross-sections; and the volume of erosion and deposition within user-specified polygons.

An in-depth analysis of the hydrodynamics, sediment transport patterns and morphology changes for existing conditions and for the seventeen alternative inlet configurations that have been modelled is presented below in Sections 8 and 9.

8 Baseline Results for Existing Conditions

The initial bathymetry for the status quo scenario (existing conditions) is shown in Figure 8.1. The status quo scenario represents the case where there is no intervention at Shippagan Gully; meaning no changes to the existing bathymetry or structures. Included in the status quo scenario is a representation of the collapsed jetty on the east side of the inlet in its current state, the curved wharf on the west side of the inlet and the 100m length of rubble extending north the northern tip of the curved wharf. Simulation results from the long-term (6 years) and short term (25 hour) storm simulations of the status quo scenario are presented in this section.

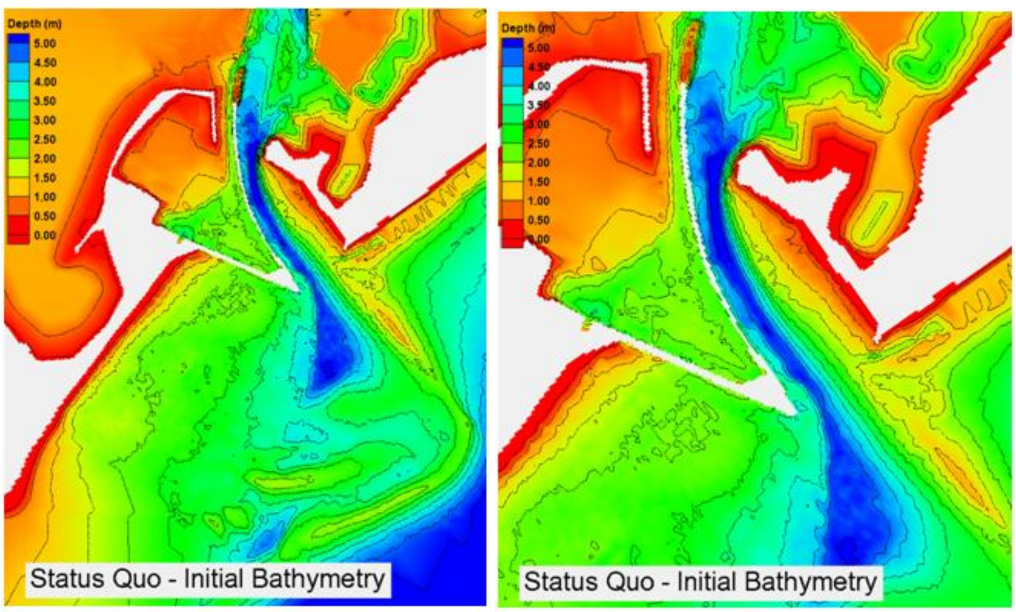

Figure 8.1 – Initial bathymetry for status quo scenario, interpolated from 2010 survey data and navigation chart.

8.1 Hydrodynamics

8.1.1 Tidal Hydrodynamics

The flow fields predicted by the numerical model at times with strong flood and ebb currents are shown in Figure 8.2. These velocities are representative of the maximum velocities observed within the inlet during non-storm conditions. The highest velocities within the inlet occur during the ebb flow, with depth averaged velocities reaching speeds of up to 2.1 m/s at the narrowest point of the channel. The sand spit on the east side of the inlet causes a narrowing of the channel, which produces a concentration of the current and a corresponding increase in velocity at, and immediately south of the channel constriction. The ebb current is non-uniform across the inlet mouth, and is much weaker (0.1-0.3 m/s) on the eastern part of the inlet mouth near the sand spit. In fact, while the tide is ebbing, the water on the eastern side of the inlet mouth flows slowly into the inlet from south to north, opposite to the main ebb flow exiting through the western side of the inlet mouth. In other words, there is bi-directional flow with a counter-clockwise circulation within the inlet mouth during ebb flows.

The highest velocities reached during the flood flow (1.1 m/s) are located near the narrowest point of the inlet, similar to where the maximum ebb flow velocities are observed. It is important to note that the maximum flood velocities are almost half of the maximum ebb velocities. As mentioned previously, this strong imbalance between ebb and flood flows is due to the fact that the tidal lagoon bisects the Acadian peninsula and is open to the sea at two locations where there is an appreciable phase lag in the tidal cycle. The flood current is more uniform across the inlet mouth than the ebb current. The maximum velocities in the eastern part of the inlet mouth are on the order of 0.5 m/s with flow entering the inlet. These results, combined with the results for ebb flows, indicate that the water on the east side of the inlet mouth rarely flows towards the sea.

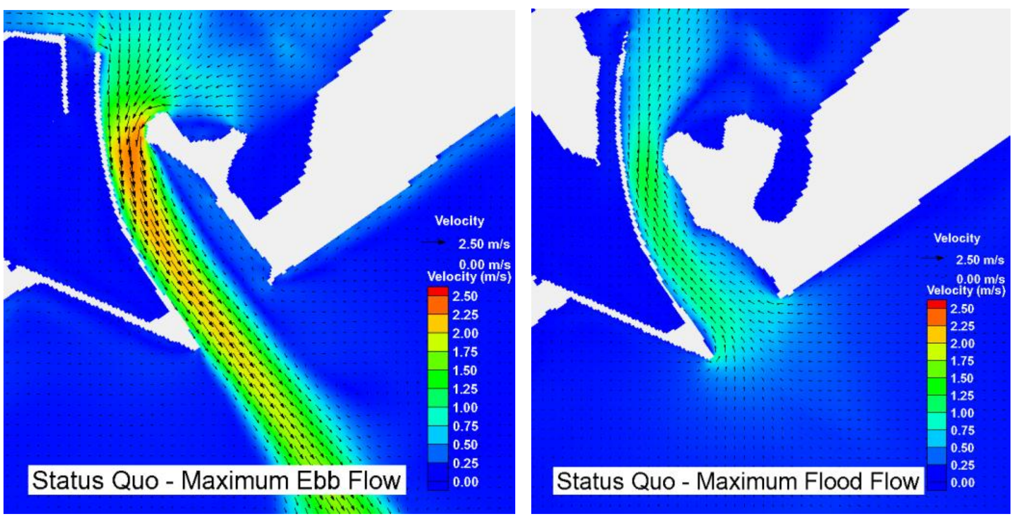

Figure 8.2 – Velocities and flow patterns during strong ebb and flood tides for existing conditions.

8.1.2 Nearshore Hydrodynamics During Storms

Along with the long-term simulation, several shorter 25 hour simulations were conducted to investigate the hydrodynamic and sediment processes at the existing inlet (status quo configuration) during various idealized storms. As described previously in Section 6.3, the storm simulations included a 6 hour growth period followed by a 13-hour period of steady energetic conditions, followed by a 6-hour decay period. Results from these storm simulations are presented below in order to shed light on the hydrodynamics at the inlet at times when energetic wave conditions prevail.

8.1.2.1 Influence of wave direction

The residual currents (net time-averaged currents) calculated for each storm are compared in Figure 8.3 to Figure 8.5. The easterly storm (Figure 8.3) forces a longshore current near the shore and over the ebb shoal, flowing from NE to SW on both sides of the inlet. The strong ebb jet emerging from the inlet mouth is deflected towards the west in this case. For the southerly storm (Figure 8.5), the longshore current on both sides of the inlet reverses and flows from SW to NE as expected. The strong ebb jet is deflected towards the east in this case, and the residual circulation on the ebb shoal is generally weaker and more variable. The southeasterly storm (Figure 8.4) generates much weaker longshore currents than the other two storms. The residual circulations on the ebb shoal are also rather mixed for the southeasterly storm, compared with the other storm directions. In all three cases, the residual currents within the inlet mouth are bi-directional; flowing strongly towards the Gulf of St. Lawrence on the west side of the inlet mouth parallel to the curved training wall, and flowing into the lagoon on the east side of the inlet mouth along the edge of the sand spit. This prominent clockwise circulation within the inlet mouth has likely contributed to the growth and elongation of the sand spit that has formed on the eastern side of the inlet mouth, which now threatens safe navigation through Shippagan Gully. These results show that the residual currents flowing in and out from the inlet mouth are weaker during storms from the east than during storms from the southeasterly or southerly directions.

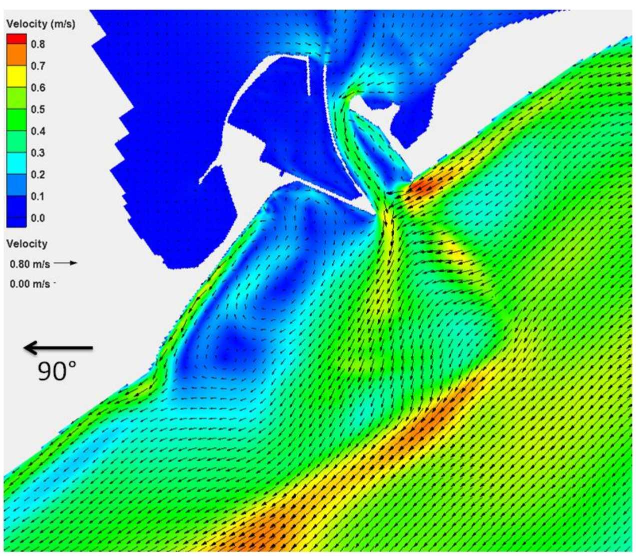

Figure 8.3 – Residual currents for idealized storm with waves approaching from the east (90°).

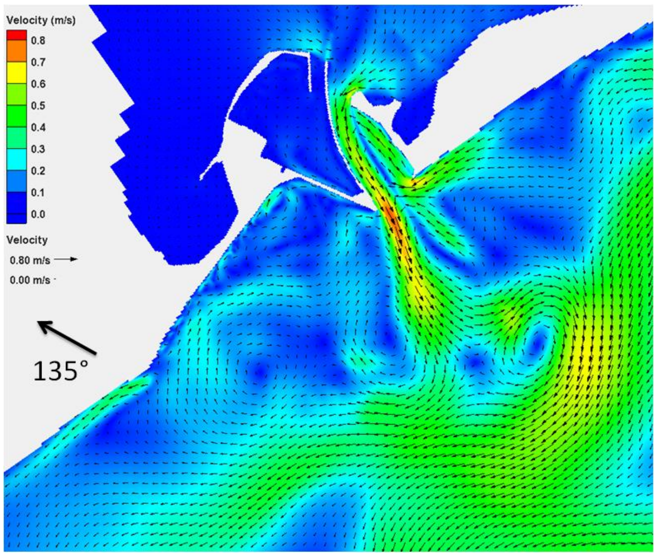

Figure 8.4 – Residual currents for idealized storm with waves approaching from the south-east (135°).

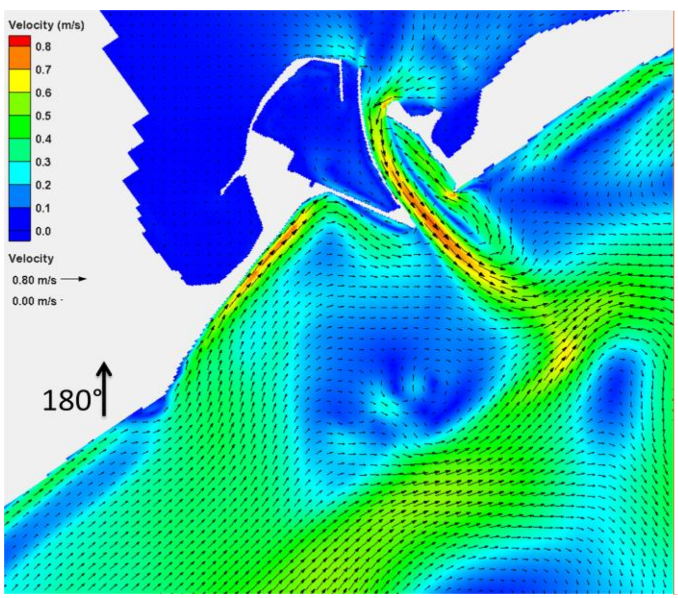

Figure 8.5 – Residual currents for idealized storm with waves approaching from the south (180°).

Comment [m7]: Too big for the format…

8.1.2.2 Influence of storm surge

The easterly storm was also simulated with storm surge, and the residual currents for this case are shown in Figure 8.6. The influence of a 1m storm surge can be seen by comparing these results to those shown in Figure 8.5. It is apparent that excluding storm surge has a significant impact on the magnitude of the residual currents, which were reduced throughout much of the computational domain. This is most evident just outside the inlet mouth near the tip of the broken jetty where the residual currents have decreased from ~0.75 m/s to ~0.6 m/s. Within the inlet, the residual currents are similar for both cases, which indicates that they are fairly insensitive to storm surge.

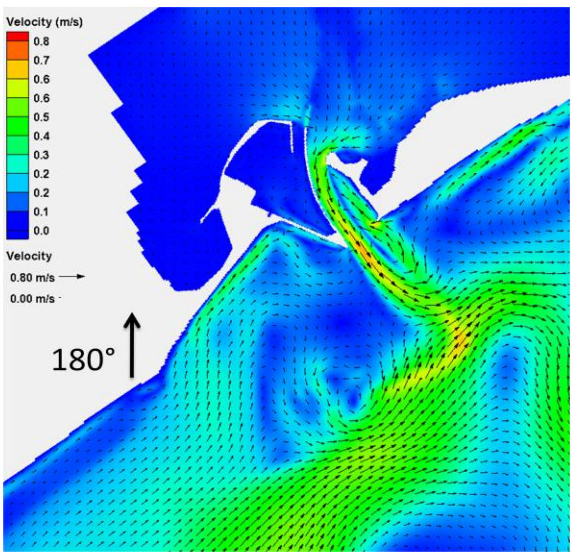

Figure 8.6 – Residual currents for idealized storm approaching from the east (90°) without storm surge.

8.2 Sediment transport patterns

8.2.1 Long term sediment transport patterns

Plotted in Figure 8.7 is the time-averaged sediment flux calculated over the entire 6 year simulation. The largest sediment transport occurs offshore of the inlet mouth and is driven by the strong ebb currents exiting the west side of the inlet mouth. However, significant amounts of sediment are also transported into the eastern side of the inlet mouth - these sediments are delivered to the inlet mouth by the wave-driven longshore current flowing along the shoreline from the NE. The model results suggest that after entering the inlet, some this sediment is deposited within the eastern part of the inlet mouth. The navigation issues within the inlet stem from this longshore sediment transport passing around the tip of the damaged jetty and entering the east side of the inlet mouth. The south-westerly flowing longshore current and longshore sediment flux are generated mainly by the effects of energetic waves approaching from easterly directions.

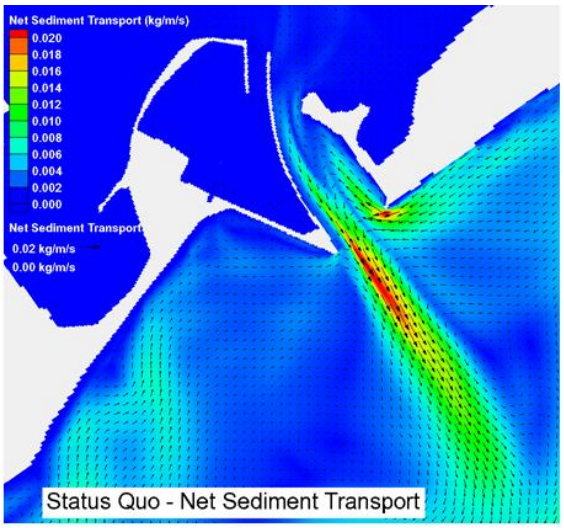

Figure 8.7 – Long-term time-averaged sediment flux for the status quo scenario.

The cumulative sediment flux across the north and south limits of the inlet were calculated from the numerical model results and are plotted in Figure 8.8. In this figure, positive values and trends denote sediment flowing northwards, while negative values and trends denote sediment flowing southwards. The location of these two cross-sections is shown in Figure 8.9. The cumulative sediment flux across the inlet entrance has an overall negative trend, indicating that over the entire simulation, the volumes of sediment flowing southwards out of the inlet mouth exceed the volumes flowing northwards into the inlet. The short positive pulses of sediment flux that occur at various times during the simulation indicate the effects of intermittent storms pushing sediment into the inlet mouth. During non-stormy times, the volumes flowing south out of the inlet generally exceed the volumes flowing north. The sediment flux across the lagoon entrance is very small in comparison to the flux across the inlet mouth. In the numerical model, very little sediment is transported in either direction at this location.

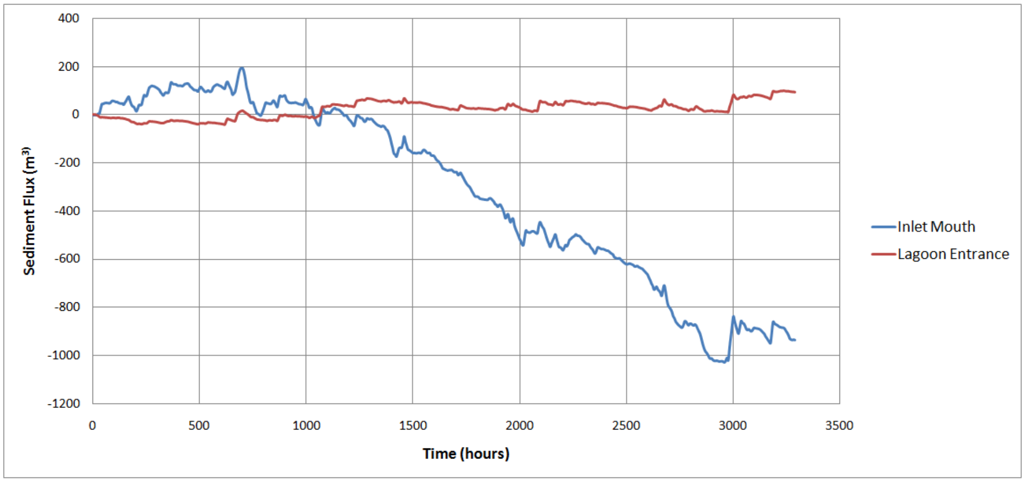

Figure 8.8 - Sediment flux across the inlet mouth (blue) and lagoon entrance (red); positive defined as flow towards north, negative defined as flow towards south.

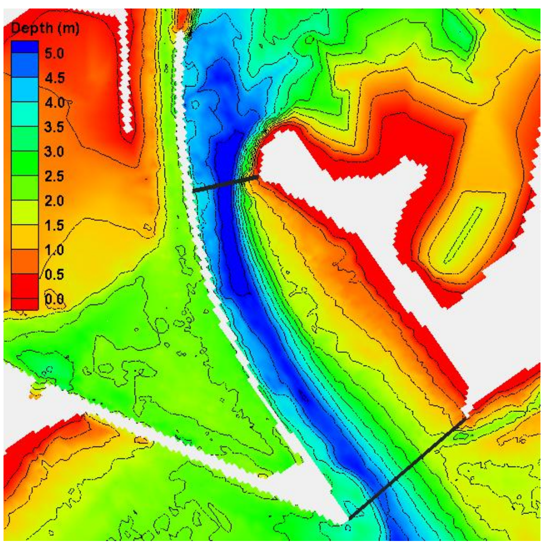

Figure 8.9 - Location of cross-sections for sediment flux analysis.

8.2.2 Sediment transport patterns during storms

The prevailing wave conditions and storm surge have a strong influence on the hydrodynamic and sediment processes along the shoreline, on the ebb shoal and at the inlet mouth. The effect of wave direction and storm surge on the movement of sediment around the inlet can be assessed by examining results for several of the 25-hour simulations of storm conditions. The time-averaged sediment flux has been computed for similar 25 hour storms approaching from three different directions (90°, 135°, 180°) as well as for 25 hour storms simulated with and without a 1 m surge in water level.

8.2.2.1 Influence of wave direction

The time-averaged sediment flux calculated from simulation results for three similar 25 hour storms with waves approaching from 90°, 135°, 180° are plotted in Figure 8.10 to Figure 8.12. The wave breaking caused by the easterly approaching storm (Figure 8.10) drives strong longshore sediment transport parallel to the coast, from NE to SW. Due to the 4 m significant wave height that was modelled, most of the wave breaking and longshore sediment transport occurs in deeper water beyond the -5 m depth contour. Most of this sediment flows past the inlet without entering it. The portion of longshore sediment transport entering the inlet is split into two pathways, which are shown in Figure 8.13a. The primary (stronger) pathway travels along the existing navigation channel and the secondary (weaker) pathway travels along the east side of the inlet. The primary sediment transport pathway through the inlet may be responsible for sediment deposition within the existing navigation channel.

The south-easterly approaching storm (Figure 8.11) drives a weaker and less uniform longshore sediment transport from NE to SW, when compared to the easterly storm; however, as in the case of the easterly storm, most of the sediment transport occurs in deeper water a fair distance from the coast. In contrast to the easterly storm, Figure 8.13b shows that the south-easterly storm produces a single sediment transport pathway flowing into the east side of the inlet. Virtually no sediment flows into the inlet along the navigation channel for this case. The wave-driven sediment transport along the east side of the inlet is strongest at the inlet mouth and gradually reduces further into the inlet. Eventually a point within the inlet is reached where the wave energy has completely dissipated and can no longer drive sediment transport.

The storm approaching from the south (Figure 8.12) drives a longshore sediment transport parallel to the coast, from the SW to the NE, opposite of the flow generated by the easterly storm. As in the other cases, the main longshore transport occurs in deeper water well away from shore. As the longshore transport travels towards the inlet, it is directed along the ebb shoal and continues towards the NE. The longshore sediment transport is generally weaker for this direction, due to the fact that the southerly storm had a significant wave height of 3 m, compared to the 4 m waves simulated from the other two directions. As seen in Figure 8.13c, the southerly storm produces sediment transport only along the east side of the inlet; with no sediment transport along the navigation channel. The sediment transport along the east side of the inlet is comparable in magnitude to the south-easterly storm, although it does not penetrate as far into the inlet.

Unlike the long-term simulation of the status quo (Figure 8.7), the modelled storm scenarios do not show a net sediment transport exiting the west side of the inlet. Therefore, after a large storm, the ebb flow must mobilize and entrain sediment deposited along the navigation channel and carry it offshore and out of the inlet. During these storms, the wave-driven longshore transport far exceeds the sediment transport forced by the ebb jet exiting the west side of the inlet mouth. Hence the pronounced sediment flux driven by the ebb jet seen in Figure 8.7 cannot be seen in Figure 8.10 - Figure 8.12.

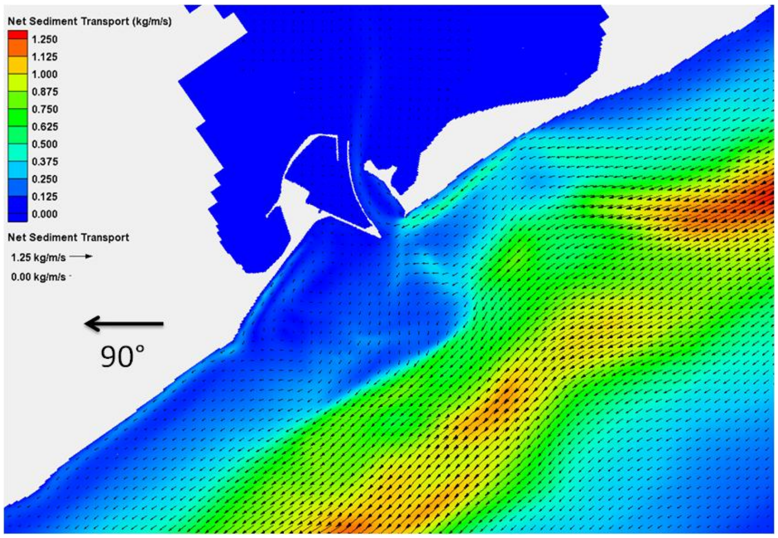

Figure 8.10 - Time-averaged sediment flux for 25 hr storm with waves approaching from the east (90°).

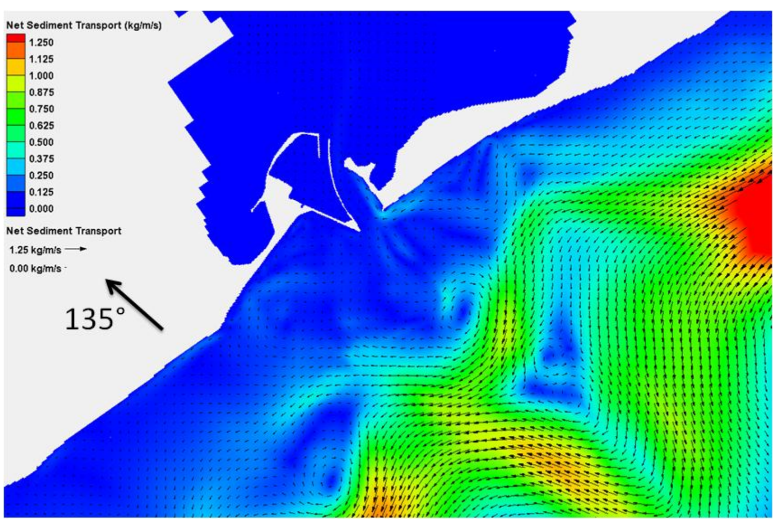

Figure 8.11 - Time-averaged sediment flux for 25 hr storm with waves approaching from the south-east (135°).

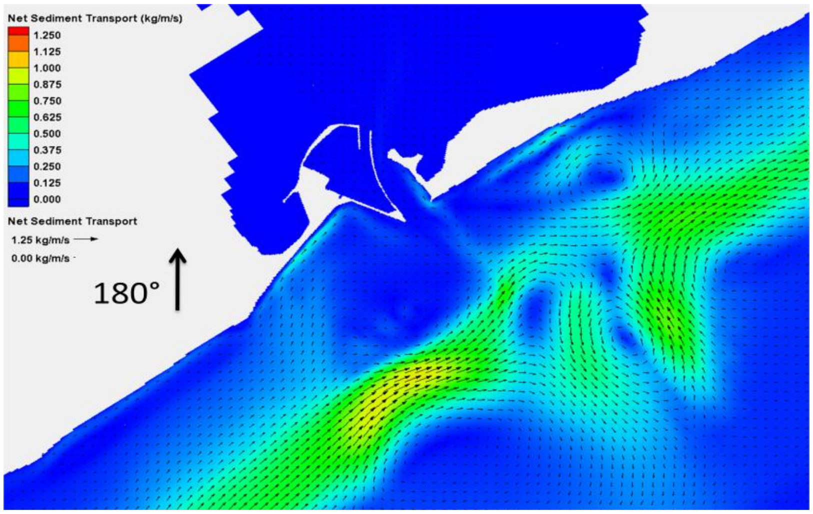

Figure 8.12 - Time-averaged sediment flux for 25 hr storm with waves approaching from the south (180°).

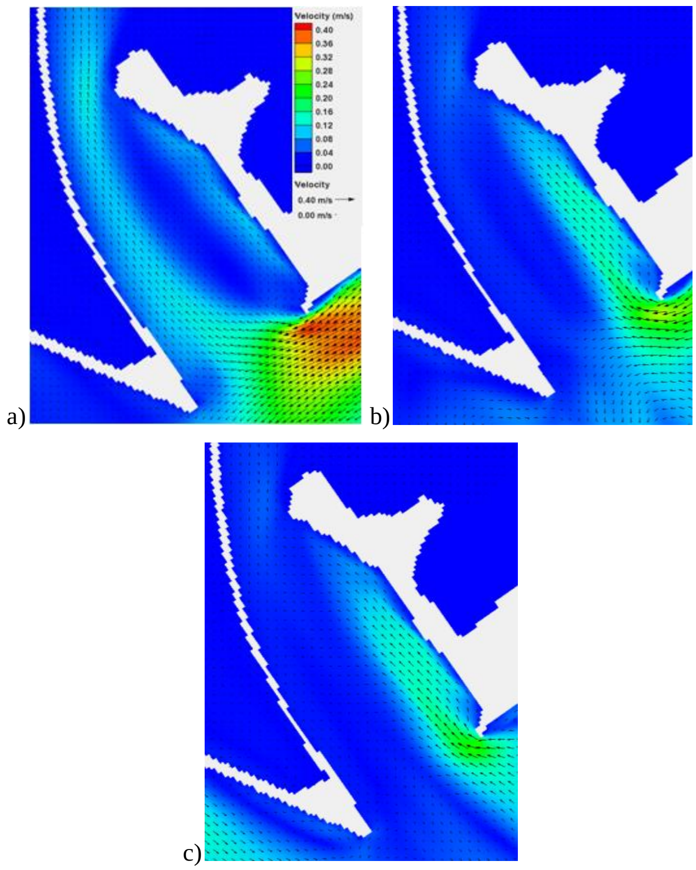

Figure 8.13 – Time-averaged sediment flux at the inlet mouth for similar 25 hour storms with waves approaching from: a) east (90°); b) south-east (135°); and c) south (180°).

8.2.2.2 Influence of storm surge

The idealized southerly (180°) storm was modelled with and without a 1 m storm surge. The time-averaged sediment flux at the inlet mouth for these two simulations is compared in Figure 8.14. The 1m surge clearly contributes to increasing the flux of sediment entering through the east side of the inlet mouth. The 1m surge also helps drive the sediment further into the inlet mouth. This comparison indicates that storm surge allows more wave energy to penetrate into the inlet mouth, and the additional wave energy strengthens the transport of sediments into the eastern part of the inlet mouth. These processes very likely contribute to the buildup and maintenance of the sand spit. Since the effects of storm surge were not included in the long-term simulations, it is likely that the growth of the sand spit is under-estimated in these simulations.

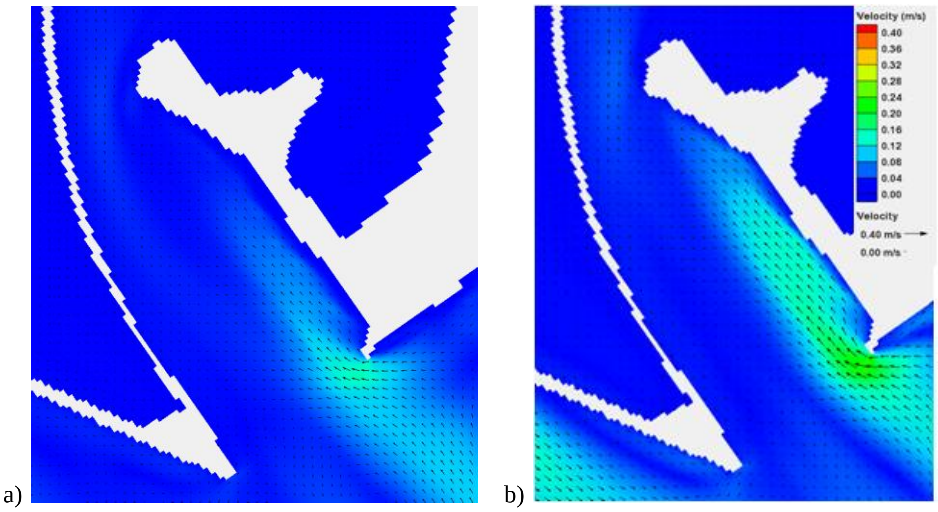

Figure 8.14 - Time-averaged sediment flux at the inlet mouth for a 25 hour storm with waves from the south: a) without storm surge; b) with 1 m storm surge.

8.3 Patterns of Erosion and Deposition

For each simulation, maps defining the morphology change were developed by subtracting the seabed elevation at the start of the simulation from the seabed elevation at the end of the simulation, on a cell by cell basis. Thus, positive change denotes deposition (increased elevation), while negative change denotes erosion (decreased elevation). A morphology change map highlights areas where the numerical model suggests that deposition or erosion may occur. However, as discussed in Section 6.6, since the model only provides a simplified and approximate simulation of nature, the model's predictions of morphology change are uncertain, and should therefore be interpreted with caution. In particular, the model's prediction of sediment processes and morphology change in shallow water near shorelines is unreliable.

In the figures in this report, erosion is indicated using cool colours (blues) while deposition is mapped using warmer colours (greens, yellows and reds). Grey is used to denote areas where the seabed elevation did not change significantly over the course of the simulation.

8.3.1 Erosion and deposition – Long term trends

The morphology change calculated for the long-term (6 year) simulation of coastal processes for existing conditions is shown in Figure 8.15. Outside the inlet, the model predicts that deposition will occur over large areas southwest of the inlet mouth, including portions of the ebb shoal and the foreshore. This deposition is balanced by erosion in other areas, including offshore and eastern portions of the ebb shoal and the shallow foreshore northeast of the inlet. It appears that in general, sediment is redistributed from the offshore and eastern parts of the ebb shoal to the foreshore SW of the inlet.

Within the inlet mouth, the model predicts that modest deposition will continue within the navigation channel and along the eastern edge of the channel, while significant erosion occurs at the northwestern tip of the sand spit and along the spit's western shore. The model suggests that most of the deposition in the channel is due to sediment entering the inlet from the sea (not the lagoon), pushed by the combined effects of waves and the flood tide. The erosion along the western shore of the sand spit could well be over-estimated in this simulation, due to the fact that the effects of storm surge were not included. The elongation of the sand spit that has occurred over the past decades is not replicated in the model. It is quite possible that the real sand spit has reached a natural equilibrium and will not elongate further. On the other hand, it is also possible that the model's predictions of morphology change in the shallow waters near sand spit are unreliable.

The polygon shown in Figure 8.16, which includes an area of 33,280 m^2, was defined to represent the current navigation channel, and the simulation results shown in Figure were analyzed to determine the total volumes of deposition and erosion within the polygon. The deposition was estimated at 3,746 m^3 over six years, while the erosion was calculated as 2,281 m^3 over six years. The net volume change is 1,465 m^3.

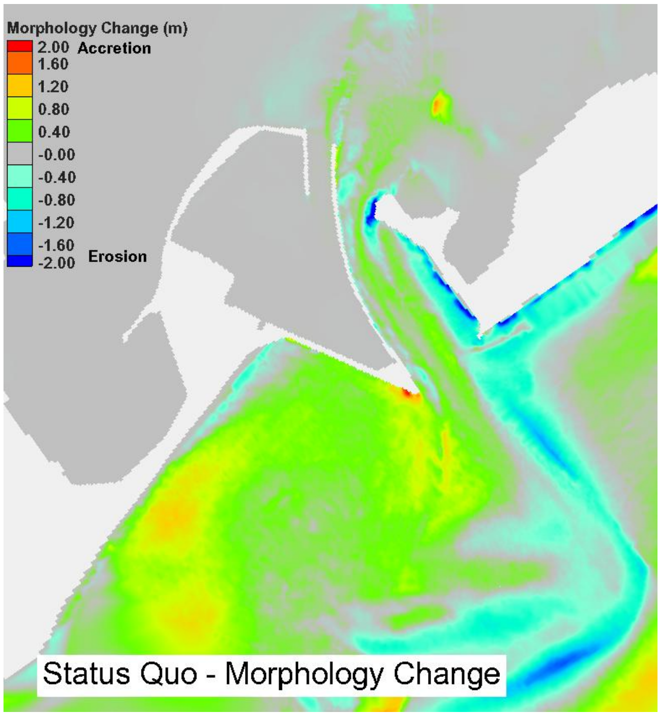

Figure 8.15 – Calculated morphology change after 6 years for existing conditions (status quo scenario).

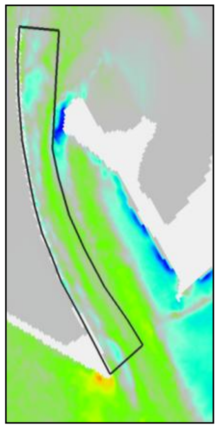

Figure 8.16 – Definition of polygon for calculating deposition and erosion volumes within the navigation channel.

8.3.2 Erosion and Deposition – Trends during storms

Morphology change maps were prepared for each of the idealized 25-hour storms that were modelled. The sensitivity of morphology change to the incident wave direction and the inclusion of a 1 m storm surge can be discerned by comparing these results.

8.3.2.1 Influence of wave direction

Morphology change maps for three similar 25 hour storms with 1 m storm surge and with waves approaching from 90°, 135° and 180° are compared in Figure 8.17. The patterns of morphology change for each storm direction closely mirror the time-averaged sediment transport patterns seen in Figure 8.13. As the NE to SW longshore sediment transport created by the easterly storm approaches the inlet, some sediment is deposited on the east side of the inlet mouth, as shown in Figure 8.17a. This sediment deposition causes a narrowing of the navigation channel at the inlet mouth, which reflects the measured bathymetry change over the recent years (see Figure6.23). Within the inlet, sediment is deposited along the western shore of the sand spit and along the navigation channel, following the two sediment transport pathways shown in Figure 8.13a.

The south-easterly (Figure 8.17b) and southerly (Figure 8.17c) storms produce similar deposition trends along the navigation channel, within the inlet mouth and offshore of the inlet. Compared to the easterly storm, both the southerly and south-easterly storms cause less deposition along the navigation channel and offshore of the inlet. However, the south-easterly and southerly storms create larger amounts of sediment deposition along the east side of the inlet compared to the easterly storm. In all three storm scenarios, deposition along the east side of the inlet begins at the inlet mouth and continues to near the northern end of the sand spit.

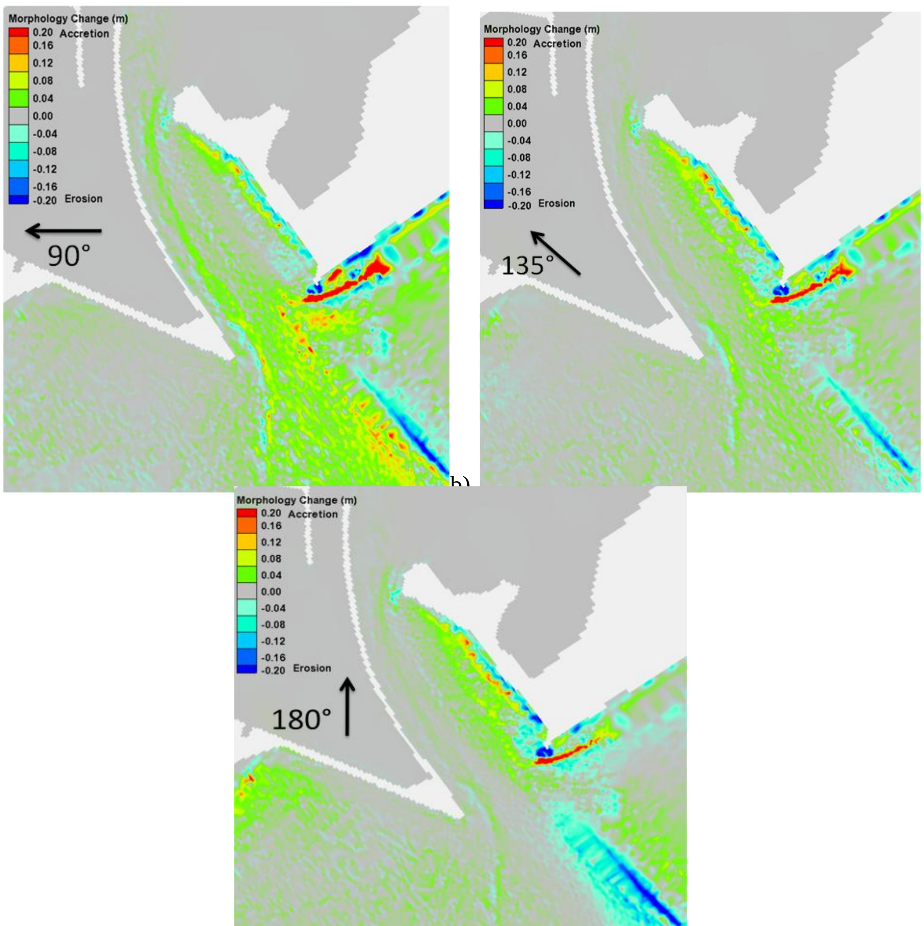

a) b) c)

Figure 8.17 - Morphology change due to similar 25 hour storms with waves approaching from a) east (90°), b) south-east (135°) and c) south (180°) directions.

8.3.2.2 *Influence of storm surge*

The influence of storm surge on morphology change mirrors the influence on time-averaged sediment flux discussed in Section 8.2.2.2, as expected. Morphology change maps for easterly and southerly 25 hour storms that excluded storm surge are shown in Figure 8.18. The influence of storm surge can be judged by comparing these images to those shown in Figure 8.17. The reduced amount of deposition within the inlet produced by simulations without storm surge indicates that storm surge is clearly responsible for increasing the volume of sediment deposited within the inlet mouth and for depositing sediment deeper within the inlet. The additional deposition is linked to an increase in the amount of wave energy that is able to penetrate into the inlet mouth when water depths over the ebb shoal are increased. This additional wave energy mobilizes more sediment and reinforces the current running into the inlet along the edge of the sand spit. Both of these processes contribute to increased deposition deep within the inlet mouth.

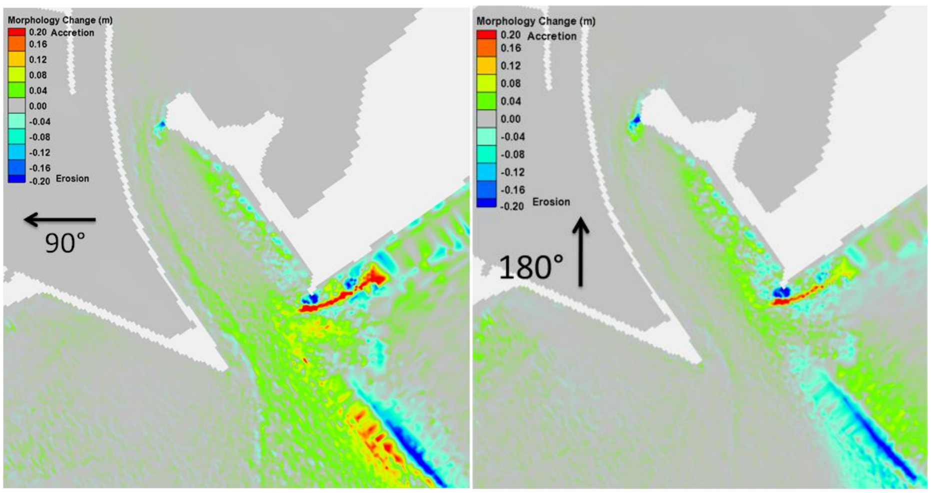

Figure 8.18- Modelled changes in seabed elevation without the effects of storm surge due to storms from the a) east (90°) and b) south (180°) directions.

9 Results for Phase I Scenarios

The simulation results for existing conditions discussed in Section 8 contributed to an improved understanding of the hydrodynamic and sedimentary processes at the inlet. With this knowledge in hand, the refined and recalibrated numerical model was used to simulate coastal processes for three scenarios from the Phase I study in order to assess the impact of the model refinement and confirm the earlier results. The results for these three configurations/scenarios were used as a starting point when designing the 15 new inlet configurations that were modelled later on.

The three Phase I scenarios that were re-modelled are shown in Figure 9.1. They are:

- scenario B2 - a 140 m long jetty perpendicular to the shore with a 140 m wide inlet mouth;
- scenario B3 - a 140 m long jetty perpendicular to the shore with a dogleg at 70 m and a 140 m wide inlet mouth; and
- scenario H1b - a training wall on the east side of the inlet ending in the Scenario B2 jetty with dredging to -1.5 m along the training wall.

Each scenario was modelled for a 6 year time period starting from the 2010 bathymetry using the synthetic water levels and wave conditions described in Section 6.3.

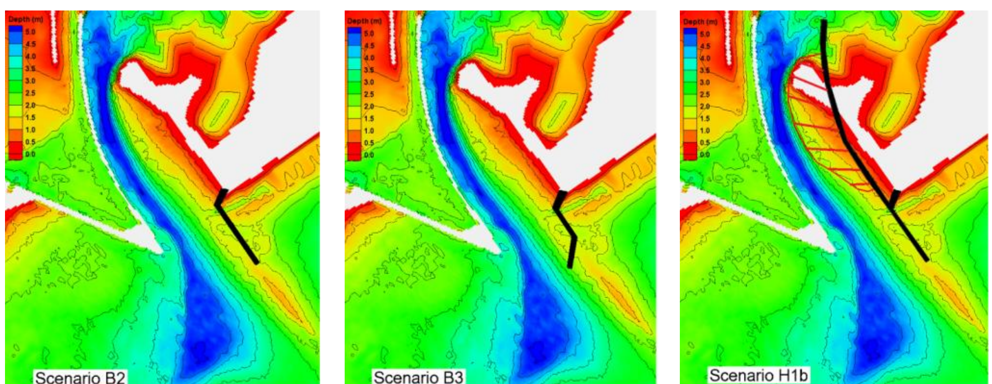

a) b) c)

Figure 9.1– Three inlet configurations from the Phase I study: a) Scenario B2; b) Scenario B3; c) Scenario H1b.

9.1 Hydrodynamics

The maximum flood and ebb flows for scenarios B2, B3 and H1b are shown in Figure 9.2 to Figure 9.4, while the maximum flood and ebb flows for existing conditions are shown in Figure . Within the inlet mouth, the ebb and flood flows for scenario B2 are very similar to existing conditions. During the ebb flow, the new jetty causes a flow recirculation on the NE side of the jetty, which results in slightly higher velocities (~0.3 m/s) on the east side of the inlet compared to the status quo (~0.22 m/s). The flow recirculation during the ebb flow in scenario B2 causes flow towards the lagoon along the east side of the inlet.

The dog-leg jetty modelled in Scenario B3 partially constricts the flows entering and exiting the inlet during flood and ebb tide, resulting in slightly increased velocities compared to existing conditions. During the ebb flow, peak velocities at the inlet mouth increase from 1.65 m/s to 1.8 m/s, compared to existing conditions. Scenario B3 (Figure 9.3) shows a similar recirculation behind the new dog-legged jetty; however the velocities only reach a speed of ~0.2 m/s. The addition of the dog-legged jetty reduces the width of the inlet mouth, thereby leading to increased velocities. The peak velocities near the central and northern parts of the inlet mouth are not affected. In addition, the angled portion of the jetty redirects the ebb jet westward as it exits the inlet.

Unlike the two previous scenarios, the model predicts large changes in hydrodynamics for scenario H1b (Figure 9.4) compared to the status quo situation (Figure 8.2). For scenario H1b, the peak velocities in the inlet mouth during both ebb and flood are lower and the flows are more uniform across the channel width. The channel widening provides a larger two-dimensional flow cross-section, therefore decreasing the maximum velocities observed during the ebb flow from 2.1 m/s to 1.6 m/s. In the status quo scenario, the flow within the inlet mouth during ebb tide was bi-directional, towards the north on the east side and towards the south on the west side. As a result, the ebb jet was confined to the western part of the inlet mouth, near the curved training wall. No such bi-directional flow is predicted for scenario H1b. In this case, the ebb jet is weaker and wider, filling the full channel width. This ebb flow may help flush out sediments deposited in the eastern part of the channel during flood tides, preventing sediments from accumulating in this area.

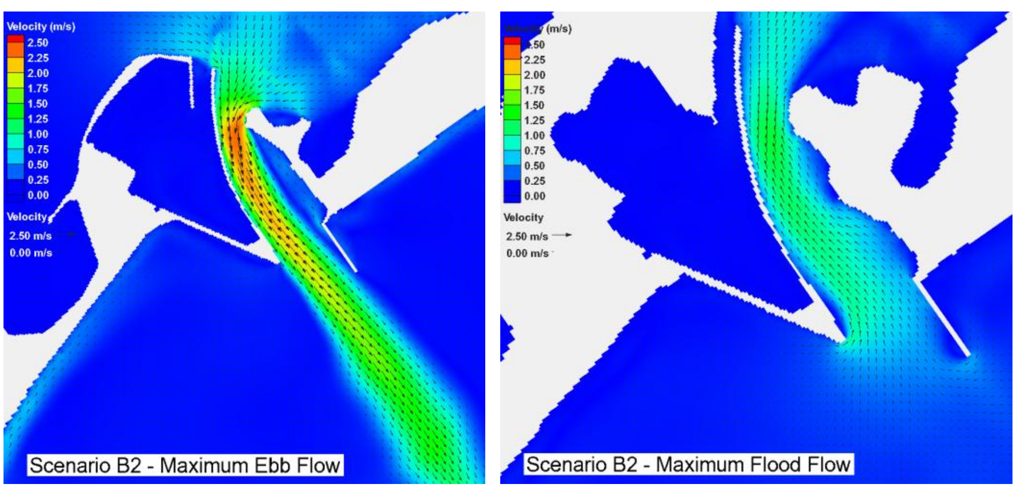

Figure 9.2- Maximum ebb (left) and flood (right) flow for scenario B2.

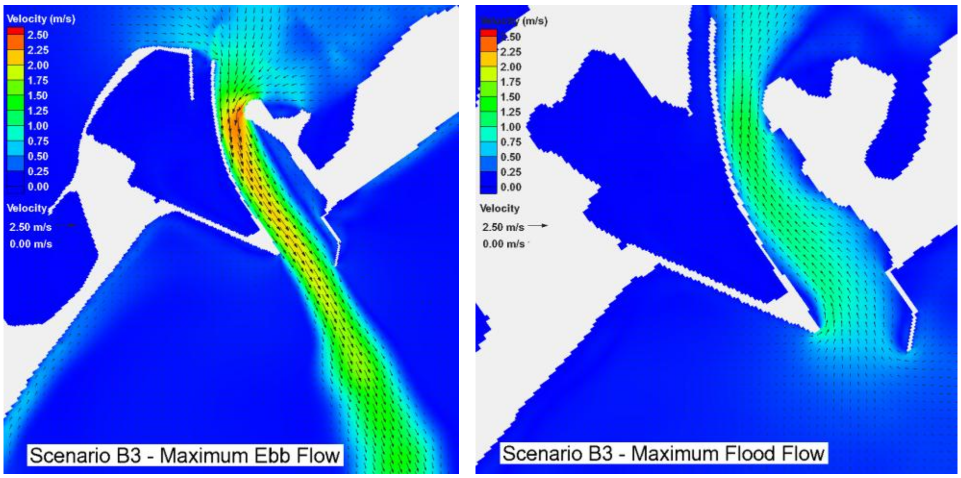

Figure 9.3- Maximum ebb (left) and flood (right) flow for scenario B3.

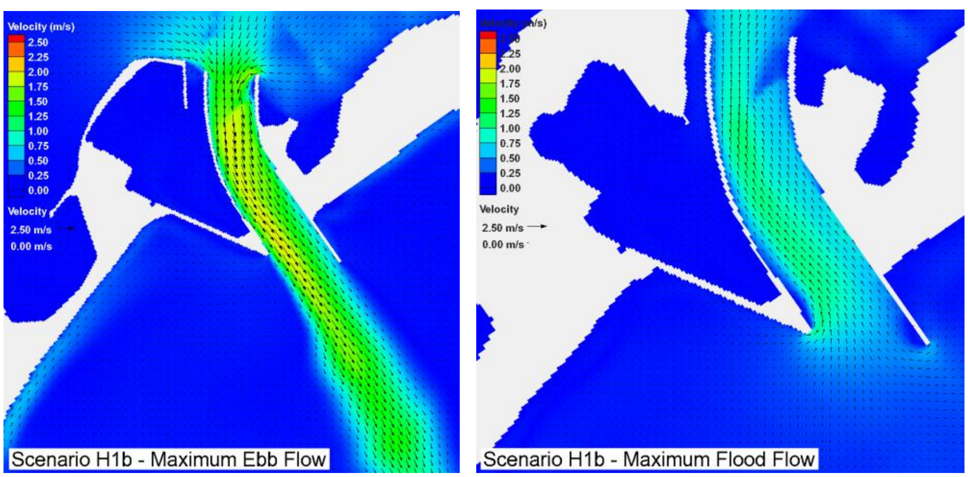

Figure 9.4- Maximum ebb (left) and flood (right) flow for scenario H1b.

9.2 Sediment transport Patterns

The time-averaged sediment transport vectors and magnitudes for scenarios B2, B3 and H1b are plotted in Figure 9.5. An equivalent plot for existing conditions is shown in Figure 8.7. In scenario B2 (Figure 9.5a), a portion of the longshore sediment transport arriving from the NE is trapped behind the jetty while the remainder travels around the jetty and into the east side of the inlet. The model results indicate that the B2 jetty is not entirely effective in blocking sediment from entering the inlet. On the other hand, the model results indicate that the dog-leg jetty modelled in scenario B3 (Figure 9.5b) is more effective at preventing sediment from entering the inlet. Some of the sediment is retained behind the jetty while some is swept offshore by the strong ebb jet onto the ebb shoal and beyond.

In scenario H1b (Figure 9.5c) as in scenario B2, some sediment arriving from the NE travels around the tip of the jetty (which extends from the training wall), entering the east side of the inlet. However, this sediment transport pathway is weaker in scenario H1b than in scenario B2, which can be explained by the differences in hydrodynamics during ebb and flood for each scenario. For scenario B2, the bi-directional flow within the inlet mouth during ebb tide helps propel sediment further into the inlet along the sand spit. The same bi-directional flow does not exist within the inlet mouth for scenario H1b. The ebb flow in scenario H1b reduces the amount of sediment entering the east side of the inlet. For all three scenarios (B2, B3 and H1b), the simulation results indicate that the relatively strong ebb jet drives a similar flow of sediment flowing south-southeast across the ebb shoal.

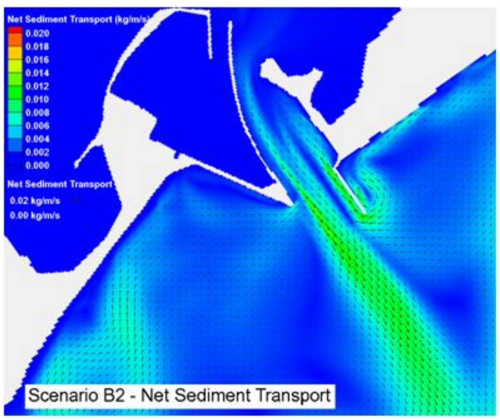

a)

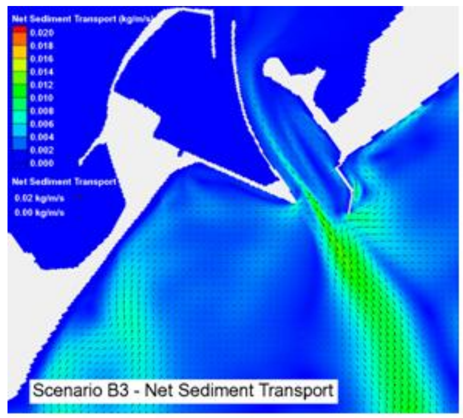

b)

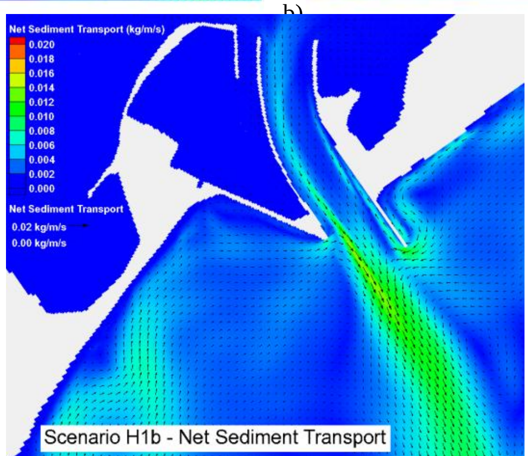

c)

Figure 9.5- Time-averaged sediment flux for six year simulation of: a) scenario B2; b) scenario B3; and c) scenario H1b.

9.3 Patterns of Erosion and Deposition

The long-term (6 year) estimates of morphology change for the three Phase I scenarios are shown in Figure 9.6 and compared to equivalent results from the status quo scenario. As mentioned previously, due to the challenges and uncertainties inherent in predicting morphology change, these results should be interpreted with caution.

The model results suggest that all three scenarios will reduce the amount of deposition within the eastern part of the inlet. The reduction is perhaps greatest for scenario H1b. All three scenarios include new jetties which reduce, to varying degrees, the amount of sediment that enters the inlet from the west. The model results also suggest that of these three options, scenario B3 is the most effective at reducing deposition within the existing navigation channel within the inlet. Of these three options, scenario H1b is perhaps the least effective at preventing deposition within the existing navigation channel. This could be related to the reduced strength of the ebb flows within the inlet mouth for scenario H1b. The wider inlet modelled in scenario H1b leads to weaker ebb flows, which are then not able to flush the sediment deposited by easterly storms. The channel widening does, however, help prevent deposition within the eastern part of the inlet. In the status quo situation, the sand spit shelters the east side of the inlet from the high ebb velocities, allowing deposition to occur in the low velocity area. By removing this constriction, the east side of the inlet is exposed to higher velocities (~1.5 m/s) exiting the inlet, which are able to flush away any sediment deposited by storm waves. The model results also show up to 3 m of erosion along the new training wall in scenario H1b. This erosion, along with a thin strip of erosion seen along the centre of the inlet, is highly sensitive to the initial sediment sizes (D_{50}, D_{35}, D_{90}) that were assumed in these areas. The sediment sizes in this area were chosen based on calibration results, but nonetheless, this issue should be taken into consideration when assessing these model results.

Ensuring that the inlet mouth and offshore area remains clear of deposition is important for improving navigability and navigation safety. Within the inlet mouth and offshore of the inlet, scenario B2 shows a reduced amount of deposition compared to existing conditions. This can be attributed to the jetty trapping some the NE to SW longshore sediment transport created by easterly waves, and diverting some sediment onto the ebb shoal. Compared to the status quo, scenario B3 shows a reduction of deposition within the inlet mouth, similar to scenario B2. However, a ~0.5 m high mound of deposition is predicted south of the tip of the jetty in scenario B3 (not present for scenario B2), which could pose a potential threat to safe navigation. It appears that this mound of sediment is produced by sand flowing along the east side of the jetty (pushed by the wave-driven longshore current) and then settling in the navigation channel. This deposition is not seen in the results for scenario B2 since the jetty in scenario B2 has a different alignment. The B2 jetty directs the longshore sediment transport onto the ebb shoal east of the navigation channel. Slightly more deposition is predicted within the navigation channel outside the inlet for Scenario H1b, compared to scenario B2. This increased deposition may be related to the weaker ebb jet not being able to flush away as much of the sediment deposited by storm waves.

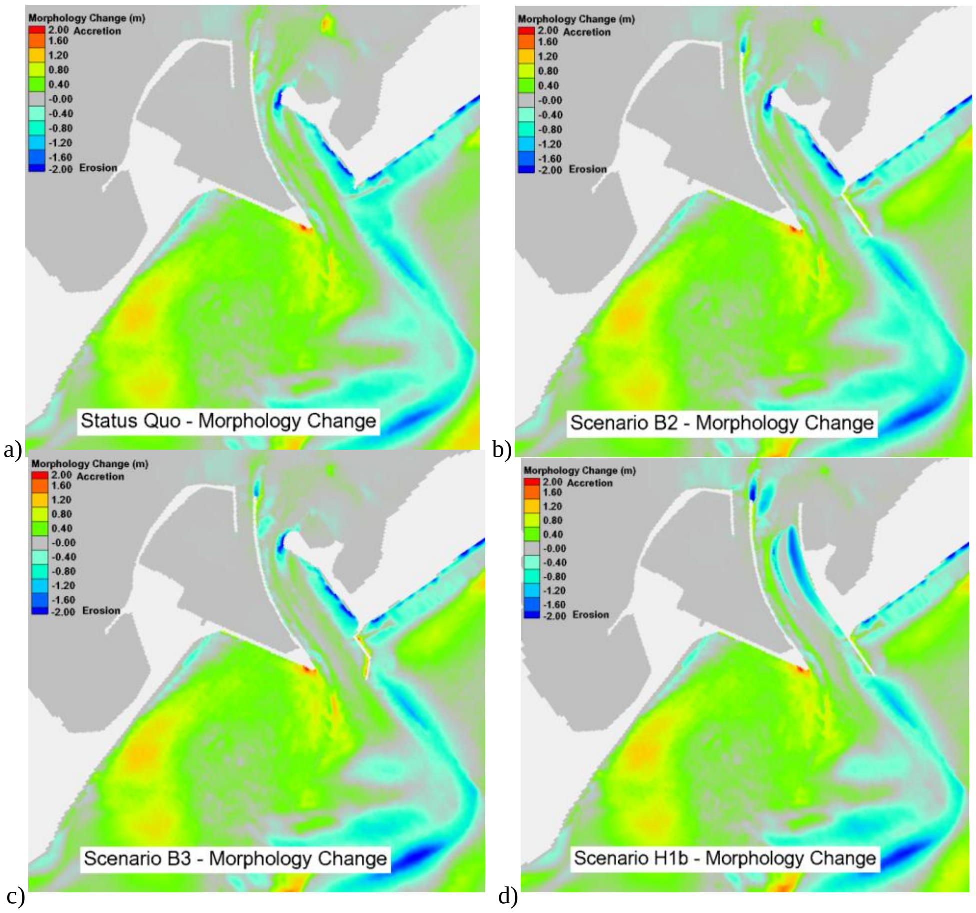

Figure 9.6 - Morphology change after 6 years for: a) status quo; b) scenario B2; c) scenario C3; and d) scenario H1b.

9.4 Comparison Between Phase I and Phase II Results

There are large discrepancies between the morphology change results produced by the model employed in the Phase I study and the results from the model developed for the current study. Figure 9.7 shows the long-term morphology change results from the Phase I study for the three inlet configurations that were remodelled. These images can be compared to those shown above in Figure 9.6. The significant differences could be due to several factors, including:

- the different spatial resolution in each model;
- the change in how sediment transport, and therefore morphology change, is calculated in each model; and

- the different initial seabed sediment properties assumed in each model.

As discussed in Section 6.1.3.2, the simplistic sediment transport algorithm used in the Phase I model may result in build-up of deposition in areas with large assumed D_{50} values. After a storm event in the Phase I model, the longshore sediment transport (assumed D_{50} of 0.6 mm) deposited within the inlet did not retain the proper sediment size once it was deposited. Instead, the deposited sediment took on the sediment size of the area of where it was deposited (assumed D_{50} of 10 mm). The strong ebb flow was not able to erode the storm deposition, since the sediment was now of a much larger size. This led to a build-up of sediment in areas where the seabed D_{50} was larger than what could be re-mobilized by the ebb flow. This spurious sediment accumulation is seen in all three of the Phase I results (scenario B2, B3 and H1b), where in each case, large amounts of deposition were predicted within the inlet and offshore of the inlet. The multiple grain size sediment transport algorithm employed in the current model is able to erode fine sediment deposited in areas where large bed sediments are assumed. The phase II model is believed to provide a better, more realistic representation of the sediment transport processes occurring at Shippagan Gully, thereby increasing the accuracy of the morphology change results.

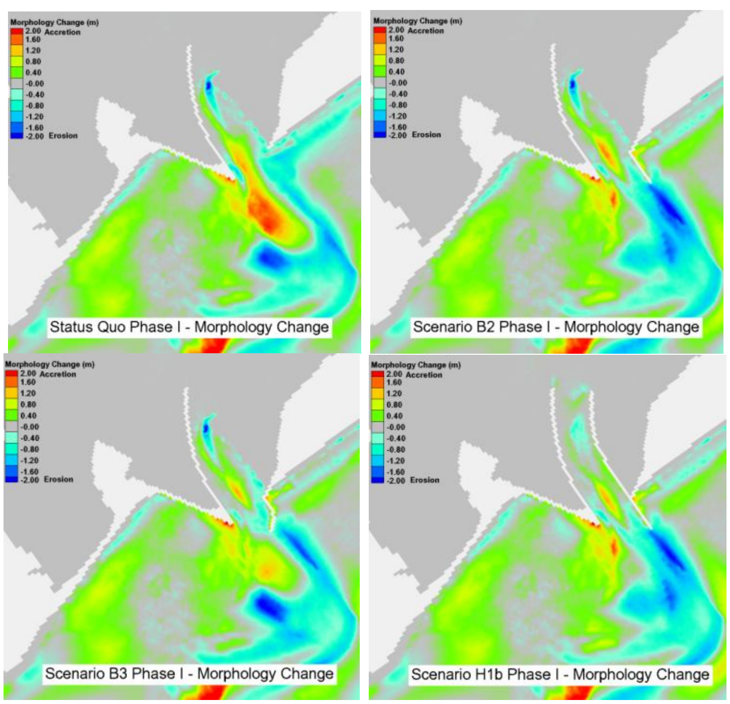

Figure 9.7- 6 year morphology change maps from the Phase I study for existing conditions and for scenarios B2, B3 and H1b.

10 Results for New Inlet Configurations

The seventeen alternative inlet configurations that were modelled using the refined and re-calibrated CMS model are segregated into four main groups: configurations with no added structures; configurations with a new shore-parallel eastern jetty, configurations with a new shore-perpendicular eastern jetty and configurations with a new training wall. More information on the seventeen scenarios is presented in Section 7.1. Presented in this chapter is an in depth analysis of the hydrodynamics, sediment transport patterns and morphology changes predicted by the model for the fifteen different inlet configurations.

10.1 Scenarios Without New Structures (B, F)

Scenarios B and F represent two new inlet configurations formed without constructing any new structures. Scenario B (shown in Figure 7.4) consists of removing 100 m of rubble and remains of sheet pile from the northern tip of the curved wharf. This part of the structure, shown in Figure 10.1, has deteriorated over time and currently causes a navigation hazard for vessels transiting the inlet and entering Le Goulet harbour. The rubble is most hazardous at high tide when the rubble-mound foundation of the deteriorated wharf is completely submerged, leaving only the corroded sheet pile visible. Removing this 100 m of deteriorated structure will allow for safer navigation around the entrance to Le Goulet harbour, which is located to the west of the existing wharf.

Scenario F (shown in Figure 7.5) is formed by dredging a curved channel through the inlet that is 110 m wide at its base and at least 4 m deep at low tide. The channel, dredged to the -4m elevation, begins at the lagoon entrance and extends to the inlet mouth. The east side of the dredged channel has a 1:5 (rise:run) side slope, which starts at the -4 m dredging depth and extends up to the existing grade (as shown in Figure 7.2). The goal of scenario F is to provide a deep, wide channel for navigation within the inlet without introducing any additional structures.

Figure 10.1 – 100 m long deteriorated structure at north end of the wharf.

10.1.1 Hydrodynamics

The purpose of removing the deteriorated structure at the northern tip of the wharf is to improve navigation safety near the entrance to Le Goulet harbour. Therefore, it is important to ensure that removing that part of the structure does not adversely affect flow velocities and patterns. Figure 10.2 and Figure 10.3 show simulation results at times with strong ebb and flood flows for existing conditions and for scenario B. Figure 10.2a indicates relatively high velocities at the tip of the wharf, which are a result of water flowing over the submerged rubble. At high tide, the rubble-mound is fully submerged, which produces a smaller cross-section over the rubble-mound for the ebb flow to travel. The reduced cross-section causes a corresponding increase of velocities. When the rubble is removed in scenario B (Figure 10.2b), the high velocity region is eliminated, producing a more uniform flow field around the harbour entrance.

Figure 10.3 shows that removing the deteriorated structure has very little influence on the flow field during flood tides. Based on these model results, removing the 100 m of structure from the northern tip of the curved sheet-pile wharf is expected to improve navigation safety around the entrance to Le Goulet harbour.

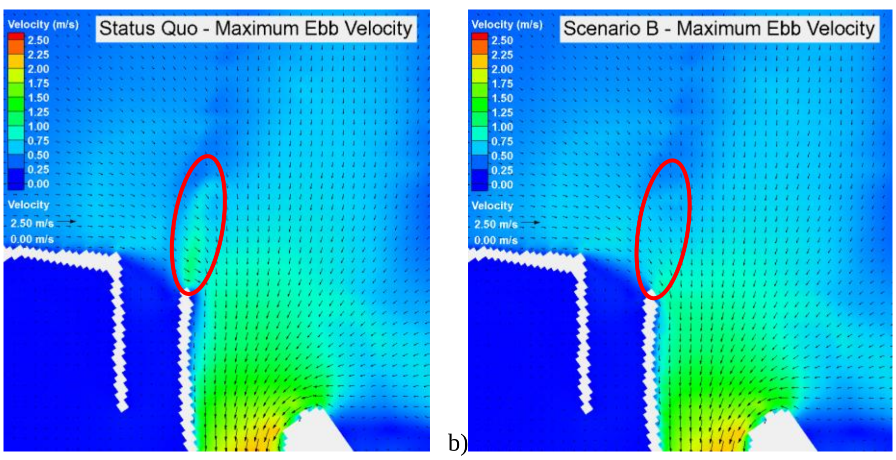

a) b)

Figure 10.2- Maximum ebb velocity for: a) status and b) scenario B (red circle indicates area where deteriorated structure was removed).

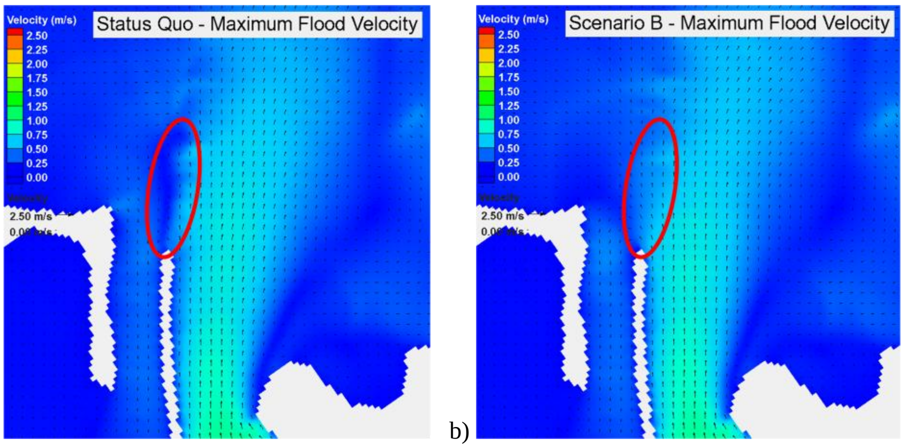

a) b)

Figure 10.3- Maximum flood velocity for: a) status quo and b) scenario B (red circle indicates area where deteriorated structure was removed).

The velocities and flow patterns for scenario F during strong ebb and flood tides are shown in Figure 10.4. Overall, the maximum velocities during ebb and flood flows are noticeably weaker for scenario F than for existing conditions (see Figure 8.2). The ebb flow in particular is also much more uniformly distributed across the inlet width. The peak ebb velocities have been reduced by ~20% (1.7 m/s in scenario F compared to 2.1 m/s in the status quo) and the peak flood velocities have been reduced by ~30% (0.75 m/s compared to 1.1 m/s). This reduction in peak velocities can be attributed to the substantial dredging work which has created a channel with a significantly larger cross-sectional area. Dredging a 110 m wide channel through the inlet increases the cross-sectional area, which subsequently decreases the velocities within the inlet. The velocity decrease will benefit the navigability of the channel, but may also lead to increased deposition within the channel. In addition, since the northern part of the sand spit has been removed, the east side of the inlet is no longer sheltered from the main ebb flow. This eliminates the re-circulating bi-directional flow pattern seen during ebb flows for existing conditions. Instead, the flow emerging from the inlet mouth during ebb tides will be more uniform and more evenly distributed across the full inlet width. This will help prevent sediments from accumulating within the eastern part of the inlet.

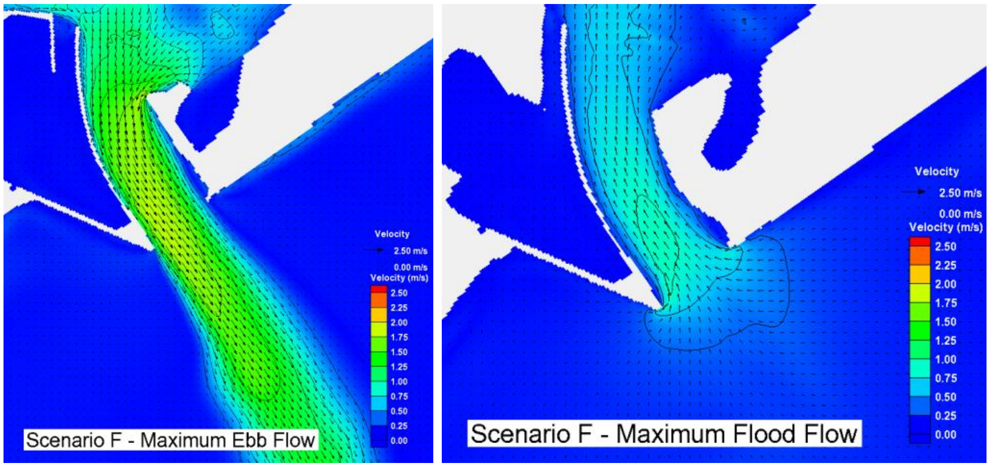

Figure 10.4– Velocities and flow patterns during strong ebb (left) and flood (right) tides for scenario F.

10.1.2 Sediment Transport Patterns

The difference in sediment transport patterns after the removal of the rubble in scenario B is negligible compared to the status quo scenario. Overall, the sediment transport patterns predicted for scenario B, shown in Figure 10.5a are virtually identical to the patterns predicted for the status quo scenario.

The results for scenario F shown in Figure 10.5b reveal that introducing a 110 m wide dredged channel through the inlet has a significant effect on the time-averaged sediment transport patterns, as one might expect. The ebb jet for scenario F tends to be wider and weaker than for existing conditions, and this change has a significant influence on sediment fluxes within and outside the inlet. However, it is important to bear in mind that these results, like the others presented in this report, are dependent on the composition of the seabed sediments that have been assumed in each location. The dredging in scenario F has caused weaker ebb flows on the west side of the inlet, while simultaneously increasing ebb velocities on the east side of the inlet. Consequently, there is less southbound sediment transport on the west side of the channel and more southbound sediment transport on the east side. This pattern continues on the ebb shoal outside the inlet. The dredging in scenario F appears to shift the area where the most intense sediment transport occurs towards the west, while maintaining a similar magnitude and direction. The increased net sediment transport on the east side of the inlet may cause erosion of the seabed, which is reflected in the morphology change results presented below.

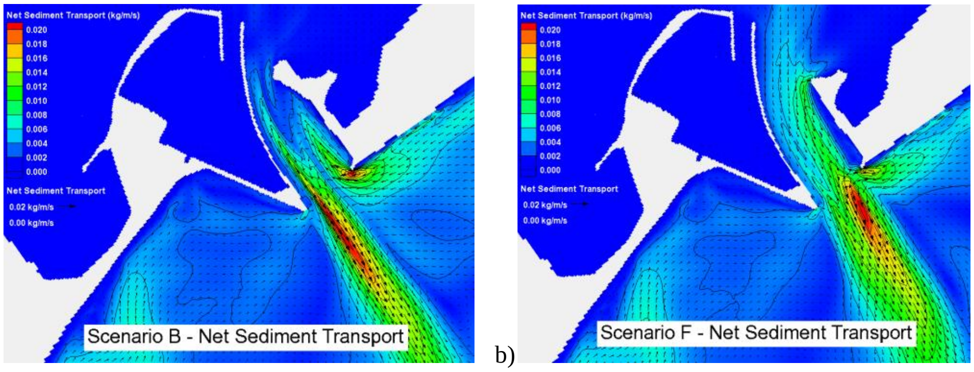

Figure 10.5 – Long-term time-averaged sediment flux for scenarios B and F.

10.1.3 Morphology Change

Morphology change estimates for existing conditions and for scenario B are compared in Figure 10.6. The differences between the two scenarios are very small. Compared to existing conditions, scenario B features slightly more deposition on the eastern side of the harbour entrance and slightly less erosion to the east of the former deteriorated structure. Further away from the north end of the curved wharf, results for these two scenarios are virtually identical.

It can be seen from Figure 10.7 that the long term (6 year) morphology change predicted for scenario F mirrors the sediment transport patterns shown in Figure 10.5. Up to 4 m of erosion is predicted over the eastern side of the inlet, beyond the eastern edge of the 110 m wide channel. This large erosion is partially due to the shallow depths and relatively fine sediments that were assumed in this area. The sediment sizes in this area were based on sediment samples collected on the sand spit beach during field investigations, as discussed in 5.2. In addition, it should be kept in mind that the numerical model could not be fully calibrated in this area because the available hydrographic surveys did not extend over the eastern part of the inlet.

The model predicts a moderate amount of deposition within the 110 m wide navigation channel for scenario F. This deposition may be related to the slower ebb velocities being unable to flush out all the sediments deposited within the navigation channel during storms. Deposition patterns outside the inlet for scenario F are similar to those for existing conditions. Without a new longer east jetty to obstruct the NE to SW longshore sediment transport, some sediments arriving from the northeast are able to penetrate into the inlet, while others are able to settle within the inlet mouth and offshore of the inlet.

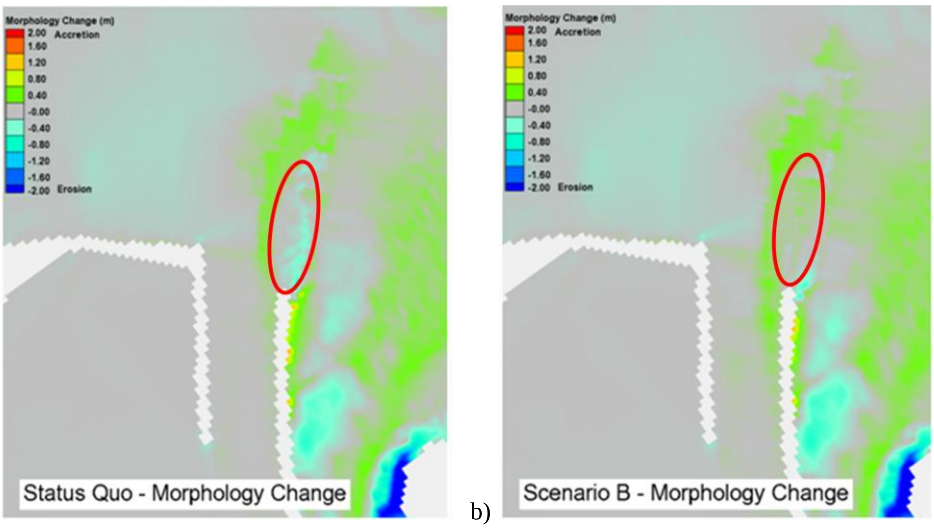

a) b)

Figure 10.6 – 6 year morphology change near the harbour entrance for: a) status quo and b) scenario B (red circle indicates area where deteriorated structure was removed).

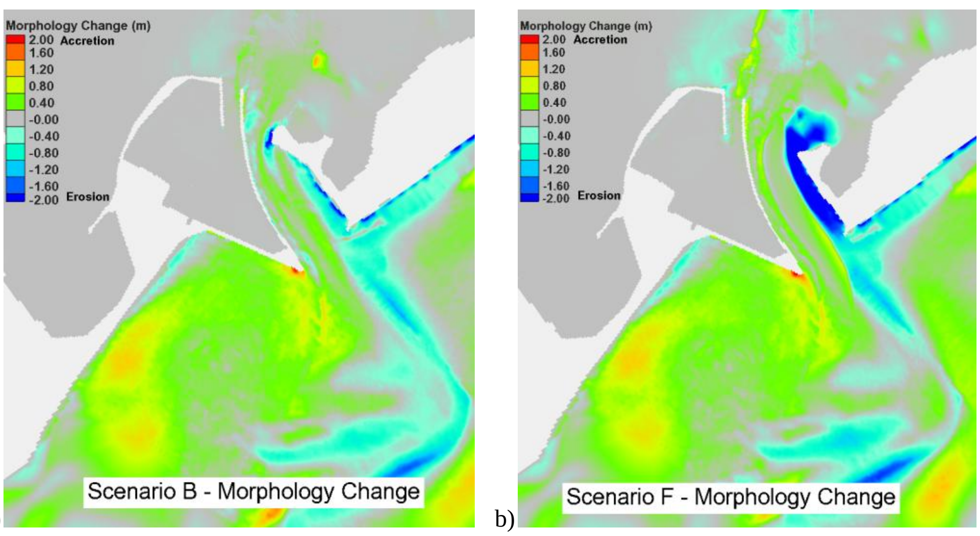

a) b)

Figure 10.7 – 6 year morphology change for: a) scenario B and b) scenario F.

10.2 Scenarios with 50m East Jetty (C1, C2, C3)

The main cause of deposition along the east side of the inlet is due to longshore sediment transport approaching from the northeast being deposited within the inlet, especially during storms. One way to lessen this deposition would be to construct a new, nearly shore parallel jetty on the east side of the inlet mouth. Such a jetty may trap longshore sediment transport flowing southwest along the coast, may deflect the sediment onto the ebb shoal, and will help shelter the inlet from storm waves approaching from easterly directions. Results for three scenarios, all featuring a 50 m long, nearly shore-parallel jetty located on the east side of the inlet mouth, are presented below. In these scenarios, the new jetty was positioned such that it aligned with the collapsed jetty that is currently on the east side of the inlet. A jetty in this orientation will shelter the east side of the inlet from easterly storm waves, while simultaneously reducing the width of the inlet entrance. The new jetty addition is 50 m long and reduces the width of the inlet entrance to 110 m. Three different scenarios were modelled with this jetty configuration:

- Scenario C1 (Figure 10.8a) – 50 m east jetty (vertical walls) with no change to the initial bathymetry;
- Scenario C2 (Figure 10.8b) - 50 m east jetty (vertical walls) + 110 m wide channel dredged to -4m, (as in Figure 7.2); and
- Scenario C3 (Figure 10.8c) - 50 m east jetty (vertical walls) + 110 m wide channel dredged to -4m with a 1:1.5 non-erodible revetment to +3 m along the eastern edge of the dredged channel (see Figure 7.3).

The initial bathymetries for each scenario are compared in Figure 10.8. Presented below is an analysis of the hydrodynamics, sediment transport patterns and morphology change predicted by the model for each of these scenarios, and how they compare to the status quo situation.

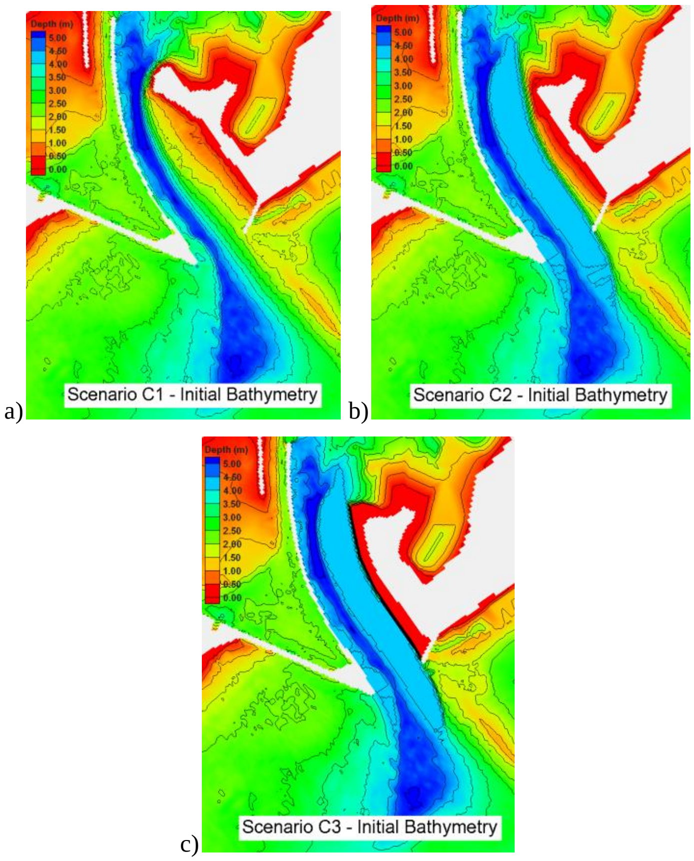

Figure 10.8 - Initial bathymetries for the three scenarios with shore-parallel jetties: a) scenario C1; b) scenario C2; and c) scenario C3.

10.2.1 Hydrodynamics

Presented in Figure 10.9 are the flow fields for each scenario during times with strong ebb and flood flows. Comparable results for existing conditions are presented in Figure 8.2. For scenario C1, the ebb flows are similar to existing conditions, while the flood flows are stronger near the inlet entrance due to the presence of the jetty, which partially constricts the flood flows. For scenarios C1 and C2, the new jetty causes a notable flow recirculation along the east side of the inlet. During ebb tide, the flow recirculates counter-clockwise, redirecting flow back towards the sand spit. This leads to velocities of 0.4 m/s, roughly double what occurs along the east side of the inlet in the status quo. An opposite situation occurs during flood tide, where the flow recirculation is clockwise, sending flow back towards the jetty. Unlike the ebb flow recirculation, the velocities within the recirculation zone during the flood flow are weaker in scenarios C1 and C2 in comparison to the status quo.

For scenario C2 (construction of a 110 m wide, 4m deep dredged channel), the ebb flows throughout most of the inlet are significantly weaker (~15%, 2.1 m/s reduced to 1.8 m/s) than for existing conditions and for scenario C1. This is due to the extensive dredging works modelled in scenario C2, which produce a channel that is wider and much less constricted. For scenario C2, the peak flows occur near the inlet entrance, in contrast to existing conditions, where the peak flows occur near the northern tip of the sand spit. Near the inlet entrance, the flood flows for scenario C2 are similar to those for scenario C1, but further inland, the flood flows are weaker for scenario C2 than for scenario C1. This can be attributed to the northeastern part of the sand spit being removed in scenario C2. The recirculation zone in the eastern part of the inlet is smaller for scenario C2 than for scenario C1. Without the sand spit sheltering the east side of the inlet, the ebb flow is no longer constricted and is able to travel along the entire width of the inlet. The result is a smaller recirculation zone on the lee side of the jetty, while the remainder of the inlet is subjected to a seaward flow.

The armoured revetment modelled in scenario C3 produces a relatively uniform flow field throughout the entire length of the inlet. The peak ebb velocity for scenario C3 is 1.8 m/s at the inlet mouth, identical to scenario C2. Overall, both the ebb and flood velocities through the inlet are weaker for scenario C3 than for the existing conditions. However, due to the presence of the non-erodible revetment restricting the inlet width, the peak velocities for scenario C3 are slightly higher than the peak velocities for scenario C2. The notable flow recirculations observed in scenarios C1 and C2 do not occur for scenario C3, due to the presence of the armoured revetment.

10.2.2 Sediment Transport Patterns

Figure 10.10 shows the time-averaged sediment transport patterns near the inlet for scenarios C1, C2 and C3. A comparable image for existing conditions can be seen in Figure 8.7. Compared to the status quo, scenario C1 shows a reduced amount of longshore sediment transport entering the east side of the inlet mouth. In scenario C1, the longshore sediment transport arriving from the NE splits into two pathways at the tip of the jetty. One pathway is directed into the inlet mouth, driving sediment into the east side of the inlet, while the second sediment pathway merges with sediment being carried offshore by the strong ebb jet.

The dredging in scenario C2 has significantly altered the sediment transport patterns seen in the status quo results. In the status quo (Figure 8.7), there are two main streams of net sediment transport within the inlet mouth. The first stream emerges from the west side of the inlet mouth and flows offshore. The second stream approaches the inlet from the NE, flows around the broken jetty, and enters the eastern part of the inlet. In contrast to this, the simulation results for scenario C2 indicate a single large sediment stream emerging from the inlet and flowing offshore. The substantial amount of sediment transport located offshore of the inlet in scenario C2 results from a combination of two sediment sources; longshore sediment transport produced by easterly waves and ebb flow driven sediment transport emerging from the central and eastern parts of the inlet. Once the longshore sediment transport reaches the inlet, it is redirected towards the tip of the jetty where it merges with sediment carried seaward by the ebb flow.

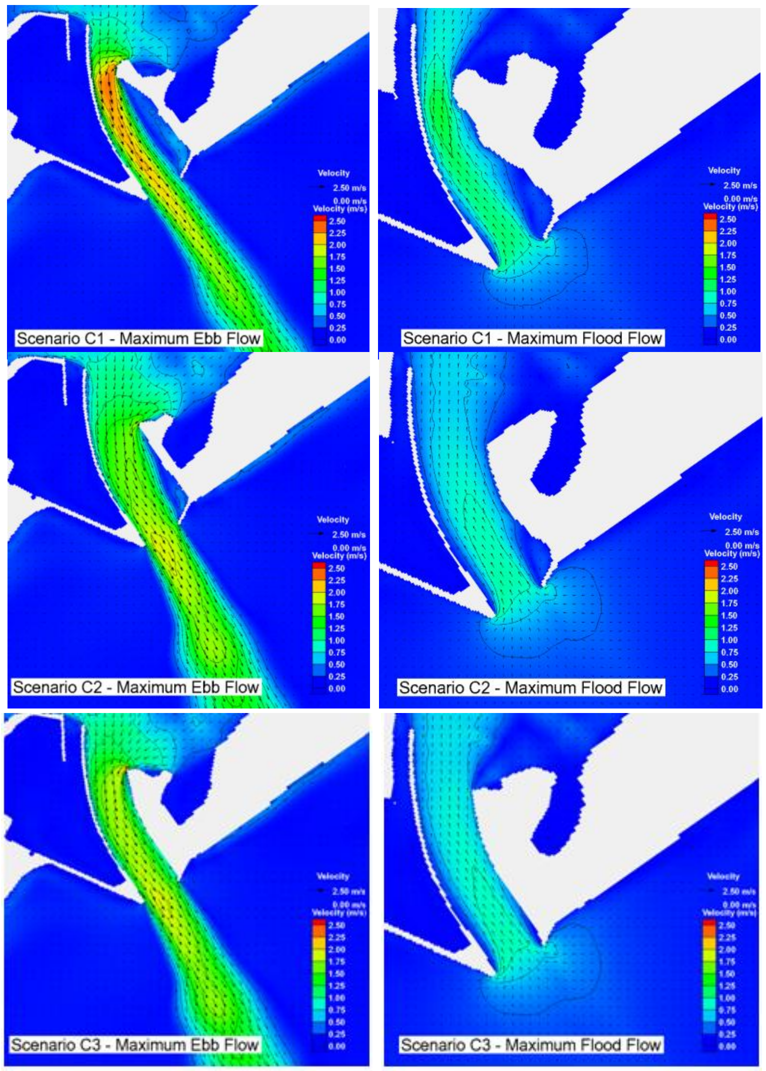

a)

b)

c)

Figure 10.9 – Velocity fields during strong ebb and flood tides for scenarios: a) C1; b) C2; and c) C3.

Similar to scenario C2, the results for scenario C3 show very little sediment entering the inlet from the south. The longshore sediment transport arriving from the northeast is deflected offshore by the jetty and carried offshore by the ebb jet. The constant inlet width of 110 m modelled in scenario C3 produces a more uniform ebb flow, which subsequently produces a more uniform net sediment transport compared to the status quo.

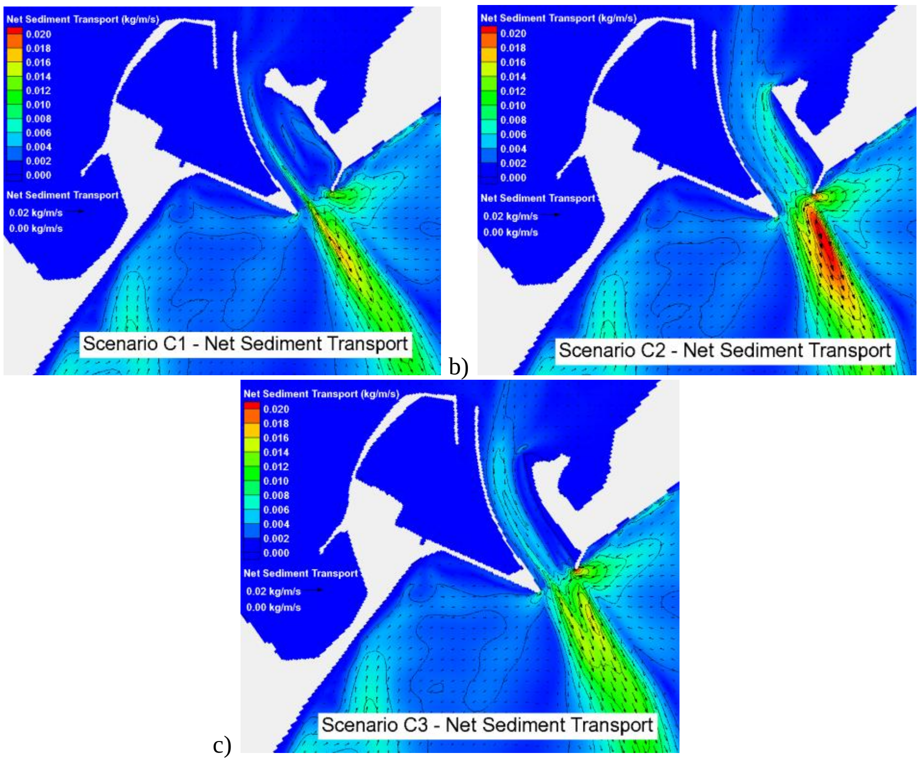

a) b) c)

Figure 10.10 - Time-averaged sediment transport flux for scenarios: a) C1; b) C2; and c) C3.

10.2.3 Morphology Change

The morphology change predictions for scenarios C1, C2 and C3 are compared in Figure 10.11. Comparable results for existing conditions can be seen in Figure 8.15. As noted previously, these predictions are uncertain and should be interpreted with caution. The numerical predictions show reduced amounts of deposition within the inlet for all three scenarios, compared to existing conditions. As discussed in the beginning of Section 10.2, a new east jetty helps prevent longshore sediment transport arriving from the northeast from entering the inlet. The jetty in scenario C1 (Figure 10.11a) allows only a fraction of this longshore sediment transport to enter the inlet; thereby reducing deposition along the east side of the inlet compared to results for existing conditions. The patterns of deposition within the inlet are similar for both the C1 and status quo scenarios.

Significant differences can be observed between the morphology changes for scenario C2 (Figure 10.11b), for scenario C1, and for existing conditions. In particular, for scenario C2, a large zone of erosion is predicted along the northern and western sides of the sand spit. This erosion is caused by the higher velocities along the east side of the inlet (discussed in Section 10.2.1) eroding the fine sediments in this area. This erosion is sensitive to the initial sediment grain size that was assumed along the east side of the inlet and the simulation results should be interpreted with this in mind. The deposition along the current navigation channel is greater for scenario C2 than for either scenario C1 or existing conditions. This increase in deposition can be attributed to the increased inlet width modelled in scenario C2 – the greater width leads to weaker ebb flows which are less able to flush out sediments deposited by occasional storms. The simulation results for scenario C2 indicate a zone of sediment deposition south of the jetty tip. As the longshore sediment transport is redirected along the jetty, some sediment is deposited along the eastern edge of the ebb jet. This deposition may represent a potential navigation hazard. Ideally, sediment arriving from the northeast should be either trapped behind the jetty or deflected offshore onto the ebb shoal, away from the navigation channel.

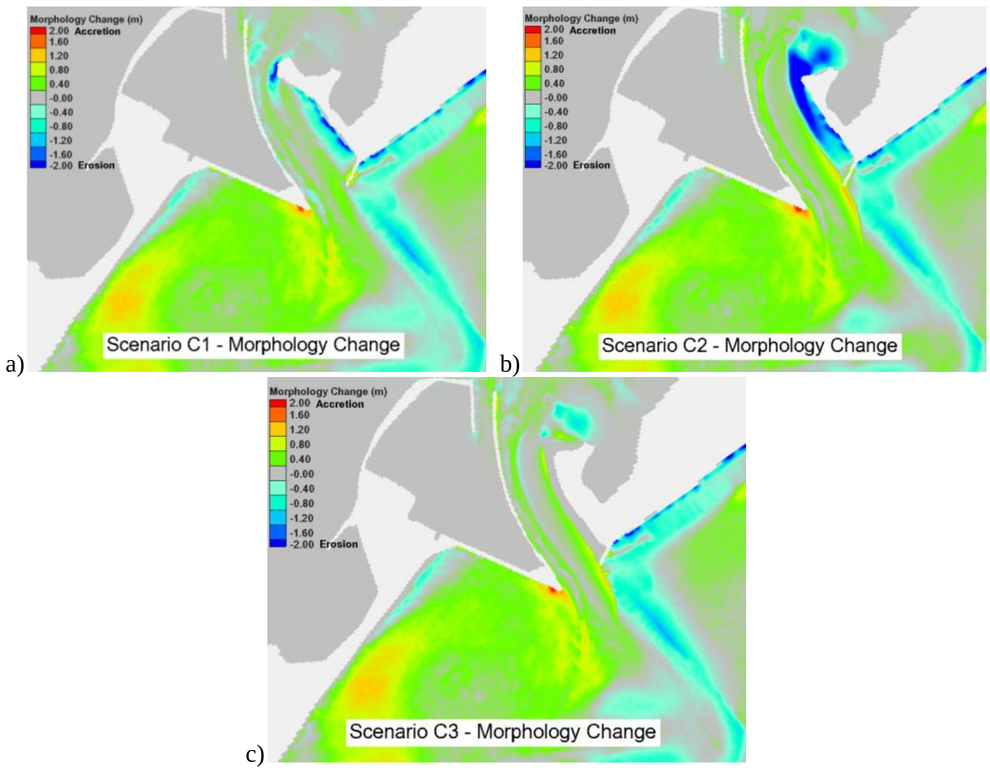

Figure 10.11 - 6 year morphology change for scenarios: a) C1; b) C2; and c) C3.

The introduction of a non-erodible revetment in scenario C3 (Figure 10.11c) appears to address some of the weaknesses of scenario C2. Within the channel in scenario C3, there are only two areas of moderate deposition; along the navigation channel (similar to the status quo) and along the toe of the revetment. The remainder of the inlet remains clear of deposition throughout the six year simulation. However, as in the case of scenario C2, a similar mound of deposition is predicted near the tip of the jetty for scenario C3. Ideally, rather than accumulating near the navigation channel, sediment arriving from the northeast should be either trapped behind the jetty or deflected offshore onto the ebb shoal, away from the navigation channel.

To aid in assessing these results further, the three cross-sections shown in Figure 10.12 have been defined, and the long-term morphology change along these three channel cross-sections have been calculated for each scenario. The morphology changes along these three cross-sections for scenarios B, C1, C2 and C3 are compared in Figure 10.13. In this figure, distance is referenced to the curved training wall on the west side of the inlet. Also, negative values indicate erosion and positive values indicate deposition. Along cross-section 1, scenarios C1 and C3 offer a reduction in deposition along the majority of the cross-section, compared to scenario B. The deposition for scenario C2 is greater than for scenario B in the zones between 20 m – 40 m and beyond 80 m. The increase in deposition beyond 80 m for scenarios C2 and C3 represents sediment accumulation in the eastern part of the 110m wide dredged channel. (The same 110m wide dredged channel is not included in scenarios B or C1.)

At cross-section 2, the patterns of erosion and deposition are similar for all four scenarios between 0m and 90 m. Between 15 m and 30 m, erosion is more pronounced for scenarios B and C1 than for scenarios C2 and C3. Beyond 90 m, deposition is predicted for scenarios C2 and C3, but not for scenarios B and C1. As at cross section 1, the increase in deposition beyond 90 m for scenarios C2 and C3 represents sediment accumulation in the eastern part of the 110m wide dredged channel.

Over most of cross-section 3, the deposition for scenario C2 is equal to or less than the deposition for scenario B. On the other hand, the patterns of morphology change for scenarios C1 and C3 are, for the most part, similar to the pattern for scenario B. Between 15 m and 30 m, increased deposition is predicted for scenarios C2 and C3 compared with the status quo.

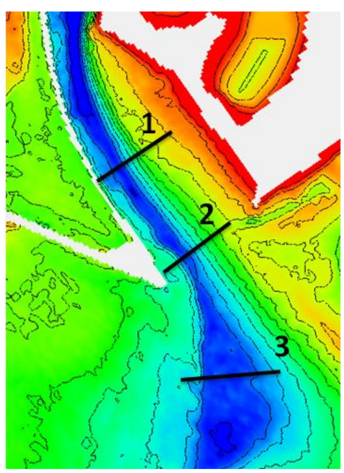

Figure 10.12 - Location of three channel cross-sections defined to help assess morphology change.

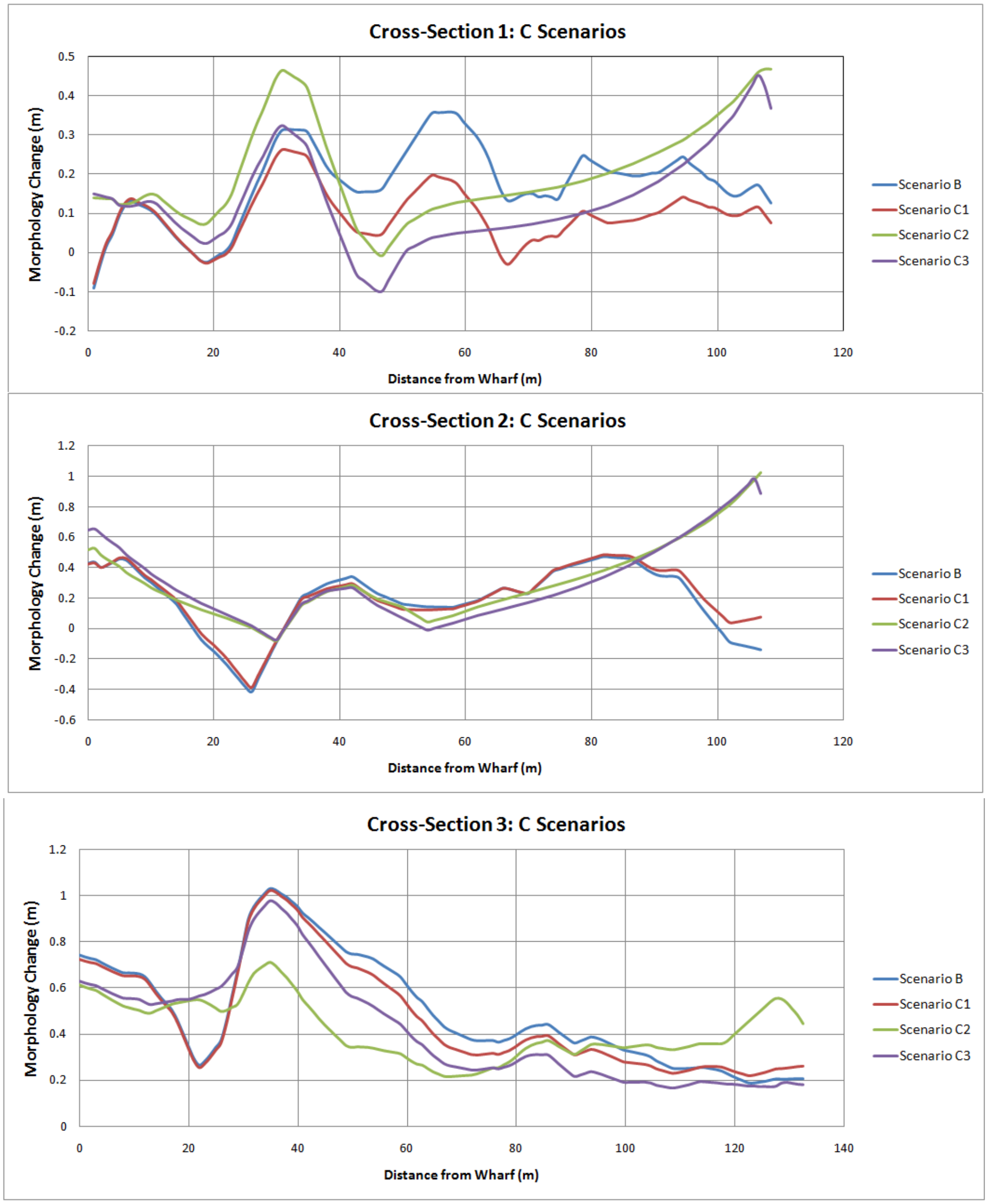

Figure 10.13 - Morphology change along 3 channel cross-sections for scenarios B, C1, C2 and C3.

10.3 Scenarios with 110m Wide Channel + Curved East Jetties (E1, E2a, E2b, E3, E4)

Simulation results for five scenarios which all include new curved or "dog-leg" jetties located on the east side of the inlet mouth are presented and discussed in this section. All five scenarios also include a 110 m wide channel through the inlet dredged to -4 m depth. The curved jetty length varies from 100 m to 200 m. The layouts and initial bathymetries for each of these scenarios are compared in Figure 10.14. The five scenarios are:

- Scenario E1 - 150 m curved jetty (vertical walls) with initial bathymetry similar to scenario F (110m wide channel dredged to -4 m);
- Scenarios E2a - 150 m curved jetty (vertical walls) + 110 m wide channel dredged to -4 m + non-erodible revetment to +3 m along the eastern edge of the dredged channel;
- Scenario E2b – 150 m curved rubble-mound jetty + 110 m wide channel dredged to -4 m + non-erodible revetment to +3 m along the eastern edge of the dredged channel;
- Scenario E3 - 200 m curved jetty (vertical walls) + 110 m wide channel dredged to -4 m + non-erodible revetment to +3 m along the eastern edge of the dredged channel; and
- Scenario E4 - 100 m curved jetty (vertical walls) + 110 m wide channel dredged to -4 m + non-erodible revetment to +3 m along the eastern edge of the dredged channel.

10.3.1 Hydrodynamics

The flow fields during strong ebb and flood tides for scenarios E1 – E4 are presented in Figure 10.15 and Figure 10.16. Equivalent images for existing conditions are presented in Figure 8.2. For each of these scenarios, the peak ebb and flood velocities are reduced compared to existing conditions. This reduction is due in large part to the fact that the 110 m wide channel dredged to -4 m depth significantly increases the cross-sectional area of the flow channel passing through the inlet. Due to this increase in cross-sectional area, the same discharge is conveyed with lower velocity. The ebb flow field for scenario E1 is similar to that for scenario C2 (Figure 10.9b), where the maximum ebb currents are weaker than for existing conditions, and occur in a different location. This similarity is to be expected since the only difference between scenarios C2 and E1 is the shore-perpendicular extension to the east jetty. The jetty extension deflects the ebb jet slightly towards the west outside the inlet, but otherwise has little influence on the ebb flows. The jetty extension also modifies the flood flows at the inlet mouth, but has little influence on flood flows deeper within the inlet.

For scenario E1, as for scenario C2, during both ebb and flood flows, a zone of relatively still water occurs within the inlet, within the small bay formed west and northwest from the root of the east jetty. Weak eddies are formed in this small bay during both ebb and flood flows. The small bay and the weak eddies are no longer present in scenarios E2-E4.

Scenarios E2a, E2b, E3 and E4 are all similar to each other and to scenario C3, the main difference being the length of the shore-perpendicular portion of the east jetty. The longer jetties (i.e. scenario E3) tend to deflect the ebb jet further to the west outside the inlet than do the shorter jetties (i.e. scenarios C3 and E4). The longer jetties also cause the flood flow to enter the inlet from the SSW direction, instead of from the SE direction, which is the present situation. For existing conditions, seawater entering the inlet during flood tide flows in a northwesterly direction. However, with a longer east jetty, seawater enters the inlet flowing in a more north-northeasterly direction. The flood flows then turn towards the north-northwest within the inlet to follow the curved channel leading to the lagoon. This change in flow direction shifts the maximum flood velocities towards the east side of the inlet compared to the status quo and scenarios without a shore-perpendicular jetty extension (i.e. scenarios C1, C2 and C3). For scenarios E1 – E4, during flood flows, a low velocity zone can be observed near the existing curved wharf. The low velocity zone is largest near the inlet mouth and tapers towards the north. This low velocity zone is caused by flow separation at the southern apex of the curved wharf.

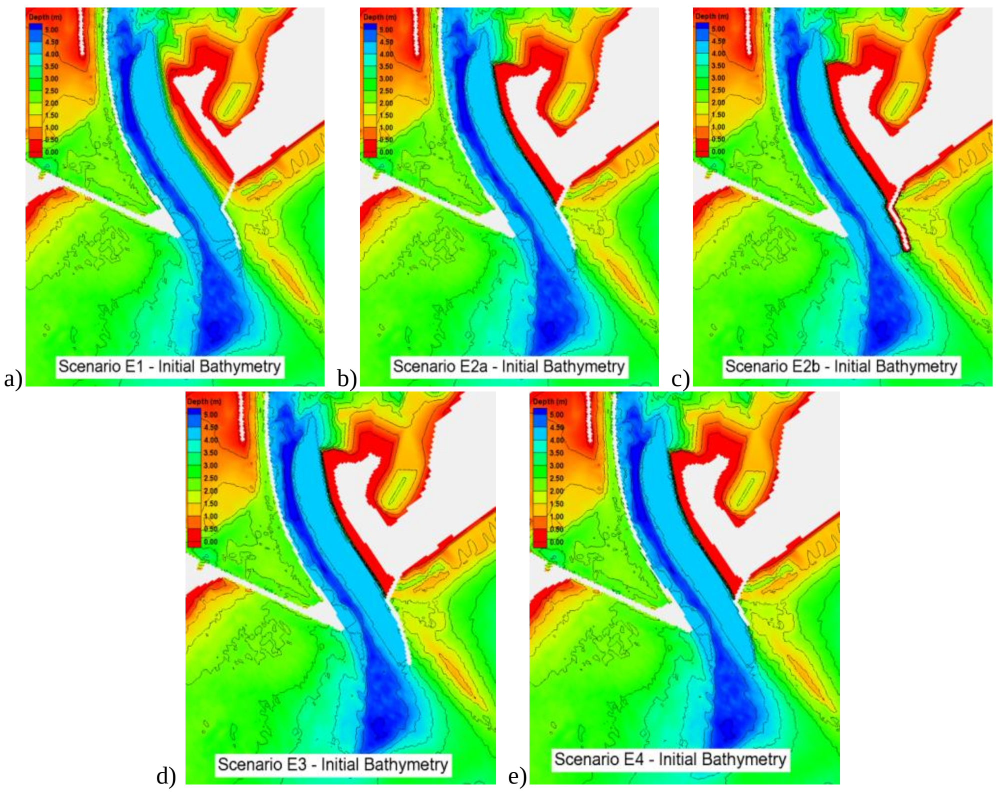

Figure 10.14 - Initial bathymetries for five scenarios with 110 m wide channels dredged to -4 m and curved east jetties: a) scenario E1, b) scenario E2a, c) scenario E2b, d) scenario E3 and e) scenario E4.

a)

b)

c)

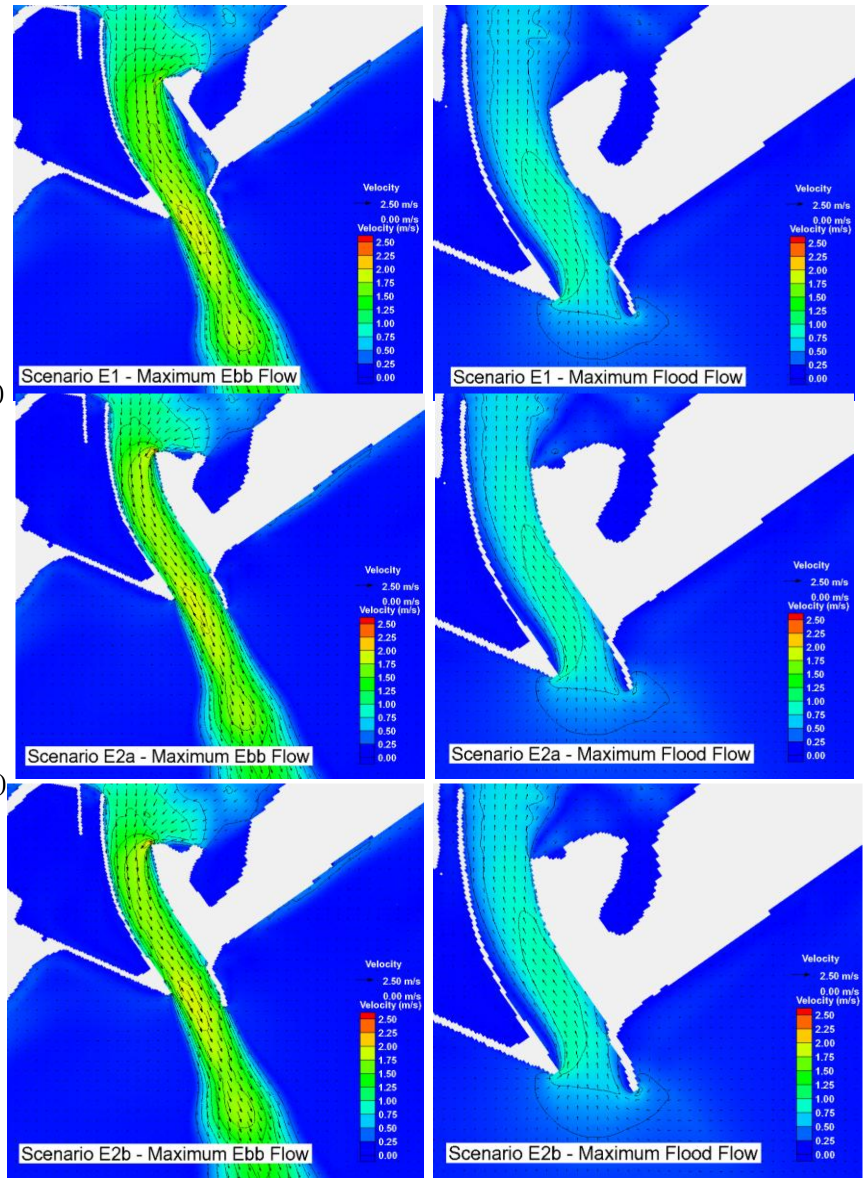

Figure 10.15 - Flow fields during strong ebb and flood tides for scenarios: a) E1, b) E2a and c) E2b.

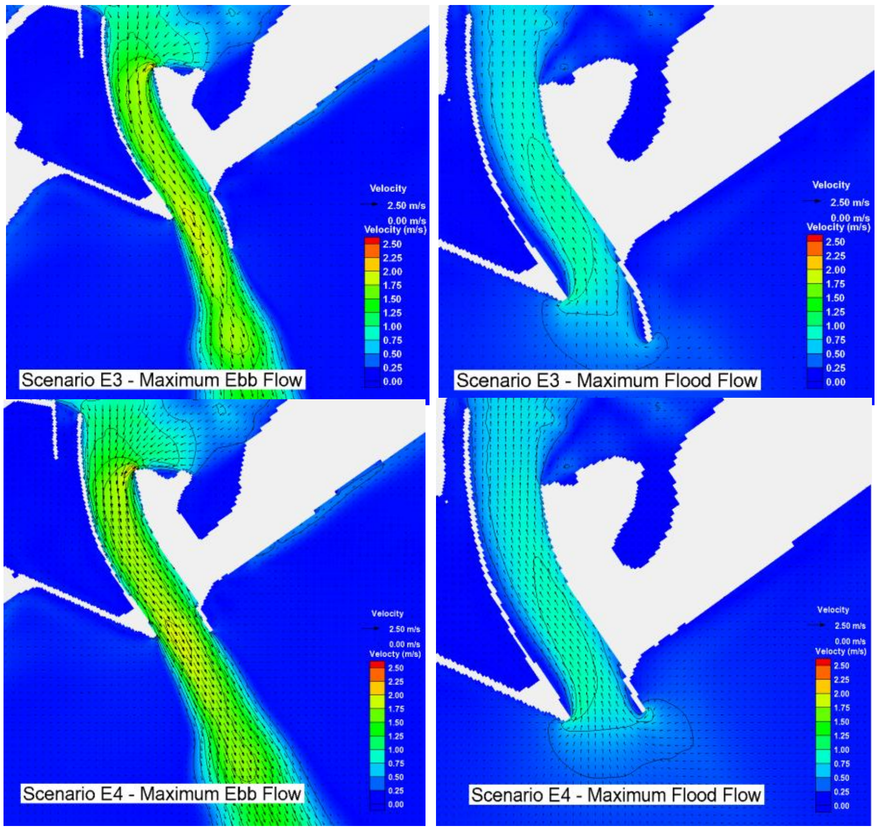

a)

b)

Figure 10.16 – Flow fields during strong ebb and flood tides for scenarios: a) E3 and b) E4.

10.3.2 Sediment Transport Patterns

The time-averaged sediment flux derived from the long-term (6 year) numerical simulations of coastal processes for scenarios E1-E4 are presented in Figure 10.17. The time-averaged sediment flux for existing conditions is mapped in Figure 8.7. In the status quo scenario, on average sediments flowed into the eastern part of the inlet mouth and flowed out of the western part of the inlet mouth. Unlike the status quo situation, no time-averaged sediment flux entering the inlet is predicted for scenarios E1-E4. Instead, results for all five scenarios show a net sediment transport exiting the inlet at all locations across the inlet mouth. These results suggest that the curved jetties modelled in these scenarios are able to trap and/or divert the sediments arriving from the northeast, preventing these sediments from entering the inlet. The curved jetties serve as an effective barrier to the longshore sediment transport.

For scenario E1, the net sediment transport rate is largest outside the inlet south from the tip of the east jetty. Here, the longshore sediment transport arriving from the northeast merges with sediment emerging from the inlet and is propelled seaward by the ebb flows emerging from the inlet. The governing sediment transport processes are similar for scenarios E2 – E4.

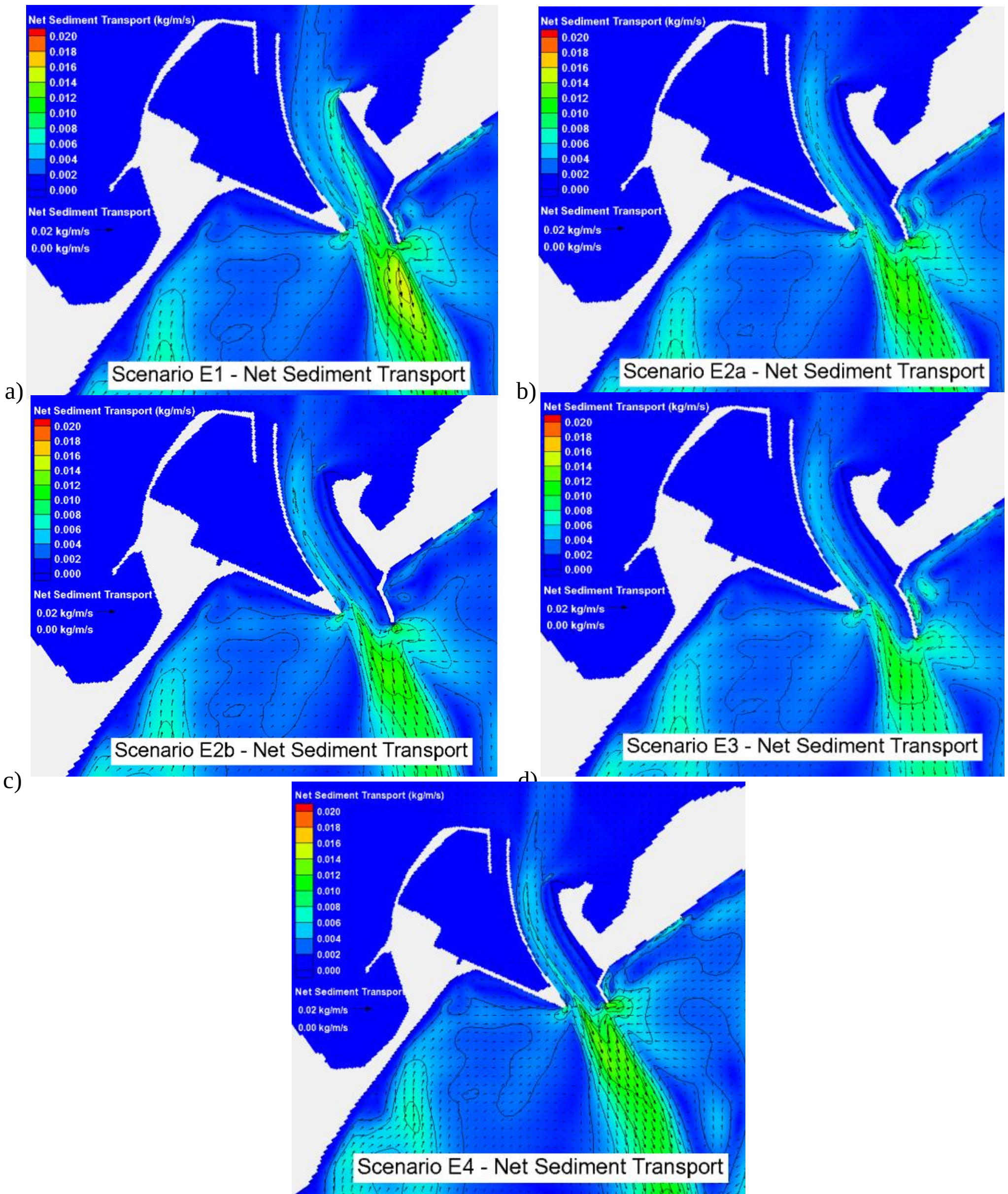

Figure 10.17 - Time-averaged sediment transport flux for scenarios: a) E1; b) E2a; c) E2b; d) E3; and e) E4.

The results for scenarios E2a (Figure 10.17b), E2b (Figure 10.17c) and E3 (Figure 10.17d) and E4 (Figure 10.17e) all reveal similar patterns of time-averaged sediment transport flux. Within the inlet, the majority of the net sediment transport occurs along the western side of the inlet (with a similar magnitude as the status quo) and little net sediment transport occurs on the eastern side. Offshore of the inlet, the jetties re-redirect the longshore sediment transport away from the inlet mouth until it merges with the sediment being transported seaward by the ebb flows emerging from the inlet mouth. The longer jetty modelled in scenario E3 traps more of the longshore sediment transport than the shorter jetties modelled in the other scenarios, leading to a smaller net sediment transport travelling seaward.

10.3.3 Morphology Change

Morphology change maps derived from the long-term (6 year) simulations of coastal processes for scenarios E1-E4 are shown in Figure 10.18. The morphology change map for existing conditions is shown in Figure . As noted previously, the numerical model's predictions of morphology change are uncertain and these results should therefore be interpreted with caution.

The amount of deposition within the inlet is less for scenarios E1-E4 than for the status quo situation. The results shown in (Figure 10.18a) for scenario E1 are very similar to the results for scenario C2 shown in Figure 10.11, with deposition occurring in the deepest part of the current navigation channel and along the east side of the inlet mouth. However, the curved jetty modelled in scenario E1 redirects the longshore sediment transport arriving along the coast from the northeast and shelters the inlet from easterly storm waves. The curved jetty reduces deposition within the inlet mouth, and helps prevent sediment from settling in the navigation channel. A moderately-sized mound of deposition (0.5 m high) is observed near the tip of the curved jetty, which is a result of longshore sediment transport travelling along the jetty and being deposited near the jetty tip.

Deposition within the inlet is even less for scenarios E2a (Figure 10.18b) and E2b (Figure 10.18c) than for scenario E1. A 7 m high (-4 m to +3 m) non-erodible revetment running the full length of the inlet was modelled in these two scenarios (as in scenarios E3 and E4). The toe of the new revetment is offset 110 m from the existing wharf. This revetment reduces the inlet width (compared to scenario E1) which in turn increases velocities within the inlet (as seen in Figure 10.16c). The stronger ebb flows are able to flush away more of the sediments deposited in the channel during storms. Within the inlet mouth and further offshore of the inlet, the morphology change patterns for scenarios E2a and E2b are similar to the results for scenario E1. All three of the scenarios with 150m curved jetties show improvement over the status quo situation.

Although the differences in morphology change between scenarios E2a, E3 and E4 are small, the degree of improvement within the inlet appears to be proportional to the east jetty length, with slightly less deposition within the inlet for the longer 200 m jetty (scenario E3) and slightly more deposition within the inlet for the shorter 100 m jetty (scenario E4). However, increased deposition is observed near the jetty tip for the longer jetty, while decreased deposition is observed near the jetty tip for the shorter jetty. These results suggest that increasing the east jetty length may help to reduce deposition within the inlet slightly, but may also increase deposition near the jetty tip. The curved east jetties modelled in these scenarios help to protect the inlet mouth from wave-driven sediment transport arriving along the coast from the northeast. However, the presence of a longer east jetty may also make it more difficult for ships to enter the inlet in certain conditions.

Comment [P8]: Alain removed this sentence, no reason was given.

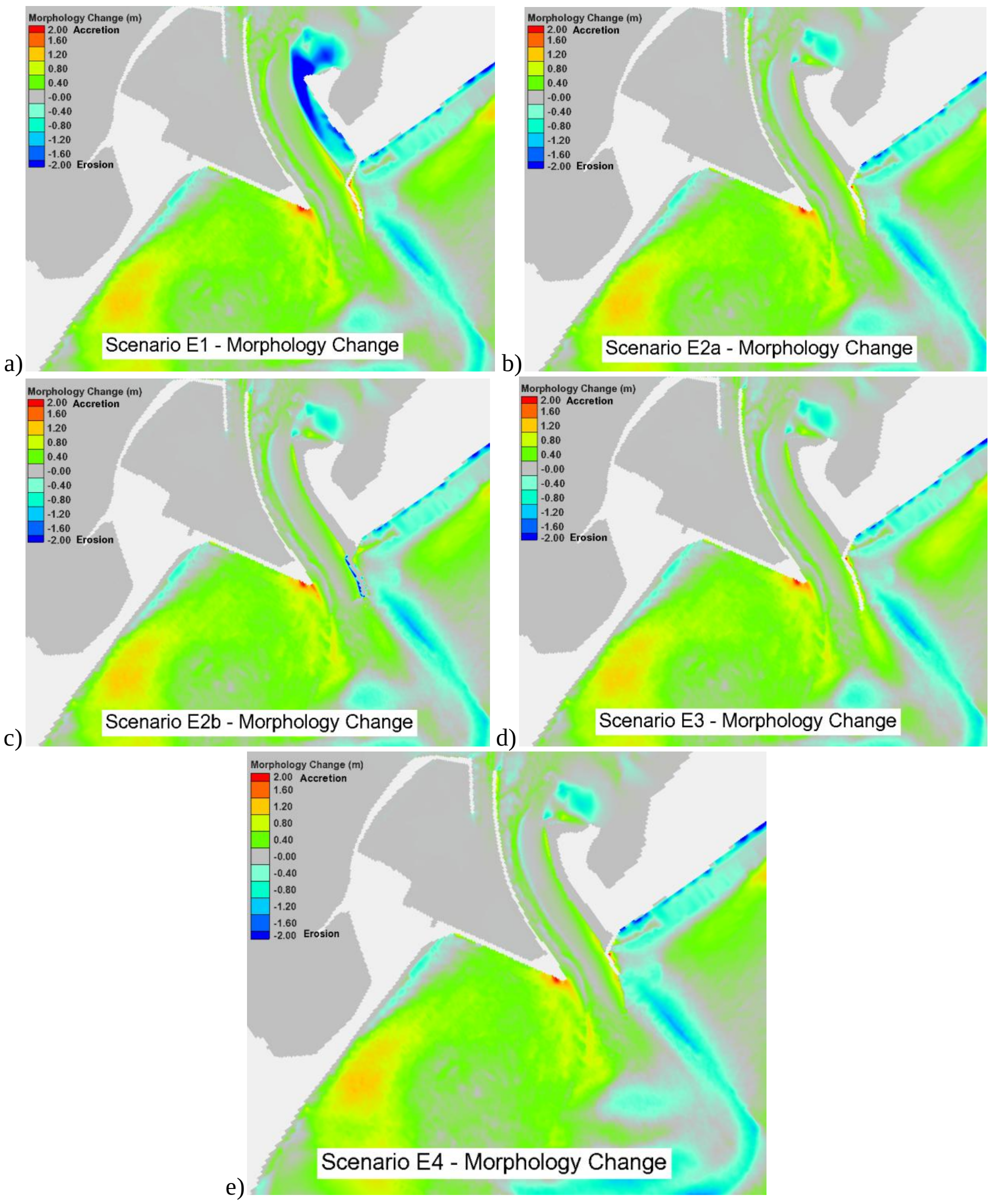

Figure 10.18 - 6 year morphology change for scenarios: a) E1; b) E2a; c) E2b; d) E3; and e) E4.

The morphology change results for scenarios E1-E4 along the three cross-sections shown in Figure 10.12 are plotted in Figure 10.19. The morphology change results for scenario B are also included for reference. Along cross-section 1, a similar pattern of deposition and erosion with horizontal distance can be seen for scenarios E1-E4; however, beyond the 30 m mark, the deposition for scenario E1 is ~10cm larger than for the other scenarios with curved jetties. The deposition between the 25 m and 45 m stations is attributable to sediment settling in the deepest part of the current navigation channel (where depths exceed -5 m), and this deposition should not endanger safe navigation. For scenarios E2a-E4, the amount of deposition over most of cross-section 1 is generally slightly less than for the status quo situation (scenario B).

At cross-section 2, the morphology changes for scenarios E1-E4 are all similar to each other and are also similar to those for scenario B. The main differences being reduced erosion between 15 m and 30 m, and increased deposition beyond the 95 m mark.

At cross-section 3, between 20 m and 90 m, the deposition for scenarios E1-E4 is less than for the status quo situation (scenario B). The reduction in deposition is generally greatest for scenario E3 (200 m curved jetty) and least for scenario E4 (100 m curved jetty). From 0 m to 20 m, deposition is greatest for scenario E2b, while the other scenarios give similar results. Beyond 100 m, deposition for scenarios E1-E3 is greater than for scenarios B and E4. The deposition increase near 120 m is greatest for scenario E3 (~0.7 m). The increased deposition beyond 100 m reflects the increased deposition that occurs near the tip of curved jetties, as seen in Figure 10.18.

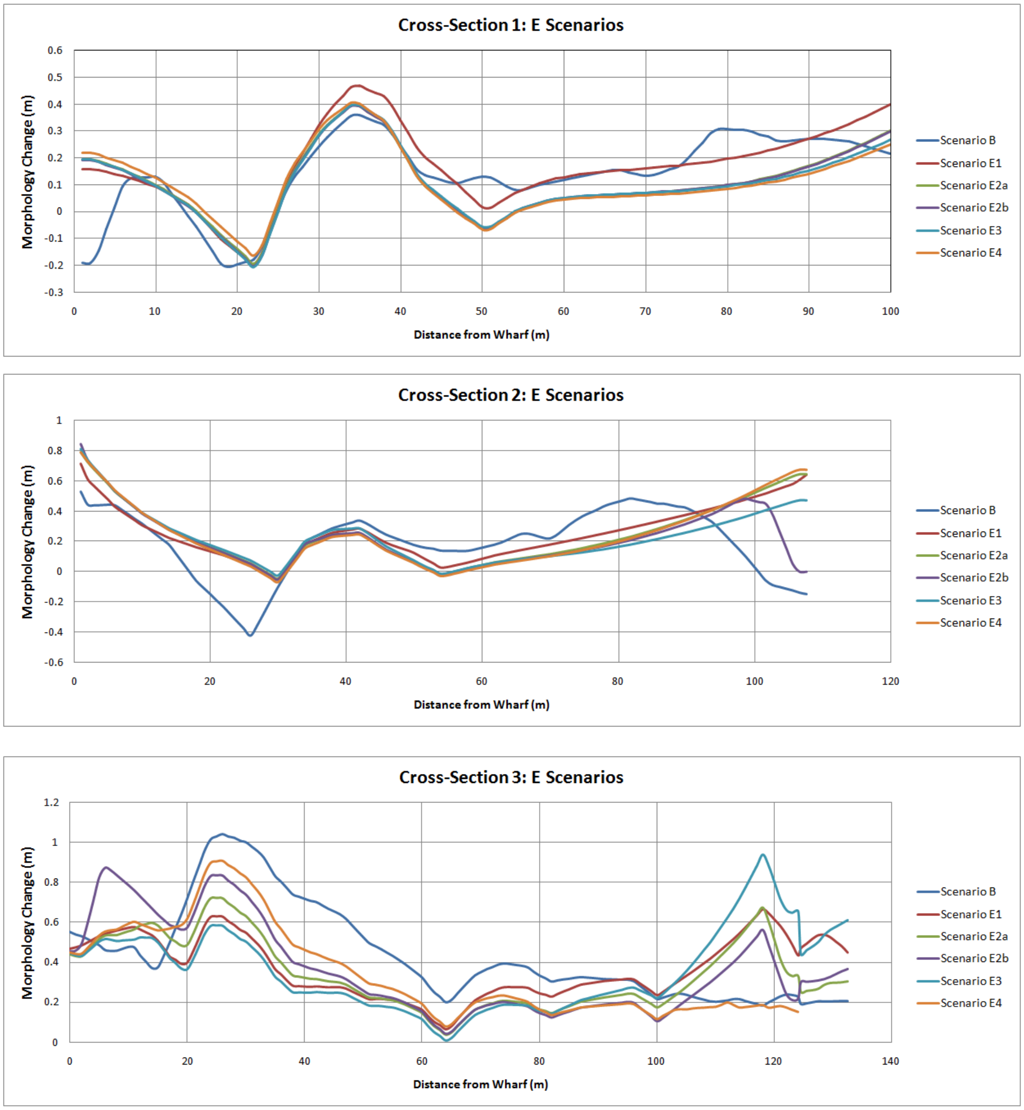

Figure 10.19 - Morphology change along 3 channel cross-sections for scenarios B, E1, E2a, E2b, E3 and E4.

10.4 Scenarios with Dredging and a New Training Wall (D1 - D7)

Seven scenarios that included a 360 m long solid vertical training wall located on the east side of the inlet, aligned either parallel to, or nearly parallel to the existing wharf structure, were modelled. The new vertical wall extended from the inlet entrance to the northern tip of the sand spit, and the horizontal distance between the wharf and the new training wall varied from 80 m to 110 m. The extent of the dredging work between the wharf and the new training wall was also varied. In all scenarios, it was assumed that the area to the east of the new training wall was backfilled to an elevation above +3 m. For five of the seven scenarios, a 150 m long curved jetty with vertical walls extending offshore was assumed at the southern end of the new training wall, whereas a 50 m shore-parallel jetty was assumed for the other two scenarios. The layouts and initial bathymetries for each of these scenarios are compared in Figure 10.20 and in Figure 7.6. The seven scenarios are:

- Scenario D1 (Figure 10.20a) – 360 m long curved training wall on east side of inlet, 110 m channel width at inlet mouth gradually reducing to 80 m width at lagoon entrance, 50 m shore-parallel jetty, dredging to -4 m.
- Scenario D2 (Figure 10.20b) - same as scenario D1 but with dredging to -3 m.
- Scenario D3 (Figure 10.20c) - same as scenario D2 but combined with a 150 m long curved east jetty.
- Scenario D4 (Figure 10.20d) - same as scenario D3, but with 100 m width at inlet mouth (instead of 110 m).
- Scenario D5 (Figure 10.20e) - 360 m long curved training wall on east side of inlet combined with a 150 m long curved east jetty, 110 m wide channel through inlet dredged to -4 m.
- Scenario D6 (Figure 10.20f) - same as scenario D3, but with dredging to -4 m.
- Scenario D7 (Figure 10.20g) - same as scenario D4, but with dredging to -4 m.

A brief analysis and comparison of the hydrodynamics, net sediment transport patterns and morphology changes for these seven scenarios is presented below.

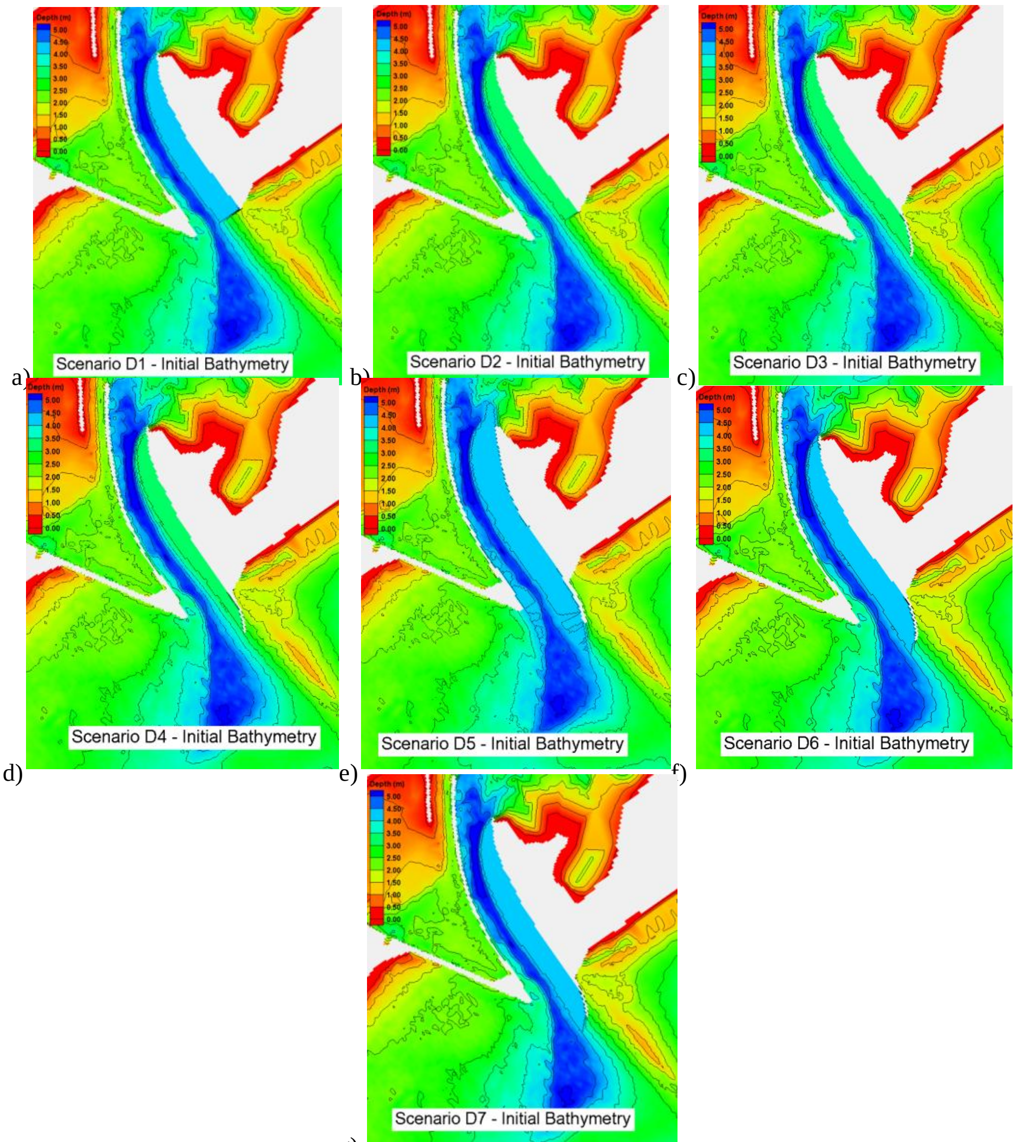

Figure 10.20 - Initial bathymetries for seven scenarios with a 360 m long curved training wall: a) scenario D1, b) scenario D2, c) scenario D3, d) scenario D4, e) scenario D5, f) scenario D6 and g) scenario D7.

10.4.1 Hydrodynamics

The flow fields during strong ebb and flood tides for scenarios D1 – D7 are presented in Figure 10.21 and Figure 10.22. Equivalent images for existing conditions are presented in Figure 8.2. The model results show that all seven training wall scenarios provide reduced velocities within the inlet during the ebb and flood flows. This is attributed to the increased cross-sectional area of the flow channel, which allows the same discharge to be conveyed with lower velocity. Compared to existing conditions, the ebb flows in particular are more evenly distributed across the channel width, including at the inlet mouth. The peak velocities for scenarios D1-D4, D6 and D7 are all similar at ~2.0 m/s during ebb flow (compared to 2.2 m/s in the status quo) and ~0.9 m/s during flood flow (compared to 1.1 m/s in the status quo). Due to the wider inlet width modelled in scenario D5 (Figure 10.22b), the peak ebb velocities for this scenario decrease to ~1.8 m/s, while the peak flood velocities decrease do not exceed 0.8 m/s.

The 150 m long curved east jetties modelled in scenarios D3-D7 are responsible for a similar redirection of the flood flow at the inlet mouth as was observed in the results for scenarios E1-E4. The flood flows approach the inlet mouth from the south-southwest, and turn within the inlet to follow the curved channel leading to the lagoon. As for scenarios E1-E4, during flood tides, a flow separation occurs at the southern apex of the existing wharf, and a zone of low-velocity flow prevails within the inlet along the southern portion of the curved wharf. The peak velocities during flood flows occur in the western part of the inlet near the new training wall, but the peak flood velocities are only roughly half the speed of the peak ebb velocities. As for scenarios E1-E4, the curved east jetties modelled in scenarios D3-D7 deflect the ebb jet slightly towards the west outside the inlet. For scenarios D1 and D2, which do not include a shore-perpendicular east jetty, the flood flows approach the inlet mouth mainly from the southeast, the flow separation zones on either side of the inlet mouth are small, and the highest flood velocities (~0.9 m/s) occur near the centre of the channel, midway between the existing wharf and the new training wall.

Like the non-erodible revetment modelled in scenarios E2-E4, the vertical training wall modelled in scenarios D1-D7 eliminates the large zone of re-circulating flow that forms along the eastern part of the inlet during ebb flows for existing conditions (see Figure). This recirculation develops for existing conditions because the northwestern part of the sand spit constricts the flow entering the inlet from the lagoon and forces it towards the west side of the inlet near the curved wharf. The recirculation on the eastern side of the inlet can be avoided by cutting back the sand-spit to remove the flow constriction at the northern end of the inlet. The northeastern part of the sand spit is removed for scenarios C2, C3, D1-D7, E1-E3, H1b and F, hence the large ebb recirculation is reduced or eliminated for all of these scenarios.

Overall, the model results indicate that all seven training wall scenarios will benefit navigation through the inlet due to the decrease in ebb and flood velocities. However, the presence of a second training wall along the east side of the inlet too close to the existing training wall, may also increase the risk of collision in certain conditions.

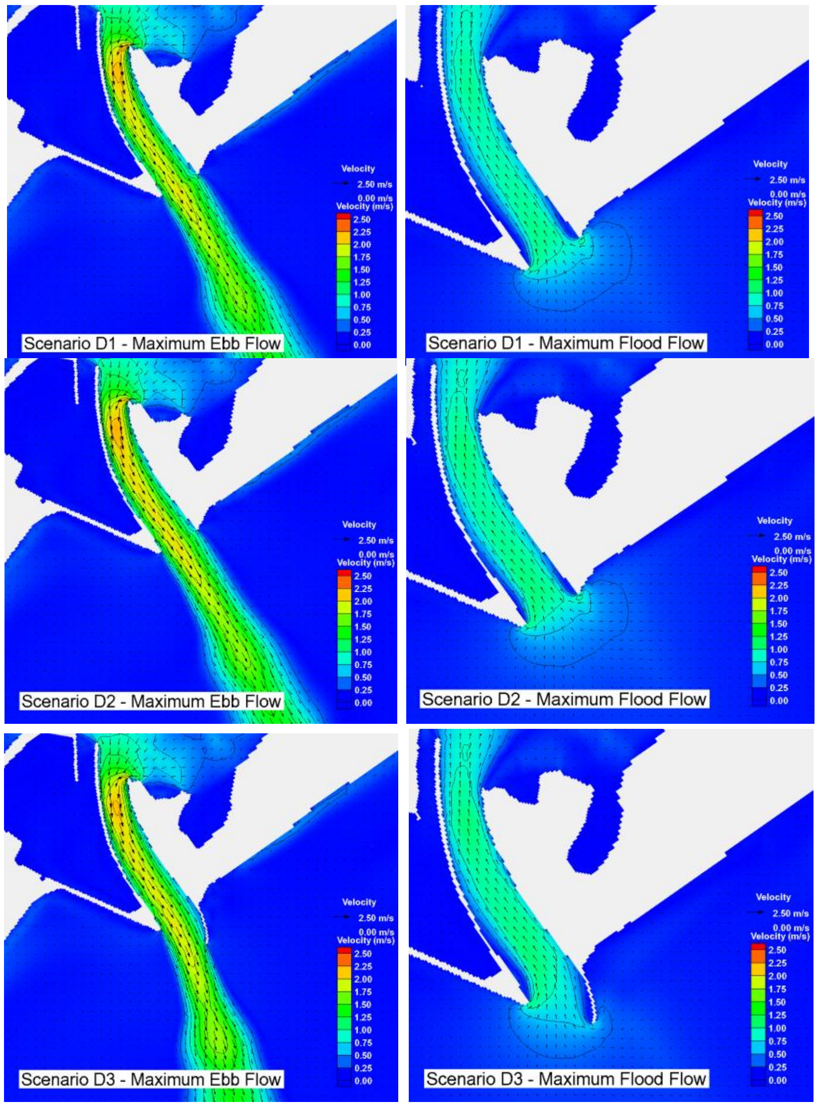

a)
b)
c)

Figure 10.21 - Flow fields during strong ebb and flood tides for scenarios: a) D1; b) D2; and c) D3.

a)
b)
c)
d)
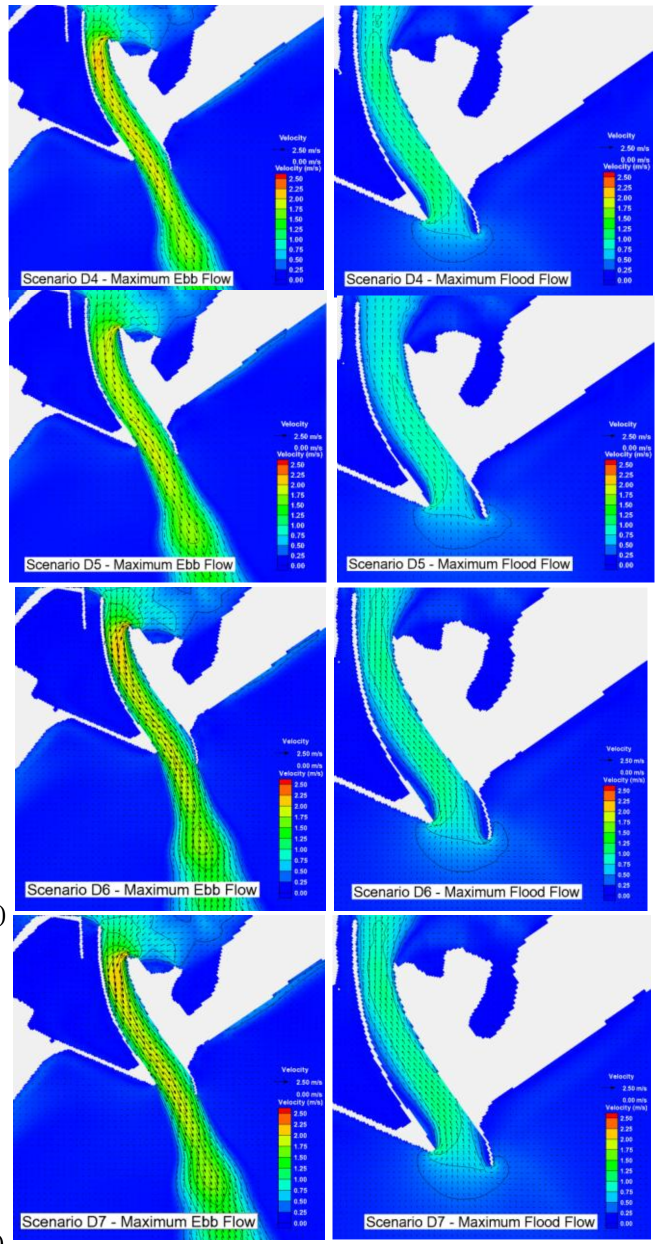

Figure 10.22 – Flow fields during strong ebb and flood tides for scenarios: a) D4; b) D5; c) D6; and d) D7.

10.4.2 Sediment Transport Patterns

The time-averaged sediment flux derived from the long-term (6 year) numerical simulations of coastal processes for scenarios D1-D7 are presented in Figure 10.23 and Figure 10.24. The time-averaged sediment flux for existing conditions is mapped in Figure 8.7.

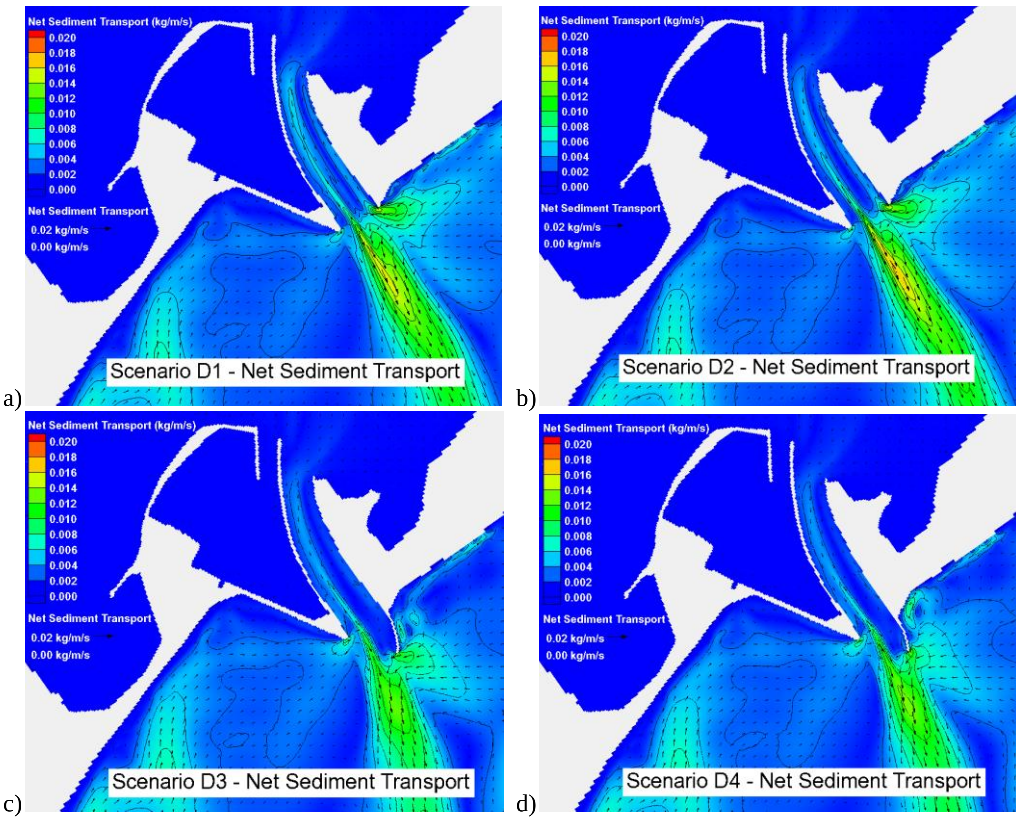

Figure 10.23 - Time-averaged sediment flux for scenarios: a) D1; b) D2; c) D3; and d) D4.

As in the status quo situation, the results for scenarios D1 (Figure 10.23a) and D2 (Figure 10.23b) show two main sediment transport pathways at the inlet mouth. The first pathway consists of sediment exiting the inlet on the west of the inlet mouth, while the second pathway consists of sediment entering the eastern side of the inlet mouth. Without an extended shore-perpendicular east jetty, some of the longshore sediment transport arriving from the northeast is able to flow around the tip of the 50 m long shore-parallel jetty and enter the east side of the inlet. This issue is resolved in scenarios D3 – D7 by extending the 50 m jetty seaward by 100 m (150 m east jetty length). This longer east jetty traps some of the longshore sediment transport and redirects some of it away from the inlet mouth. A similar process was observed for the other scenarios with curved east jetties (i.e. scenarios E1-E4).

The model results for scenarios with a 360 m long training wall combined with a 150 m curved east jetty (scenarios D3 - D7) indicate a single sediment transport pathway flowing south on the western side of the inlet mouth. The eastern pathway flowing into the inlet has been blocked by the longer east jetties. Overall, all seven scenarios with 360 m long vertical training walls produce reduce the time-averaged sediment flux within the inlet (compared to the status quo situation) and the five scenarios that include a 150 m long curved east jetty effectively prevent sediments from entering the east side of the inlet.

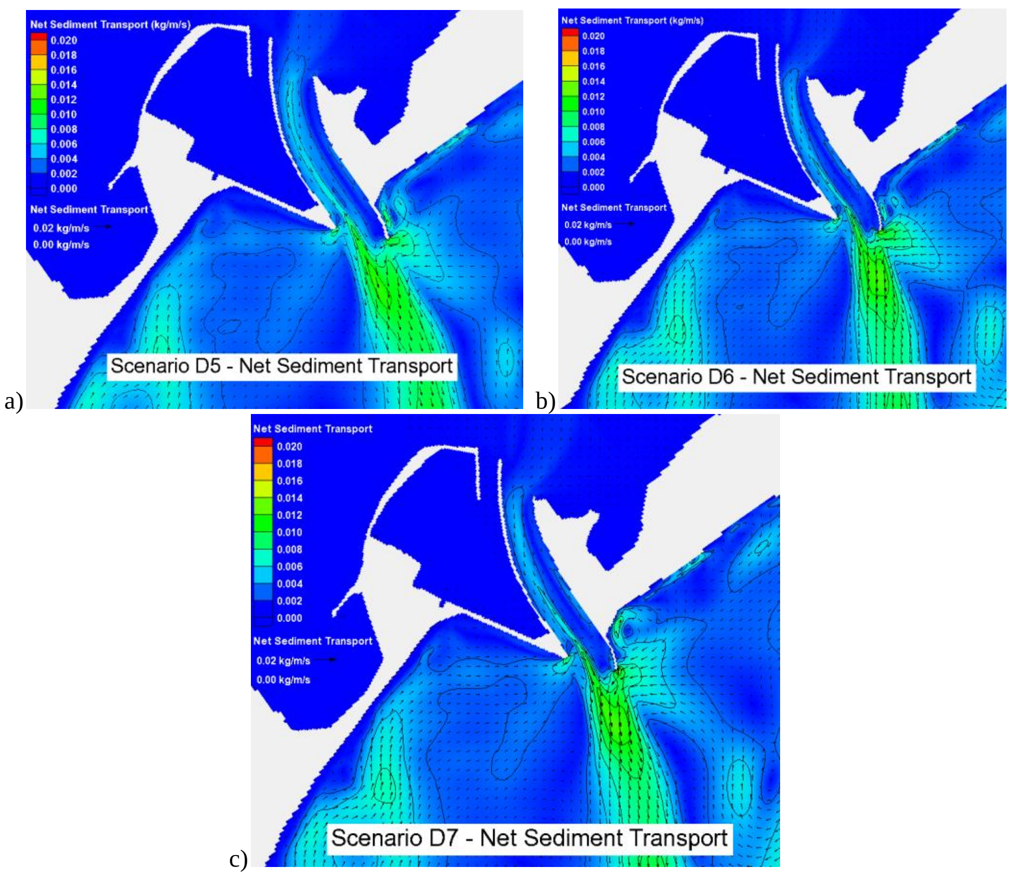

Figure 10.24 - Time-averaged sediment flux for scenarios: a) D5; b) D6; and c) D7.

10.4.3 Morphology Change

Morphology change maps derived from the long-term (6 year) simulations of coastal processes for scenarios D1-D7 are shown in Figure 10.25 and Figure 10.26, while comparable results for existing conditions can be seen in Figure 8.15. As noted previously, these predictions are uncertain and should therefore be interpreted with caution.

Results for scenarios D1 (Figure a) and D2 (Figure 10.25b) indicate large amounts of deposition (up to 2 m) along the east side of the inlet mouth near the southern limit of the dredging. The deposition in both scenarios is likely a result of longshore sediment transport entering the east side of the inlet and settling in the southeast corner of the dredged area. The remainder of the inlet remains relatively clear of deposition, aside from small patches of deposition along the navigation channel. Offshore of the inlet, the deposition patterns for scenarios D1 and D2 are similar to the deposition patterns in the status quo scenario.

Overall, the results for scenarios D3 – D7 are similar to each other, and these scenarios offer some advantages over the status quo situation. The results in Figure 10.25 and Figure 10.26 indicate that the 150m long curved east jetties modelled in scenarios D3-D7 are effective in preventing sediments from accumulating within the inlet mouth. The jetties are effective in protecting the inlet mouth from deposition caused by easterly storm waves. Similar to the other scenarios with curved east jetties, for scenarios D3-D7, the model predicts significant amounts of deposition south from the tip of the curved jetty. As discussed previously, this sediment likely arrives from the northeast as wave-driven longshore transport. If these deposits were to occur in the real world, they could represent a potential hazard to navigation.

The only notable difference between the results for scenarios D3 and D4 is the amount of deposition on the western side of the curved east jetty. For scenario D3, the deposition in this area reaches a height of 0.9m, whereas for scenario D4, virtually no deposition accumulates there. The smaller inlet width modelled in scenario D4 leads to a small increase in ebb flow velocities. Also, the jetty alignment for scenario D4 is slightly less curved than the alignment for scenario D3. Together, the changes due to these factors are evidently sufficient to flush away the sediments deposited on the west side of the jetty in scenario D3.

Results for scenario D5 (Figure 10.26a) indicate a narrow sliver of deposition (up to 0.5 m high) along the face of the new east training wall, in the zone near the wall where the ebb and flood velocities are diminished. This slight deposition should not affect navigability, as vessels are not expected to approach the new training wall. Results for scenario D5 also show small patches and strips of deposition (up to 0.25 m high) along the route of the current navigation channel. These deposits represent partial infilling of the deeper parts of the existing navigation channel, where depths exceed 5 m at low tide, and as long as they remain small, do not pose a threat to safe navigation. The small zone of deposition seen on the west side of the curved east jetty in results for scenario D3 (deposition height up to 0.9 m) can also be seen in the results for scenario D5 (deposition height up to 1.2 m). However, on a positive note, the amount of deposition south of the jetty tip is slightly less for scenario D5 than for scenarios D3, D4, D6 or D7.

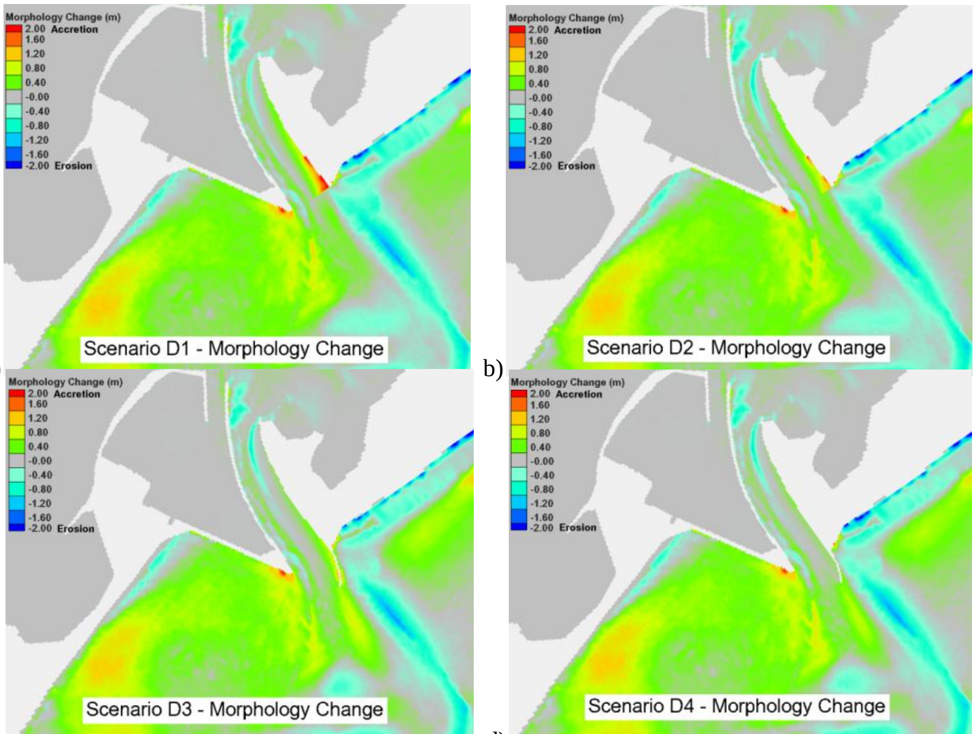

a) b) c) d)

Figure 10.25 - 6 year morphology change for scenarios: a) D1; b) D2; c) D3; and d) D4.

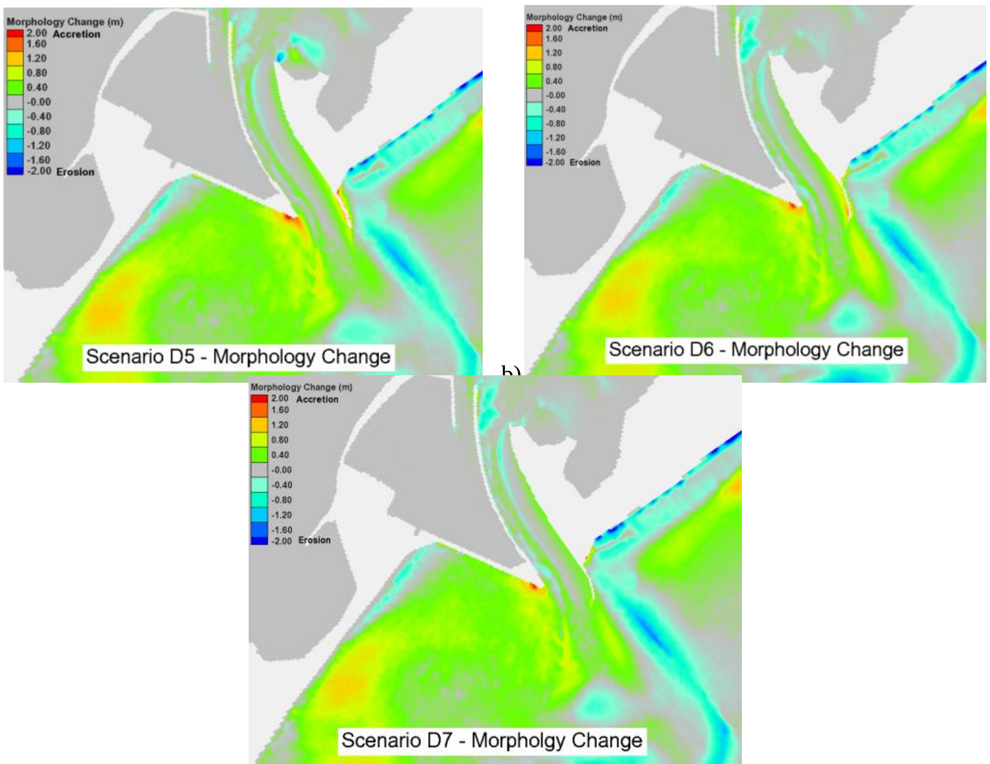

a) b) c)

Figure 10.26 - 6 year morphology change for scenarios: a) D5; b) D6; and c) D7.

The morphology change results for scenarios D1-D7 along the three cross-sections shown in Figure 10.12 are plotted in Figure 10.27. The morphology change results for scenario B are also included for reference. The results indicate reductions in deposition (compared to existing conditions) along significant portions of the three cross-sections for all scenarios.

At cross section 1, between 10 m and 40 m, the patterns of deposition and erosion for scenarios D1-D7 are virtually identical to each other and to the result for scenario B. Between 40 m and 80 m, the results for scenarios D1-D7 show less deposition than the status quo. Beyond ~90 m, the deposition for scenarios D1, D2 is greater than for scenario B, while the deposition for scenarios D3-D7 is similar to existing conditions. The increased deposition towards the end of cross-section reflects an accumulation of sediment near the face of the new training wall.

At cross-section 2, between 0 m and ~65 m, the patterns of deposition and erosion for scenarios D1-D7 are virtually identical to each other and to the result for scenario B. Beyond 80 m however, the results for scenarios D1 and D2 show significantly increased deposition, reaching up to 1.9 m at the face of the new training wall for scenario D1, and up to 1.2 m for scenario D2. Lesser amounts of deposition are predicted near the new training wall for scenarios D3-D7.

The morphology change results along cross-section 3 emphasize the effects of the new training walls and the curved east jetties on morphology changes near the navigation channel outside the inlet.

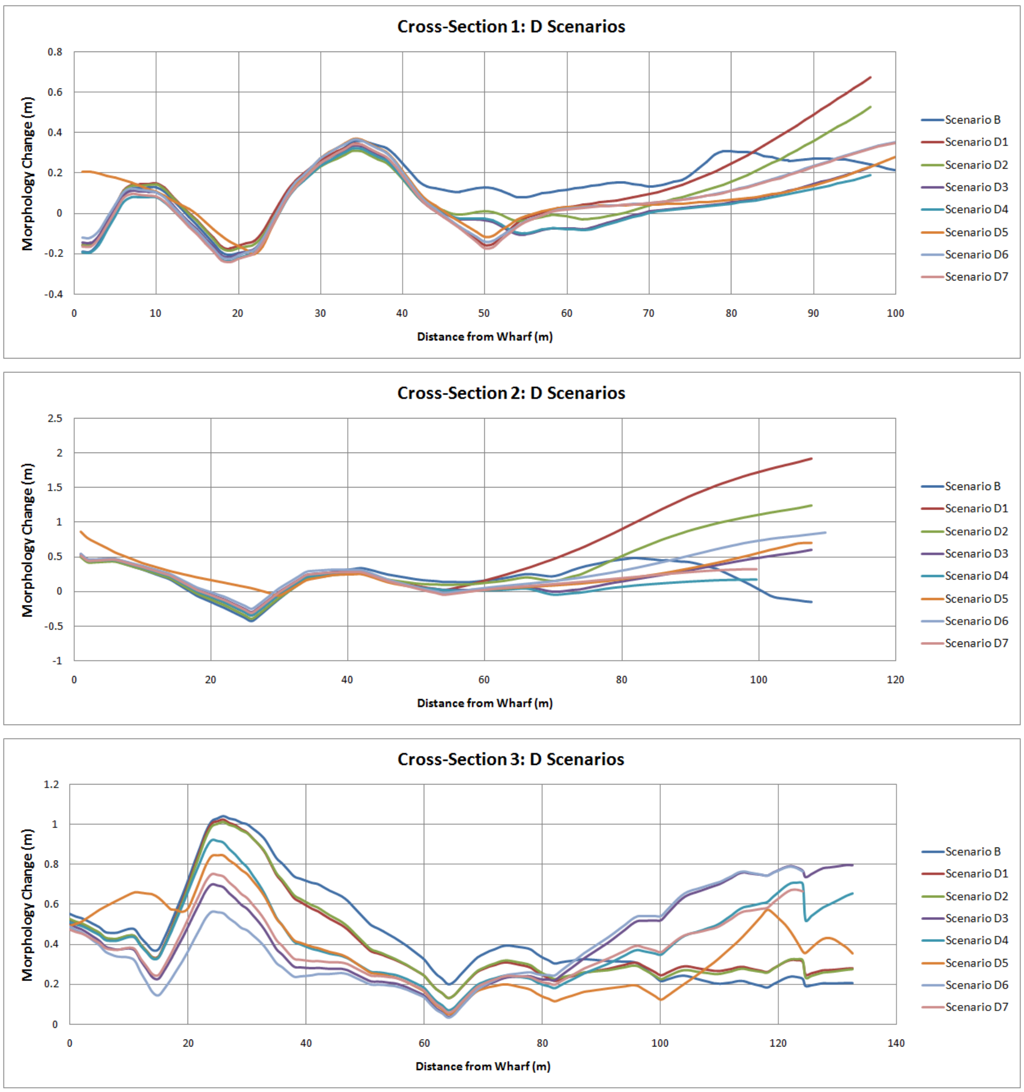

Figure 10.27 - Morphology change along 3 different cross-sections for scenario B, D1 - D7.

The morphology change results along cross-section 3 highlight the effects of the new training walls and the curved east jetties on morphology changes near the navigation channel outside the inlet. At cross-section 3, between 20 m and 85 m, the deposition for scenarios D1-D7 is less than for the status quo situation (scenario B). Over this zone, the reduction in deposition is generally greatest for scenario D6 and least for scenarios D1 and D2. From 0 m to 20 m, deposition is greatest for scenario D5, while the other scenarios give similar results to each other and to existing conditions. Over the eastern part of the cross-section (beyond ~90 m), the deposition for scenarios D3, D4, D6 and D7 increases and becomes greater than the deposition for existing conditions and scenarios D1 and D2, which remains small. The increased deposition beyond 100 m reflects the increased deposition that occurs near the tip of curved jetties, as seen in Figure 10.25.

10.5 Scenarios with a 130m Wide Channel (G1-G4)

Four scenarios which include a 130 m wide dredged channel were modelled and the simulation results are presented and discussed in this section. The scenarios include combinations of 1:1.5 sloped non-erodible revetment, training wall, 50 m jetty and a 200 m jetty. The layouts and initial bathymetries of these scenarios are shown and compared in Figure 10.28. The four scenarios are:

- Scenario G1 (Figure 10.28a) - 130 m wide channel dredged to -4 m + non-erodible revetment to +3 m along the eastern edge of the dredged channel + 50 m east jetty with vertical walls;
- Scenario G2 (Figure 10.28b) - 130 m wide channel dredged to -4 m + non-erodible revetment to +3 m along the eastern edge of the dredged channel + 200 m east jetty with vertical walls;
- Scenario G3 (Figure 10.28c) - 130 m wide channel dredged to -4 m + 360 m long curved training wall on east side of inlet + 50 m east jetty with vertical walls; and
- Scenario G4 (Figure 10.28d) - 130 m wide channel dredged to -4 m + 360 m long curved training wall on east side of inlet + 200 m east jetty with vertical walls.

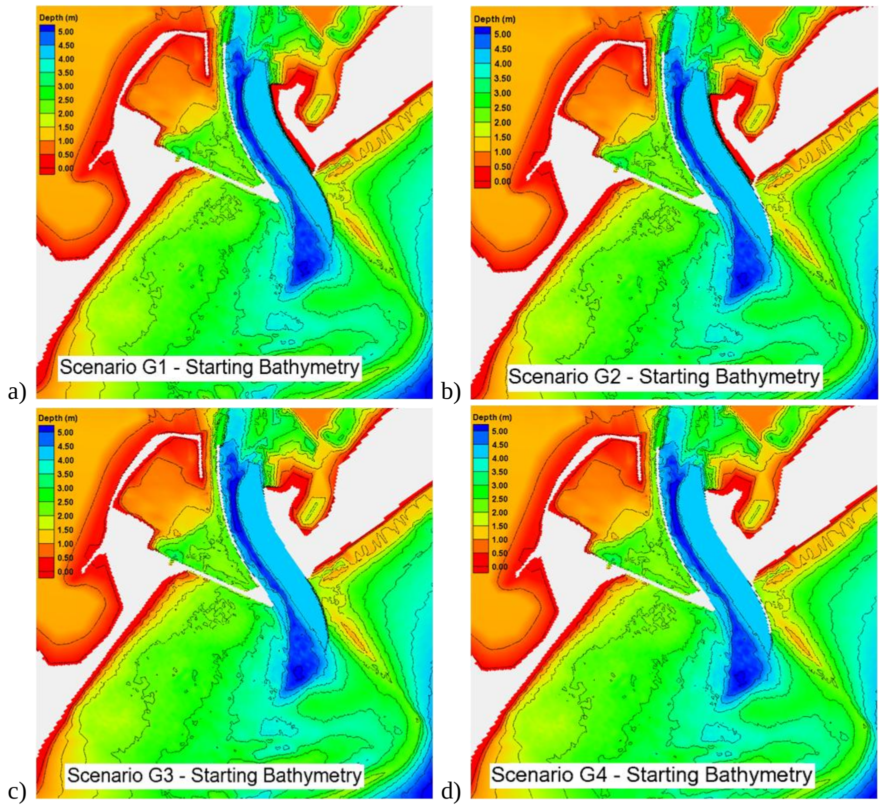

Figure 10.28 - Initial bathymetries for five scenarios with 130 m wide channels dredged to -4 m: a) scenario G1; b) scenario G2; c) scenario G3; and d) scenario G4.

10.5.1 Hydrodynamics

The flow fields during strong ebb and tide flows for scenarios G1-G4 are presented in Figure 10.29 and Figure 10.30. Similar images for the existing conditions are presented in Figure 8.2. All four of the scenarios presented in this section show reduced velocities within the inlet during the ebb and flood flows. Following the trends previously discussed in this report, the reduction of the velocities is attributed to the increase in cross-sectional area of the flow channel. This allows for the same discharge to be conveyed with a lower velocity. The ebb flow field in scenario G1 is similar to that of scenario C3 (Figure 10.9c), producing a much more uniform velocity field throughout the entire length of the inlet compared to the status quo. The similarity between scenario G1 and C3 is expected since the only difference is the width of the dredged channel (130 m for G1 and 110 m for C3). The peak ebb velocity for scenario G1 is 1.66 m/s at the inlet mouth. This is reduced compared to scenario C3 (peak ebb velocity of 1.8 m/s) and the status quo (peak ebb velocity of 2.1 m/s). A similar situation is seen in the maximum flood flow results for scenario G1. The flow field is similar to that of scenario C3, but with a reduced peak flood velocity of 0.72 m/s compared to 0.8 m/s.

The hydrodynamics of scenario G2 are similar to scenario E3 (Figure 10.16a), the main difference being the wider dredged channel in scenario G2 produces slightly lower velocities. The peak ebb and flood velocities in scenario G2 are 1.65 m/s and 0.75 m/s respectively, while scenario E3 produces peak ebb and flood velocities of 1.79 m/s and 0.82 m/s. The distribution of velocities within the inlet are similar to scenario E3, including the influence the 200 m long jetty, particularly the shore-perpendicular portion, has on the flow field immediately offshore of the inlet. As in scenario E3, the jetty in scenario G2 deflects the ebb jet to the west offshore of the inlet. During the flood flow, the jetty causes the flow to enter the inlet from the SSW direction instead of from the SE direction as seen in scenario G1 and the status quo scenario. The change in the flow direction shifts the maximum flood velocities towards the east side of the inlet compared to the status quo. In addition, during the flood flow a low velocity zone is located near the existing wharf. This zone is largest near the inlet mouth and tapers towards the north end of the inlet. Again, these velocity field patterns observed during the flood flow are also seen in the results for scenario E3.

The flow fields for scenario G3 are very similar to scenario G1 and the flow fields for scenario G4 are very similar to scenario G2. This is expected since the only difference between scenario G3 and G1 (also G4 and G2) is that scenario G3 (and G4) were modelled with a vertical training wall instead of a non-erodible revetment. The peak ebb and flood velocities for scenario G3 are 1.70 m/s and 0.70 m/s, which are similar to the peak ebb and flood velocities of scenario G1 (1.66 m/s and 0.72 m/s). The distribution of velocities for scenario G3 and G1 are virtually identical, with both scenarios providing a more uniform velocity field throughout the inlet compared to the status quo (Figure). The influence of the 200 m jetty on the flow field of scenario G2 is again observed in scenario G4. The westward redirection of the ebb jet and the shift of maximum flood velocities are both present in scenario G4.

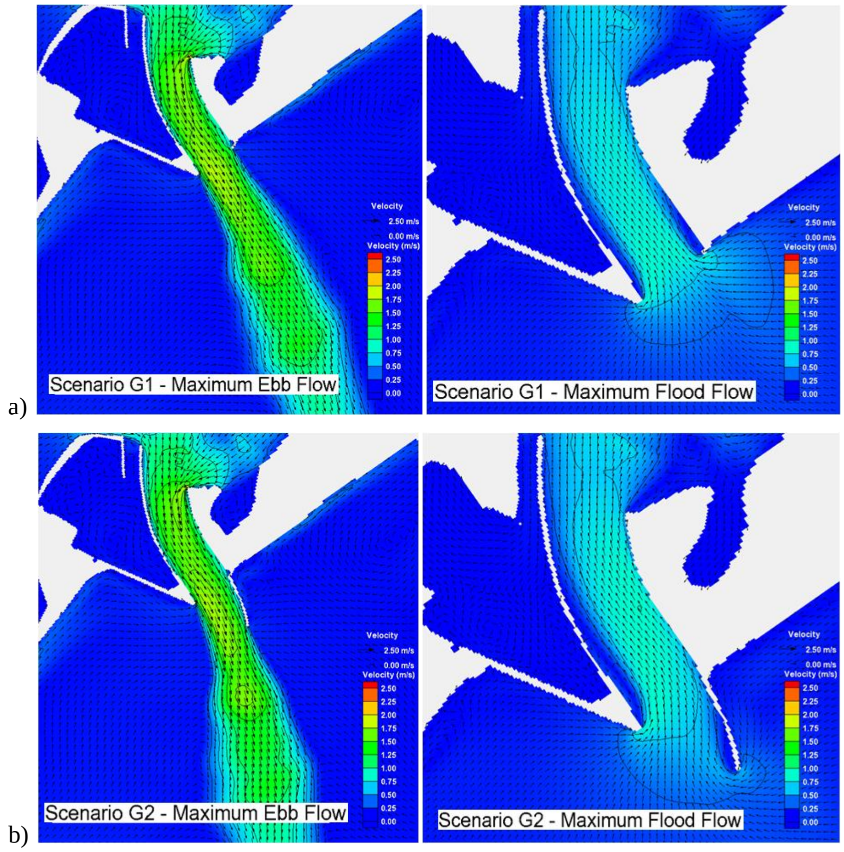

Figure 10.29 - Flow fields during strong ebb and flood tides for scenarios: a) G1 and b) G2.

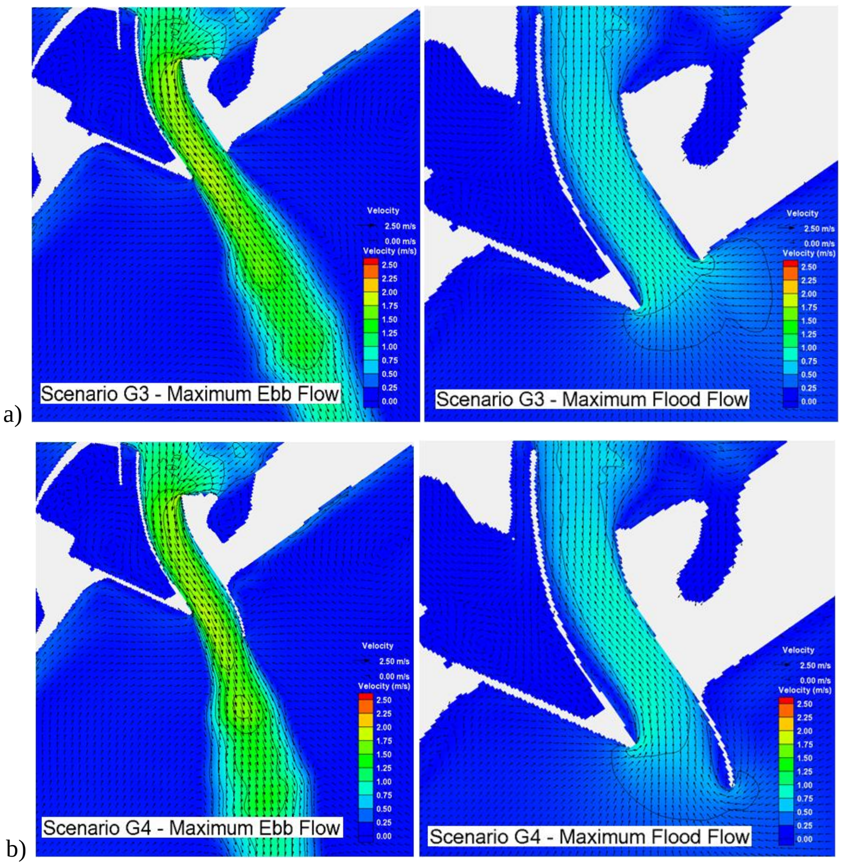

Figure 10.30 - Flow fields during strong ebb and flood tides for scenarios: a) G3 and b) G4.

10.5.2 Sediment Transport Patterns

The time-averaged sediment flux patterns for scenarios G1-G4 are presented in Figure 10.31, while a comparable image for the existing conditions is shown in Figure 8.7. Scenarios G1 and G3 show similar sediment transport patterns, with the largest amount of sediment transport occurring offshore of the inlet, just south of the 50 m jetty. This sediment is likely longshore sediment transport arriving from the northeast, which is deflected offshore by the jetty and carried seaward by the ebb jet. A similar sediment transport pattern is seen in scenario C3 (Figure 10.10c). In scenario G3, little sediment transport occurs next to the curved training wall on the east side of the inlet. This result is absent from the scenario G1 sediment transport results, where larger amounts of south travelling sediment transport occurs throughout the entire width of the inlet, including next to the revetment.

Scenarios G2 and G4 show similar sediment transport patterns when compared to each other, as well as when compared to scenario E3 (Figure 10.17d). The addition of a shore-perpendicular jetty extension in scenario G2 and G4 appears to reduce the amount of sediment transport occurring within the inlet mouth and offshore of the inlet when compared to scenarios G1 and G3. The shore-perpendicular jetty re-directs the longshore sediment transport away from the inlet mouth until it merges with the sediment being transported seaward from the ebb flows. Similar to scenario G3, scenario G4 shows little sediment transport next to the curved training wall on the east side of the inlet. A similar trend is seen in scenario D5 (Figure 10.24a), where there is little sediment transport on the east side of the 110 m dredged channel, next to the new curved training wall.

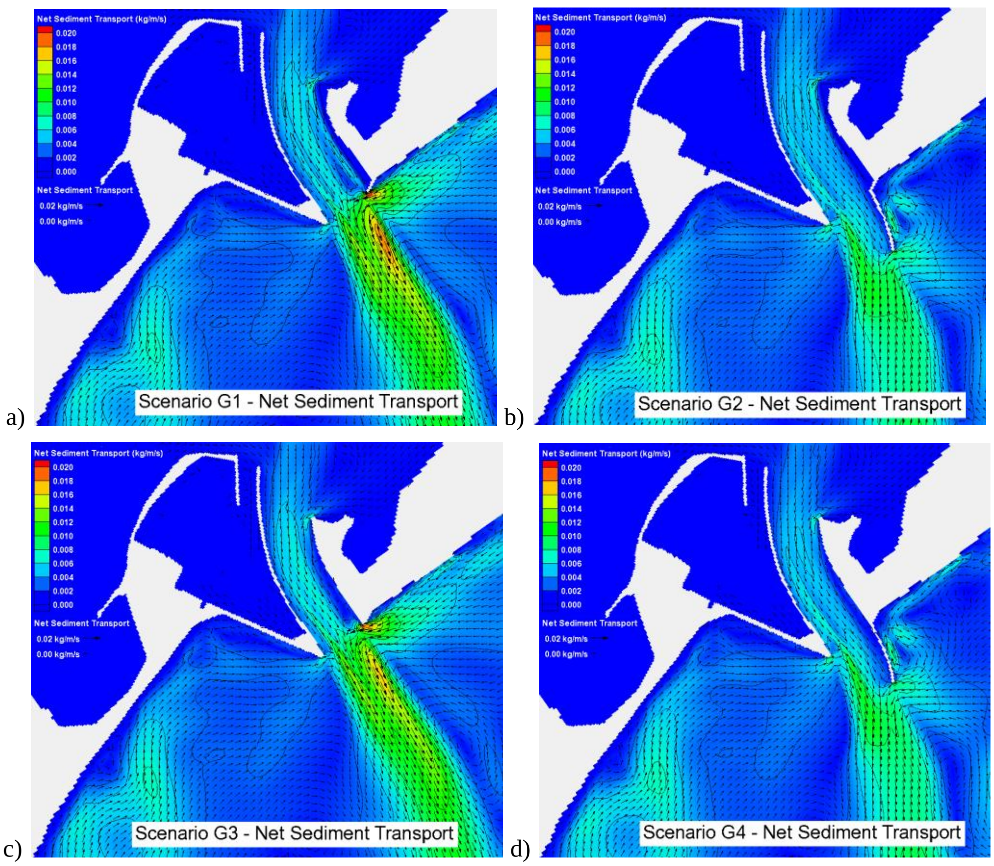

Figure 10.31 - Time-averaged sediment transport flux for scenarios: a) G1; b) G2; c) G3; and d) G4.

10.5.3 Morphology Change

The morphology change maps derived from the long-term (6 year) simulations for scenarios G1-G4 are shown in Figure 10.32. A comparable morphology change map for the status quo is shown in Figure

8.15. As noted previously, the numerical model's predictions of morphology change are uncertain and these results should therefore be interpreted with caution.

All four modelled scenarios, G1-G4, show an improvement regarding the deposition within the inlet when compared to the existing conditions. Scenarios G1 and G2 show a similar deposition patterns, with deposition occurring along the deepest part of the current navigation channel and along the revetment on the east side of the inlet, particularly at the inlet mouth. Scenario G2 shows deposition at the tip of the jetty, which is consistent with the results from the other scenarios modelled with a shore-perpendicular jetty (scenarios E1-E4 and D3-D7). Scenario G2 shows that the addition of a jetty reduces the amount of deposition offshore of the inlet, producing a slightly improved situation for ship navigation.

The major differences in deposition for scenarios G3 and G4 is the increased deposition along the training wall. The deposition along the training wall is larger in magnitude compared to scenarios G1 and G2 (1.5m compared to 0.95m), and it also extends further north, into the inlet. This increase in deposition is likely related to the net sediment transport patterns discussed in Section 10.5.2. As seen in Figure 10.31, scenarios G3 and G4 show little sediment transport occurring next to the new training wall. Similar to what is observed in scenario G2, the jetty in scenario G4 reduces deposition offshore of the inlet by trapping and redirected the longshore sediment transport arriving from the northeast.

The morphology change results for scenarios G1-G4 all indicate areas of erosion around the northern tip of the revetment (in scenarios G1 and G2) or the training wall (in scenarios G3 and G4). Smaller amounts of erosion are also observed in this area for the scenarios with a 110 m wide channel, E1-E4. This erosion may be a result of the assumed initial sediment grain sizes within this area. As the dredged channel increases in size, the structure on the east side of the channel, either a revetment or training wall, is moved further east. Moving the structures eastward places them further away from the coarse sediment assumed within the existing inlet, and into a zone of assumed finer sediment. The end result is areas that were not initially subjected to significant velocities in the simulation of existing conditions are now subjected to velocities of up to 1.5 m/s in scenarios G1-G4. Therefore, the extent of erosion at the northern tip of the inlet is dependent on the sediment assumed in the area, and with all of the results, should be interpreted with that in mind.

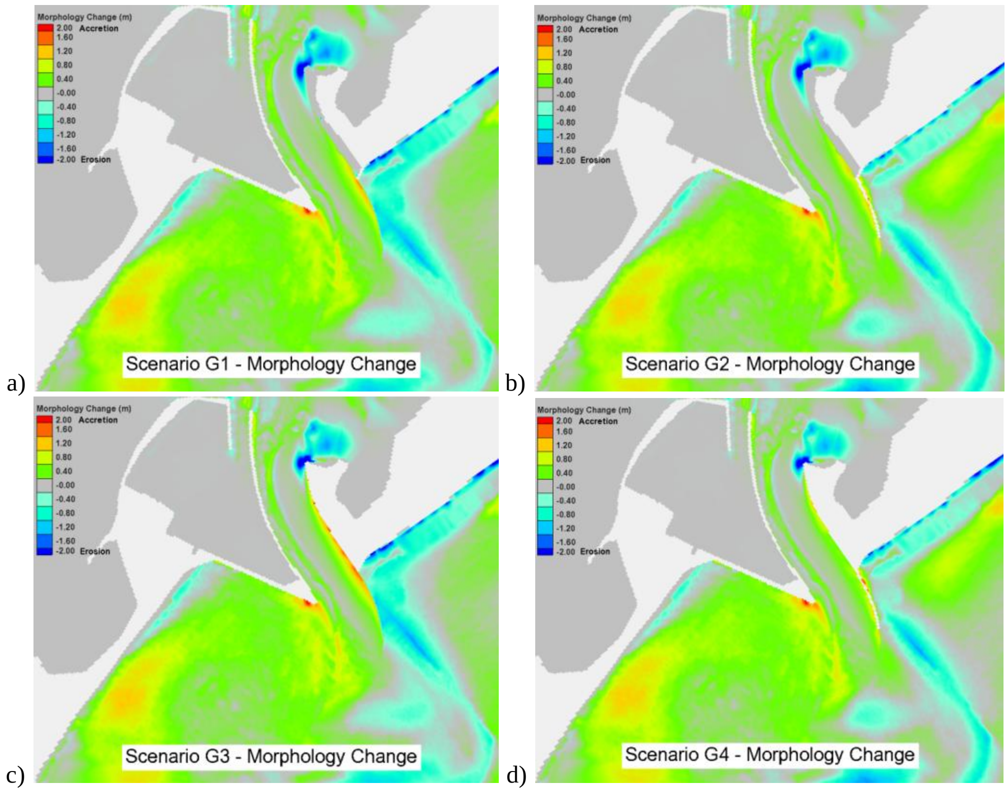

Figure 10.32 - 6 year morphology change for scenarios: a) G1; b) G2; c) G3; and d) G4.

The morphology change results for scenarios G1-G4 along the three cross-sections shown in Figure 10.12 are plotted in Figure 10.33. The morphology change results for scenario B are also shown as reference. Along cross-section 1, all scenarios, G1-G4 show deposition along the first 5m of the cross-section, instead of the erosion seen in scenario B. The deposition and erosion trends for scenarios G1 and G4 between 10 m and 45 m are similar to scenario B. After 45m, scenarios G1-G4 show reduced amounts of deposition, up to 0.2m, for the remainder of the cross-section.

At cross-sections 2, scenarios G1-G4 show increase deposition for the first 25m of the cross-section. From 40 m until the end of the cross-section, scenarios G1-G4 are similar to each other, all reducing the amount of deposition compared to scenario B up until 90 m, where there is a significant increase in deposition compared to scenario B. 90 m along the cross-section is the location where sediment begins to deposit along the new structure on the east side of the inlet, whether it be a revetment (scenario G1 and G2) or a training wall (scenario G3 and G4).

Cross-section 3 shows that scenarios G1-G4 provide reduced deposition offshore of the inlet when compared to scenario B. The addition of a jetty in scenarios G2 and G4 appear to further reduce the deposition all along the cross-section until the last 5 m. At 120 m, scenarios G2 and G4 show an increasing amount of deposition, which is the deposition occurring at the jetty tip.

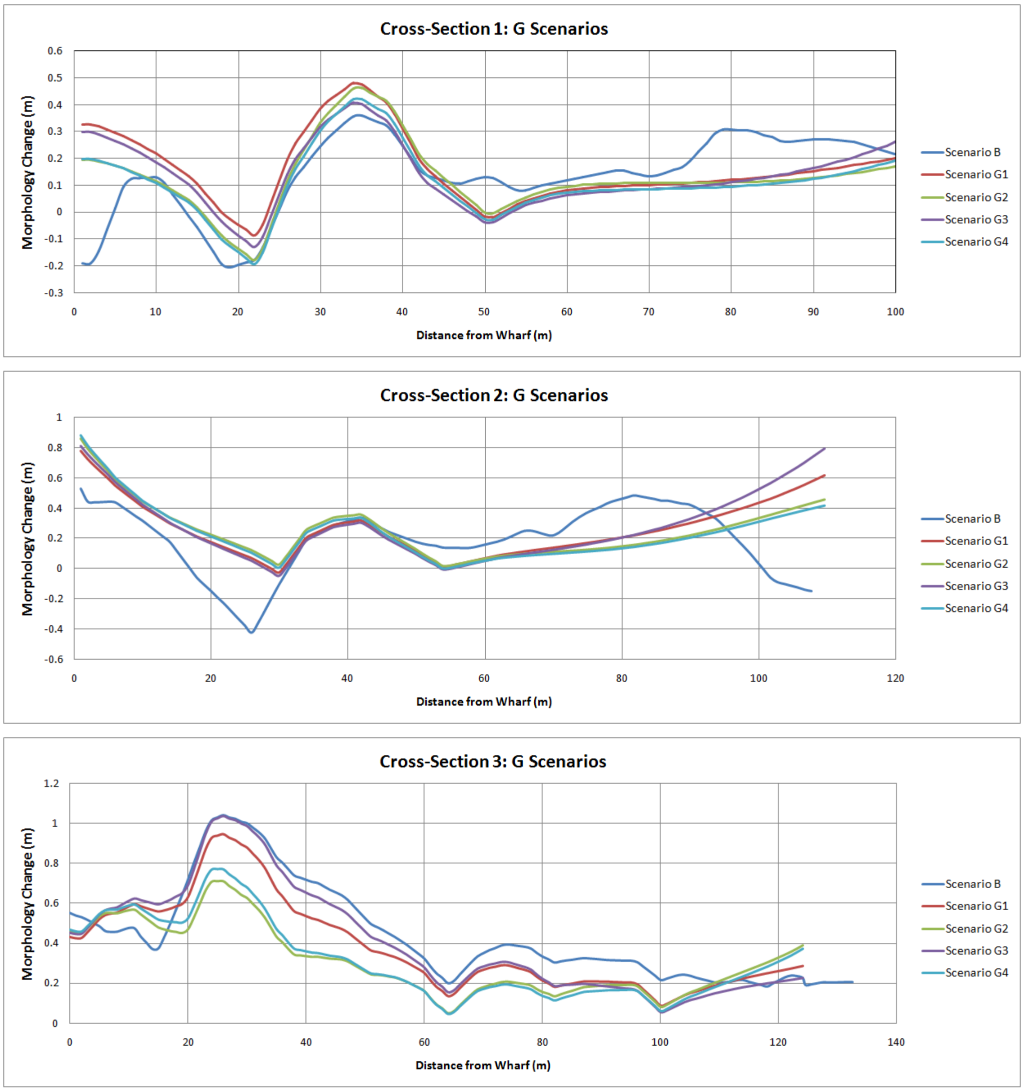

Figure 10.33 - Morphology change along 3 different cross-sections for scenarios B and G1-G4.

11 Assessment of Potential Impacts Southwest of the Inlet

Any sediment trapping structure placed along a coastline, such as the various jetties modelled in this study, has the potential to cause shoreline erosion down-drift of the inlet. A jetty placed on the up-drift side of an inlet will trap a portion of the longshore sediment transport. The retention of sediment at the inlet may lead to a reduction in the flow of sediment down-drift of the inlet, which in turn may cause the down-drift shoreline to erode and retreat. The shoreline southeast of Shippagan Gully has already experienced down-drift erosion following the construction of two jetties in the 1880's. The red line in Figure 11.1 shows the original shoreline position at Shippagan Gully, prior to this jetty construction. The jetties constructed in the 1880's altered the coastal processes at the inlet and disrupted the flow of sediment moving along the coast from northeast to southwest, which led to the shoreline recession that can be seen today. A rubble-mound shore-protection structure (indicated by black circle on Figure) has been constructed immediately southwest of the inlet in order to prevent the coastline from receding any further.

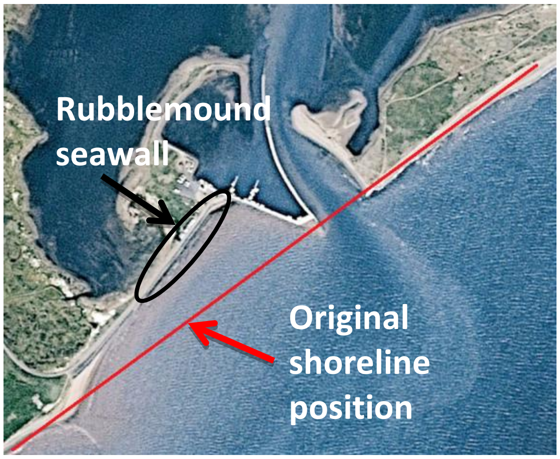

Figure 11.1 - Downdrift erosion at Shippagan Gully, red line indicates original shoreline location, black circle indicates location of rubble-mound shore-protection.

Most of the inlet configurations modelled in this study will alter the coastal processes at the inlet and may alter the flow of sediment reaching the down-drift shoreline. Such alterations may cause the down-drift shoreline to recede or advance, depending on whether the net longshore sediment flux flowing towards the southwest is reduced or increased. In this section, simulation results for four scenarios (D4, E2a, E3 and E4) are compared to those for scenario B (existing conditions) in order to investigate the potential impact that changes at the inlet might have on nearshore sediment processes down-drift (southwest) of the inlet.

Unfortunately the CMS numerical model that was employed in this study is not the appropriate tool for simulating changes in shoreline position directly. However, the CMS model can be used to estimate longshore sediment transport rates and patterns of erosion and deposition, including the changes due to alterations at the inlet. Shoreline impacts may be inferred from these changes. Shoreline recession can be expected if sediment fluxes are reduced (relative to existing conditions), whereas shoreline advancement can be expected if sediment fluxes are increased.

Potential changes south-west of the inlet are also analyzed using another numerical model, GenCade. GenCade is a one-dimensional numerical model that is specifically designed to calculate shoreline changes over long time periods, such as years or decades. The GenCade model results are used to judge how different lengths of jetties will affect the shoreline downdrift, south-west, of the inlet.

11.1 Longshore Sediment Transport Rate

In Phase I of the Shippagan Gully study, the potential longshore sediment transport rate was calculated using two well-known longshore sediment transport equations; CERC (1984) and Kamphuis (1991). The CERC (1984) formula can be written as:

$$Q_{s=}\frac{I_s}{(\rho_s-\rho)(1-n)g} \qquad (11.1)$$

where:

$$I_s = 0.39P_{asb}$$

and

$$P_{asb} = \frac{1}{16}\frac{\rho g^{3/2}}{\gamma_{sb}^{1/2}}H_{sb}^{5/2}sin2\alpha_b$$

The input data into the CERC formula are: sediment density (ρ_s), water density (ρ), sediment porosity (n), significant wave breaking height (H_{sb}), breaking wave depth (d_b) and breaking wave angle relative to shoreline (α_b).

The Kamphuis (1991) formula can be written as:

$$Q_k = 6.4\times10^4 H_{sb}^2 T_{op}^{1.5} m_b^{0.75} D^{-0.25} sin^{0.6}2\alpha_b \qquad (11.2)$$

In addition to the parameters used in the CERC formula, this formula includes: wave period (T_{op}), beach slope (m_b) and mean sediment grain diameter (D). In the Phase I study, these equations were used to develop estimates of the potential longshore sediment transport rate along the coast near Shippagan Gully. A net potential sediment flux of 2,036 m^3/year flowing towards the southwest was obtained using the CERC formula, while a flux of 2,658 m^3/year (also towards the southwest) was obtained using the Kamphuis method. Further details are provided in NRC Technical Report CHC-CTR-129 (June, 2011).

11.2 Potential changes in longshore sediment transport rate using CMS Model Results

One factor that will influence shoreline evolution down-drift of the inlet is the longshore sediment transport rate, particularly changes in the rate at which sediments are transported along the coast. Working with the simulation results obtained using the refined CMS model, the longshore sediment transport rates across the eight shore-perpendicular cross-sections shown in Figure 11.2 were calculated for scenarios B, D4, E2a, E3 and E4. Each cross-section extends from the shore out to the -5 m depth contour. Time histories of the net sediment transport at each cross-section for scenario B are shown in Figure 11.3, where positive values indicate sediment transport travelling from NE to SW and negative values indicate sediment transport travelling from SW to NE. Equivalent plots for the other four scenarios with modified inlet configurations are presented in Figure 11.4 – Figure 11.7.

As shown in Table 11.1 for scenario B (existing conditions), the net longshore sediment flux is greatest (1,951 m^3/year) at cross-section 1 (located up-drift of the inlet), and second greatest (1,640 m^3/year) at cross-section 6 (located down-drift of the inlet, past the reattachment point). It is reassuring to note that the net longshore sediment transport rates derived from the numerical results at these two cross-sections are similar to, but slightly less than the theoretical estimates of the potential transport rate obtained using the CERC and Kamphuis formulas. Since the up-drift sediment flux exceeds the down-drift flux by a small margin, this suggests that some sediment is being either retained at the inlet or lost to deeper waters offshore. Cross-sections 3 and 4 (located immediately down-drift of the inlet) both have a small amount of net longshore sediment transport (398 m^3/year and 9 m^3/year respectively). As seen in Figure 11.3, very little sediment transport occurs through cross-section 4. Cross-section 5 (located at the reattachment point) is the only location where the net longshore sediment transport rate is negative, with a value of -920 m^3/year. This result suggests that the eastbound flux exceeds the westbound flux at cross-section 5.

The results for scenarios B, D4, E2a, E3 and E4 are summarized in Table 11.1. Influence of east jetty length on longshore sediment transport for the eight cross-sections is shown in Figure 11.8. Based on these results, the following observations can be made.

- There is a net longshore sediment transport towards the southwest at cross-sections 1-4 and 6 for all scenarios.
- There is a net longshore sediment transport towards the northeast at cross-section 5 for all scenarios.
- There is a decrease in net longshore sediment transport rate at cross-section 2 for all new scenarios relative to the status quo. The decrease is roughly proportional to the jetty length.
- There is an increase in net longshore sediment transport rate at cross-sections 3 and 4 for all new scenarios, relative to the status quo. At cross-section 4, the increase is roughly proportional to jetty length.
- The change in net longshore sediment transport rate at cross-section 5and 6 is roughly proportional to jetty length.
- There is no change in net longshore sediment transport rate at cross-section 7 and 8 for all new scenarios.

Some of the increase in the longshore sediment transport rate at cross-sections 3 and 4 can be attributed to the westward deflection of the ebb jet outside the inlet observed for scenarios with longer curved east jetties. These results indicate that the net longshore sediment transport rate at cross-section 7 and beyond is virtually unaffected by the changes to the configuration of the inlet that have been considered here. This suggests that these inlet configuration changes will have little influence on the evolution of the shoreline down-drift from cross-section 7.

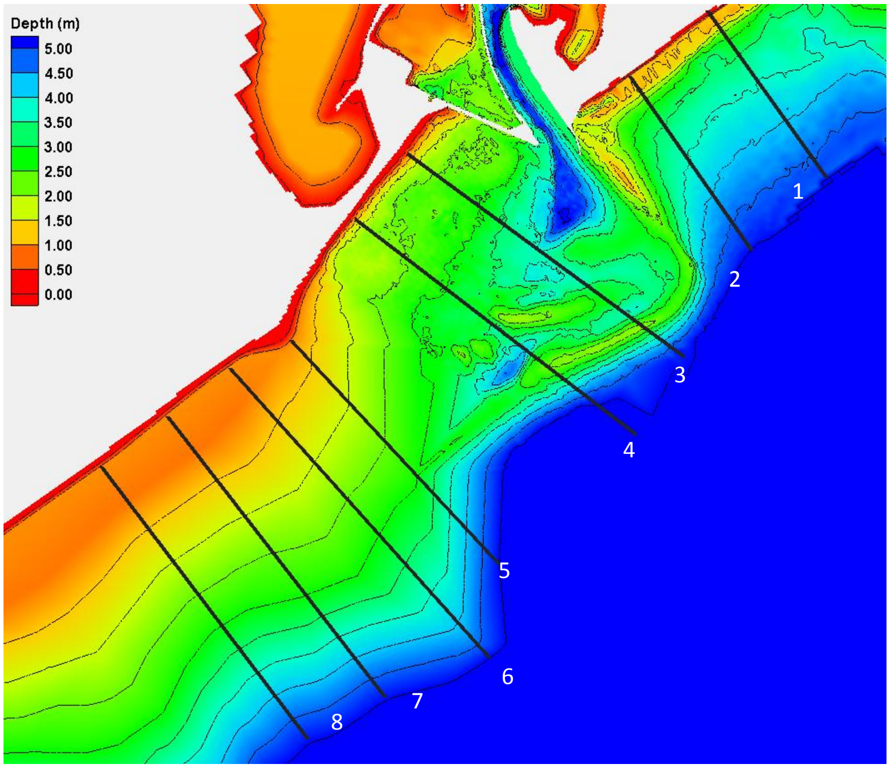

Figure 11.2 - Location and orientation of the eight cross-sections used in analysis of longshore sediment transport rate.

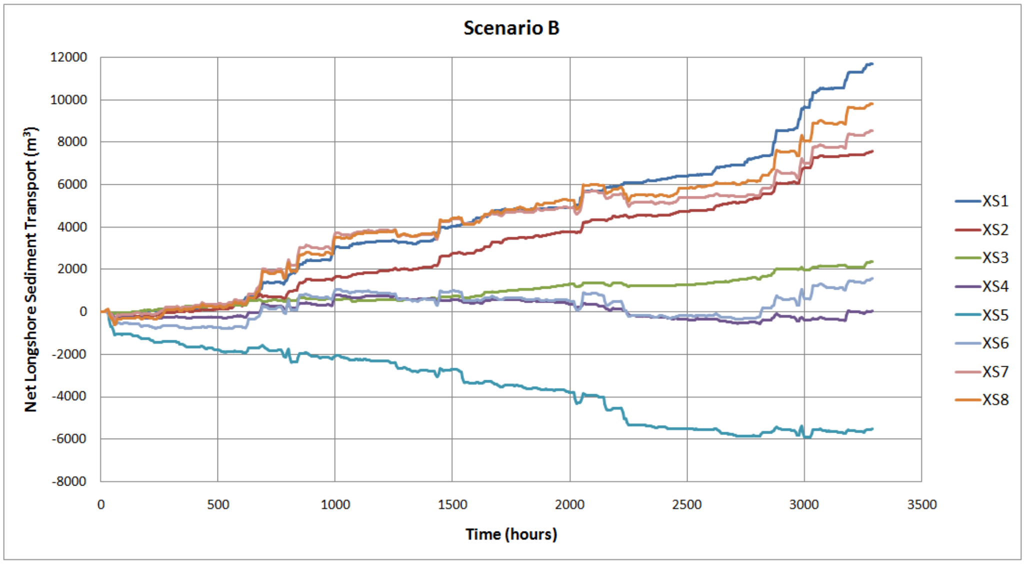

Figure 11.3 - Cumulative longshore sediment transport at cross-sections 1-8 for scenario B; positive values indicate NE to SW transport, negative values indicate SW to NE transport.

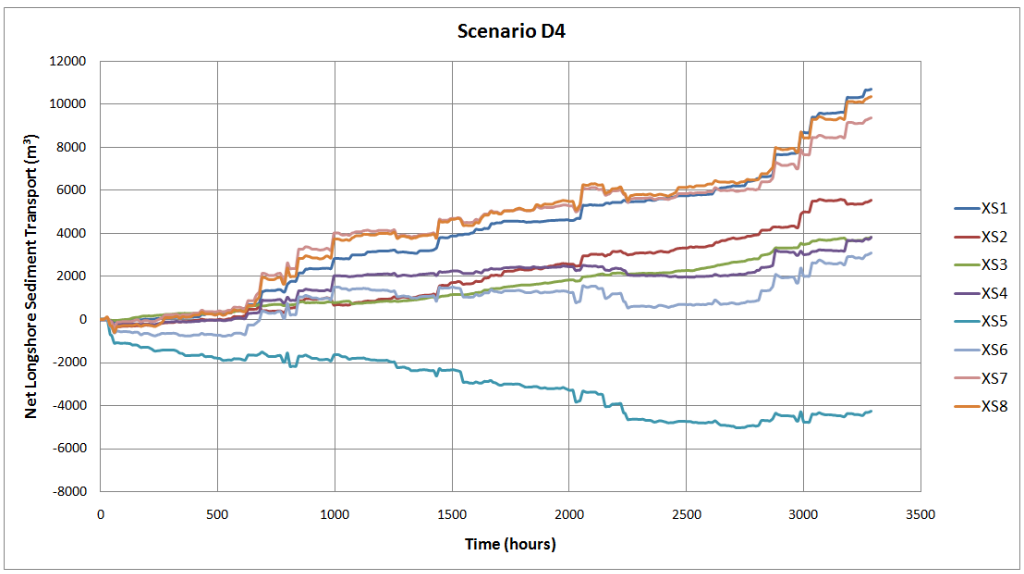

Figure 11.4 - Cumulative longshore sediment transport at cross-sections 1-8 for scenario D4; positive values indicate NE to SW transport, negative values indicate SW to NE transport.

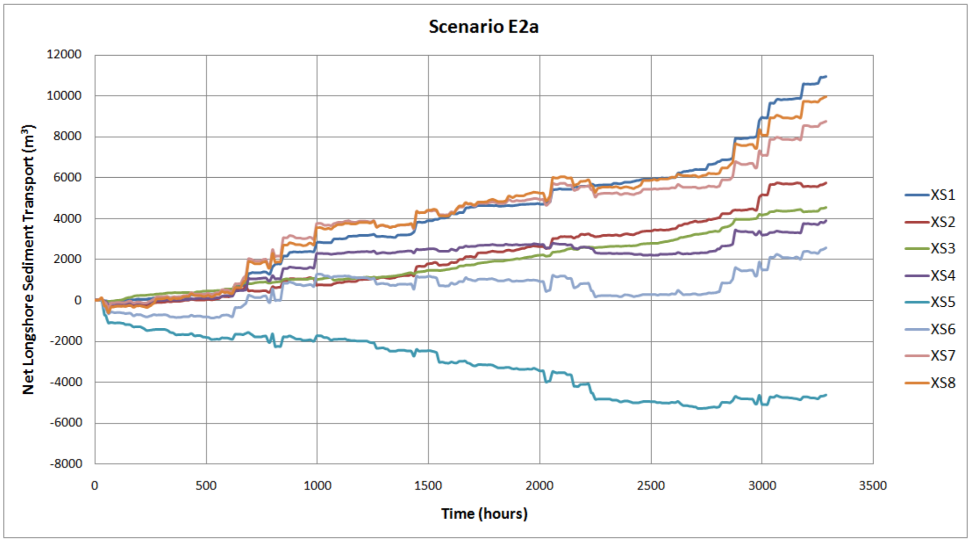

Figure 11.5 - Cumulative longshore sediment transport at cross-sections 1-8 for scenario E2a; positive values indicate NE to SW transport, negative values indicate SW to NE transport.

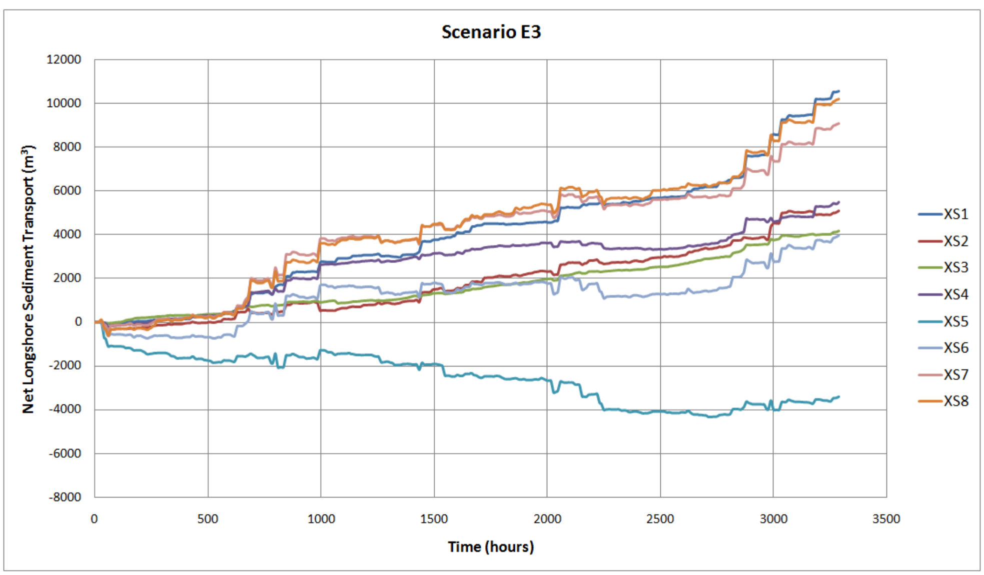

Figure 11.6 - Cumulative longshore sediment transport at cross-sections 1-8 for scenario E3; positive values indicate NE to SW transport, negative values indicate SW to NE transport.

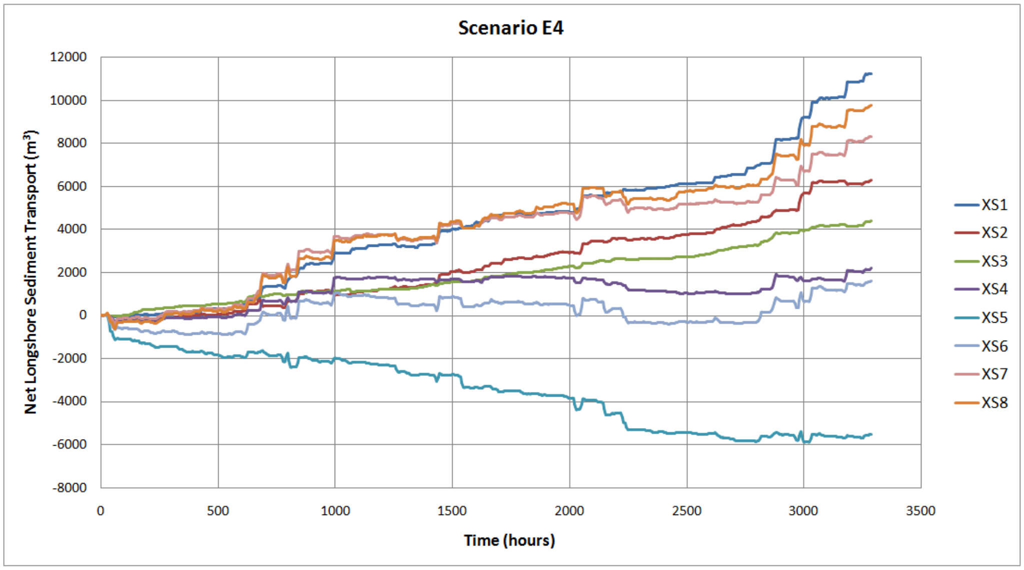

Figure 11.7 - Cumulative longshore sediment transport at cross-sections 1-8 for scenario E4; positive values indicate NE to SW transport, negative values indicate SW to NE transport.

Table 11.1 - Summary of net sediment transport rate across cross-sections 1-8.

Scenario ID	Jetty Length (m)	Total Net Longshore Sediment Flux (m^3/year)							
		Arc 1	Arc 2	Arc 3	Arc 4	Arc 5	Arc 6	Arc 7	Arc 8
B	0	1951	1264	398	9	-920	261	1428	1640
E4	50	1876	1049	734	366	-919	269	1387	1626
D4	100	1784	926	638	638	-712	519	1558	1726
E2a	100	1827	957	760	652	-769	431	1459	1660
E3	150	1763	853	694	917	-567	661	1517	1701

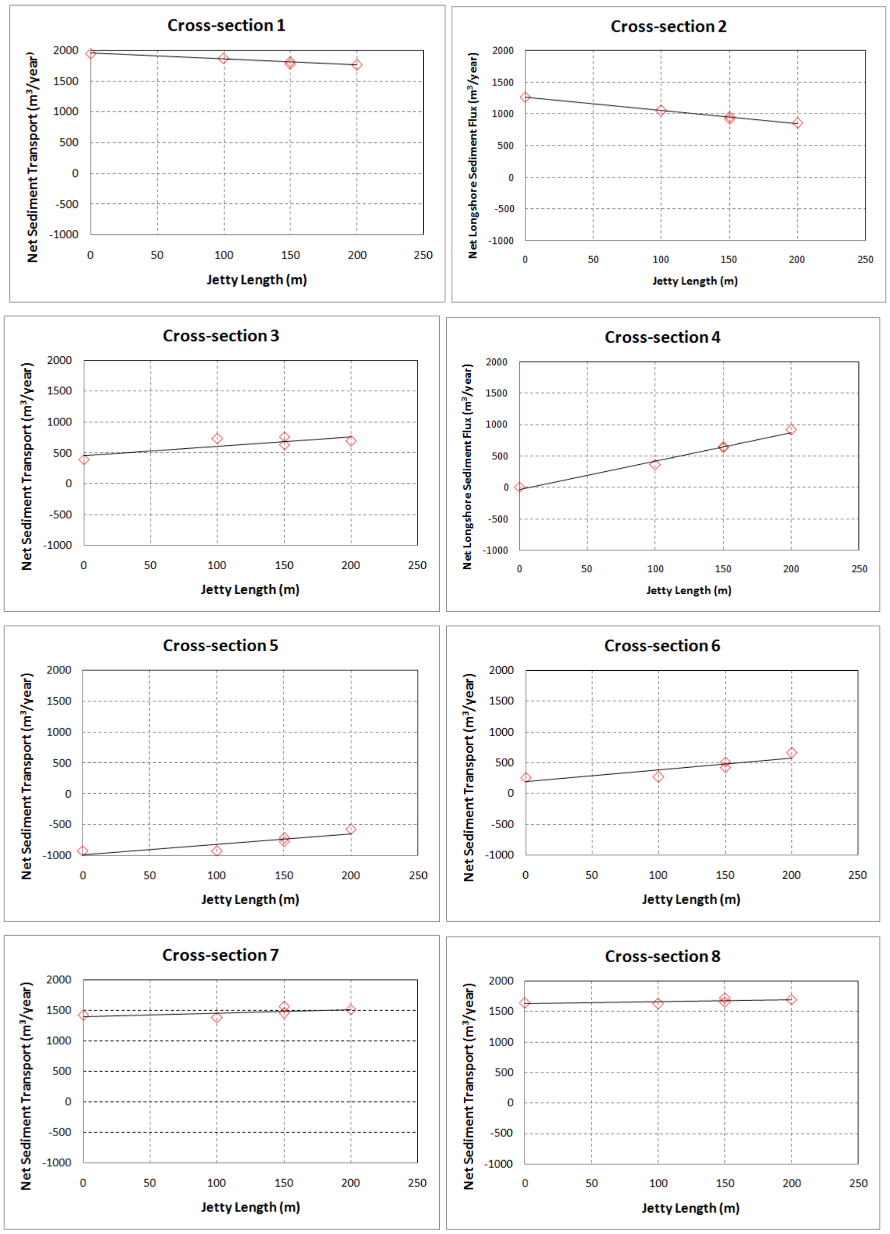

Figure 11.8 – Influence of east jetty length on longshore sediment transport for the 8 cross-sections.

11.3 Potential changes in Erosion and Deposition using CMS Model Results

The modelled changes in seabed elevation near the shoreline may also be used as an indicator of potential shoreline movement. Deposition in the nearshore zone is normally linked to shoreline accretion over the long term, while erosion in the nearshore zone is normally linked to shoreline recession.

The modelled volume of erosion and deposition in five different nearshore areas over six years has been calculated for the same five scenarios (B, D4, E2a, E3 and E4). The five nearshore areas all extend from the -0.5 m depth contour down to the -3m depth contour, and are shown in Figure 11.9. Area 1 is located up-drift from the inlet, while areas 2-5 are located southwest of the inlet. A summary of the results is shown in Table 11.2. The model results indicate that changing the configuration of the inlet impacts erosion and deposition volumes in areas 1, 3, 4 and 5, but not in area 2. Moreover, for areas 1, 3 and 4, the degree of change is linked to the length of the east jetty that was modelled. The influence of east jetty length on net volumetric change for the five areas is shown in Figure 11.10.

In area 1, the net change for scenario B is -5,200 m^3 (negative representing erosion) after the six year simulation, while the four scenarios with a new east jetty all show a positive net change (representing deposition) in area 1. Hence, the new jetties lead to increased deposition in zone 1, as expected. The amount of deposition change is also roughly proportional to the jetty length, with more net deposition (24,646 m^3) for the longer 200 m jetty, and less net deposition (13,904 m^3) for the shorter 100 m jetty. The increased net deposition within area 1 is a direct result of the east jetty modelled in each scenario trapping a portion of the NE to SW longshore sediment transport. The longest jetty (200 m in scenario E3) traps the most, while the shortest jetty (100 m in scenario E4) traps the least, which is expected.

Down-drift of the inlet, the simulation results suggest net deposition in nearshore area 2 and net erosion in areas 3, 4 and 5 for all scenarios. The modified inlet configurations modelled in scenarios D4, E2a, E3 and E4 have negligible impact on area 2. The modified inlet configurations appear to slightly reduce the net erosion in area 3, and increase the net erosion in areas 4, and 5. These results suggest that the inlet modifications that have been modelled might cause the shoreline along areas 4 and 5 to retreat slowly from its current position over the long term.

Overall, the results suggest that introducing a jetty on the east side of the inlet will increase nearshore deposition up-drift of the inlet (in area 1) and increase nearshore erosion past the reattachment point (areas 4 and 5). Moreover, the magnitude of the changes in these areas is roughly proportional to the east jetty length. However, whether or not the increased down-drift erosion is enough to cause any significant change to the shoreline cannot be determined from these results.

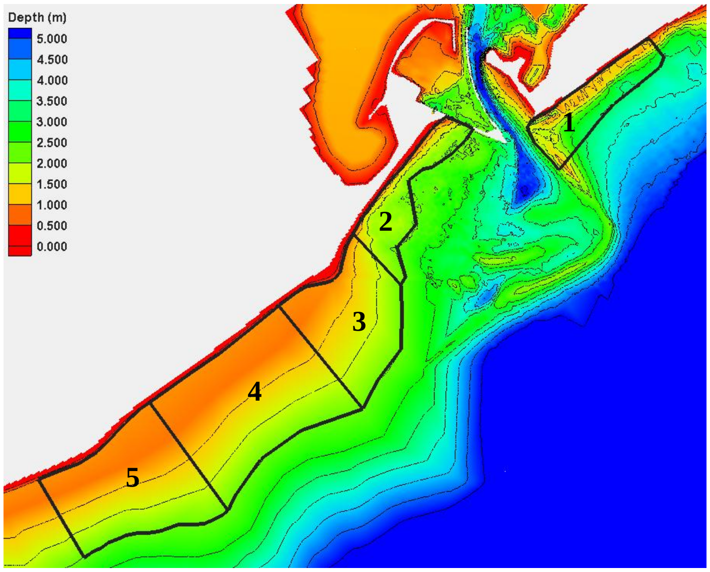

Figure 11.9 - Location of the five areas defined for analysis of nearshore erosion and deposition.

Table 11.2 - Volume of erosion and deposition for scenarios B, D4, E2a, E3 and E4.

		Scenario B (no jetty)	Scenario E4 (100 m jetty)	Scenario D4 (150 m jetty)	Scenario E2a (150 m jetty)	Scenario E3 (200 m jetty)
Area ID	Area (m^2)	Net Sediment Balance (m^3/year)	Net Sediment Balance (m^3/year)	Net Sediment Balance (m^3/year)	Net Sediment Balance (m^3/year)	Net Sediment Balance (m^3/year)
1	113620	-867	2317	3179	3276	4108
2	106820	10106	10483	10342	10428	10283
3	214260	-2755	-2254	-2394	-2165	-2024
4	375626	-2019	-2316	-2718	-2574	-2769
5	283389	-835	-1187	-1034	-1238	-1446

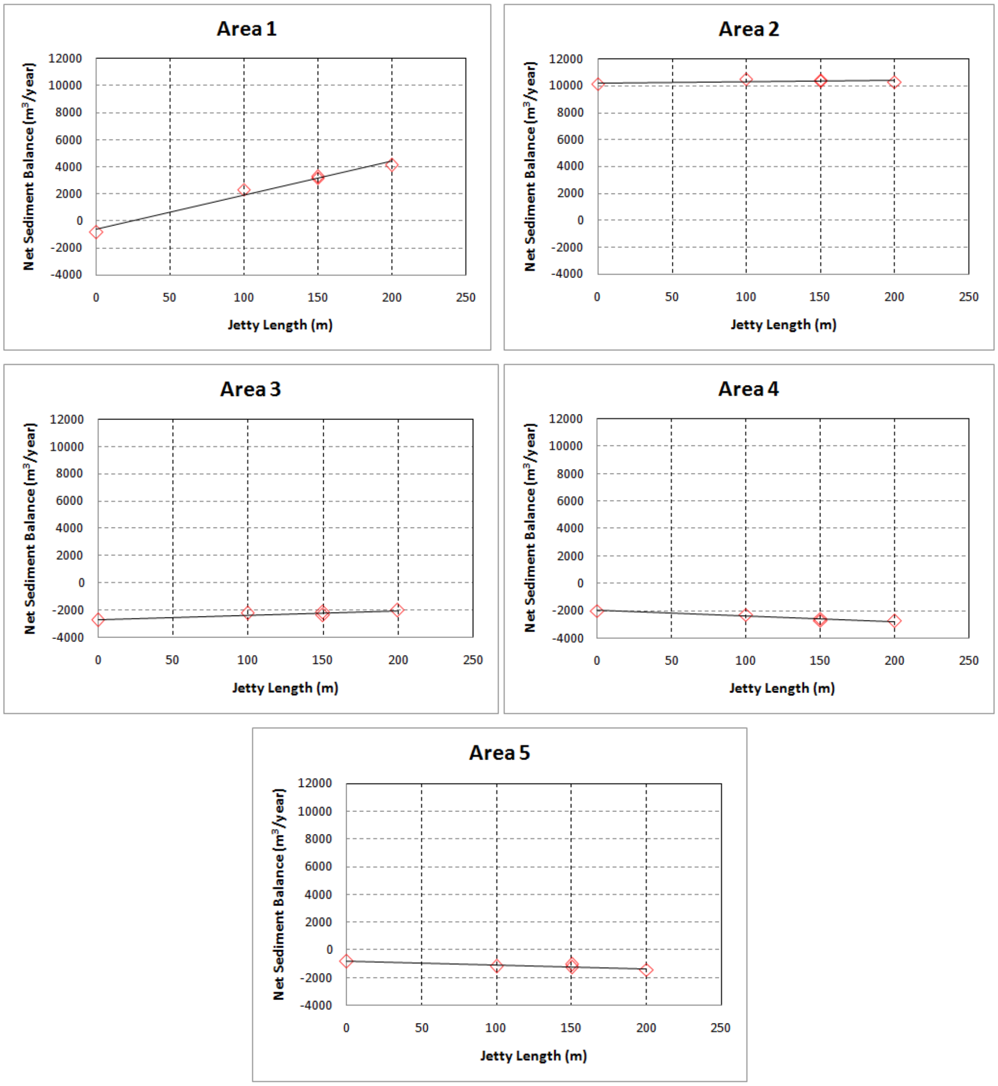

Figure 11.10 - Influence of east jetty length on net volumetric change for the 5 areas.

11.4 Potential changes in seabed elevation at points

The numerical predictions of morphology change have been analyzed in detail at 8 locations distributed along the shoreline northeast and southwest of the inlet. The eight locations are mapped in Figure

11.11. Points 1-5, 7 and 8 are all located along the -0.5 m depth contour; points 1 and 2 are located northeast of the inlet while the other points are located southwest of the inlet. Point 6 was located in an area with significant deposition near point 5. The morphology change time histories at these locations for scenarios B, D4, E2a, E3 and E4 were extracted and compared.

In most of these locations (points 1, 3-6 and 8), the variation of seabed elevation over time was virtually identical for all five scenarios, suggesting no changes in these locations due to the inlet modifications that were modelled. The morphology change time histories for points 2 and 7 are shown in Figure 11.12. At point 2, the new inlet configurations modelled in scenarios D4, E2a, E3 and E4 reduce the erosion compared to existing conditions (scenario B), and the amount of reduction is roughly proportional to the east jetty length. The model results for point 7 suggest that new inlet configurations are responsible for increasing the deposition at the reattachment point, and that the scale of increase is roughly proportional to the east jetty length.

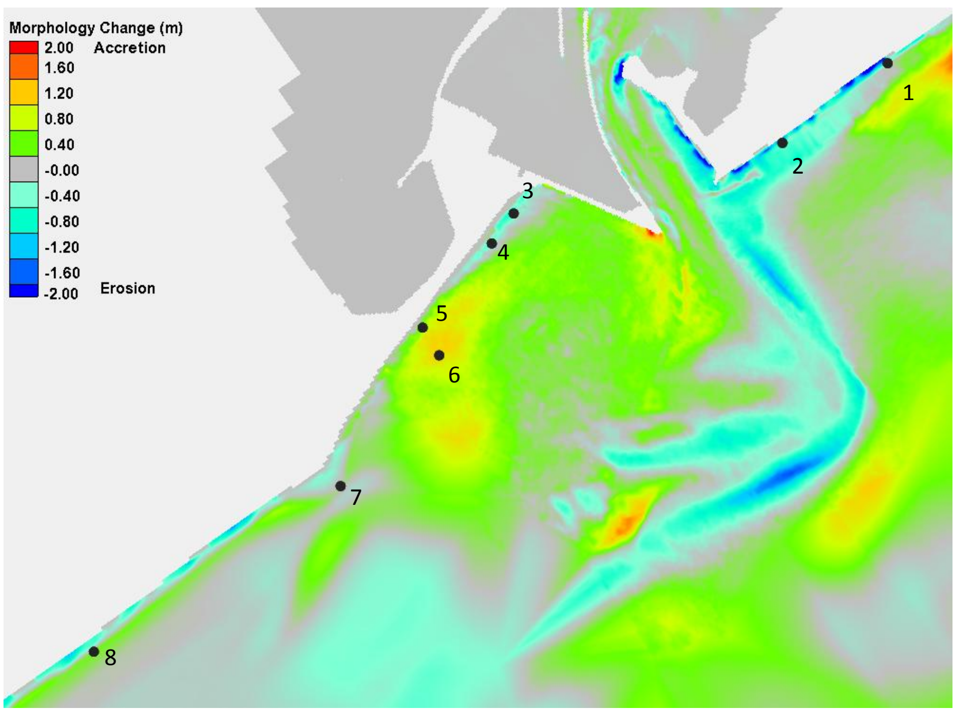

Figure 11.11 – Location of the eight points selected for analysis of morphology change.

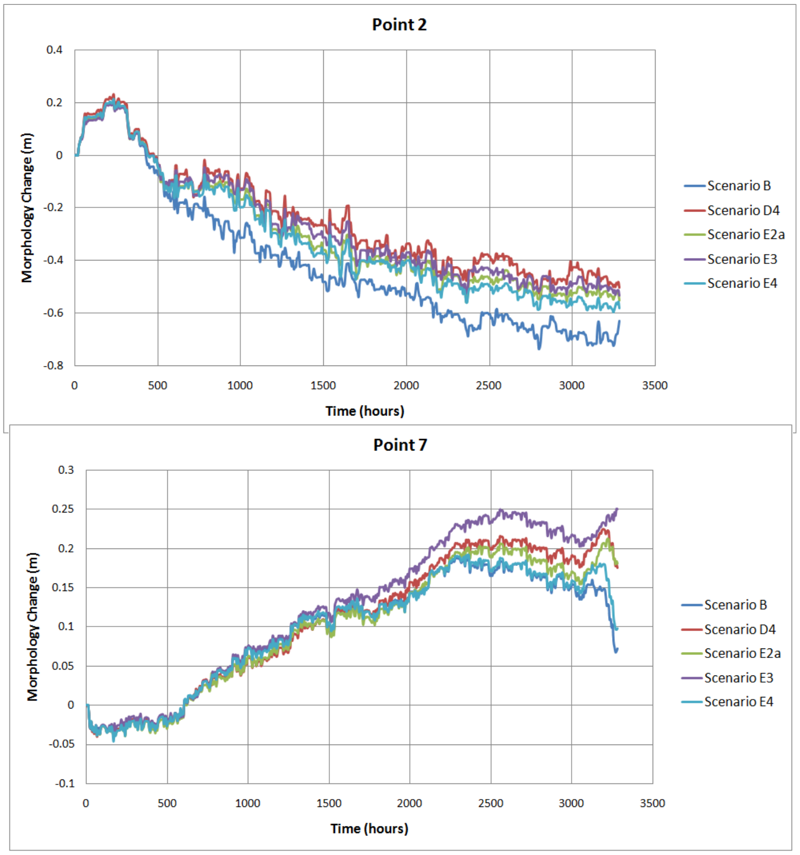

Figure 11.12 – Morphology change time series for points 2 and 7.

11.5 GenCade Model

The GenCade numerical model is a newly developed model by the USACE that is used for calculating sediment transport and morphology change along coastal regions and volumetric evolution of shoals and sand bypassing at inlets and engineered structures (Frey *et al*., 2012). GenCade is essentially the synthesis of two previous shoreline models, Genesis (Hanson and Kraus, 1989) and Cascade (Larson et al., 2003). The goal of combining the two models is to provide a model which combines project-scale, engineering design-level calculations with regional scale, planning-level calculations in order to analyze and accurately resolve both the local modifications and regional cumulative effects of coastal projects and inlets (Frey *et al*., 2012).

11.5.1 Governing Equations

The main governing equation used to calculate the shoreline position in GenCade is based on the conservation of sand volume. Assuming the right-handed Cartesian coordinate system shown in Figure

11.13, the y-axis points offshore and the x-axis is orientated parallel to the trend of the coastline. Given this coordinate system, the governing shoreline change equation is as follows:

$$\frac{\partial y}{\partial t} + \frac{1}{(D_B + D_C)}\left(\frac{\partial Q}{\partial x} - q\right) = 0 \qquad (11.4)$$

where: y = shoreline position (m)
x = distance alongshore (m)
t = time (s)
D_B = berm elevation (m)
D_C = closure depth (m)
Q = longshore sand transport rate (m^3/s)
q = source or sink of sand, $q = q_s + q_o$

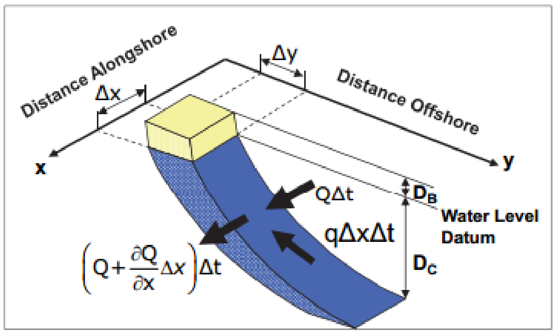

Figure 11.13 – Sketch of coordinate system used in shoreline change calculation.

The following equation is used to calculate the longshore sediment transport rate:

$$Q = (H^2 C_g)_b \left(a_1 \sin 2a_b + \left(a_3 \frac{\bar{v}_t}{u_m} - a_2 \frac{\partial H_b}{\partial x}\right) \cos a_b\right) \qquad (11.5)$$

where: Q = longshore sediment transport rate (m^3/sec)
H = wave height (m)
C_g = wave group speed (m/sec)
Subscript b = wave breaker position
$\bar{v}_t$ = mean current
u_m = maximum wave-induced near-bottom horizontal velocity at wave breaking (m/sec)
H_b = breaking wave height (m)
a_1, a_2, a_3, a_b = non-dimensional parameters

There is a sub-model within the GenCade model that is used to calculate the breaking wave height and angle based on the offshore wave conditions. This sub-model is called the internal wave model. The internal wave model calculates the wave characteristics by first obtaining an approximation of the breaking wave height without including wave diffraction and then modifying the results by accounting for changes to the wave field by each diffraction source. Without diffraction, there are three unknowns required to calculate the breaking wave height: the wave height, angle and depth at breaking. The model uses three equations are required to obtain these values.

The following equation is used to calculate the height of breaking waves which have been transformed by refraction and shoaling:

$$H_b = K_R K_S H_{ref} \qquad (11.6)$$

where: H_b = breaking wave height at an arbitrary point alongshore (m)
K_R = refraction coefficient
K_S = shoaling coefficient
H_{ref} = wave height at the offshore reference depth

The refraction coefficient and shoaling coefficients are calculated as follows:

$$K_R = \sqrt{\frac{\cos\theta_1}{\cos\theta_2}} \qquad (11.7)$$

$$K_S = \sqrt{\frac{C_{g1}}{C_{g2}}} \qquad (11.8)$$

where: θ_1 = starting angle of the ray
θ_2 = the angle of arrival
C_{g1} = group velocity at starting depth (m/sec)
C_{g2} = group velocity at end depth (m/sec)

If there are no structures to produce diffraction, the undiffracted wave characteristics are input into the sediment transport calculations. However, if diffraction producing structures are present, the breaking wave heights and diffractions are recalculated. The new breaking wave height is calculated with the following equation:

$$H_b = K_D \theta_D H_b^{`} \qquad (11.9)$$

where: K_D = diffraction coefficient
θ_D = diffraction angle
$H_b^{`}$ = breaking wave height without diffraction.

11.5.2 Model Assumptions and Limitations

As with any numerical model, GenCade only offers a representation of the complex modelled processes. Therefore, there are a number of assumptions and limitations present in the GenCade model. The overlying assumptions of the model are:

- the beach profile shape remains constant;
- the shoreward and seaward depth limits of the profile are constant;

- sand is transported alongshore by the action of breaking waves and longshore currents;
- the detailed structure of the nearshore circulation is ignored; and
- there is a long-term trend in shoreline evolution.

Since GenCade is a one-dimensional numerical model, there are a number of processes that occur at a tidal inlet that are not able to be produced by the numerical model. For example, as discussed in the CMS model results, the ebb flow has a significant impact on the sediment transport processes around the inlet. The interaction of the longshore sediment transport with the ebb and flood flows cannot be reproduced by GenCade because of the one-dimensional nature of the model. In addition, GenCade is not able to model the wave breaking that occurs along the ebb shoal. The breaking waves along the ebb shoal plays an important role in the sediment transport patterns around the Shippagan Gully inlet because it allows longshore sediment transport to naturally bypass the tidal inlet and reattach downdrift of the inlet. Due to the various assumptions and limitations within the numerical model, the model results should be interpreted with this in mind.

11.5.3 GenCade Model Setup

The one-dimensional grid for the GenCade model was setup such that it is oriented parallel to the main trend of the coastline near Shippagan Gully. The computational domain extends approximately 4 km north east (updrift) of the inlet and approximately 5.5 km south west (downdrift) of the inlet. The grid size was set to 10m over the entire domain, which can be seen in Figure 11.14. The shore protection structure, shown in Figure 11.1, is included in the GenCade grid as the blue line in Figure 11.14 and the initial shoreline is represented by the green line. The shore protection structure is positioned behind the initial shoreline and it is set such that the shoreline is not able to erode past the structure. The Shippagan Gully inlet was assumed to be in equilibrium, which means that the morphological characteristics of the inlet (such as ebb shoal, attachment bar, etc.) are fully developed. Since these features are fully developed, none of the longshore sediment transport is used by the inlet processes to create these morphologic features. Therefore, the inlet was not modelled within GenCade and instead, the location of the inlet on the coast was modelled as a regular shoreline.

The boundary conditions were set at each end of the computational grid. There are three options for boundaries within the GenCade model: pinned, moving and gated. For this study, the boundary at each end of the grid was set to pinned. A pinned boundary condition means that the boundary will not move from the initial shoreline position over the length of the simulation. This boundary condition is reasonable for this study since the computational domain extends such a large distance on each side of the inlet. The non-moving shoreline at each boundary should not affect the results in the area of interest, closer to the inlet.

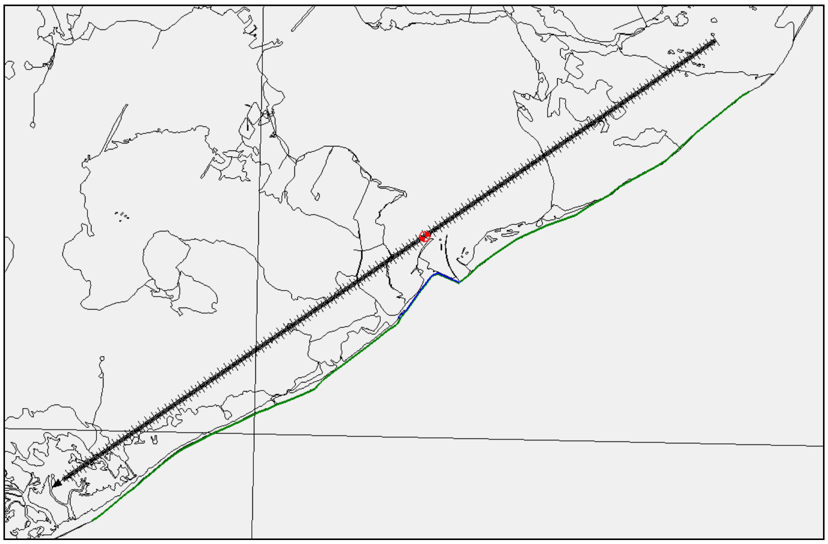

Figure 11.14 - GenCade model grid; initial shoreline is in green and shore protection structure is in blue.

The wave conditions that were input into the GenCade model are a statistically accurate wave dataset that was developed based on the MSC50 hindcast in a similar manner that was described in Section 6.3.2. This wave datset included both normal and extreme wave conditions approaching from five directions (60°, 90°, 120°, 150° and 180°). The one year dataset was repeated as many times as necessary in order to provide the wave input for any simulation length. The waves were set at an offshore depth of 16m, which corresponds to the depth of the MSC50 hindcast grid point.

For every model simulation, including the model calibration runs, the time step was set to 0.5 hours and the model results were output at a 168 hour interval, which is every seven days. Also, the grain size was set to 0.45 mm for the entire computational domain. The selected sediment grain size is based on the sediment sample analysis that was presented in Section 5.2.

11.5.4 Model Calibration

Once the GenCade grid was constructed, the model was then calibrated to ensure the model provides meaningful results. The GenCade calibration was done by changing a number of parameters in an attempt to get the modelled longshore sediment transport rate to match the theoretical longshore sediment transport rate. The theoretical longshore sediment transport rate lays between 2036 m^3/year and 2658 m^3/year, which was calculated in Section 11.1. The parameters used to calibrate the GenCade model are the average berm height, the closure depth, the smoothing parameter and two longshore transport equation coefficients, K1 and K2. The average berm height represents the berm height for the entire length of the coastline within the GenCade model. For this study, the average berm height was set to 1.0 m. The closure depth was set to 20 m and represents the offshore depth beyond which the depths do not change with time. The smoothing parameter is a variable which effects how closely the depth contours follow the shoreline. If the depth contours directly replicated the shoreline, abrupt changes in the shoreline would cause unrealistic wave transformations. The smoothing parameter affects the degree of which the offshore contours are smoothed from the shoreline. The smoothing parameter was set to 25 for this study. The last two calibration parameters, K1 and K2, are coefficients in the longshore sediment transport equation. The K1 coefficient mainly affects the amount of longshore sediment transport over the entire model domain and K2 affects the shoreline evolution in areas influenced by wave diffraction near structures (Frey *et al.*, 2012). These coefficients were adjusted through many calibration runs and the K1 coefficient was set to 0.02 and the K2 coefficient was set to 0.25.

These parameters were adjusted until there was a reasonable match between the modelled longshore transport rate and the theoretical longshore transport rate. The best calibration run resulted in a modelled longshore transport rate of 8816 m^3/year from NE to SW. This modelled transport rate is approximately three times higher than the theoretical transport rate. Typically, the model should be calibrated to measured shoreline change or recorded longshore transport rates. Since this data was not available for this study, theoretical transport values had to be used. Therefore, the calibrated transport rates may not completely reflect the transport rates experienced at the Shippagan Gully inlet. However, the modelled scenarios can be compared to the status quo scenario and the relative change between scenarios can be observed.

11.5.5 Model Results

The model result for the status quo scenario is shown in Figure 11.15. The initial shoreline is indicated by the green line and the modelled shoreline after a ten year simulation is represented by the brown line. As seen in the status quo results, there is a slight advance of the shoreline updrift of the inlet and an advancement of the shoreline immediately west of the inlet. The advancement of the shoreline west of the inlet may be attributed to waves approaching from the south-west. As waves approach from the south-west, the longshore sediment transport travelling SW to NE will be trapped by the structure on the west side of the inlet. The sediment trapped by the structure will not able to be carried away by the easterly approaching waves because of the structure sheltering the area. The attachment point south-west of the inlet is smoothed out by the model since the one-dimensional model is not able to model the sediment inlet bypassing. Elsewhere in the model domain, which is not included in the results shown in Figure 11.15, there is no significant change after the 10 year simulation.

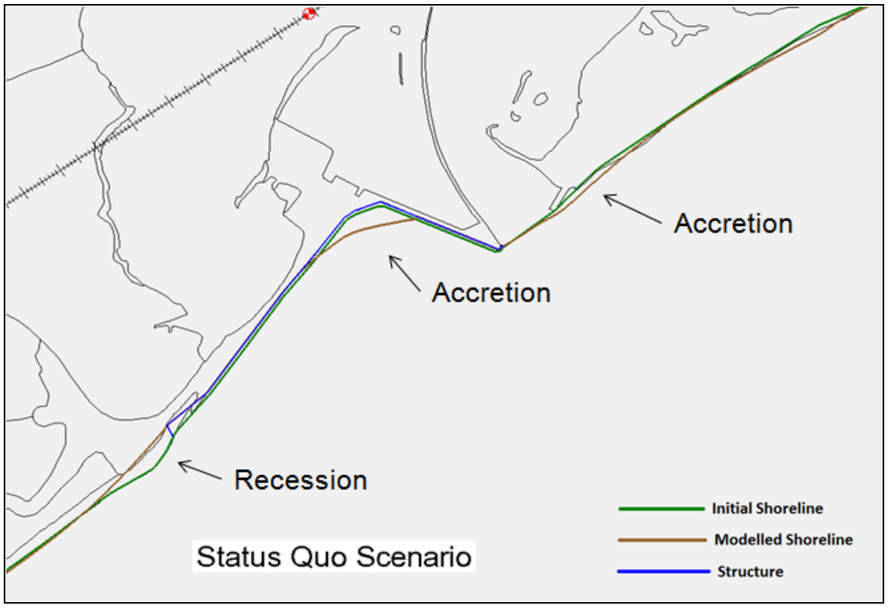

Figure 11.15 – GenCade model results of shoreline change for the status quo scenario. Green line indicates initial shoreline position and the brown line indicates the shoreline position after a 10 year simulation.

Figure 11.17 shows the model results for three scenarios, each with a different jetty length: a) a 50 m jetty, b) a 100 m jetty and c) a 150 m jetty. Higher resolution images of each scenario can be found in Appendix E – Additional GenCade Images. Each of the jetty scenarios do not indicate a very significant change south-west of the inlet when compared to the model results of the status quo. The shoreline immediately updrift (north-east) of the inlet has advanced in each of the jetty scenario. The 50 m jetty causes the smallest advance of the shoreline at 13.5 m and the 150 m jetty causes the largest shoreline advance of 27.5 m. The 100 m long jetty falls in between and causes a shoreline advancement of 22 m. As expected, the largest shoreline advancement occurs adjacent to the jetty and shoreline advancement tapers down over 300 m to the north-east of the jetty.

Plotted in Figure 11.16311.16 is the difference between the final shoreline in the status quo scenario and the final shoreline in each of the jetty scenarios. Positive values indicate the shoreline in the jetty scenarios extends further seaward than the shoreline in the status quo scenario and negative values indicate the opposite case. As seen in this graph, the shoreline retreats up to 18m more than the status quo, immediately downdrift (SW) of the jetties. This shoreline retreat is caused by the jetties trapping the NE to SW longshore sediment transport. A small amount of shoreline erosion is seen at 800m in Figure 11.16311.16, where the rubblemound shore protection structure ends. From 900m and onward, the results show that all modeled jetty lengths have a negligible impact on the shoreline.

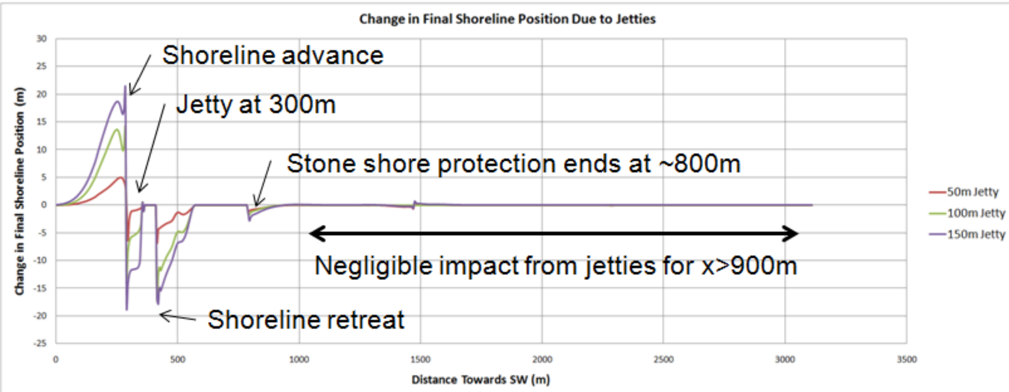

Figure 11.163 – Influence of jetties on final shoreline position relative to the status quo

In general, the GenCade model results do not show any negative impacts to the shoreline at distances greater than approximately 500m downdrift of the jetties. Typically, one would expect the shoreline immediately downdrift of the inlet to erode with the addition of a new sediment trapping jetty. However, since this area has previously experienced large amounts of shoreline erosion, it is protected by a rubblemound structure and therefore the model does not indicate any erosion of the shoreline past the structure. The GenCade results show that there will be essentially no significant shoreline retreat past the end of the rubblemound structure, further south-west of the inlet.

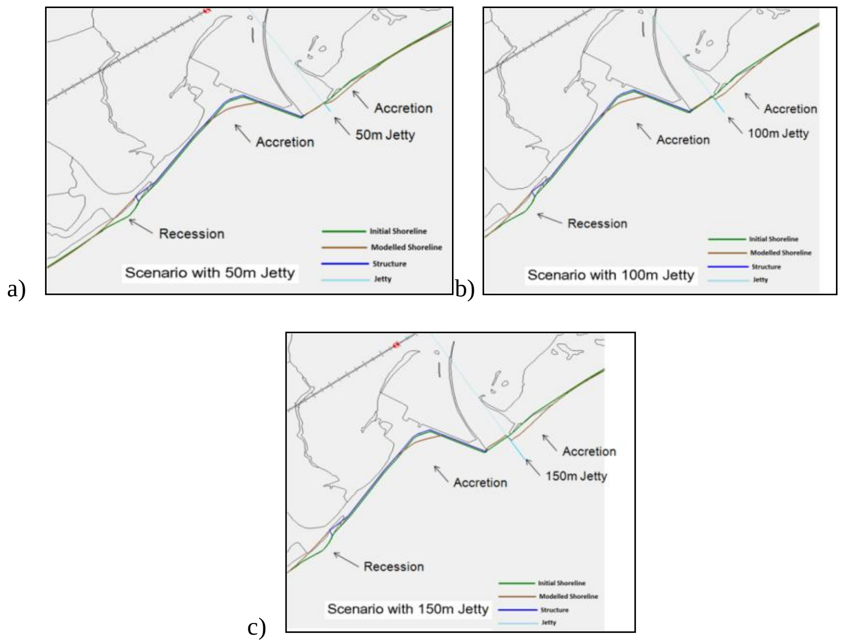

Figure 11.17 – GenCade model results for shoreline change after a 10 year simulation period for a scenario with: a) a 50 m long jetty, b) a 100 m long jetty and c) a 150 m long jetty.

12 Conclusions

Based on the numerical modelling results presented in Chapters 8-11, a number of conclusions can be drawn:

- Utilizing the newly added features to the CMS modelling system (telescoping grid and multiple grain size sediment transport) creates large differences in the morphology change results between the model developed for this study and the model developed for the Phase I study. The differences are mainly a result of the different sediment transport calculation schemes used in each model. The Phase I model shows large build up of deposition in some areas where a large d_{50} value was initially assumed. This build up of deposition is not present in the morphology change results of the newly refined CMS model.

- The maximum velocity within the inlet during the ebb flow (2.1 m/s) and flood flow (1.1 m/s) occur in the location where the sand spit on the east side of the inlet causes a narrowing of the channel. It is also important to note that the maximum flood flow is approximately half of the maximum ebb flow. The model results also show that during both the flood and ebb flow there is no seaward flow on the east side of the inlet. This indicates that the water on the east side of the inlet mouth rarely flows towards the sea.

- The morphology change results showed that deposition will continue to occur along the east side of the navigation channel if the status quo is maintained. This deposition is problematic because it causes the narrowing of the navigation channel.

- The recommended scenarios for Shippagan Gully should have a balance between lower inlet velocities and lower deposition within the inlet. The recommended scenarios are based off a summary of the various key performance indicators that is presented in Appendix D – Summary of Key Performance Parameters. Four of the performance indicators, maximum ebb velocity, maximum flood velocity, deposition within the inlet and minimum inlet width are graphed and compared in Figure 12.1 and Figure 12.2. From Figure 12.1, it can be seen that the "G scenarios", scenarios with a 130 m inlet width, provide the lowest ebb and flood velocities, which increases the ease of navigation through the inlet. However, due to the lower velocities, the G scenarios show larger amounts of deposition within the inlet (shown in Figure 12.2) when compared to the status quo.

- The three best performing scenarios as chosen by the recommendation of the author are: scenario D5, scenario D7 and scenario E2a. Scenario D5 is the scenario which has a 110 m wide channel with a training wall ending in a 150 m jetty and dredging to -4 m. In scenario D5, the maximum velocities experienced in the inlet are reduced by 20% compared to the status quo and the deposition within the inlet is reduced by 20% compared to the status quo. Scenario D7 is the scenario with a channel that tapers from 100 m down to 80 m with a training wall ending in a 150 m jetty and dredging to -4 m. This scenario reduces maximum velocities by 10% and the deposition within the inlet is reduced by 40%. The third recommended scenario, scenario E2a has a 110 m wide channel dredged to -4 m with a rock revetment ending in a 150 m long jetty. In scenario E2a, the maximum velocities are reduced by 20% and the deposition within the inlet is reduced by 10%.

- From the CMS modelling results, it was found that the only significant change along the coastline is on the updrift (north-east) side of the newly added jetties. This change is caused by the jetties trapping the longshore sediment transport arriving from the north-east. In addition to the CMS model results, an additional numerical model, GenCade, was employed for this study. From the GenCade results, there was no significant shoreline change downdrift of the inlet. The only area of major change was updrift of the inlet, similar to the results found from the CMS numerical model.

- It is important to keep in mind the restrictions and limitations of both the CMS and GenCade numerical model employed in this study. Shippagan Gully is a very complex inlet due to the asymmetry of tidal forcing, numerous historical engineering interventions and the highly complex interaction of both hydrodynamic and morphodynamic coastal processes. However, the model results and observations made during this study can be used by PWGSC to help make informed decisions about the future engineer works at the Shippagan Gully tidal inlet. In addition, the various modelling techniques and methods developed to analyze the results in this study can be applied in future studies of tidal inlets.

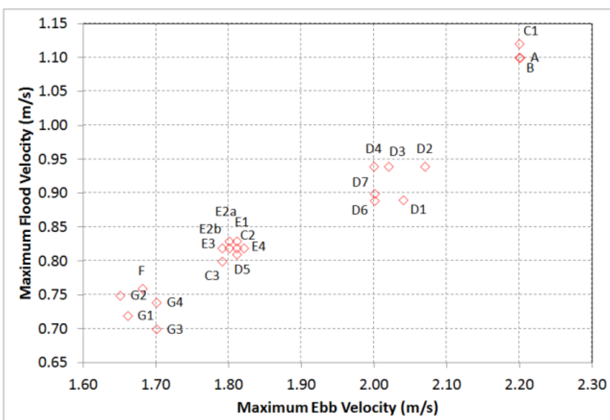

Figure 12.1 – Comparison graph of maximum flood velocity vs. maximum ebb velocity.

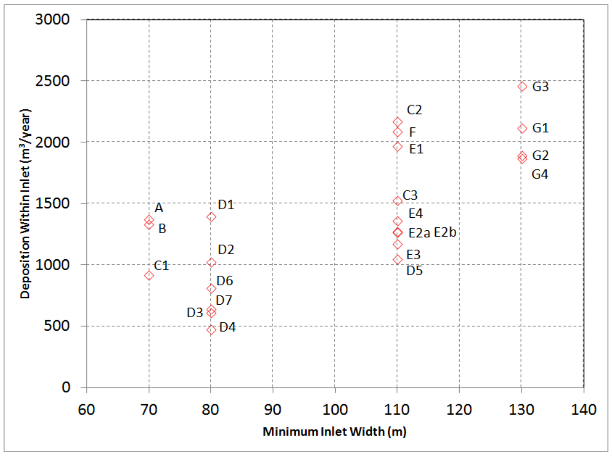

Figure 12.2– Comparison graph of deposition within the inlet vs. minimum inlet width.

13 Future Work

The current study has been successful in furthering our understanding of the complex coastal processes present at Shippagan Gully and provides a good basis for the future work at this tidal inlet. However, there is still much work to be done concerning Shippagan Gully and tidal inlets in general.

The numerical model employed in this study, as with any model, is only as accurate as the calibration and validation conducted on the model. Therefore, any additional field information will help make the model more accurate and allow it to better predict the hydrodynamics and morphology change of various scenarios. The hydrodynamic calibration can be improved by measuring the water level within the inlet for a month long period. This will allow for the water levels and velocities to be calibrated over an entire tidal period. To improve the morphology change calibration additional sediment samples could be taken from the seabed. This will further help with constructing an initial d_{50} map, especially offshore of the inlet, around the ebb shoal area.

Through the simulations conducted in this study, it was found that storms are responsible for large amounts of sediment deposition within the inlet. These observations were made based on model runs that used an idealized 25 hour storm. It may be useful to use actual storms that have caused large amounts of morphology change in the past as an input into the CMS model. This may allow us to observe how the historical storms have helped shape the inlet morphology over the past few decades.

As seen from the model results, a number of scenarios perform in a similar manner in respect to hydrodynamics and morphology change. An interesting aspect to this study would be to conduct a cost analysis on the various scenarios. One scenario may perform slightly better than another, but it also may come with a higher cost. This may aid in the decision making process for the future works at Shippagan Gully.

Finally, future work on another tidal inlet with tidal forcing from two sources, such as the case at Shippagan Gully, may help further the knowledge on this phenomenon. As found in this study, the phase lag between the tidal forcing causes the ebb flow to be twice as strong (on average) as the flood flow. This results in a well-defined crescentic ebb shoal and virtual no flood shoal. By studying other inlets that possess similar ebb and flood flow imbalance, conclusions can be made based on the ratio between the strength of the flood and the strength of the ebb flow. From these conclusions, it would be possible to categorize the morphology features at inlets with an imbalanced ebb and flood flow, similar to the categories that already exist for idealized tidal inlets.

References & Bibliography

Aquaveo. "Water Modeling Solutions, SMS 10.1". XMS Wiki. http://xmswiki.com/xms/SMS:SMS. (2011).

Bahnold, R.S. (1968). Deposition in the Process of Hydraulic Transport. *Sedimentology*, Vol. 10. Pp 45-56.

Bailard, J., 1981. An energetics total load transport model for a plane sloping beach. J. Geophysical Research, 86, C11, 10938-10954.

Battjes, J.A. and J. Janssen, (1978). Energy loss and set-up due to breaking of random waves. *Proceedings 16th International Conference Coastal Engineering*, ASCE, pp. 569-587.

Benoit 2005, TOMAWAC software for finite element sea state modelling, release 5.5 User Manual, EDF-LNHE, France.

Bijker, E.W., 1968. Mechanics of sediment transport by the combination of waves and current. Proc. 23rd Int. Conf. on Coastal Engineering, 147-173.

Bruun, P. (1987). Sediment By-Passing Across Coastal Inlets by Natural Means, by R. Silvester. Discussion. *Coastal Engineering*, Vol. 11, pp. 175-181.

Bruun, P. (1990). Improvement of Bypassing and Backpassing at Tidal Inlets. *Journal of Waterway, Port, Coastal and Ocean Engineering*, ASCE, New York, NY, Vol. 116(4), pp. 494-501.

Buttolph, A.M, C.W. Reed, N.C. Kraus, N. Ono, M. Larson, B. Camenen, H. Hanson, T. Wamsley and A.K. Zundel, 2006. Two-dimensional Depth-Averaged Circulation Model CMS-M2D: Version 3.0, Report 2, Sediment Transport and Morphology Change. USACE Report ERDC/CHL TR-06-9, 148p.

Buttolph, A.M., W.G. Grosskopf, G.P. Bass and N.C. Krauss, (2006). Natural Sand Bypassing and Response of Ebb Shoal to Jetty Rehabilitation, Ocean City Inlet, Maryland, USA. *Proceedings 30th Coastal Engineering Conference*, World Scientific Press, Vol. 3, pp. 3344-3356.

Camenen, B., Larson, M., 2007. A Unified Sediment Transport Formulation for Coastal Inlet Application. USACE Report ERDC/CHL CR-07-1, 247p.

Cooper A.J., 1996, Telemac Modelling System, Validation Document, Rapport Électricité de France-DER, HE-43/96/006/A.

D'Alpaos, A., S. Lanzoni, D. Marani and A. Rinaldo, (2010). On the tidal prism – channel area relations. *Journal of Geophysical Research*, Vol. 115, 2010.

Dabajnia, M. and Watanabe, A., 1992, Sheet flow under non-linear waves and currents. Proc. Int. Conf. on Coastal Engineering, 2015-2029.

Davis, R.E and D.M. FitzGerald, 2004. Beaches and Coasts, Blackwell Science Ltd, Oxford, UK (2004) 419 pp.

Davis Jr., R.A., Hayes, M.O., 1984. What is a Wave-dominated Coast? Hydrodynamics and Sedimentation in Wave-Dominated Coastal Environments. Marine Geology 60, 313–329.

Dean, R.G. and R.A. Dalrymple, 2002. Coastal Processes with Engineering Applications. Cambridge University Press, Cambridge, pp. 413-448

Demirbilek, Z. and V. Panchang, (1998). CGWAVE: A Coastal Surface Water Wave Model of the Mild Slope Equation. Technical Report CHL-98-XX, USACE, Vicksburg, MS.

Dronkers, L.L.)1964). Tidal Computations in Rivers and Coastal Waters. North Holland Publishing Company.

Einstein, H.A. (1942). Formulas or the Transport of Bed Sediment. *Trans. American Society of Civil Engineers*, Vol. 107. Pp. 561-574.

FitzGerald, D.M., N.C. Kraus and E.B. Hands, (2000). Natural Mechanisms of Sediment Bypassing at Tidal Inlets. USACE Report ERDC/CHL CHETN-IV-30, 10p.

Forrester, W.D. (1983). Canadian Tidal Manual, Canada Fisheries and Oceans, Ottawa.

Goda, Y. (1970). A synthesis of breaker indices. *Transactions of the Japan Society of Civil Engineers.* Vol 13. Pp. 227-230.

Goda, Y. (1985). Random seas and design of maritime structures. Tokyo: University of Tokyo Press.

Frey, A. E., Connell, K. J., Hanson, H., Larson, M., Thomas, R. C., Munger, T. S., and Zundel, A., 2012. GenCade Version 1 Model Theory and User's Guide. Coastal and Hydraulics Laboratory, USACE.

Galvin, C. J., Jr. 1971, Wave climate and coastal processes, Water Environments and Human Needs, MIT Press, Cambridge, Mass. pp. 44-78

Hervouet, J-M., 2007. Hydrodynamics of Free Surface Flows. John Wiley & Sons Press, 2007.

Hervouet J.-M; Lang P.; 2000; Telemac-2D version 5.0, Validation Document, Rapport Électricité de France-DER, HP-73/2000/042/A.

Josenhans, Heiner.; 2007. Atlas of the Marine Environment and Seabed Geology of the Gulf of St. Lawrence; Commission géologique du Canada, Dossier public 5346, 75 pages

Kamphuis, J.W. (2000). Introduction to Coastal Engineering and Management. World Scientific Publishing Co. Pte. Ltd., Singapore.

Kraus, N.C., 2008, Engineering of Tidal Inlets and Morphologic Consequences. In: Kim, Y. (editor), Handbook of Coastal Engineering, World Scientific Press, Singapore, 39 p.

Lin, L., Demirbilek, Z., Mase, H., Zheng, J., Yamada, F., 2008, CMS-Wave: A Nearshore Spectral Wave Process Model for Coastal Inlets and Navigation Projects. USACE Report ERDC/CHL CR-08-13, 131p.

Logan, S., Nistor, I., Cornett, A., Faure, T., Drouin, A., 2012. Morphological modelling of a highly dynamic tidal inlet at Shippagan Gully, Canada. Proc 2012 Int. Conf. on Coastal Eng. (ICCE), Santander, Spain.

Luettich, R., and J. Westerink, (2011). A (Parallel) Advanced Circulation Model for Oceanic, Coastal and Estuarine Waters. User's Manual v49. University of North Carolina at Chapel Hill, Institute of Marine Sciences, Morehead City, NC.

Mase, H. (2001). Multidirectional random wave transformation model based on energy balance equation. *Coastal Engineering Journal*, Vol. 43, pp. 317-337.

Meyer-Peter, E., and R. Muller, (1948). Formulas for Bed-load Transport. Proc., International Association for Hydraulic Research, 2nd Meeting, Stockholm, Sweden, pp. 39-64.

Militello, A. And A.K. Zundel, (2003). USACE Report ERDC/CHL CHETN-IV-60, 14p.

Nwogu, O.G. and Z. Demirbilek, (2001). BOUSS-2D: A Boussinesq Wave Model for Coastal Regions and Harbors. ERDC/CHL TR-01-25, Coastal and Hydraulic Laboratory, United States Army Corps of Engineers, Vicksburg, MS.

Pratt, T.C., T.L. Fagerburg and D.C. McVan, (2000). Field Data Collection of Coastal Inlets. USACE Technical Report ERDC/CHL CETN-IV-24, 12p.

Rosati, J.D. and N.C. Kraus (1999). Formulation of Sediment Budgets at Inlets. USACE, Coastal Engineering Technical Note IV-15, Rev. September 2009. 20p.

Sanchez, A., Lin, L., Demirbilek, Z., Beck, T., Brown, M., Li, H., Rosati, J. Wu, W., Reed, C., 2012. Coastal Modelling System Draft User Manual. Coastal and Hydraulics Laboratory, USACE.

Seabergh, W.C. and N.C. Kraus, (2003). Progress in Management of Sediment Bypassing at Coastal Inlets: Natural Bypassing, Weir Jetties, Jetty Spurs, and Engineering Aids in Design. *Coastal Engineering Journal*, Vol. 45, No. 4, pp. 533-563. World Scientific.

Shields, A. (1936). Application of Similarity Principles and Turbulence Research to Bed-Load Movement. Communications of the Prussion Research Institute for Shipbuilding. Berlin, 1936.

Smith, J.M., A.R. Sherlock and D.T. Resio, (2001). STWAVE: Steady-State Spectral Wave Model – User's Manual for STWAVE, Version 3.0. ERDC/CHL SR-01-1, Coastal and Hydraulics Laboratory, United States Army Corps of Engineers, Vicksburg, MS.

Soulsby, R., 1997, Dynamics of Marine Sands. Thomas Telford Press.

Swail, V.R., V.J. Cardone, M. Ferguson, D.J. Gummer, E.L. Harris, E.A. Orelup and A.T. Cox, 2006. The MSC50 Wind and Wave Re-analysis. Environment Canada and Oceanwather Inc. 9th International Workshop on Wave Hindcasting and Forecasting, Sep 25-29, Victoria BC, Canada, 2006.

USACE, (1984). "Shore Protection Manual". United States Army Corps of Engineers, Coastal Engineering Laboratory, Vicksburgh, MS.

Van Rijn, L.C., (1984). Sediment Transport, Part I: Bed-Load Transport. ASCE, *Journal of Hydraulic Engineering*, Vol. 110, pp. 1431-1456.

Van Rijn, L.C., (1998). Principles of coastal morphology. Aqua Publications, Amsterdam, The Netherlands.

Villaret, C. 2004, SYSIPHE Software, release 5.4 User Manual, EDF-LNHE, France.

Watanabe, A., 1987. Three dimensional numerical model of beach evolution. Proc. Coastal Sediments '87. ASCE. 802-817.

Appendix A - Additional Calibration Cross-Sections

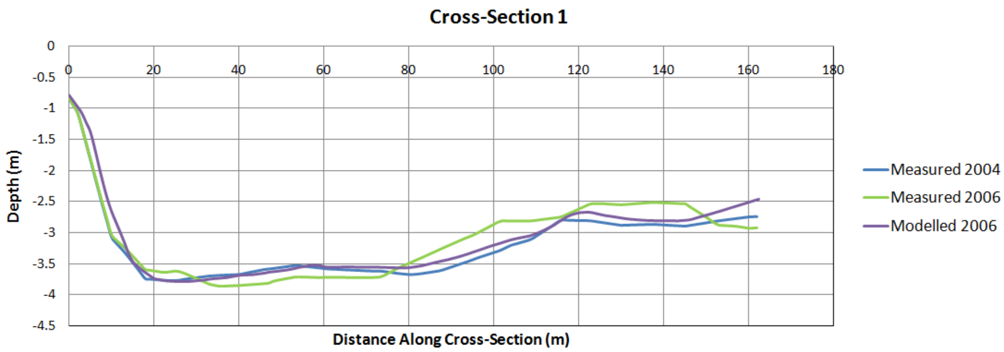

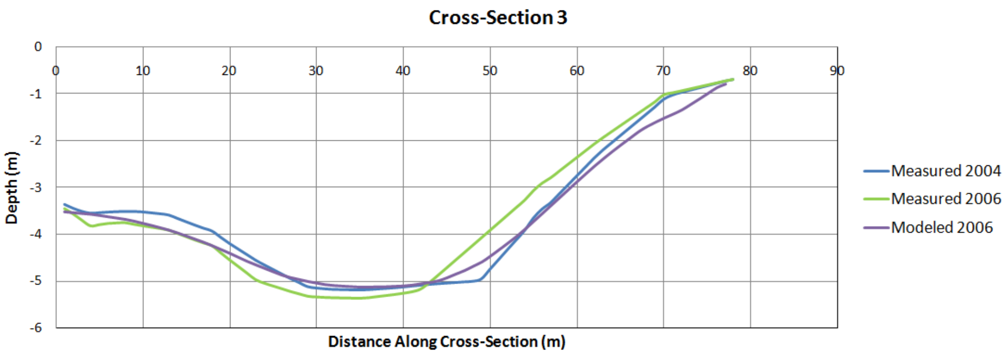

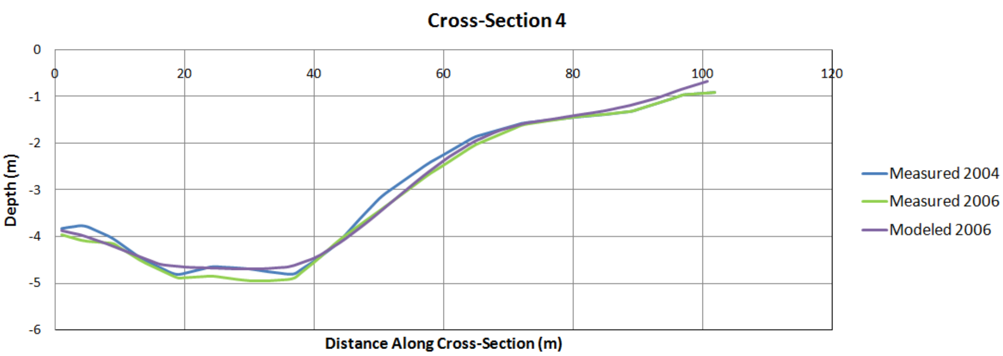

Figure 4 – Additional cross-sections for 2004-2006 morphology change calibration

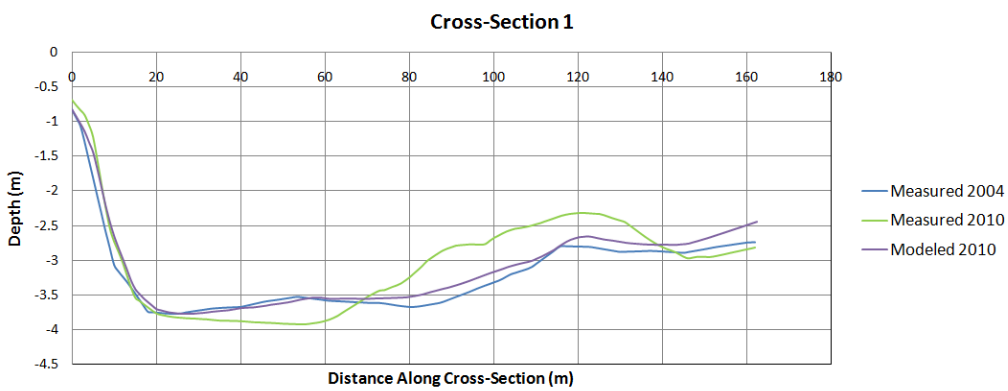
Cross-Section 1
Depth (m)
Distance Along Cross-Section (m)
Measured 2004
Measured 2010
Modeled 2010

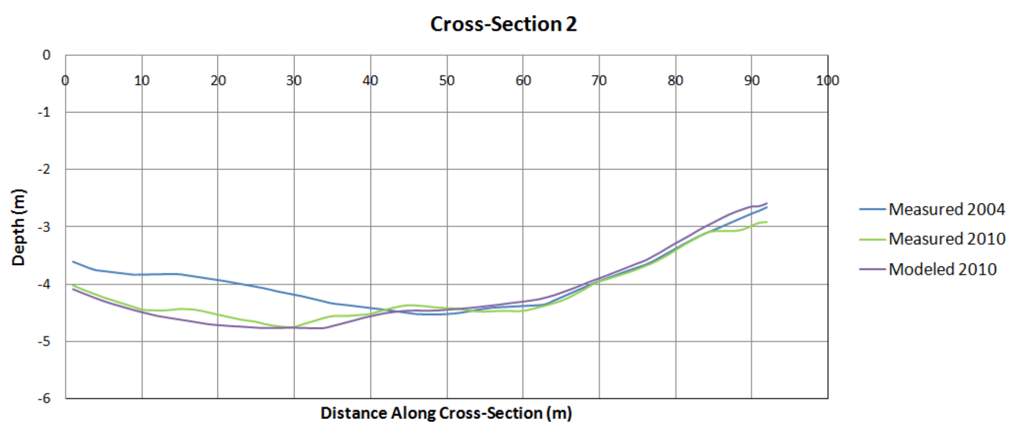
Cross-Section 2
Depth (m)
Distance Along Cross-Section (m)
Measured 2004
Measured 2010
Modeled 2010

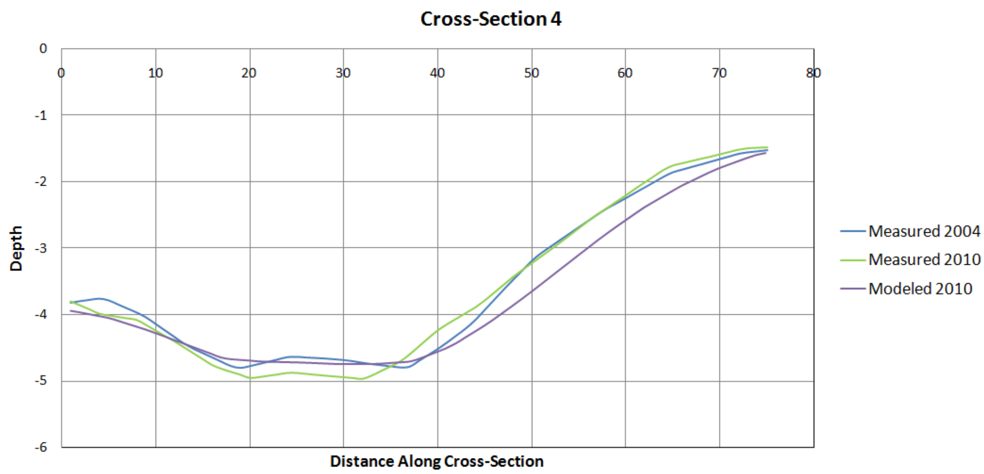

Figure 5 – Additional cross-sections for 2004-2010 morphology change calibration.

Appendix B - Grain Size Distribution Curves

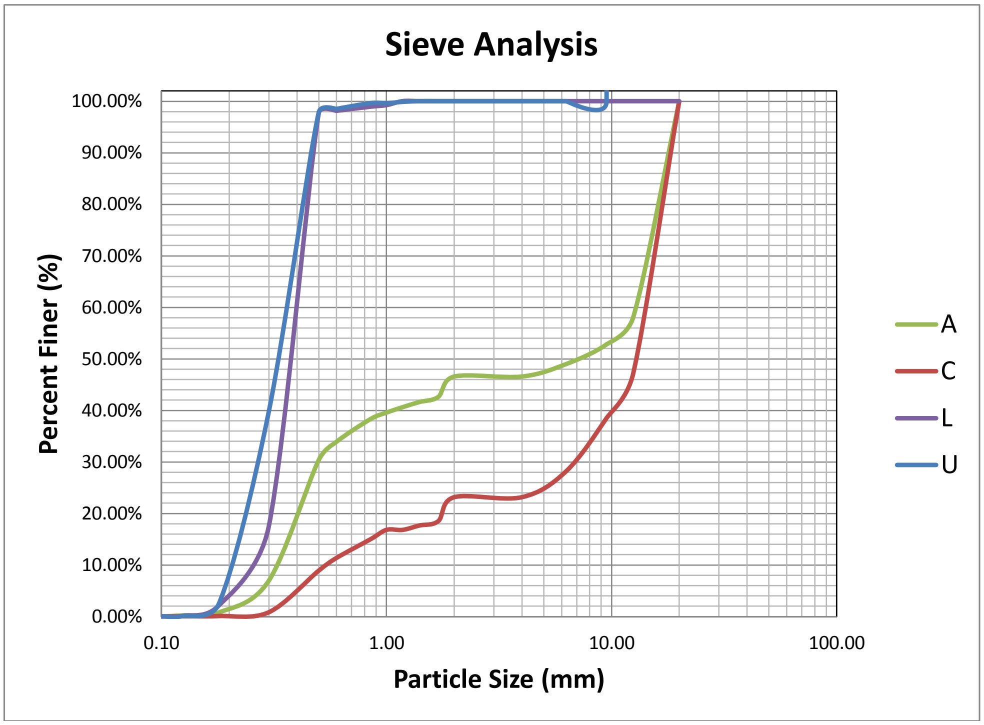

Figure 6 – Sieve analysis of sediment samples collected in May 2012.

GEMTEC
CONSULTING ENGINEERS AND SCIENTISTS

Client:	Public Works & Government Services Canada
Project:	Le Goulet Wharf Assessment Structure 302 and 304
Project #:	0542698

Soils Grading Chart

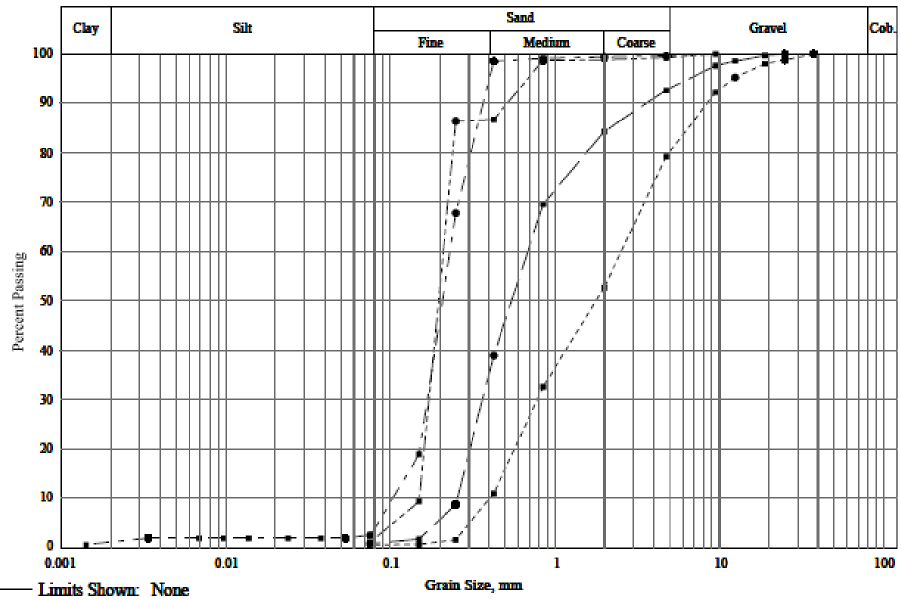

Limits Shown: None

Line Symbol	Description	Borehole/ Test Pit	Sample Number	Depth	% Cob.+ Gravel	% Sand	% Silt	% Clay	Date Sampled
—— ——	Sample A		1		7.3	91.9	0.8		12-08-24
- - - - - - -	Sample B		1		20.9	78.6	0.5		12-08-24
— - — -	Sample C		1		0.4	97.5	1.0	1.1	12-08-24
— - - — -	Sample D		1		0.7	98.3	1.0		12-08-24

Line Symbol	Sample Description	AASHTO	D_{10}	D_{15}	D_{50}	D_{85}	% 5-75μm
—— ——	Sand , trace gravel, trace silt	A-1-b	0.2556	0.2792	0.5464	2.1529	---
- - - - - - -	Gravelly sand , trace silt	A-1-b	0.4025	0.4840	1.7833	6.4749	---
— - — -	Sand , trace gravel, trace silt, trace clay	A-2-4	0.1037	0.1275	0.2076	0.3366	0.26
— - - — -	Sand , trace gravel, trace silt	A-2-4	0.1507	0.1557	0.1964	0.2477	---

GEMTEC
Consulting Engineers and Scientists

Client:	Public Works & Government Services Canada
Project:	Le Goulet Wharf Assessment Structure 302 and 304
Project #:	0542698

Soils Grading Chart

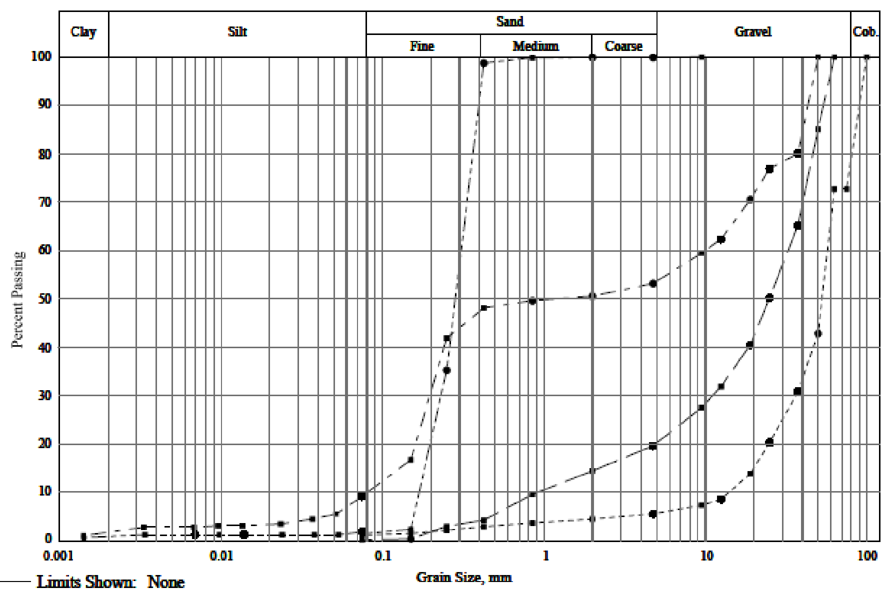

Line Symbol	Description	Borehole/ Test Pit	Sample Number	Depth	% Cob.+ Gravel	% Sand	% Silt	% Clay	Date Sampled
—— ——	Sample E		1		80.4	19.5	0.1		12-08-24
-------	Sample F		1		94.5	4.4	1.1		12-08-24
— - — -	Sample G		1		46.8	44.0	7.4	1.7	12-08-24
—-—-—	Sample H		1		0.1	98.5	0.6	0.9	12-08-24

Line Symbol	Sample Description	AASHTO	D_{10}	D_{15}	D_{50}	D_{85}	% 5-75µm
—— ——	Gravel , some sand , trace silt	A-1-a	0.9218	2.2123	24.8659	49.9216	---
-------	Cobbley gravel , trace sand, trace silt	A-1-a	14.0423	19.9624	52.8485	85.3730	---
— - — -	Gravel and sand , trace silt, trace clay	A-1-b	0.0811	0.1285	1.1947	40.2652	6.41
—-—-—	Sand , trace gravel, trace silt, trace clay	A-2-4	0.1690	0.1826	0.2827	0.3787	0.19

GEMTEC Consulting Engineers and Scientists	Client: Public Works & Government Services Canada Project: Le Goulet Wharf Assessment Structure 302 and 304 Project #: 0542698	Soils Grading Chart

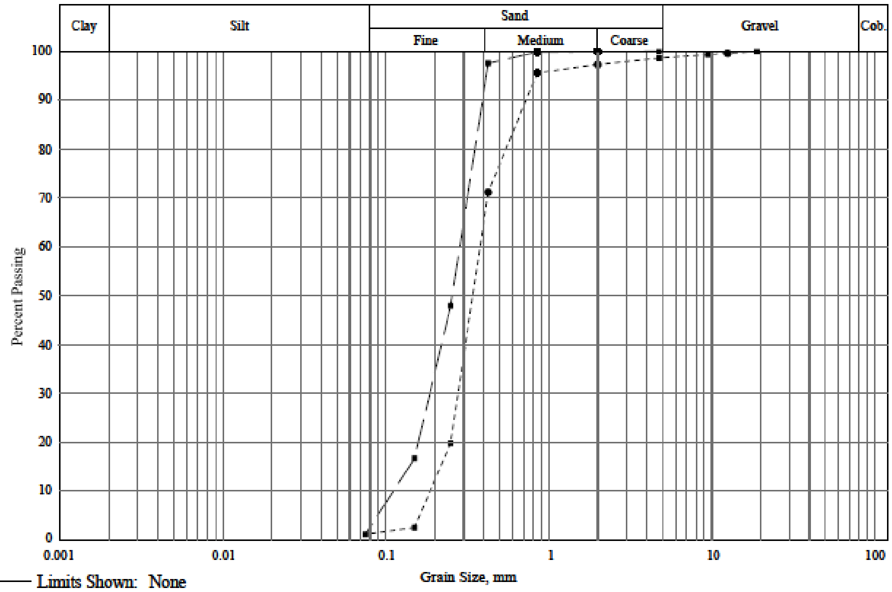

Limits Shown: None

Line Symbol	Description	Borehole/ Test Pit	Sample Number	Depth	% Cob.+ Gravel	% Sand	% Silt	% Clay	Date Sampled
— —	Sample I		1		0.0	98.9	1.1		12-08-24
-------	Sample J		1		1.4	97.5	1.2		12-08-24

Line Symbol	Sample Description	AASHTO	D_{10}	D_{15}	D_{50}	D_{85}	% 5-75μm
— —	Sand , trace silt	A-2-4	0.1113	0.1391	0.2556	0.3715	---
-------	Sand , trace gravel, trace silt	A-2-4	0.1871	0.2168	0.3414	0.6290	---

Appendix C - Velocity Calibration

Table 1. Velocity Calibration Table.

Time	Measured Velocity	D - 0.065_0.03_0.035_0.02_0.022			F - 0.065_0.03_0.035_0.025_0.022			Phase I Calibrated Model		
		Vel	Rel Err	Abs Err	Vel	Rel Err	Abs Err	Vel	Rel Err	Abs Err
8:16	1.180	**1.573**	0.393	0.393	**1.455**	0.275	0.275	**1.160**	-0.016	0.016
8:18	1.500	**1.481**	-0.019	0.019	**1.360**	-0.140	0.140	**1.030**	-0.469	0.469
8:18	0.690	**0.746**	0.056	0.056	**0.819**	0.129	0.129	**0.810**	0.121	0.121
8:19	1.430	**1.379**	-0.051	0.051	**1.255**	-0.175	0.175	**1.080**	-0.350	0.350
8:30	1.500	**1.151**	-0.349	0.349	**1.038**	-0.462	0.462	**1.000**	-0.495	0.495
8:33	1.190	**1.260**	0.070	0.070	**1.185**	-0.005	0.005	**1.040**	-0.151	0.151
8:35	1.290	**1.260**	-0.030	0.030	**1.185**	-0.105	0.105	**1.020**	-0.268	0.268
8:37	0.300	**0.328**	0.028	0.028	**0.444**	0.144	0.144	**0.520**	0.225	0.225
8:42	1.190	**1.292**	0.102	0.102	**1.265**	0.075	0.075	**1.080**	-0.107	0.107
8:43	1.160	**0.839**	-0.321	0.321	**0.825**	-0.335	0.335	**1.000**	-0.164	0.164
8:44	0.680	**0.630**	-0.050	0.050	**0.620**	-0.060	0.060	**0.920**	0.237	0.237
8:51	0.820	**1.009**	0.189	0.189	**0.987**	0.167	0.167	**1.020**	0.196	0.196
8:55	0.780	**0.636**	-0.144	0.144	**0.630**	-0.150	0.150	**0.830**	0.047	0.047
8:56	0.740	**0.636**	-0.104	0.104	**0.630**	-0.110	0.110	**0.830**	0.089	0.089
8:58	0.380	**0.421**	0.041	0.041	**0.416**	0.036	0.036	**0.390**	0.008	0.008
8:58	0.560	**0.434**	-0.126	0.126	**0.429**	-0.131	0.131	**0.390**	-0.165	0.165
9:33	0.490	**0.410**	-0.080	0.080	**0.360**	-0.130	0.130	**0.410**	-0.080	0.080
9:33	0.260	**0.410**	0.150	0.150	**0.360**	0.100	0.100	**0.410**	0.150	0.150
15:35	-0.940	**-0.620**	0.320	0.320	**-0.594**	0.346	0.346	**-0.510**	0.427	0.427
15:36	-0.960	**-0.620**	0.340	0.340	**-0.594**	0.366	0.366	**-0.510**	0.445	0.445
15:38	-0.630	**-0.498**	0.132	0.132	**-0.461**	0.169	0.169	**-0.460**	0.167	0.167
15:40	-0.500	**-0.527**	-0.027	0.027	**-0.469**	0.031	0.031	**-0.460**	0.043	0.043
15:42	-0.460	**-0.509**	-0.049	0.049	**-0.512**	-0.052	0.052	**-0.500**	-0.036	0.036

15:45	-0.860	**-0.670**	0.190	0.190	**-0.648**	0.212	0.212	**-0.600**	0.263	0.263
15:49	-0.290	**-0.429**	-0.139	0.139	**-0.432**	-0.142	0.142	**-0.500**	-0.214	0.214
15:49	-0.520	**-0.429**	0.091	0.091	**-0.432**	0.088	0.088	**-0.500**	0.018	0.018
15:49	-0.600	**-0.429**	0.171	0.171	**-0.432**	0.168	0.168	**-0.500**	0.096	0.096
15:52	-0.680	**-0.376**	0.304	0.304	**-0.364**	0.316	0.316	**-0.340**	0.341	0.341
15:53	-0.780	**-0.287**	0.493	0.493	**-0.286**	0.494	0.494	**-0.340**	0.442	0.442
15:54	-0.270	**-0.367**	-0.097	0.097	**-0.318**	-0.048	0.048	**-0.210**	0.056	0.056
15:55	-0.460	**-0.359**	0.101	0.101	**-0.312**	0.148	0.148	**-0.190**	0.272	0.272
16:15	1.050	**0.839**	-0.211	0.211	**0.855**	-0.195	0.195	**0.900**	-0.153	0.153
16:18	0.800	**0.760**	-0.040	0.040	**0.765**	-0.035	0.035	**0.820**	0.021	0.021
16:38	0.410	**0.752**	0.342	0.342	**0.705**	0.295	0.295	**0.600**	0.190	0.190
16:38	0.360	**0.752**	0.392	0.392	**0.705**	0.345	0.345	**0.600**	0.237	0.237
		Average	**0.059**	**0.164**		**0.050**	**0.180**		**0.050**	**0.200**
		RMSE	**0.209**			**0.215**			**0.239**	

Appendix D – Summary of Key Performance Parameters

Scenario ID	Jetty Length (m)	Dredging Depth (m)	Channel Width (m)		Maximum Ebb Velocity (m/s)			Maximum Flood Velocity (m/s)		
			At Inlet Mouth	At Lagoon Entrance	Zone 1	Zone 2	Zone 3	Zone 1	Zone 2	Zone 3
A	N/A	N/A	150	70	2.20	2.02	1.97	1.11	0.98	0.80
B	N/A	N/A	150	70	2.20	2.03	1.95	1.10	0.97	0.80
C1	50	N/A	110	70	2.20	2.05	1.95	1.12	0.95	0.95
C2	50	4	110	110	1.42	1.56	1.82	0.69	0.80	0.82
C3	50	4	110	110	1.78	1.64	1.79	0.69	0.77	0.80
D1	50	4	110	80	2.04	1.82	1.88	0.89	0.84	0.88
D2	50	3	110	80	2.07	1.89	1.90	0.94	0.88	0.89
D3	150	3	110	80	2.02	1.85	1.86	0.94	0.87	0.89
D4	150	3	100	80	2.00	1.85	1.88	0.94	0.88	0.93
D5	150	4	110	110	1.77	1.72	1.81	0.73	0.81	0.80
D6	150	4	110	80	2.00	1.75	1.80	0.89	0.86	0.88
D7	150	4	100	80	2.00	1.76	1.82	0.90	0.86	0.90
E1	150	4	110	110	1.45	1.53	1.81	0.68	0.83	0.82
E2a	150	4	110	110	1.75	1.60	1.80	0.68	0.81	0.82
E2b	150	4	110	110	1.75	1.60	1.80	0.68	0.81	0.83
E3	200	4	110	110	1.74	1.60	1.79	0.70	0.82	0.82
E4	100	4	110	110	1.76	1.63	1.81	0.70	0.80	0.82
F	N/A	4	150	110	1.50	1.65	1.68	0.60	0.76	0.74
G1	50	4	130	130	1.62	1.51	1.66	0.61	0.68	0.72
G2	200	4	130	130	1.61	1.50	1.65	0.66	0.75	0.71
G3	50	4	130	130	1.68	1.61	1.70	0.63	0.68	0.70
G4	200	4	130	130	1.64	1.58	1.70	0.66	0.74	0.64

Scenario ID	Morphology Change Within Inlet Polygon (m^3/year)			Morphology Change Within Offshore Polygon (m^3/year)		
	Deposition	Erosion	Net Change	Deposition	Erosion	Net Change
A	1370	877	494	1466	43	1423
B	1333	918	415	1463	44	1419
C1	921	896	25	1433	30	1403
C2	2172	73	2099	1647	6	1641
C3	1526	174	1351	1561	8	1553
D1	1398	788	610	1355	49	1306
D2	1026	849	177	1388	37	1351
D3	615	871	-257	1462	17	1445
D4	476	896	-420	1265	19	1246
D5	1050	370	679	1521	7	1514
D6	813	797	16	1554	15	1539
D7	643	818	-175	1238	18	1219
E1	1967	81	1886	1530	6	1525
E2a	1269	180	1090	1385	6	1378
E2b	1272	209	1063	1249	198	1050
E3	1172	177	995	1264	6	1258
E4	1360	184	1176	1466	8	1459
F	2090	135	1955	1716	1	1715
G1	2119	749	1370	1746	34	1712
G2	1895	718	1177	1531	2	1529
G3	2457	566	1891	1801	7	1794
G4	1871	528	1343	1486	2	1484

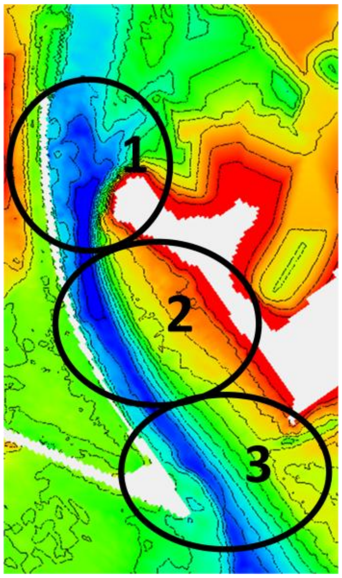

Maximum velocity measurement zones.

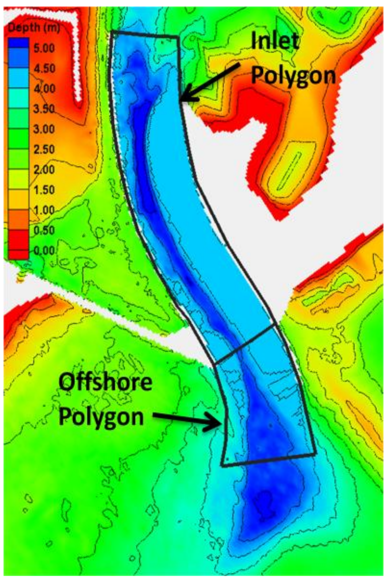

Polygons used to calculate morphology change volumes

Appendix E – Additional GenCade Images

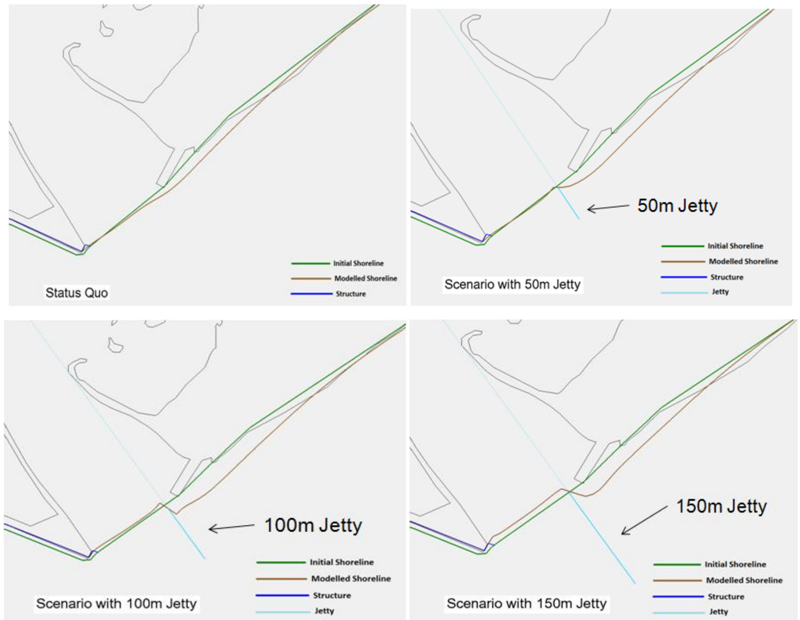

Model results at the inlet.

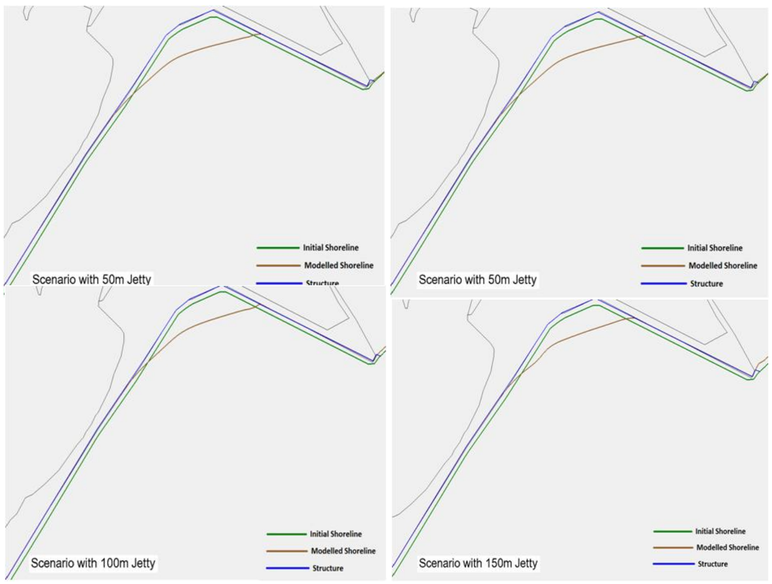

Model results immediately SW of the inlet.

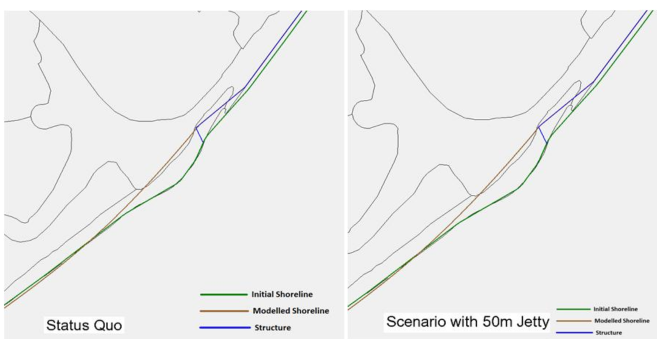

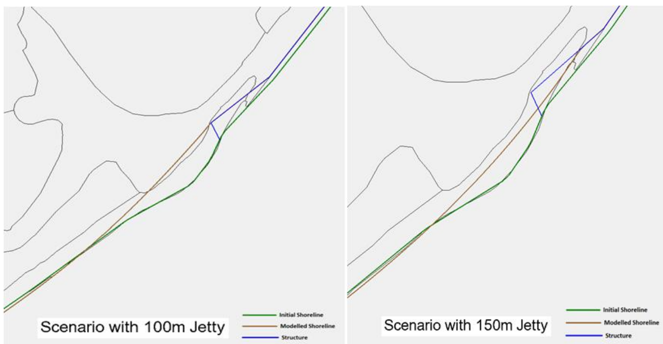

Model results at SW end of rubblemound structure.